Sheffield Hallam University

A Sheffield Hallam University thesis

Investigations of Catalyst and Energy Storage Materials Using ^{57}Fe Mössbauer Spectroscopy

Alex Scrimshire

A thesis submitted in partial fulfilment of the requirements of

Sheffield Hallam University

For the degree of Doctor of Philosophy

December 2018

Declaration

I hereby declare that this thesis submitted for the degree of PhD is the result of my own research and that this thesis has not been submitted for higher degree to any other university or institution.

Alex Scrimshire

Dedication

For my loving parents, brother and partner.

Acknowledgements

First and foremost, I give great thanks to my director of studies, Professor Paul Bingham, who suggested I pursue a PhD and went on to provide equal parts support, guidance, patience and a second serving of patience. The chance of this thesis being completed would be next to zero were it not for his knowledge, motivation and dedication.

The late Sue Forder was a keystone to my own personal development, and to my developed interest in Mössbauer Spectroscopy. Sue was always a pleasure to be around, and always happy to help with any issue, drawing from her vast experience and intellect. My desire to continue working with Mössbauer Spectroscopy is due, in large parts, to her input.

For all the will in the world, very little work could have been done for this thesis, or much else within MERI, were it not for the efforts of our expansive technical and academic team. I'd also like to thank all of the MERI technical and administrative teams for keeping the wheels turning and making sure we're all able to do our part.

I'd like to acknowledge Sheffield Hallam University and Johnson Matthey for funding this project, as well as the scientists of JMTC for their valuable input of their time and knowledge to aid in these studies, and for entrusting me with the responsibility of conducting this research appropriately and successfully.

To all of the friendships that have been made over the last few years, I thank from the bottom of my heart. For making the last few years some of the most interesting and enjoyable, I thank Ben Allsopp ✿, Shuchi Vaishnav, Cristina Pascual-Gonzalez, Georgia Christopoulou, and everyone else in Paul's research group.

For keeping me focused, keeping me motivated and otherwise keeping me sane, I owe a debt of gratitude to my beloved Ronak, without whom I'm not sure this ever would've gotten finished.

Finally, I'd like to thank my family for the support, patience and belief they've had in me during my life. I couldn't have done this without you.

Abstract

To improve the understanding of how functional materials operate is key to developing the next generation of materials in their respective fields. In complex, mixed-phase systems this can often be problematic due to the presence and interference from non-active phases such as support systems or matrices that complicate the data from spectroscopic techniques. The use of techniques that can observe single elements can be a powerful method by which to observe the phase of interest. Mössbauer spectroscopy is a powerful, isotope specific spectroscopic technique that uses gamma rays to probe the hyperfine structure of the nucleus. In this work ^{57}Fe Mössbauer spectroscopy was employed in a collaborative effort with industrial scientists from Johnson Matthey to help develop shared understanding of a selection of industrially important materials.

Lanthanum ferrites are used as heterogeneous three-way catalyst materials for petrol car emission control; iron carbides play important roles in Fischer-Tropsch synthesis; iron molybdates are catalysts for the oxidation of methanol to formaldehyde; and lithium iron phosphate is an energy storage material. These were all chosen to be a part of the studies contained in this thesis. The motivations behind the catalytic studies were of a similar theme – improve the understanding of how these materials operate, how they age, and how changes to the synthesis process and resulting material properties can influence the performance of the materials. The materials chosen, the methods of their synthesis and the differences between them, with performance data for their respective application, chosen for their industrial relevance, were related to their hyperfine structure through ^{57}Fe Mössbauer spectroscopy. Debye temperatures of iron carbides and rare-earth orthoferrite perovskites were approximated through variable temperature Mössbauer spectroscopic studies and other techniques. The studies of lithium iron phosphate, initially of powdered samples, some of which were extracted from electrodes, culminated in in-operando Mössbauer measurements of full cells at the ESRF synchrotron facility. Commercial materials were studied along with the effect of fabricating electrodes, and the charge state of electrodes, yielding useful information on their hyperfine structure. The studies herein, driven by industrial questions, have shown the strengths of Mössbauer spectroscopy for these various research fields.

List of Publications

AHMADZADEH, Mostafa, OLDS, Travis, **SCRIMSHIRE, Alex**, BINGHAM, Paul and MCCLOY, John (2018). Structure and properties of $Na_5FeSi_4O_{12}$ crystallized from $5Na_2O\text{-}Fe_2O_3\text{-}8SiO_2$ glass. Acta Crystallographica Section C: Structural Chemistry, 74, 1595-1602.

MARY, Nicolas, REBOURS, Marius, CASTEL, Elena, VAISHNAV, Shuchi, DENG, Wei, BELL, Anthony, CLEGG, Francis, ALLSOPP, Benjamin, **SCRIMSHIRE, Alex** and BINGHAM, Paul (2018). Enhanced thermal stability of high-bismuth borate glasses by addition of iron. Journal of Non-Crystalline Solids, 500, 149-157.

DESHKAR, Ambar, AHMADZADEH, Mostafa, **SCRIMSHIRE, Alex**, HAN, Edmund, BINGHAM, Paul, GUILLEN, Donna, MCCLOY, John and GOEL, Ashutosh (2018). Crystallization behavior of iron- and boron-containing nepheline ($Na_2O\bullet Al_2O_3\bullet 2SiO_2$) based glasses: Implications on the chemical durability of high-level nuclear waste glasses. Journal of the American Ceramic Society, 4, 1-21.

SCRIMSHIRE, Alex, LOBERA, Alex, BELL, Anthony, JONES, Hywel, STERIANOU, Iasmi and BINGHAM, Paul (2018). Determination of Debye Temperatures and Lamb-Mössbauer Factors for $LnFeO_3$ Orthoferrite Perovskites (Ln = La, Nd, Sm, Eu, Gd). Journal of Physics: Condensed Matter, 30 (10).

CASSIDY, Simon J., ORLANDI, Fabio, MANUEL, Pascal, HADERMANN, Joke, **SCRIMSHIRE, Alex**, BINGHAM, Paul and CLARKE, Simon J. (2018). Complex magnetic ordering in the oxide selenide $Sr_2Fe_3Se_2O_3$. Inorganic Chemistry, 57 (16), 10312-10322.

PAGE, Jacob, TOPPING, Craig, **SCRIMSHIRE, Alex**, BINGHAM, Paul, BLUNDELL, Stephen and HAYWARD, Michael (2018). Doped Sr_2FeIrO_6 – phase separation and a $J_{eff} \neq 0$ state for Ir^{5+}. Inorganic Chemistry, 57 (16), 10303-10311.

BINGHAM, Paul, VAISHNAV, Shuchi, FORDER, Sue, **SCRIMSHIRE, Alex**, JAGANATHAN, Balaasaran, ROHINI, Jiji, MARRA, James, FOX, Kevin, PIERCE, Eric, WORKMAN, Phyllis and VIENNA, John (2017). Modelling the sulfate capacity of simulated radioactive waste borosilicate glasses. Journal of Alloys and Compounds, 695, 656-667.

SCRIMSHIRE, Alex, LOBERA, Alex, KULTYSHEV, Roman, ELLIS, Peter, FORDER, Sue and BINGHAM, Paul (2016). Variable temperature ^{57}Fe-Mössbauer spectroscopy study of nanoparticle iron carbides. Croatica Chemica Acta, 88 (4).

Conferences

Johnson Matthey Academic Conference 2015, Loughborough. "*Advanced Spectroscopy of Catalytic and Energy Materials*" Poster

MERI Research Symposium 2015, Sheffield Hallam University. "*Advanced Spectroscopy of Catalytic and Energy Materials*" Poster

The Mediterranean Conference on the Application of the Mössbauer Effect (MECAME), 7 – 10 June 2015, Zadar, Croatia. "*Variable temperature Mössbauer spectroscopy study of nano-particle iron carbides*" Poster

Johnson Matthey Academic Conference 2016, Loughborough. "*A Mössbauer Spectroscopic Study of Lithium Iron Phosphate Cathodes*" Poster

Johnson Matthey Academic Conference 2017, Loughborough. "*Applications of Mössbauer Spectroscopy in Developing Next Generation Catalyst and Energy Materials*" Oral Presentation

MERI Research Symposium 2016, Sheffield Hallam University. "*Using Mössbauer Spectroscopy to develop improved catalysts and batteries*" Oral Presentation

The Mediterranean Conference on the Application of the Mössbauer Effect (MECAME), 27 – 31 May 2018, Zadar, Croatia. "*Determination of Debye Temperatures and Lamb-Mössbauer Factors for LnFeO$_3$ Orthoferrite Perovskites (Ln = La, Nd, Sm, Eu, Gd)*". Oral Presentation

Society of Glass Technology Conference 2018, Murray Edwards College Cambridge, 2 – 5 September 2018. "*Structural role and crystallisation behaviour of iron in aluminosilicate glasses for radioactive waste immobilisation*". Oral Presentation

Prizes and Awards

Best Young Scientist 2015 – Awarded at MECAME 2018 to best young scientist presenting that year.

Paul Award 2018 – Awarded at SGT 2018 "for the best presentation (clarity, technical content) as voted by the audience."

Contents

List of Abbreviations

B_{eff}	Magnetic Zeeman splitting
BET	Brunauer–Emmett–Teller
CNAC	Citrate-nitrate auto-combustion
CS, δ	Centre shift, Chemical isomer shift
CTAB	Cetyltrimethylammonium bromide
EDX	Energy dispersive X-ray spectroscopy
EPMA	Electron probe micro-analyser
ESRF	European Synchrotron Radiation Facility
FSP	Flame spray pyrolysis
FTS	Fischer-Tropsch Synthesis
$\Gamma/2$	Linewidth – half width at half maximum
ICDD	The International Centre for Diffraction Data
ICP	Inductively coupled plasma [mass spectrometry]
IS	Isomer shift
JMTC	Johnson Matthey Technology Centre
LFP	Lithium iron phosphate
MERI	Materials and Engineering Research Institute
NMP	N-methyl-2-pyrrolidone
OCV	Open circuit voltage
OSC	Oxygen storage capacity
PEIS	Potentiostatic electrochemical impedance spectroscopy
PGM	Platinum-group metal
PVDF	Polyvinylidene fluoride
SEM	Scanning electron microscope
SHU	Sheffield Hallam University
SODS	Second order Doppler shift
THC	Total hydrocarbons
Θ_D	Debye temperature
TWC	Three-way catalysis
QS, ΔeQ	Quadrupole splitting
XRD	X-ray diffraction
XRF	X-ray fluorescence

1 Introduction

"It is important that good communication be maintained between industrial scientists and Mössbauer spectroscopists so that the unique properties of the technique and the contribution it can make to industrial research are identified and fully realized." – Frank J. Berry, 2002 [1]

This quote from Professor Frank Berry is as pertinent today, 16 years later, as it was when he originally wrote it in his 2002 publication entitled "Industrial applications of Mössbauer spectroscopy" [1]. One could argue that it may in fact be more pertinent, as the diversity of materials being produced through the ever-increasing variety of processes has only increased in this time. Through working closely with industrial colleagues at Johnson Matthey Research Centre, the studies herein aim to maintain the good communication advocated by Professor Berry, and to showcase the unique properties of Mössbauer spectroscopy and how they can benefit many fields of research. In the studies that follow, several catalyst materials have been explored, as well as cathode materials for lithium-ion batteries, with the materials selected in order to yield the most useful information for the advancement of their applications. Each self-contained chapter will focus on an individual application, complete with the relevant background literature, material characterisation and spectroscopic studies. The techniques will be explored in some detail, and the theories that govern them.

The Mössbauer effect, discovered by Rudolf Mössbauer in 1957 [2], is the phenomenon of emission or absorption of a γ-ray photon, without the loss of energy due to recoil, and without thermal broadening. The resultant monochromatic electromagnetic radiation, with the proper instrumentation, can be used to resolve minute energy differences between two nuclear levels, to a resolution approaching 1 in 10^{12} eV [3]. First observed for ^{191}Ir, the Mössbauer effect has now been detected in over 40 elements, including ^{197}Au, ^{129}I, ^{121}Sb and the most commonly studied ^{57}Fe (see Table 1.1). Laboratory transmission ^{57}Fe Mössbauer spectroscopy utilizes Doppler shifted γ-ray photons emitted by a ^{57}Co source, oscillating at constant acceleration relative to the sample. When the modulated γ-ray energy matches the excitation energy of the ^{57}Fe atoms in the

sample, absorption can occur, which is observed as a reduction in transmission by the detector. From Mössbauer spectra, information regarding the nuclear environment around ^{57}Fe can be determined, including the oxidation state, co-ordination number and local environment, and the presence or absence of an internal magnetic field [3]. Due to the sensitivity of Mössbauer spectroscopy, and the amount of information it can yield about a material, the areas in which it has been used are wide-reaching, and include materials science medicine, astronomy, and biochemistry (illustrated in Figure 1).

Table 1.1. Common Mössbauer Isotopes. (Spin states; gd = ground state, ex = excited state)

| Isotope	Natural abundance (%)	Spin states (gd)	(ex)	Eγ [4] (keV)	Source isotope	Half-life [4]	Line width [5] (mm s^{-1})
^{57}Fe	2.14	1/2	3/2	14.4	^{57}Co [6]	271.8 d	0.2
^{99}Ru	12.8	3/2	5/2	89.4	^{99}Rh [7]	16.1 d	0.3
^{119}Sn	0.63	1/2	3/2	23.8	^{119m}Sn [8]	293.1 d	0.8
^{121}Sb	2.1	5/2	7/2	37.2	^{121m}Sn [9]	55 y	1.8
^{127}I	100	5/2	7/2	57.6	^{127m}Te [10]	109 d	0.8
^{193}Ir	61.5	1/2	3/2	73.0	^{193}Os [11]	30.5 h	1.4
^{197}Au	100	3/2	1/2	77.3	^{197}Pt [12]	19.9 h	1.9
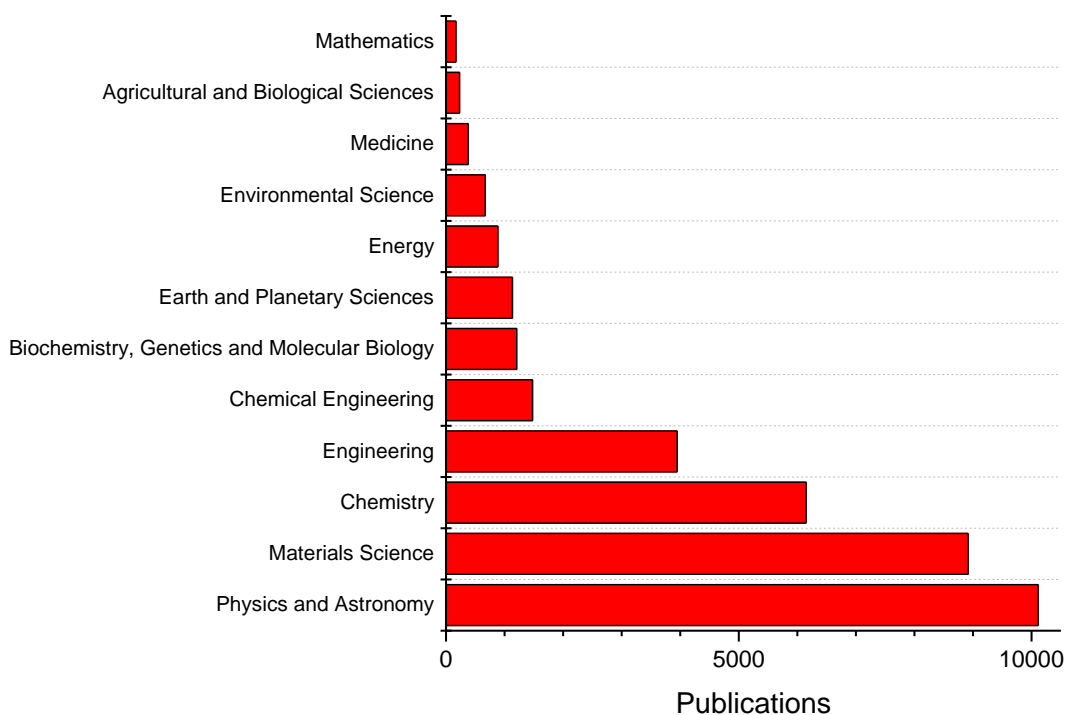
Figure 1.1. Top 12 subject fields with publications in Scopus® containing keyword "Mössbauer" since 1965. Represents 35,272 of 35,691 publications.

In a *Scopus* search of all articles available through the online search engine published since 1959, 45,203 articles contained "Mössbauer" as a keyword; of those, 29,535 also had the keyword of "iron" – 10,000 papers were published on ^{57}Fe Mössbauer spectroscopy between 1953 and 1982 alone [13]. ^{57}Fe has the most advantageous combination of properties, as presented in Table 1.1, including a low natural linewidth, relatively long half-life, and sufficient isotopic abundance. Similar, and equally valuable information can be obtained from the other Mössbauer active isotopes, however, ^{57}Fe Mössbauer spectroscopy is by far the most popular. The popularity of ^{57}Fe Mössbauer spectroscopy can, in part, be attributed to the wide range of iron-bearing materials and the equally wide range of applications in which they are used. Recent publications utilising Mössbauer spectroscopy include investigations into the superconductivity of antiperovskite $Sr_{3-x}SnO$ [14], multiferroic $Bi_{0.85}Nd_{0.15}FeO_3$ [15], anion doping of lithium iron phosphate for energy storage application [16]–[19], and the effects of crystal formation and phase separation of nepheline in nuclear waste glasses [20]. Mössbauer spectroscopy has also proved useful in radiopharmacology [21], plant nutrition [22] and in the treatment of cancer through magnetic hyperthermia [23]. The accessibility of many Mössbauer active isotopes, as shown in Table 1.1, allow for a wide range of materials and applications to be investigated using this powerful and unique technique.

The focus of this work is on the application of Mössbauer spectroscopy to several industrially relevant catalyst and energy storage materials, each of which have their own chapter. The catalyst systems studied are rare-earth iron orthoferrite perovskites for petrol vehicle emission control, iron carbides as catalysts for Fischer-Tropsch synthesis and iron molybdates for the oxidation of methanol to formaldehyde. Energy storage materials focus on lithium iron phosphate as the active material on Li-ion battery cathodes. The materials studied were selected following discussions between the author, supervisory team, and research scientists of Johnson Matthey Technology Centre, Sonning Common, with the aims of answering their crucial, industrially relevant questions. Iron in these materials plays an active role in their application, acting as catalyst iron sites, or the redox site in battery cathodes. Due to the isotope-specific nature of the technique, Mössbauer spectroscopy can probe the local nuclear

environment of the iron in these systems and yield useful information regarding its oxidation state, co-ordination and magnetic structure, which can aid in understanding how the iron facilitates its role in the materials' application. Of most importance to industry are questions regarding the active sites of catalysts and how these may change during service and deactivate as the catalyst ages or be influenced by altering the composition of the material through doping; similarly, there are questions for the electrochemical applications concerning the functional role and stability of iron in these materials, and mechanisms observed through their aging. The studies to follow aim to improve the communication between industrial scientists and Mössbauer spectroscopists by contributing knowledge in these fields, directed by industry, to improve the existing products through enhanced understanding with this powerful technique.

Studies conducted into lanthanum ferrites were aimed to improve the understanding of their three-way catalytic behaviour through interpreting their hyperfine structures and catalytic performance as a result of varying their composition (A-site, B-site cation doping and A-site vacancies), synthesis methods (ball milling, flame spray pyrolysis, citrate-nitrate auto-combustion and co-precipitation) and post synthesis treatments (acid washing and iron impregnation). Superparamagnetic behaviour was observed where the synthesis method resulted in sufficiently small crystallites, most notably in the materials synthesised through flame spray pyrolysis. Definitive correlation of spectroscopic data and catalytic performance was not achieved through this project.

The investigations into both iron molybdate catalysts for the oxidation of methanol to formaldehyde and iron carbides for Fischer-Tropsch synthesis were aimed to determine the catalytically active sites and/or active phases of complex industrial catalysts. This was achieved through the investigation of fresh (as-produced) and aged (post-catalytic) materials. It was shown that the iron molybdate catalysts currently being used deactivate primarily, and to the point that they require replacement, before any changes to the iron environment occurs. The deactivation process begins with the loss of molybdate groups and may proceed to the reduction of the iron, which was not observed. Two iron carbides (Fe_3C and Fe_5C_2) were analysed from 10 to 293 K, and their Debye temperatures and recoil-free fractions were approximated through the correlation

between measured centre shifts and temperature. An approximated recoil-free fraction allows for the relative abundance of iron-bearing phases to be considered from spectroscopic relative areas. The studied mixed-phase industrial catalyst was found to be consistent with superparamagnetic α-Fe_2O_3, with a minor amount of iron reduction resulting from the catalytic ageing process.

Exploratory investigations were conducted on a range of lithium iron phosphate materials, including studies into the effects of electrode fabrication on the hyperfine structure of the material, the cause of observed electrochemical differences seen in between commercially available and between in-house $LiFePO_4$ materials, and how the relative areas of $LiFePO_4$ and $FePO_4$ vary with cell discharging. Operando measurements of electrochemical coin cells was made possible through the development of a new coin cell holder and adapted coin cell components as a part of this project. Operando measurements made possible by this can probe the iron environment of $LiFePO_4$ during operation, observing the degradation of cells through charge – discharge cycling and allow for long-term studies to be conducted on a single specimen.

1.1 Thesis Overview

The chapters in this thesis have been structured such that each of the four families of materials, grouped by application, have their own chapter, complete with introductions involving background literature, their material synthesis and characterisations, and Mössbauer spectroscopy studies. Prior to these materials sections is a general synthesis and characterisation section, following a section detailing the theory that governs Mössbauer spectroscopy and the instrumentation used. Each section is designed to be self-contained allowing the reader to receive all the relevant information for the material they are most interested in without relying heavily on having read the previous sections.

The four materials, split by application, are: rare-earth orthoferrites, primarily $LaFeO_3$ for the catalysis of petrol car emissions (CO, NO_x); iron molybdate, which catalyses the oxidation of methanol to formaldehyde; iron carbides, Fe_3C and Fe_5C_2, which are catalysts for Fischer-Tropsch synthesis as well as important metallurgical phases; and lithium iron phosphate, an energy storage material that acts as the cathode in rechargeable Li^+ ion batteries.

References

[1] F. J. Berry, "Industrial applications of Mössbauer spectroscopy," *Hyperfine Interact.*, vol. 144–145, no. 1–4, pp. 381–390, 2002.

[2] R. L. Mössbauer, "Kernresonanzfluoreszenz von Gammastrahlung in Ir191," *Zeitschrift für Phys.*, vol. 151, no. 2, pp. 124–143, Apr. 1958.

[3] N. N. Greenwood and T. C. Gibb, *Mössbauer spectroscopy*. London: Chapman and Hall, 1971.

[4] R. B. Chu, S. Y. F.; Ekström, L. P.; Firestone, "Table of Radioactive Isotopes," *The Lund/LBNL Nuclear Data Search*, 1999. [Online]. Available: http://nucleardata.nuclear.lu.se/toi/index.asp. [Accessed: 03-Nov-2018].

[5] R. V. Parish, *NMR, NQR, EPR and Mössbauer spectroscopy in inorganic chemistry*. Ellis Horwood Ltd, 1990.

[6] V. Rusanov, S. Stankov, V. Angelov, and V. Schünemann, "Line width of single-crystal Mössbauer absorption," *Nucl. Instruments Methods Phys. Res. Sect. B Beam Interact. with Mater. Atoms*, vol. 170, pp. 443–453, 2000.

[7] G. Long, M. DeMarco, D. Coffey, M. K. Toth, and M. S. Torikachvili, "Phase transitions in Sr_2YRuO_6 investigated by Mössbauer spectroscopy, magnetization, and thermodynamic measurements," *Phys. Rev. B*, vol. 87, no. 2, p. 024416, 2013.

[8] G. Ayyakannu Sundaram *et al.*, "^{119}Sn Mössbauer and Ferromagnetic Studies on Hierarchical Tin- and Nitrogen-Codoped TiO_2 Microspheres with Efficient Photocatalytic Performance," *J. Phys. Chem. C*, vol. 121, no. 12, pp. 6662–6673, 2017.

[9] C. Benndorf, L. Heletta, T. Block, H. Eckert, and R. Pöttgen, "Crystal Structure, Magnetism, ^{89}Y Solid State NMR, and ^{121}Sb Mössbauer Spectroscopic Investigations of YIrSb," *Zeitschrift für Anorg. und Allg. Chemie*, vol. 643, no. 4, pp. 294–298, 2017.

[10] T. Nishimura, H. Iwasaki, M. Takahashi, and M. Takeda, "^{127}I Mössbauer

spectra for phenyliodonium ylides," *J. Radioanal. Nucl. Chem.*, vol. 255, no. 3, pp. 499–502, 2003.

[11] J. A. Sawicki, K. Marcinkowska, and F. E. Wagner, "[193]Ir Mössbauer spectroscopy of Pt-IrO$_2$ nanoparticle catalysts developed for detection and removal of carbon monoxide from air," *Nucl. Instruments Methods Phys. Res. Sect. B Beam Interact. with Mater. Atoms*, vol. 268, no. 16, pp. 2544–2555, 2010.

[12] T. Bartsch *et al.*, "New quaternary arsenide oxides with square planar coordination of gold(i) – structure, [197]Au Mössbauer spectroscopic, XANES and XPS characterization of Nd$_{10}$Au$_3$As$_8$O$_{10}$ and Sm$_{10}$Au$_3$As$_8$O$_{10}$," *Dalt. Trans.*, vol. 44, no. 12, pp. 5854–5866, 2015.

[13] D. P. E. Dickson and F. J. Berry, *Mössbauer Spectroscopy*. Cambridge University Press, 2005.

[14] M. Oudah *et al.*, "Evolution of Superconductivity with Sr-Deficiency in Antiperovskite Oxide Sr$_{3-x}$SnO," *Sci. Rep.*, vol. 9, no. 1, pp. 1–9, 2019.

[15] X. Liu, G. Wang, J. Wu, M. Li, S. Pu, and Z. Hu, "Enhanced multiferroic properties of Bi$_{0.85}$Nd$_{0.15}$FeO$_3$ ceramics with excess Bi$_2$O$_3$," *J. Alloys Compd.*, vol. 791, pp. 200–207, 2019.

[16] T. Yu, Z. Wang, Y. Fu, Y. Xiong, and S. Guan, "Sulfur substituted LiFePO$_4$/C with improved rate performance for lithium ion batteries," *Int. J. Electrochem. Sci.*, vol. 11, pp. 5999–6008, 2016.

[17] Q. H. Le *et al.*, "Formation, structure and properties of fluoro-sulfo-phosphate poly-anionic glasses," *J. Non. Cryst. Solids*, vol. 477, no. October, pp. 58–72, 2017.

[18] M. H. Braga, C. M Subramaniyam, A. J. Murchison, and J. B. Goodenough, "Nontraditional, Safe, High Voltage Rechargeable Cells of Long Cycle Life," *J. Am. Chem. Soc.*, vol. 140, no. 20, pp. 6343–6352, 2018.

[19] K. Okada, I. Kimura, and K. Machida, "High rate capability by sulfur-doping into LiFePO$_4$ matrix," *RSC Adv.*, vol. 8, pp. 5848–5853, 2018.

[20] A. Deshkar *et al.*, "Crystallization behavior of iron- and boron-containing nepheline ($Na_2O \cdot Al_2O_3 \cdot 2SiO_2$) based model high-level nuclear waste glasses," *J. Am. Ceram. Soc.*, vol. 4, no. January, pp. 1–21, 2018.

[21] E. Kuzmann, Z. Homonnay, S. Keresztes, M. Antalffy, and J. Környei, "^{119}Sn Mössbauer study of Sn-containing radiopharmaceutical kits," *Hyperfine Interact.*, vol. 239, no. 1, 2018.

[22] A. Lengyel *et al.*, "Characterization of nanomagnetites co-precipitated in inert gas atmosphere for plant nutrition," *Hyperfine Interact.*, vol. 239, no. 1, pp. 1–7, 2018.

[23] J. Park, H. Choi, S. J. Kim, and C. S. Kim, "Examination of the magnetic hyperthermia and other magnetic properties of $CoFe_2O_4@MgFe_2O_4$ nanoparticles using external field Mössbauer spectroscopy," *AIP Adv.*, vol. 8, no. 5, 2018.

2. Mössbauer Spectroscopy

2.1 Theory of the Mössbauer effect

Otherwise known as *recoilless nuclear resonance fluorescence*, the Mössbauer effect is the resonant, and recoil-free emission and absorption of γ-ray photons by the nucleus [1]. To understand the Mössbauer effect, it is first important to familiarise oneself with more widely applicable laws of physics, primarily the law of inertia. It is known that a body at rest will remain at rest, until acted upon by an external force, this is taught in high school physics classes and is most commonly depicted through examples of balls, or boats. The same laws apply on an atomic level and are a key factor in achieving the Mössbauer effect, as the emission and absorption of a γ-ray photon are taking a body from rest and applying a force. To consider an isolated free nucleus, the emission of a γ-ray in one direction, with energy E_γ will cause the nucleus to recoil in the opposite direction, with 'recoil energy' E_R. The nucleus will have a mass of M, and will have been in free motion, in direction x, prior to emission with velocity V_x. If the energy difference between the excited state (E_e) and ground state (E_g) of the nucleus is taken to be E, it follows that $E = E_e - E_g$. To consider this event to occur only in one direction, that being in which the γ-ray is emitted and in which the nucleus recoils, the total energy of the nucleus, prior to emission, would be the sum of its kinetic energy ($\frac{1}{2}MV_x^2$) and the energy difference between spin states, E. After emission, the system will consist of the γ-ray, with energy E_γ, and the nucleus, which will have a new velocity, due to the recoil, ($V_x + v$), where v is a vector, the direction of which can be opposite to that of V_x. The kinetic energy of the nucleus can therefore be expressed as $\frac{1}{2}M(V_x + v)^2$ [2].

E_γ v

Atom at rest   **Atom after recoil**

Velocity	V_x	$V_x + v$
Energy	$E + \frac{1}{2}MV_x^2$	$E_\gamma + \frac{1}{2}M(V_x + v)^2$
Momentum	MV_x	$M(V_x + v) + E\gamma/c$
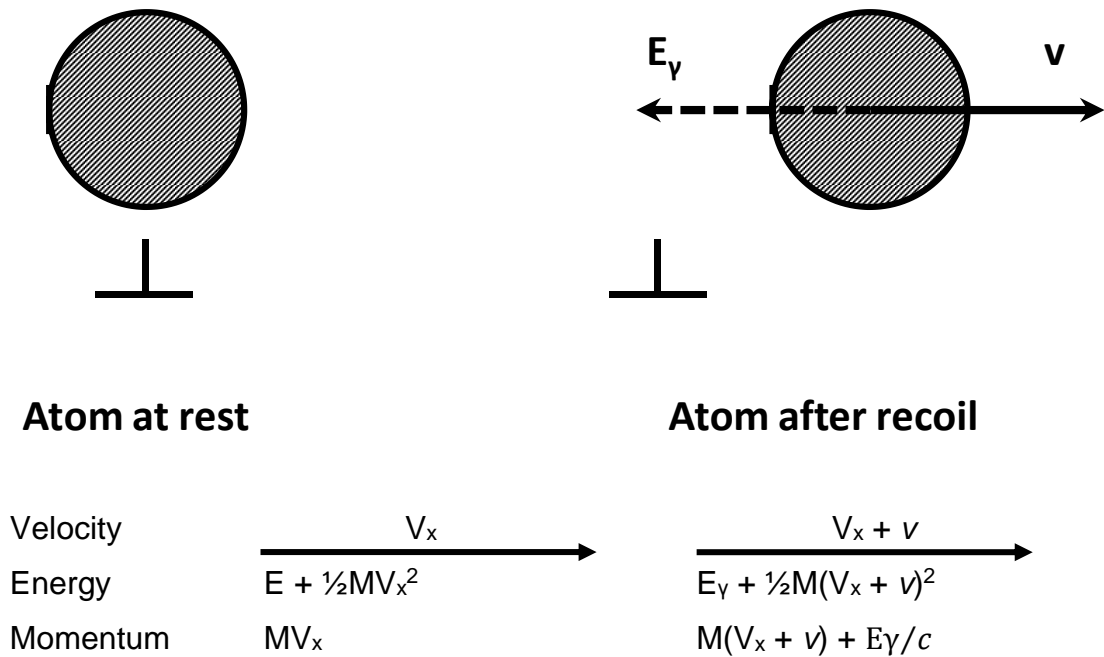
Figure 2.1. Illustrations of an atom at rest and after the emission of a γ-ray.

As there has been no energy supplied to this system, the energy prior to, and following emission, must be equal, as per the conservation of energy. For that, it is known that $E + \frac{1}{2}MV_x^2 = E_\gamma + \frac{1}{2}M(V_x + v)^2$. From this the energy that has been applied to the nucleus in the emission of the γ-ray can be calculated, the recoil energy, E_R. The difference in energy between the emitted γ-ray, E_γ, and the nuclear transition energy, E, can be expressed as ΔE, such that;

$$\Delta E = E - E_\gamma \tag{1}$$

Rearranging the expressions of the total energy in the system, in which E and E_γ are presented with M, V_x and v as;

$$E + \frac{1}{2}MV_x^2 = E_\gamma + \frac{1}{2}M(V_x + v)^2 \tag{2}$$

$$E - E_\gamma = \frac{1}{2}M(V_x + v)^2 - \frac{1}{2}MV_x^2 \tag{3}$$

$$E - E_\gamma = \frac{1}{2}M(V_x^2 + 2V_x v + v^2) - \frac{1}{2}MV_x^2 \tag{4}$$

$$E - E_\gamma = \frac{1}{2}MV_x^2 + MV_x v + \frac{1}{2}Mv^2 - \frac{1}{2}MV_x^2 \tag{5}$$

$$E - E_\gamma = MV_x v + \frac{1}{2}Mv^2 \tag{6}$$

Of these functions, $\frac{1}{2}Mv^2$ is found to be independent of the initial movements of the nucleus, meaning it is not affected by anything other than the recoil of the nucleus, while $MV_x v$ does concern this initial motion, which indicates a thermal

dependency. Referring to these functions as the recoil energy, and the Doppler-effect energy, such that;

$$E - E_\gamma = E_D + E_R \tag{7}$$

Between the translational degrees of freedom in a free atom in a gas, with random thermal motion, as considered thus far, the energy is distributed equally. From this, the kinetic energy of the nucleus prior to emission can be expressed as [3];

$$\overline{E_K} = \tfrac{1}{2}M\,\overline{V_x^2} \approx \tfrac{1}{2}kT \tag{8}$$

Where $\overline{E_K}$ denotes the average kinetic energy per translation degree of free, $\overline{V_x^2}$ is the mean square velocity of the atoms, k is the Boltzmann constant and T is the absolute temperature. To rearrange with respect to $\overline{V_x^2}$;

$$\left(\overline{V_x^2}\right)^{1/2} = \sqrt{\left(2\,\overline{E_K}\,/M\right)} \tag{9}$$

This expression can then be used to calculate the thermally dependent, mean Doppler-shift energy by introducing $\left(\overline{V_x^2}\right)^{1/2}$ in place of V_x^2 such that;

$$\overline{E_D} = Mv\left(\overline{V_x^2}\right)^{1/2} \tag{10}$$

From here, the expression for $\left(\overline{V_x^2}\right)^{1/2}$ with regards to $\overline{E_K}$ can be substituted, such that;

$$\overline{E_D} = Mv\sqrt{\left(2\,\overline{E_K}\,/M\right)} \tag{11}$$

$$\overline{E_D} = \sqrt{\left(2M^2v^2\,\overline{E_K}\,/M\right)} \tag{12}$$

$$\overline{E_D} = \sqrt{2Mv^2\,\overline{E_K}} \tag{13}$$

As it is known that $E_R = \tfrac{1}{2}Mv^2$;

$$\overline{E_D} = 2\sqrt{E_R\,\overline{E_K}} \tag{14}$$

Or, as $E_K \approx \tfrac{1}{2}kT$;

$$\overline{E_D} = \sqrt{2kTE_R} \tag{15}$$

To summarise, the nucleus upon emission will recoil in the direction opposite to the γ-ray, with recoil energy E_R. As the γ-ray energy will always be a distribution of energies around an average, this distribution of energies will be displaced by E_R. The thermal broadening of this distribution, characterised as E_D, has also been expressed, with respect to the recoil energy and average thermal energy. Although the emission has been referred to through the displacement of the γ-ray energy, and the distribution thereof, it is the same for the absorption of the γ-ray where energy is lost to recoil of the absorbing nucleus. For convention, $-E_R$ and $+E_R$ are regarded to with respect to the direction of the γ-ray. This results in two distributions of energies for the γ-ray, one displaced by $-E_R$ and one of $+E_R$, as illustrated in Figure 2.2. The region in which these distributions overlap is the region of energies in which the energy losses due to recoil may still result in nuclear γ resonance. The maximisation of this region, which is exaggerated in the illustration, is pivotal to achieving the Mössbauer effect. For ^{57}Fe Mössbauer Spectroscopy, the transition energy 14.41 keV has $E_R = 1.95 \times 10^{-3}$ eV and $\overline{E_D} \approx 1.0 \times 10^{-2}$ eV.
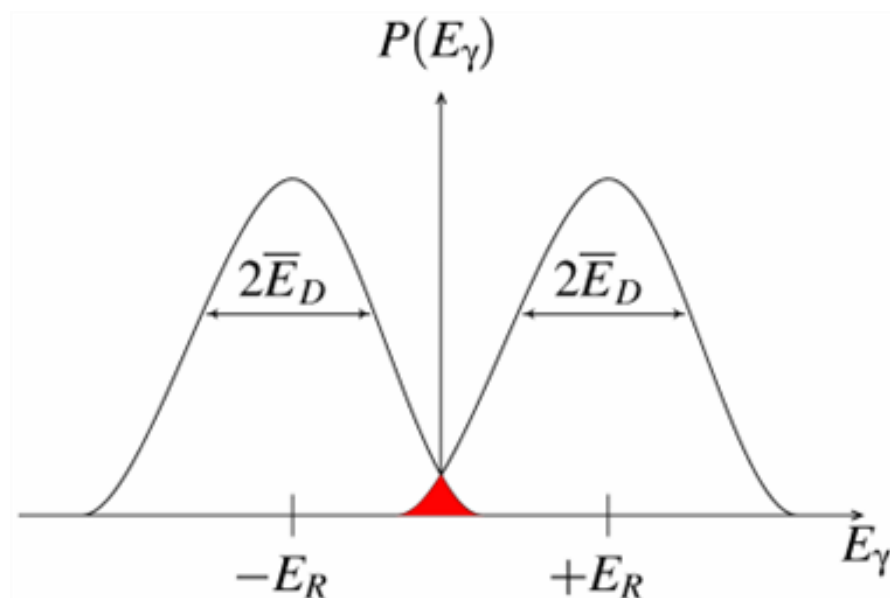
Figure 2.2. Energy distributions of nucleus emitting and absorbing γ-ray, displaced by E_R [4]. © Royal Society of Chemistry 2019.

Since these energies are related to the γ-ray energy, it is often more conventional and convenient to express them in terms of E_γ such that;

$$E_R \; = \; \tfrac{1}{2}Mv^2 \; = \; M/M \; \times \; \tfrac{1}{2}Mv^2 \; = \; (Mv)^2/2M \tag{16}$$

By translating $\tfrac{1}{2}Mv^2$ into a function of Mv, where Mv is a momentum function, momentum function as p, for the recoil momentum of the nucleus, can be expressed such that;

$$E_R \; = p/2M \tag{17}$$

For the conservation of momentum, recoil momentum p must be equal and opposite to the momentum of the γ-ray photon which can be denoted as p_γ, such that;

$$p \; = \; -p_\gamma, \quad or, \quad -Mv_\gamma \tag{18}$$

In the case of the photon, and with the situation being considered, the speed of the emitted photon will be the speed of light, c, and as such v_γ can be replaced with c;

$$p_\gamma \; = \; Mc \tag{19}$$

This can in turn be related to the energy of the γ-ray through Einstein's equation of E = mc^2 where the energy, mass and speed of the γ-ray are considered;

$$E_\gamma \; = \; Mc^2$$
$$\therefore \; M \; = E_\gamma/c^2 \tag{20}$$

$$p_\gamma \; = \; \left(E_\gamma/c^2\right)c \tag{21}$$

$$p_\gamma \; = E_\gamma/c \tag{22}$$

From here, the recoil energy can be calculated with respect to the energy of the emitted photon, and the mass of the recoiling nucleus where;

$$E_\gamma \; = p^2/M \tag{23}$$

$$E_R \; = E_\gamma{}^2/2Mc^2 \tag{24}$$

To express E_γ in eV, c as 2.998 x10^{11} and M as a.m.u., this can be simplified further to;

$$E_R \; = \; 5.369 \times 10^{-10} \; \times \; E_\gamma{}^2/M \tag{25}$$

This can also be used to relate E_D in the same terms by re-introducing E_D as a function of E_R where it was found that;

$$\overline{E_D} = 2\sqrt{E_R\,\overline{E_K}} \tag{26}$$

$$\overline{E_D} = 2\sqrt{\left(\frac{E_\gamma{}^2}{2Mc^2}\right)\overline{E_K}} \tag{27}$$

$$\overline{E_D} = E_\gamma\sqrt{2\,\overline{E_K}\,/(Mc^2)} \tag{28}$$

From these equations, the recoil energy and Doppler-effect energy can be calculated for a given gamma ray, and the amount of resonance overlap can be determined, wherein the Mössbauer effect can occur.

2.2 Theoretical linewidth of the 14.41 keV γ-ray
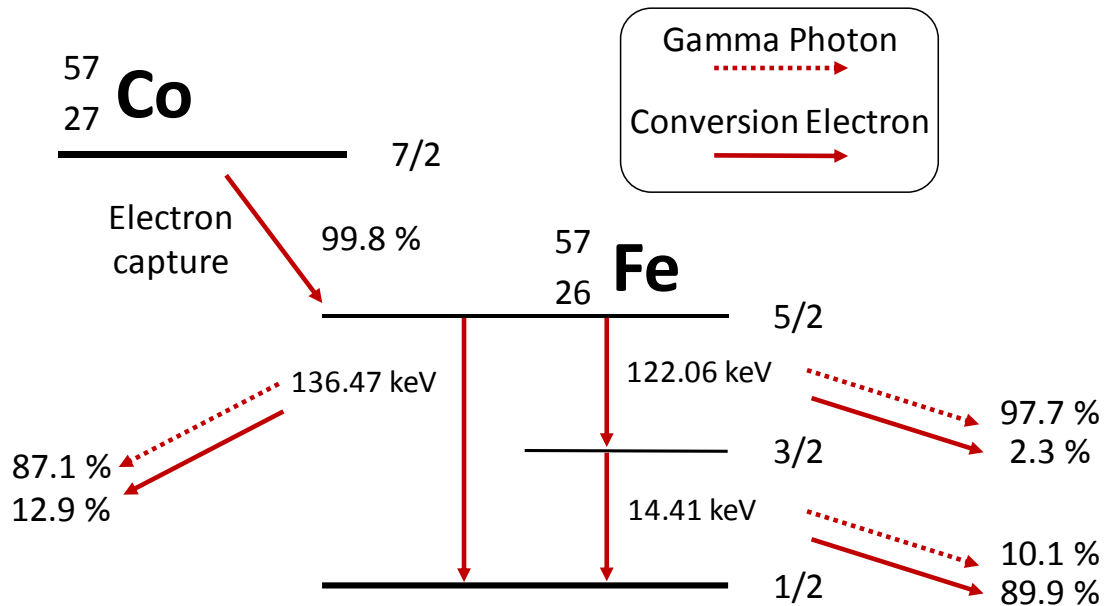
Figure 2.3. Simplified illustration of the decay scheme of ^{57}Co to ^{57}Fe. Not drawn to any scale.

From the decay of ^{57}Co to ^{57}Fe, as illustrated in Figure 2.3, that is utilised as the gamma ray source for ^{57}Fe Mössbauer spectroscopy, gamma rays of three different energies are emitted. The direct decay from 5/2 to 1/2 Fe results in the emission of a 136.47 keV gamma ray, and the cascade that involves an initial decay to 3/2 Fe results in a 122.06 keV gamma ray and a subsequent 14.41 keV gamma ray for the transition from 3/2 to 1/2 [5]. Each of these gamma rays will have a distribution of energies that are centred around the stated values; not all of the 14.41 keV rays will have this energy precisely, instead there will be some deviation. This distribution of energies about the 14.41 keV gamma ray energy, which is the gamma ray of interest for ^{57}Fe Mössbauer spectroscopy, is called its natural linewidth.

Thus far, considerations have been made regarding the displacement of the energy distributions due to recoil, and the broadening of these distributions due to the thermally dependent Doppler-effect energy. However, the natural linewidth of the γ-rays has yet to be addressed, that being the unbroadened distribution of energies, without thermal influence. For this, we regard the

Heisenberg uncertainty principle which addresses the uncertainties in energy and time with relation to Planck's constant ($h = 2\pi\hbar$). The uncertainty relation between position x and momentum p is expressed as ($\Delta x \, \Delta p \geq \hbar$) which is analogous to the relation between energy E and time t, in that;

$$\Delta E \, \Delta t \; \geq \; \hbar \tag{29}$$

For the ground state, unexcited nucleus, its life time is infinite and as such its uncertainty in energy is zero. In the excited state, in the source material for the γ-ray, its life time must be considered, from which the ΔE can be taken, where ΔE in this case is the distribution of γ-ray energies. To consider the life time of the energy, consider the half-life of its decay to make the relation;

$$t = ln2 \; \times \; t_{1/2} \tag{30}$$

Here t is the life time and $t_{1/2}$ the half-life. Considering ΔE to be the width of the distribution of energies when t = $t_{1/2}$ it is found that;

$$\Delta E \, t_{1/2} \; = \; \hbar \tag{31}$$

$$\Delta E \, (eV) = \; 4.562 \times \; 10^{-16}/t_{1/2}(s) \tag{32}$$

From this, we consider ΔE to be the linewidth of the distribution at half height, for a given $t_{1/2}$, and therefore a given γ-ray. It is important here to notice that the half-life of the γ-ray and the half-life of the Mössbauer source material are not equal. The half-life of the ^{57}Co source used for ^{57}Fe Mössbauer of 271.8 days would not be the correct half-life, for example. In the case of ^{57}Fe Mössbauer spectroscopy, the 14.41 keV γ-ray that is emitted by cascade decay of ^{57}Co, has a half-life of 97.7 ns [6];

$$\Gamma \, (eV) = \; 4.562 \times \; 10^{-16}/9.77 \; \times \; 10^{-8} \tag{33}$$

$$\Gamma \, (eV) = \; 4.67 \times 10^{-9} \, (eV) \tag{34}$$

As this process occurs both through emission and absorption, the energy distributions are associated with both the source and the absorber, and as such the theoretical Mössbauer natural linewidth (Γ_M) is double this energy distribution, such that;

$$\Gamma_M \; = \; 2 \, \Gamma \; = \; 9.34 \; \times 10^{-9} \, eV \tag{35}$$

From this, the natural linewidth of the 14.41 keV emission for ^{57}Fe being 10^{-9} eV, is much smaller than either the recoil energy E_R (x10^{-3}) and $\overline{E_D}$ (x10^{-2}) when considering a free atom, and as such is negligible. However, should the effects of recoil and thermal broadening be eliminated, then the natural linewidth would prove significant. Should that be so, then to consider the theoretical linewidth in comparison to the energy of the γ-ray one could find the theoretical resolution, such that;

$$\frac{\Gamma}{E_\gamma} = \frac{9.34 \; x10^{-9}}{14.41 \; x10^3} \approx \frac{1}{10^{12}} \tag{36}$$

2.3 Nuclear recoil resonance absorption

From previous sections, for demonstrable use and practical experimental applications, of the Mössbauer effect it would not be advisable to use isolated free nuclei for either the source or the absorber. For practical applications, solids are used as the source materials, and the absorber would also be solid, or at very least, a frozen or highly viscous liquid. To first over-simplify the reason why, the concept will be explained using the same anecdotal explanation that is delivered to undergraduate students. It has already been established that the recoil energy is too great in a free atom, which can be considered analogous to a boat in a lake. One can visualise a person leaping from the boat will leap with less force than they exerted, with some energy expended in causing the boat to recoil in the opposite direction. Should this person leap into another boat, that boat will drift in the direction of the leap, also due to recoil. This analogy was presented with the question of how this person might leap from boat to boat without either boat moving – this being to ask how one nucleus may emit a γ-ray that is absorbed by a second nucleus, without the loss of energy due to recoil effects. While this analogy may be simplistic, the solutions are elegantly similar. In the case of the boats, one may freeze the lake, such that to recoil either boat, there must be enough energy either to break the ice, or to recoil the entire lake. As for the nuclei, one can put such a demand on the recoil energy by embedding the nuclei in solid matrices and having the effective mass of the nuclei be that of the entire solid body.

The strengths of chemical bonds in solids are in the order of 1 to 10 eV, that being considerably greater than the recoil energy E_R in the case of ^{57}Fe (10^{-3} eV). Should the emitting nucleus be unable to recoil due to being bound in this solid matrix, it is due to its mass now being considered as the mass of the solid. This does not contradict previous expressions of the recoil energy whereby;

$$E_R = \frac{E_\gamma{}^2}{2Mc^2} \tag{37}$$

Increasing the value of mass M from that of a single atom to that of the solid, one can expect the recoil energy to be diminished by a factor of 10^{15} or more, as even for a fine powder one can expect 10^{15} atoms per particle. It should

be noted that this is still an oversimplification, as the atom will be free to vibrate and will not be rigidly bound in place by the lattice. The recoil energy of a single nucleus may either be taken up by the entire crystal or transferred to the lattice through increasing the vibrational energy of the solid. To consider the solid lattice as a single quantum mechanical system, the vibrational energy levels can be quantised, meaning that the vibrational energies will have discrete values and allow only certain increments. The quantisation of these energy levels can be described using Einstein's model of solids [3], which assumes a single lattice vibration frequency, ω. In this treatment, energy transfer to the lattice is only allowed in factors of ℏω (0, ℏω, 2ℏω etc…), where ℏ = h/2π, h being Planck's constant. If E_R is less than ℏω then either zero or one ℏω unit of vibrational energy may be transferred to the lattice [7]. When many emissions are considered, Lipkin shows that the average energy transferred per event must equal E_R exactly [8]. In this consideration, there will be either emission events that do not result in the transfer of energy to the lattice, which are zero-phonon transitions, and events that do transfer one phonon, with energy ℏω. If f is the fraction that result in no transfer of energy, then 1 − f will be those that do, such that;

$$E_R \;=\; (1 - f)\hbar\omega \tag{38}$$

Or with respect to f;

$$f \;=\; 1 - E_R/\hbar\omega \tag{39}$$

If no energy is transferred to the lattice, the energy is instead absorbed by the recoil of the entire crystal. As previously mentioned, the mass of the crystal may easily be that of 10^{15} atoms, which is a function in both the E_R and $\overline{E_D}$ as the reciprocal mass 1/M, such that to increase the mass diminishes both these energies and become much smaller than Γ_M. These events, zero-phonon transitions, where the energy is transferred to the entire crystal, are considered *recoilless*.

To summarise, the Mössbauer effect is the resonant emission and absorption of a gamma ray, in a solid matrix, whereby the energy of the ray is not diminished by recoil, or thermal broadening. The energy distribution of the gamma ray is dictated by the Heisenberg uncertainty principle. For clarity of the

energies being discussed, see Table 2.1, the typical energy scales for several interactions mentioned at this time [2].

Table 2.1. Typical energies of nuclear and chemical interactions. 1 eV = 1.602 x10^{-19} J, equivalent to 96.49 kJ mol^{-1}.

Interaction	Energy scale (kJ mol^{-1})
Mössbauer γ-ray (E_γ)	$10^6 - 10^7$
Chemical bonds and lattice energies	$10^2 - 10^3$
Electronic transitions	$50 - 500$
Molecular vibrations	$5 - 50$
Lattice vibrations	$0.5 - 5$
Nuclear recoil and Doppler energies (E_R, E_D)	$10^{-2} - 1$
Heisenberg linewidths (Γ_M)	$10^{-7} - 10^{-4}$

2.3.1 The recoil-free fraction, *f*

The *f* factor, which has been identified as the recoilless, or recoil-free fraction, is the fraction of emissions or absorptions that do not transfer energy to the lattice of the crystal and are therefore a parameter that would be favourable to be as large as possible for Mössbauer spectroscopy. In doing so, one must consider this factor quantitively instead of qualitatively. It has already been established that this *f* factor is dependent on three factors;

- free-atom recoil energy, which is proportional to E_γ^2
- the properties of the solid lattice
- the ambient temperature

The *f* factor should be greater when the γ-ray energy is smaller, the atom is more tightly bound in the lattice, and the temperature is lower. In order to quantify the probability of a zero-phonon γ-ray emission from a nucleus in a solid lattice, able to simultaneously change its vibrational state, reference is given to dispersion theory [7]–[9]. *f* is found to be proportional to the square of the matrix element connecting the initial $| i >$ and final $< f |$ states.

$$f = constant \text{ x } \left|< L_f \right| e^{ik.x} |L_i >|^2 \qquad (40)$$

where L_f = final state of the atom

L_i = initial state of the atom

k = wave vector of the emitted photon

x = co-ordinate vector of the centre of mass of the decay nucleus

However, in the case of zero-phonon emission, the initial and final states are normalised as the lattice modes are unchanged, removing the dependence on the state functions and resulting in [7];

$$f = e^{-k.x^2} \qquad (41)$$

As *x* is a random vibration vector, it can be replaced by $<x^2>$ which is instead the component of the mean square vibrational amplitude of the emitting nucleus, in the direction of the γ-ray. From consideration of the wave vector of the emitted photon in previous sections, although not referred to as this, it is stated that $k^2 = 4\pi^2 / \lambda^2 = E_\gamma^2 / (\hbar c)^2$, whereby λ is the wavelength of the γ-ray.

$$f = \exp\left(\frac{-4\pi\langle x^2\rangle}{\lambda^2}\right) = \exp\left(\frac{-E_\gamma{}^2\langle x^2\rangle}{(\hbar c)^2}\right) \qquad (42)$$

The indication of this is that f decreases exponentially with the square of the λ-ray energy. Therefore, there is an upper limit at which E_γ is useful for Mössbauer spectroscopy, the greatest for which is currently reported for ^{190}Os Mössbauer, with an energy 187 keV [10]. f is also found to increase exponentially with decreasing $<x^2>$, which is dependent on the rigidity of the bonding of the nucleus, and that itself is temperature dependant. Evidently, the mean displacement of the nucleus must be small in relation to the wavelength of the λ-ray to result in an appreciable f factor. The Mössbauer effect is limited to solids and viscous liquids, for this reason. To consider the relation between f and E_γ, it can be seen that for a given E_γ, since $\hbar$ (= $h/2\pi$) and c are constants, $<x^2>$ is the only variable, and it is temperature dependent. A study into the temperature dependence of the f factor, therefore, can be a powerful tool to elucidate information on the lattice dynamics of crystals and solids.

2.3.2 Debye model approximations

With regards to Mössbauer spectroscopy, the application of the Debye model [11]–[13] is most widely used to translate between the temperature dependence of the chemical isomer shift (δ), covered in the upcoming section, *2.5.1 Chemical Isomer Shift*, and the *f* factor as previously described. In lieu of covering the entirety of the Debye model and its eventual evolution to a form that is applicable to Mössbauer spectroscopy, we will consider more directly relatable presentations of the Debye model herein. A heavily abridged description of the Debye model is that it is concerning the continuum of vibrational frequencies in a harmonic oscillator approximation with distribution $N_{(\omega)}$ (= constant x ω^2), up to ω_D, the Debye frequency, its maximum value. The Debye frequency and Debye temperature θ_D are related such that;

$$\hbar\omega_D \; = \; k\theta_D \tag{43}$$

The most familiar expression to relate the Debye temperature to the *f* factor is one that is often simplified, depending on the ambient temperature in relation to the Debye temperature.

$$f = \exp\left[\frac{-6E_R}{k\theta_D}\left\{\frac{1}{4} + \left(\frac{T}{\theta_D}\right)^2 \int_0^{\theta_D/T} \frac{x \, dx}{e^x - 1}\right\}\right] \tag{44}$$

Where T ≤ θ_D this can be reduced to the approximation of;

$$f = \exp\left[\frac{-E_R}{k\theta_D}\left\{\frac{3}{2} + \frac{\pi^2 T^2}{\theta_D{}^2}\right\}\right] \tag{45}$$

At absolute zero;

$$f = \exp\left[\frac{-3E_R}{2k\theta_D}\right] \tag{46}$$

And in the high temperature limit, where T ≥ ½θ_D;

$$f = \exp\left[\frac{-6E_R T}{k\theta_D{}^2}\right] \tag{47}$$

The most simplistic form of *f* is where $f = e^{-2W}$ where *W* may be referred to as the Debye-Waller effect, or in the context of Mössbauer spectroscopy, the Lamb-Mössbauer factor. In brief, the *f* factor for a particular compound should increase

with a decrease in temperature. To consider ^{57}Fe Mössbauer spectroscopy of a mineral with a θ_D of 300 K for example, at T = 300 K one would find an f factor of 0.636, and 0.740 when T = 200 K (both using the high temperature limit function, equation 47). It can also be seen that f is larger when θ_D is larger, which is due to a high θ_D, implying a strong lattice. Referring to the equation presented at the end of the earlier section, '*The recoil-free fraction, f*' where it was stated that a decrease in f would be found when temperature was increased, leading from the vibrational amplitude of the nucleus increasing.

To summarise the previous sub-sections of this chapter, it has been shown that the Mössbauer effect is optimized for low energy γ-ray energies, with nuclei bound strongly in solid crystal lattices, at low temperatures.

2.4 Experimental Procedures

In this section, the main components of a typical Mössbauer spectrometer will be outlined, considerations that must be observed, and a brief overview of how these components work and why they are of importance. As covered in preceding sections, the Mössbauer effect can be achieved, however, the emission and absorption of a γ-ray alone has limited applications in terms of material characterisation, phase identification or any other reason for which researchers employ Mössbauer spectroscopy. In order to produce a Mössbauer spectrum, the energy of the incident γ-ray is modulated, such that the absorbing material receives rays with slightly increased, and slightly reduced energy. Outside of the theoretical explanations of previous sections, more general considerations must be given for both the emitting source material, and absorbing sample material, for modern spectrometers.
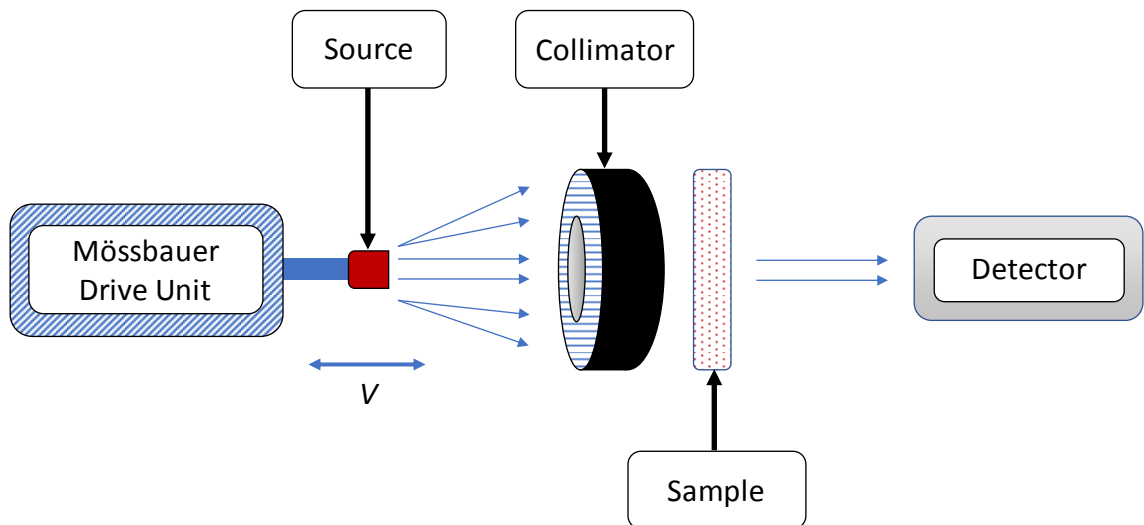
Figure 2.4. Simplified schematic overview of a transmission ^{57}Fe Mössbauer spectrometer.
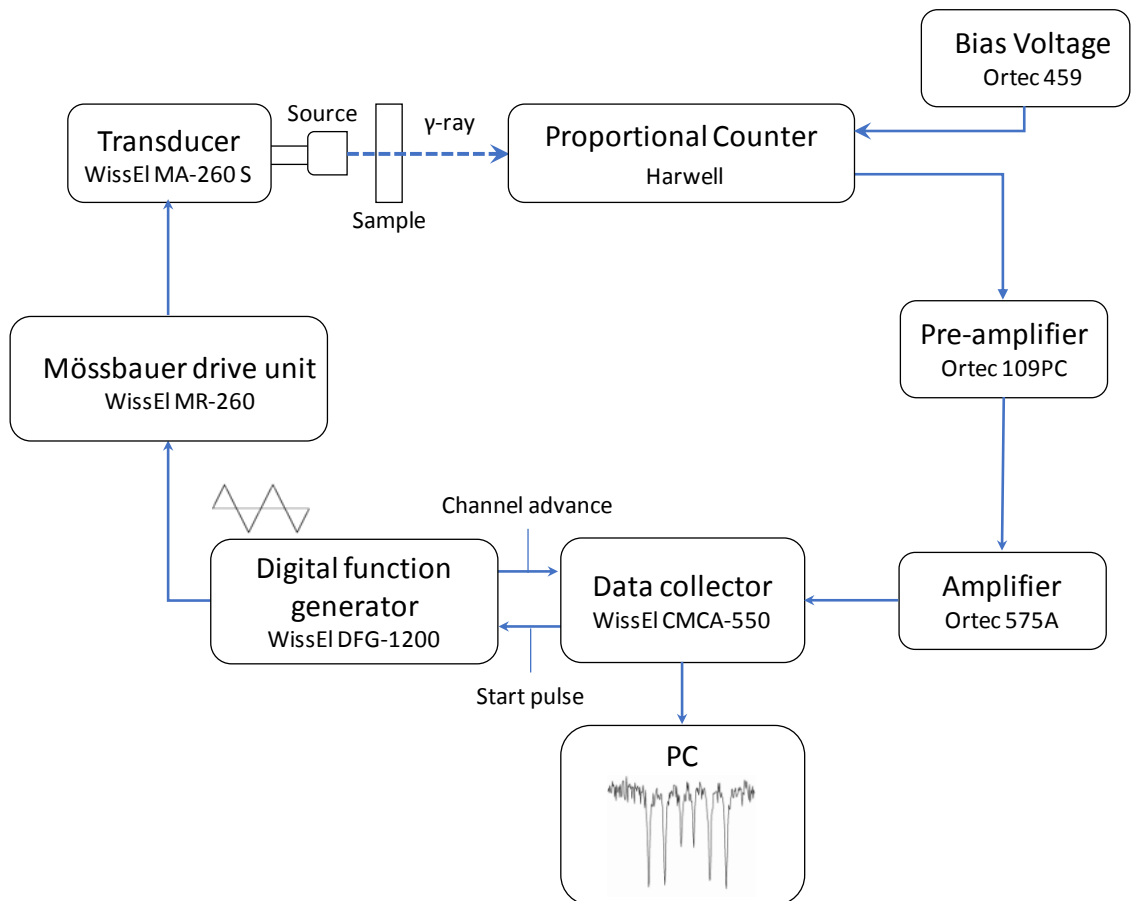
Figure 2.5. Experimental arrangement of transmission ^{57}Fe Mössbauer spectrometer.

2.4.1 Mössbauer γ-ray source

For a typical user of Mössbauer spectroscopy, the only considerations given to the source material is that it provides the appropriate γ-ray for the nuclide of interest, in quantity, and for a suitable duration of time once installed in the spectrometer. When ordering a Mössbauer source, the supplier (Ritverc © for example) will advertise the recommended working life and nominal activity of the source, along with source capsule dimensions. There are considerations, however, that the supplier will have accounted for, which may not be thought of by the average user, and which will be briefly detailed in this section.

1. **The ideal γ-ray energy is ≈ 10 to 100 keV.** This is due to the fact that energies lower than this are strongly absorbed completely in solid matter and will therefore struggle to reach the detector in a typical transmission Mössbauer spectroscopy experiment, while over 100 keV will result in greatly reduced recoil-free fractions.
2. The Heisenberg linewidth has been shown to be influenced by the half-life of the excited state, meaning the **preferable $t_{1/2}$ should be between 1 and 100 ns**, as too short a lifetime results in line broadening, obscuring any hyperfine effects.
3. The source material should generate **γ-rays with an energy profile approaching the Heisenberg linewidth, and with a single absorption line.** Although multiple-line source materials can be used in more niche applications, a single-line source results in spectra of appreciably greater convenience.
4. In conjunction with point (3), **the matrix material in which the source nuclide is embedded should have a sufficiently high Debye temperature**, such that the recoil-free fraction is substantial. This is to ensure that the source is emitting a large enough quantity of γ-rays with useful energies.
5. The amount of **ground-state resonant isotope within the source material should be kept as low as possible** to avoid self-resonance within the source itself. Self-resonance results in line broadening of the

source γ-ray, conflicting with point (3). ^{57}Co/Fe, for example, would produce γ-rays over a broader energy profile than ^{57}Co/^{56}Fe.

6. **The ground state isotope should have a sufficiently high natural abundance** to avoid the need of artificially enriching materials which one may wish to analyse, at the cost of convenience and capital. Isotopic enrichment is not an uncommon practice when the overall element is in low abundance within a material, such as in doped solid, or for in-situ measurements of the active, isotope bearing compound within a host matrix.

Due to the quantity of Mössbauer active isotopes, from hereon only ^{57}Fe shall be described, as to appreciably cover each isotope would not be conducive to a concise work. Due to the wide applications of iron in a multitude of materials science fields, as well as biological and chemical sciences, to only consider ^{57}Fe Mössbauer spectroscopy is to address the majority of Mössbauer spectroscopic studies and focus on those issues most pertinent to this study.

The prerequisites for successful nuclear resonance, as discussed in the preceding sections of this chapter, greatly favour ^{57}Fe as a candidate for Mössbauer spectroscopy. The transition energy between states is sufficiently low that a high recoil-free fraction can be achieved. The natural abundance of ^{57}Fe of ≈ 2.14% is typically high enough as to forego the need to artificially enrich materials of interest, although this may be necessary for materials with a low iron content, particularly bio-materials. The lifetime of the excited state, 98 ns, is long enough as to not obscure chemical hyperfine effects while being short enough that mechanical vibrations of the spectrometer are not typically an issue.

For the Mössbauer spectroscopy measurements conducted as part of this work, the source material was ^{57}Co in a Rhodium matrix. High purity ^{57}Co is electrodeposited onto a thin film of Rhodium (≤ 6 μm thickness) and annealed to release any internal stresses. This active component is encapsulated in a titanium alloy holder with a brazed beryllium window, sealed by laser welding, as illustrated in specifications from *Ritverc Isotope Products* [14] in Figure 2.6.
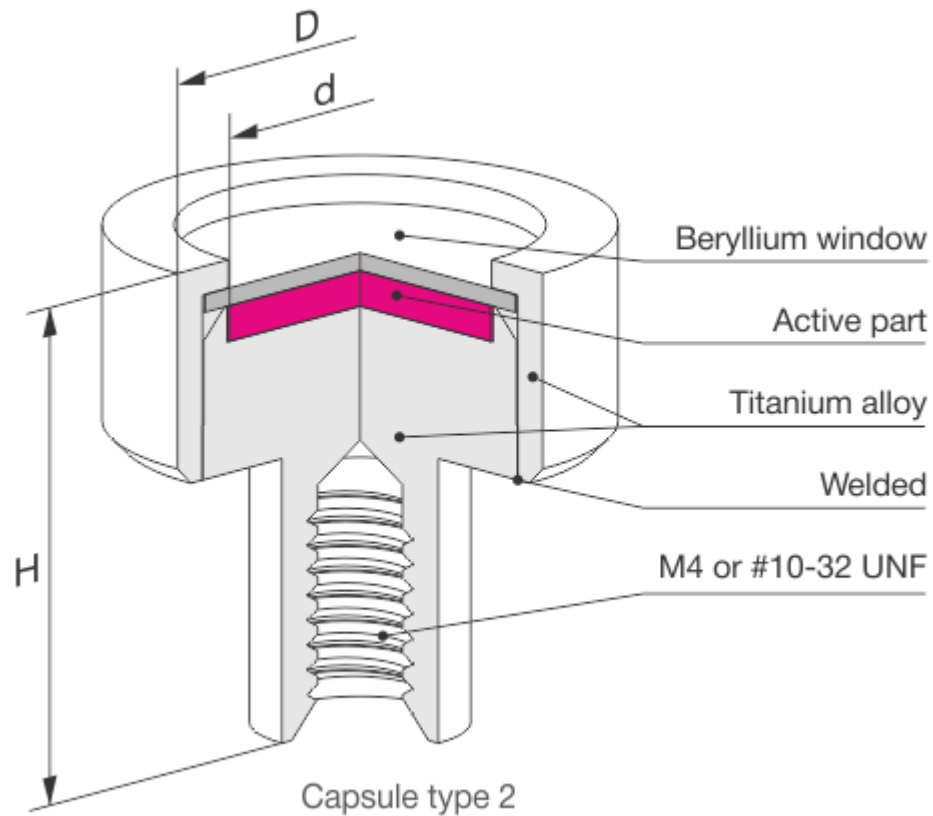
Figure 2.6. An example of a Mössbauer source: ISO C54243 [57]Co/Rh Mössbauer source from Ritverc™.D x H, 14 x 14 mm, internal diameter 8 mm. [14]

The decay of [57]Co to [57]Fe, illustrated in Figure 2.3, involves first the conversion of I = 7/2 [57]Co to I = 5/2 [57]Fe by electron capture, followed by the relaxation of the 5/2 [57]Fe, either directly to 1/2 [57]Fe, or to 3/2 and then 1/2. It is through the latter cascade decay that the 14.41 keV γ-ray is emitted, which [57]Fe Mössbauer spectroscopy utilises. The resonant absorption of the incident 14.41 keV γ-ray produces several backscattering effects, which will be covered in *absorber interactions*.

2.4.2 Mössbauer drive unit

During *Theory of the Mössbauer Effect* the energy profiles for the source and absorber materials were introduced in Figure 2.2, where it was discussed that the overlap of the two energy profiles minimises the losses due to recoil. When the local iron environments of the source and absorber materials are different, the energy levels will be different – these changes will be discussed properly in *Hyperfine interactions*. With differences in the energy levels, there is a necessity to modulate the incident γ-ray energy being emitted, in order to have the energy profiles meet, overlap, and separate one another, as illustrated in Figure 2.7. For Mössbauer spectroscopy, the energy of the incident γ-ray (E_0) is modulated as a function of velocity as the source is oscillated, at constant acceleration (linear $\Delta V/\Delta t$), towards and away from the absorber material, causing a Doppler shift [15]. Conventionally, positive velocity is when the source is moving towards the absorber. A typical ^{57}Fe Mössbauer spectrum is presented in terms of a velocity range, as the actual energy modulation is on such a small scale ($\pm 10^{-6}$ eV at a velocity range of ± 12 mm s^{-1}), where each data point can be considered as a discrete energy level.

$$E_\gamma = E_0 \pm \frac{E_0 v}{c} \tag{48}$$
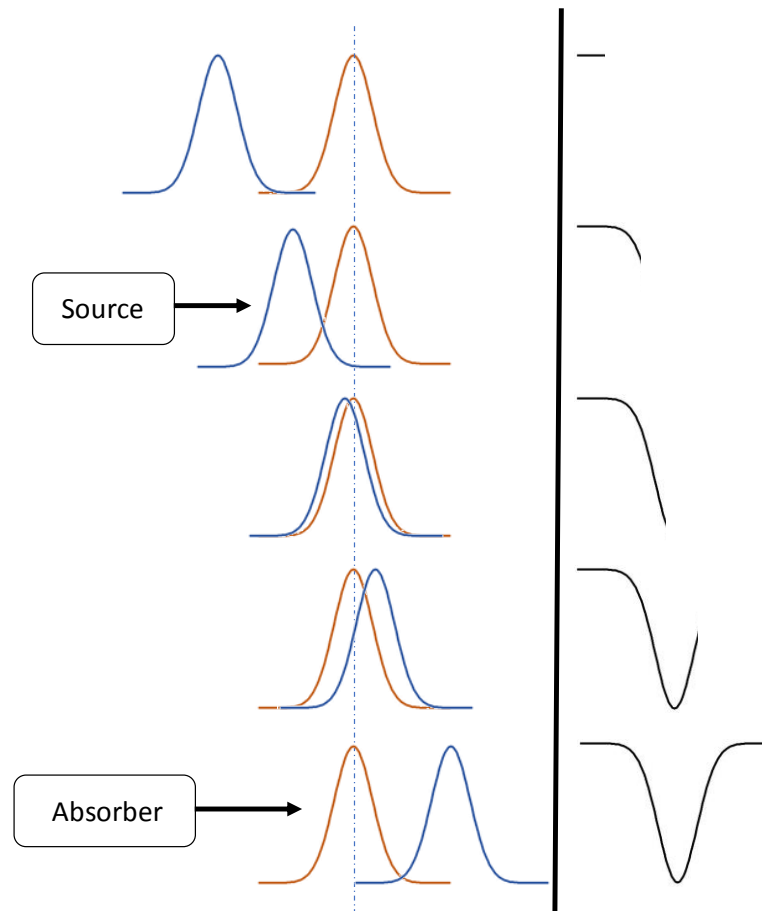
Figure 2.7. Emission and absorption spectra for the source and absorber [57]Fe overlapping and separating, and the resultant spectrum observed.

The digital function generator shown in Figure 2.5, provides a triangular signal to the Mössbauer drive unit, which calibrates this signal against a user-determined desired velocity range. This signal, fed to the drive unit (transducer), is what causes the source to be oscillated at constant acceleration, and the incident γ-rays to be Doppler shifted. The drive systems used for Mössbauer spectroscopy have evolved greatly in the 60 years since its discovery – having included motorised lathes, pendulum and hydraulic systems [7]. More modern drive systems are electromechanical transducers, which are based on two coupled coils, the drive and pickup coils, operating in a manner similar to loudspeakers. The drive coil causes the motion of the transducer elements, and the pickup coil provides a feedback signal to the driver unit proportional to the measured velocity. This internal feedback system ensures high accuracy of the resulting source velocity.

2.4.3 Absorber interactions and considerations

The resonant absorption of the 14.41 keV γ-ray by the absorbing material of interest is observed as a lack of transmission by the detector system. Any γ-rays that do not interact with the absorber material will reach the detector, and absorption will be shown as an absence of transmission at that particular velocity value. In Figure 2.8 it can be seen that the absorbed 14.4(1) keV γ-ray is re-emitted by the absorber upon relaxation, however, this will very rarely reach the detector as it is emitted over a full 4π solid angle (in all directions from a point source). There are also various electronic processes which can occur following resonant absorption, the most notable of which being the M shell conversion electron, with 14.3 keV, due to its closeness in energy to the 14.41 keV γ-ray. Although this energy difference is orders of magnitude greater than that of the hyperfine interactions observed through Mössbauer spectroscopy, this electron is still noteworthy in terms of the detector, which will be considered more in *2.4.4 γ-ray detection*.
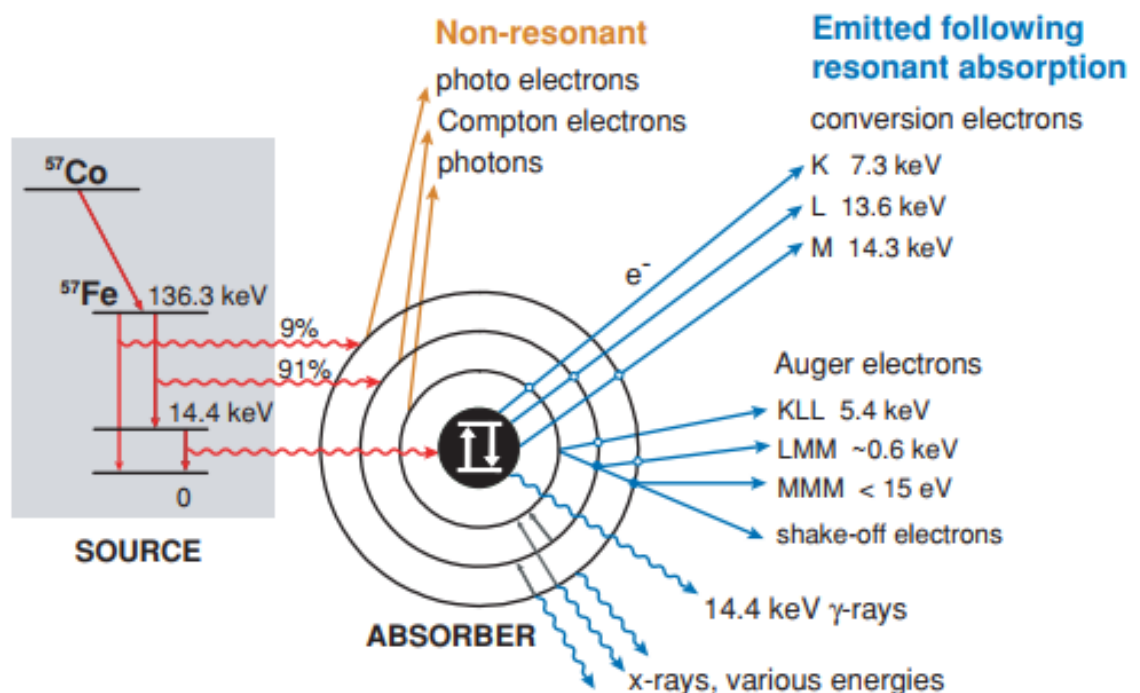

Figure 2.8. Nuclear decay scheme for [57]Co to [57]Fe and various background scattering processes for [57]Fe [16].

When preparing a sample for Mössbauer spectroscopy, there are some considerations to ensure the highest quality spectra. The Mössbauer absorber should contain enough of the isotope being studied that a spectrum can be generated in a reasonable amount of time, however, there is an upper limit to the isotopic concentration whereby the absorption lines become broadened by significant self-absorption effects [17]. In order to simplify experimental procedures, Mössbauer sample holders of constant dimensions are advised, which keep the volume of sample constant. For all studies included herein, Perspex absorber discs were prepared by lathe, to have a cavity with 15 mm ø and a depth of 1 mm, yielding an area of 1.767 cm^2. A dimensionless parameter is considered when regarding the ideal concentration of Mössbauer isotope in an absorber, called the Mössbauer thickness, t_a, whereby $t_a > 1$ saturation effects occur, and $t_a < 1$ data collection time is greater than necessary. The Mössbauer thickness is defined as;

$$t_a = \beta \eta f \sigma_0 \tag{49}$$

Where β is the multiplicity of the spectrum (typically taken as 1), η is the number of atoms of the Mössbauer isotope per cm^2, f is the recoil-free fraction and σ_0 is the absorption cross-section. To set t_a to the ideal value of 1; f is typically taken as 0.8 for ^{57}Fe [18]; σ_0 for ^{57}Fe is known to be 2.56 x 10^{-18} cm^2. With these constants, η can be calculated as;

$$\eta = \frac{1}{0.8 \times (2.56 \times 10^{-18})} \tag{50}$$

$\eta = 4.883 \times 10^{17}$ ^{57}Fe per cm^2

Which can be converted from number of atoms to a mass by;

$$\frac{4.883 \times 10^{17} \times 57}{6.02 \times 10^{23}} = 4.623 \times 10^{-5} \text{grams of } ^{57}\text{Fe per cm}^2 \tag{51}$$

As ^{57}Fe is approximately 2.16% of the total iron content, one can convert this value to the mass of total iron by;

$$\frac{4.623 \times 10^{-5} \times 100}{2.16} = 2.14 \times 10^{-3} \text{grams of iron per cm}^2 \tag{52}$$

From these equations, the mass of total iron desired per cm^2 can be derived, and since the area of the absorber discs being used is constant, only the total iron content of the material of interest is needed in order to prepare the sample for measurement. For example, if a material has a total iron content of 23 wt% the ideal sample mass loading could be calculated by;

$$2.14 \times 10^{-3} \, g \, cm^{-2} \times area \, of \, the \, absorber \times (100/(Fe \, \%)) \qquad (53)$$

If the iron concentration is 23% this would yield an ideal mass loading of 16.6mg in the absorber discs used in these studies. As only the iron concentration will vary through various ^{57}Fe Mössbauer spectroscopy studies, a simple spreadsheet was made to quickly carry out this calculation. Should the iron concentration of a material of interest be too great, the required mass of sample would be diluted with an inert, fine powder, gamma transparent material, such as graphite. This dilution ensures homogenous coverage of ^{57}Fe across the entire area of the absorber.

2.4.4 γ-ray detection

The detection of γ-rays for Mössbauer spectroscopy is, as mentioned previously, detecting the photons which have not interacted with the Mössbauer nuclides in the absorbing material. As illustrated in Figure 2.3, the decay of ^{57}Co to ^{57}Fe generates photons consisting of 136.47 keV, 122.06 keV and 14.41 keV, as such a suitable transmission Mössbauer γ-ray detector must be able to efficiently detect the resonant 14.41 keV ray, whilst rejecting the other γ-rays and any other radiations. The presence of the collimator in the experimental arrangement, in Figure 2.4, ensures that only radiation which has passed through the sample is being detected, minimising background noise and improve spectral quality.

Regarding the types of detector, the two main types which may be seen in use for Mössbauer spectroscopy, in more modern laboratory set ups are either gas-filled proportional counters, or scintillation counters. A more archaic spectrometer may use Li drifted germanium or silicon detectors, however due to the sheer size of these devices, they are becoming more antiquated [2]. On the opposite end, vis-à-vis a synchrotron facility, detection is by high purity single

crystals, however, synchrotron spectrometers have designs unlike lab-based instruments which will not be discussed here.

Scintillation detectors are most commonly used for applications where the γ-rays have energies of approximately 50 to 100 keV, however the resolution deteriorates with decreasing photon energy [7]. Although scintillation detectors offer higher potential resolutions and greater counting efficiencies, for ^{57}Fe Mössbauer spectroscopy, gas-filled proportional counters are more common place. While having a lower efficiency, the improved resolution means that a gas-filled proportional counter will generally be more reliable. Although lithium drifted detectors are a more recent development than proportional counters or scintillators, they are less widely used due to the irreparable damage which can be caused by not having them indefinitely at liquid nitrogen temperature. Their resolution for complicated decay schemes can grant them niche applications to certain isotopes, such as ^{125}Te, however at the low energy range for ^{57}Fe Mössbauer spectroscopy, the resolution has deteriorated as with scintillation detectors.

The ^{57}Fe Mössbauer spectroscopy measurements conducted as part of this work all used gas-filled proportional counters. These detectors are filled with an inert gas which is ionised by the incoming radiation, and a quench gas; a common mixture, and that used in these studies, is argon and methane (95:5 at SHU). As the incident radiation entering the detector collides with an atom of the inert gas, the atom is ionised producing an electron and positively charged ion – an 'ion pair'. Ion pairs are generated as the radiation is slowed through the length of the detector, being slowed by each pair produced where the amount of ion pairs produced is proportional to its energy. A thin tungsten filament is fixed along the length of the detector, which itself is in-line with the direction of the collimated gamma photons being detected. A bias voltage (-2.5 kV at SHU) is applied to the filament, causing it to act as an anode, and the casing therefore to act as a cathode, at which the positive ions can be detected. The charge is recorded as a voltage pulse, which is then fed to the amplification systems shown in Figure 2.5.

Discrimination of undesired impulses can be optimised using the data collection software, using a *pulse height analysis* mode, in which the data

presented are the energy profiles of the incident ionising particles. The 14.41 keV profile can be selected, through different interfaces depending on the software, while signal from other sources – most notable the 14.3 keV conversion electron as previously alluded to with regards to Figure 2.8. The optimisation of spectral quality will be covered more thoroughly during the 2.6 *Mössbauer data analysis* sub-sections.

2.4.5 Cryogenic spectrometers

For materials which exhibit temperature responses, whether they be magnetic ordering, structural phase changes or spin re-orientation, to name a few, appropriate nuclide variable temperature Mössbauer spectroscopy may be used. Historically, sub-ambient temperatures were achieved using liquid nitrogen, which resulted in many older publications presenting data down to 77 K. Modern cryogenic spectrometers utilise the controlled compression and expansion of high pressure helium gas (300 psi), which can achieve temperatures as low as 4 K, depending on the system used [19]. The works herein, where sub-ambient temperatures are reported, were conducted using a *Janis* CCS-800/204N Mössbauer cryostat, as shown in Figure 2.9, wherein the dynamic helium gas is isolated from the sample to minimise vibrations caused by the refrigerator, *Sumimoto* CH-204 SFF-N. The unit is mounted on air-filled feet, with the source and detector suspended in a lead-lined compartment, and a bellows system incorporated into the sample chamber, all with the purpose of isolating the system from any vibrations which may cause spectral line broadening. The temperature of the cold finger and the sample are measured and controlled separately using a *Lakeshore* 335 temperature controller, allowing independent temperature control of the sample and its immediate surrounding, which can either be vacuum or static helium exchange gas – this is particularly useful as maintaining the cold finger $\approx$ 3 K below the sample target temperature can greatly improve sample temperature stability. The sample is held in place 1-inch diameter copper sample mount with 25-ohm heater and temperature sensor; the cold finger similarly is equipped with a 50-ohm heater and temperature sensor, being 1.5 inch in

diameter. The heat from the system is removed using a water-cooled heat exchanger and compressor, *Sumimoto* HC-4E.
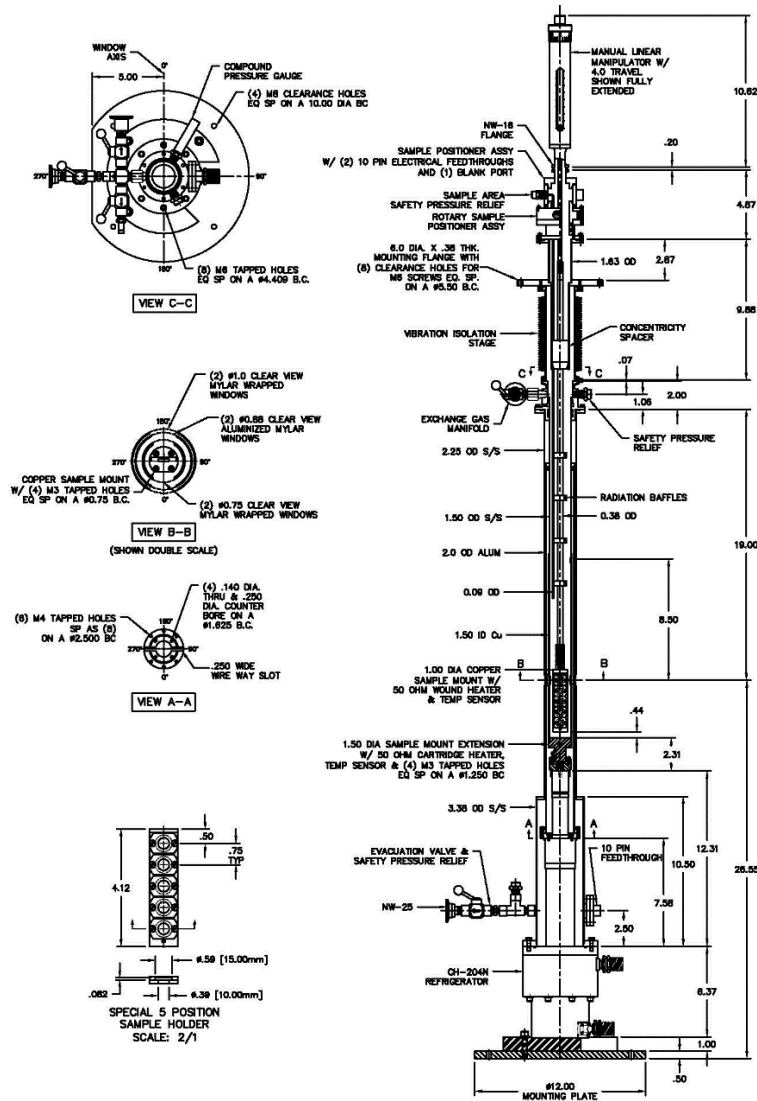
Figure 2.9. Model CCS-800/204N 10 K Cryocooler for Mössbauer Spectroscopy Mechanical Drawing [20]. © 2019 Janis Research Company, LLC.

Other than investigating temperature induced transitions, reducing the temperature of a sample during a Mössbauer measurement has a number of effects on the resultant spectra. The number of zero phonon emissions from the sample increases as the effective recoil-free fraction is increased. The Centre Shift (see 2.5.1) will increase with reduced temperature, as approximated by the Debye model. Internal magnetic field strengths tend to increase with reduced temperature and may become more well defined. The response to temperature that different materials have can be a useful tool in and of itself for studying mixed phase systems.

2.5 Hyperfine interactions

It was shown in previous sections how to achieve monochromatic γ-radiation able to resonantly be emitted and absorbed, both theoretically and experimentally, with theoretical resolution of 1 in 10^{12}. With appropriate use of the information of these sections, it is now possible to collect data using the Mössbauer effect, and to ascertain chemical information about a given material. Through proper interpretation of the data collected from Mössbauer spectroscopy, it is possible to determine the oxidation state of iron species within a material, the bonding systems, and to identify the presence of any internal magnetic field. Interactions between the nucleus and the surrounding environment are known as 'hyperfine interactions'. An overview of the three principle interactions consider by Mössbauer spectroscopy is presented in Table 2.2; **magnetic** Zeeman splitting (B_{eff} or H, in Tesla); **quadrupole** splitting (QS or ΔeQ, in mm s^{-1}); chemical **isomer shift** (CS or IS, in mm s^{-1}).

Solid state factor	Magnetic field	Electric field gradient	Electron density at nuclear site
	↓	↓	↓
Interaction	$\Delta E = \mu H$	+ QVE	+ cont $<R^2>$ ρ(0)
	↑	↑	↑
Nuclear interaction	Nuclear magnetic moment	Nuclear quadrupole moment	Mean square nuclear charge radius
	Magnetic hyperfine interaction	Electric quadrupole interaction	Chemical isomer shift

Table 2.2. Schematic representation of the hyperfine interactions.

Both the electric quadrupole and magnetic dipole interaction will generate multiple-line spectra which can impart a great deal of information about the iron environment(s) in the material. The three interactions can be presented both as a product of a nuclear term and an electronic term, the former being constant for a given γ-ray transition and the latter can vary and be related to the chemistry of the absorbing material.

2.5.1 Chemical isomer shift (δ)

In terms of a Mössbauer spectrum, the chemical isomer shift is the velocity value at which the line of symmetry lies for a particular iron site, reported as a velocity function. For a single line spectrum, this would be the centre of the absorption line. Practically speaking, the primary application of this value is to determine the oxidation state of an iron site, as there are generally discrete ranges for different oxidation states, as well as for different co-ordination numbers and spin states for those oxidation states, as presented by Dyar [16] in Figure 2.10.
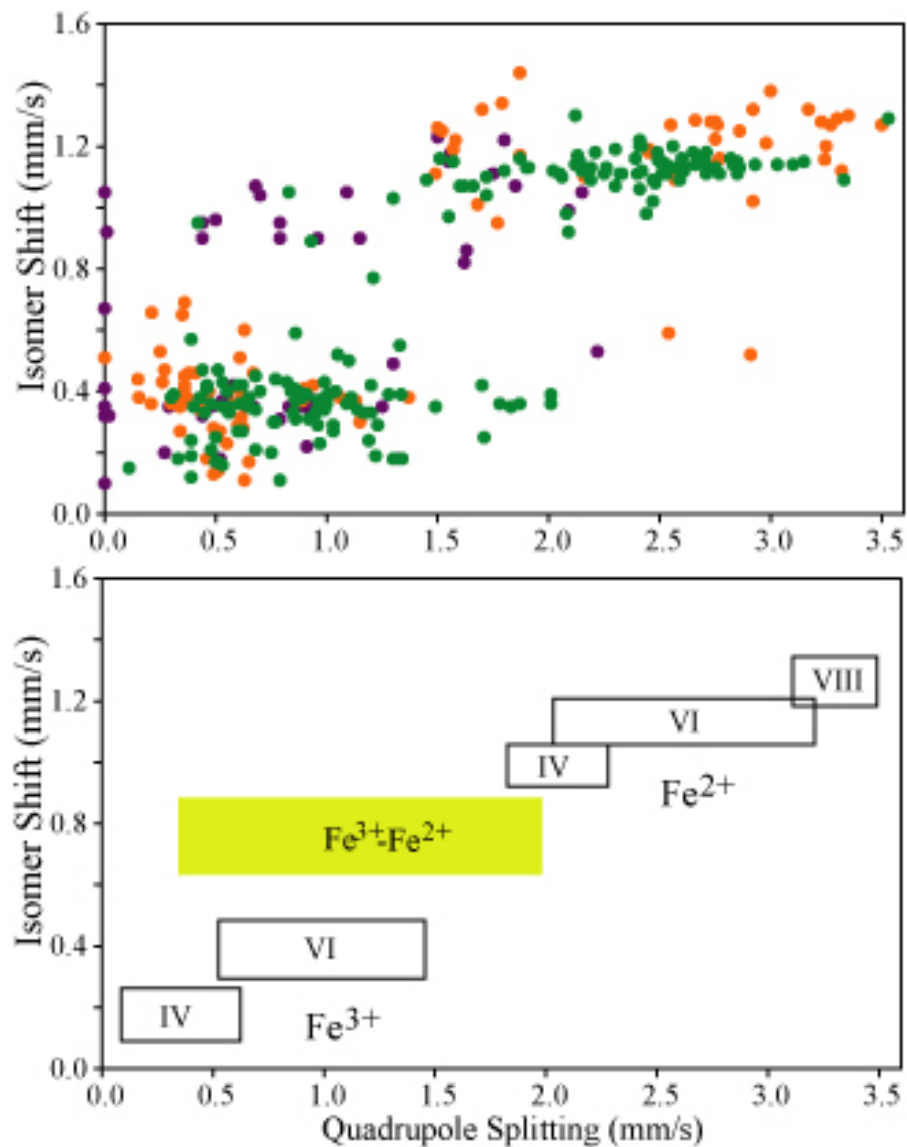

Figure 2.10.Correlation between [57]Fe isomer shift and quadrupole splitting data, at room temperature, for common rock-forming minerals [16].

The velocity function that chemical isomer shift is quoted as can be expressed as energy because of the relation of;

$$\delta = \left(^{v}/_{c}\right) \times E_{\gamma} \tag{54}$$

as such, each data point in a Mössbauer spectrum can be related to specific energy values, as can both the chemical isomer shift and quadrupole splitting.

To understand the origin of the chemical isomer shift, it is first important to move away from the idea of the nucleus as a point charge, and to consider the nucleus to have a finite volume, surrounded and penetrated by electronic charge which it electrostatically interacts with. This is of importance when considering the chemical isomer shift, as the difference in nucleus size for the ground state and excited state, which is experienced during the transition between states, is its principle origin. As it is accepted that the nucleus has a finite volume, and that the s-electron wavefunction must have a finite, non-zero value inside of the nuclear radius, it is this which is responsible for the change in electrostatic energy that is observed. Although this change is a small fraction of the total Coulombic interaction, and therefore it is not measured directly, it is possible to compare this change by using an appropriate reference, such as the incident γ-ray emitted by the Mössbauer source. Quoted chemical isomer shifts are relative to a known standard material, most commonly α-Fe, which sets the zero-velocity point and converts the data collector channel numbers into velocity units, against which the sample data are fit.
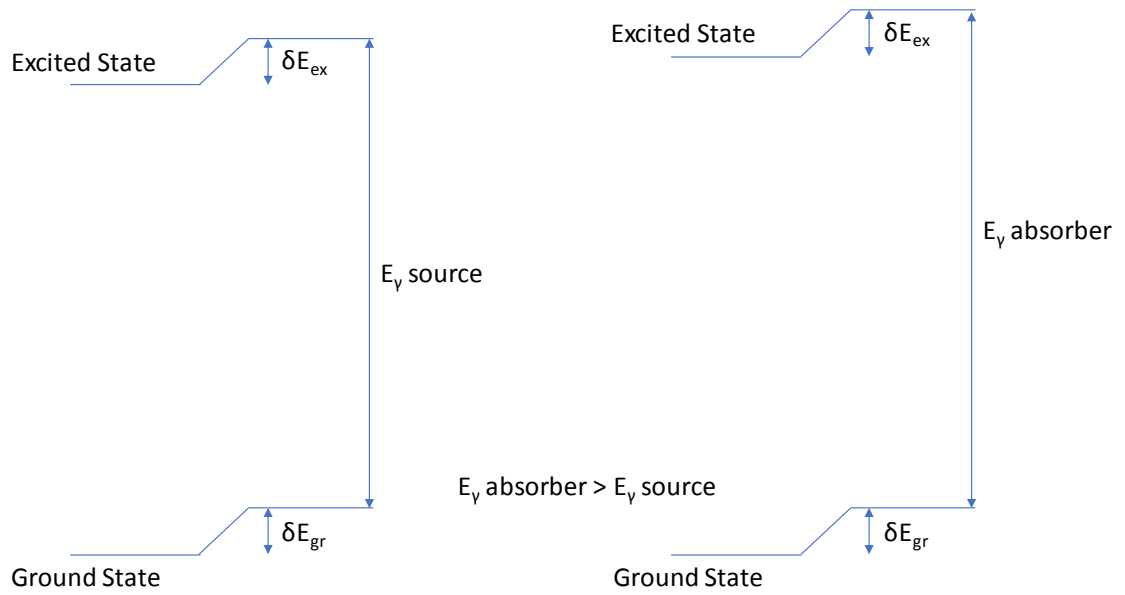
Figure 2.11. Chemical isomer shift of nuclear energy levels for a single line source (left) and absorber (right). (Not to scale).

To express the isomer shift one considers the nucleus not as a point charge, but as a uniformly charged sphere of finite volume with radius *R*, with a constant s-electron density, $|\Psi(0)|^2$, through its volume. One can consider how the electrostatic interactions differ when the nucleus is thought of as a point charge, and of possessing a radius of R, and estimate these interaction energies. Considering electronic interactions, one can therefore consider nuclear interactions to be constant such that the difference in energies, δE to be;

$$\delta E = k\,|\Psi(0)|^2 \times R^2 \tag{55}$$

Where *k* is a nuclear constant. To consider the differences between the ground and excited states, know δE and R to be different at both states, such that;

$$\delta E_{ex} - \delta E_{gr} = k\,|\Psi(0)|^2\big(R_{ex}^2 - R_{gr}^2\big) \tag{56}$$

In terms of Mössbauer spectroscopy, one considers the difference in energy levels between the nuclear transitions in the source and the absorber, which can be expressed as;

$$\delta = k\,\{|\Psi(0)|_{absorber}^2 - |\Psi(0)|_{source}^2\}\big(R_{ex}^2 - R_{gr}^2\big) \tag{57}$$

To accept that the radius changes caused as being very small, if one denotes δR as R_{ex} / R_{gr}, and allows a constant of *c* to denote a characteristic constant of the Mössbauer source, δ can be expressed as;

$$\delta = 2kR^2 \, \frac{\delta R}{R} \, \{|\Psi(0)|^2_{absorber} - c\} \tag{58}$$

By expressing δ in this way, $|\Psi(0)|^2$ of the source, and δR/R are found to be constant for a given nuclide, as such once it is known whether δR is positive or negative, the isomer shift can be related to $|\Psi(0)|^2$ of the absorber. In the case of ^{57}Fe it is known that δR/R is negative, as the excited state nucleus is smaller than the ground state, and as such the isomer shift decreases as $|\Psi(0)|^2_{absorber}$ increase [2], [7], [21]. It follows that an increase in the isomer shift implies a decrease in s-electron density. As depicted in Figure 2.10, Fe^{2+} has a greater isomer shift than Fe^{3+}, as such the s-electron density in Fe^{2+} must be less than that of Fe^{3+}.

Outer valance electron shells do not directly interact with the nuclear charge density, as the $|\Psi(0)|^2$ for p-, d- and f-electrons are zero. These orbitals do significantly interact with the nucleus by interpenetration shielding of the s-electrons. Additional outer valance electrons cause a greater shielding effect, reducing the s-electron $|\Psi(0)|^2$; $3d^64s^1$ outer configuration, for example, will have a higher s-electron density than $3d^74s^1$, and similarly for $3s^23p^63d^5$ and $3s^23p^63d^6$ due to penetration of the 3d outer orbitals into the 3s. While the radius of the nucleus is the principle influence on shifting the resonance line, both temperature and pressure also have an impact. The effect of hydrostatic compression has also been investigated for ^{57}Fe Mössbauer spectroscopy by Pound, Benedek and Drever in 1961 [22]. The temperature-dependent contributions to the isomer shift have been investigated thoroughly by Y. Hazony in 1966 [23], which looked to the Debye model to approximate the changes in isomer shift as a function of the Debye temperature. The changes to isomer shift are considered as a second order Doppler shift, expressions for which consider zero-point motion, as well as high temperature limits, as shown previously for the Debye model. The shift in energy caused by second order Doppler shift (SODS) can be expressed as [24];

$$\Delta E_{SOD} = -\frac{1}{2}\left(\langle v^2\rangle \Big/ c^2\right)E_\gamma \tag{59}$$

Where <v^2> is the mean square velocity of the atom caused by lattice vibrations. As discussed in *2.1 Theory of the Mössbauer effect*, the mean square velocity of the atom is temperature dependent while the other functions of this expression are constant for a given E_γ. This corresponds to a shift in velocity units as;

$$S_{SOD} = -(\langle v^2\rangle/2c) \tag{60}$$

For a Debye solid, Wegener found that [25];

$$\langle v^2\rangle = \frac{9}{8}\frac{k\theta_D}{M} + 3\frac{kT}{M}f\left(\frac{T}{\theta_D}\right) \tag{61}$$

As previously discussed, the *f* factor can be given by;

$$f = e^{-k^2\langle x^2\rangle} \tag{62}$$

Where *k* is the wave vector of the gamma ray and <x^2> is the mean square vibrational displacement of the Mössbauer atom in direction *k*. One can consider then that the *f* factor is a measure of <x^2>, while SODS is dependent on <v^2>, however there is no direct relation between these two, only approximations by models; the Debye model can express *f* as;

$$f = \exp\left\{-\frac{3}{4}\frac{E_\gamma^2}{Mc^2k\theta_D}\left[1 + 4\left(\frac{T}{\theta_D}\right)^2\int_0^{\theta_D/T}\frac{x\,dx}{\exp x - 1}\right]\right\} \tag{63}$$

If the *f* factor of a material has been measured, the Debye temperature θ_D can be obtained and from this, <v^2>, and the SODS. The influence of the SODS on the chemical isomer shift is why the nomenclature becomes important – some may present the directly measured shift as the isomer shift, however the isomer shift is not temperature dependant and is characteristic of the material. For this reason, the less ambiguous name of "Centre Shift" will be given to this measured parameter as to avoid any misunderstanding. The SODS can be approximated experimentally by relating the temperature dependence of the Centre Shift as [13], [26];

$$SODS = -\frac{3kT}{2Mc}\left(\frac{3\theta_D}{8T} + 3\left(\frac{T}{\theta_D}\right)^3\int_0^{\theta_D/T}\frac{x^3}{e^x - 1}dx\right) \tag{64}$$

2.5.2 Nuclear quadrupole interaction (ΔeQ)

Throughout the considerations for the chemical isomer shift, the nucleus and its charge radius were considered spherical, which is suitable for the explanations of these interactions. If a nucleus has a spin quantum number greater than I = ½, the charge distribution will be non-spherical due to having a nuclear quadrupole moment. As the chemical isomer shift is a measure of the change in s-electron density against that of the Mössbauer source, the nuclear quadrupole splitting observed through Mössbauer spectroscopy is a measure of the difference in charge symmetries. The single-line source material is a perfect cubic structure, as such the ΔeQ indicates the deviation from cubic symmetry in the bonding system. The nuclear quadrupole moment, Q, can be expressed by;

$$eQ = \int \rho r^2 (3cos^2\theta - 1) \, d\tau \qquad (65)$$

Where +e is the charge on the proton, ρ is the charge density in the volume element dτ at a distance of r from the centre of the nucleus, at angle θ to the axis of the nuclear spin. The value of Q can be either positive or negative, depending on the direction of the deformation in relation to the axis of nuclear spin, where a positive value indicates a prolate shape and a negative value indicates oblate.

Q > 0
prolate

Q < 0
oblate
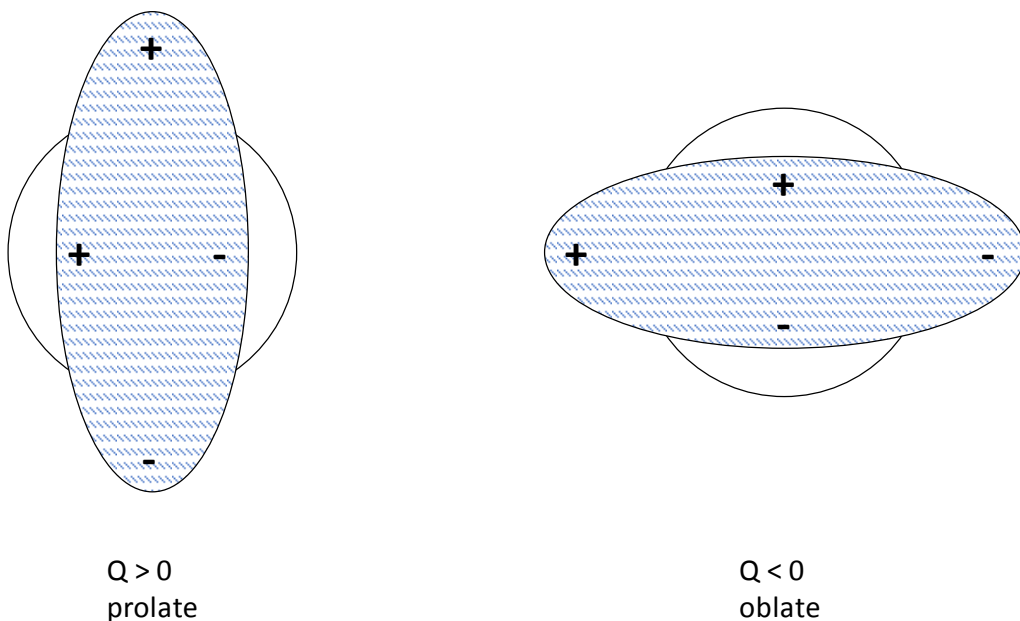
Figure 2.12. Deviation of a nucleus from spherical.

Where I and J denote the directions of the nuclear spin and the angular momentum of the electron cloud and V is the electrostatic potential, the electric field gradient at the nucleus, E, can be expressed as a tensor as;

$$E_{ij} = -V_{ij} = -\left(\frac{\delta^2 V}{\delta x_i x_j}\right) \tag{66}$$

Customarily, the axis system of the atom is defined so that V_{zz} = eq is the maximum values of the electric field gradient, $|V_{ii}|$. This allows the definition to ensure all V_{ij} terms where I and j are nonequal equal zero, leaving only three principle values, V_{xx}, V_{yy} and V_{zz}. In accordance with the Laplace equation [27], $V_{zz} + V_{xx} + V_{yy} = 0$ as the electric field gradient should be a traceless tensor (the sum of elements along the main diagonal = 0). It is therefore possible to define the electric field gradient completely using only two independent parameters, typically V_{zz} and an asymmetry parameter, η defined as;

$$\eta = \frac{|V_{xx} - V_{yy}|}{V_{zz}} \tag{67}$$

With the convention of $|V_{zz}| > |V_{yy}| \geq |V_{xx}|$ is used to ensure $0 \leq \eta \leq 1$. In this case, the z axis is the major axis, and x is the minor axis; the z axis would be the axis of symmetry.
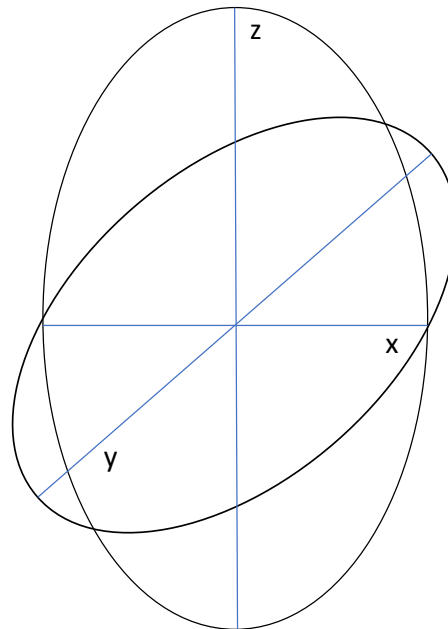
Figure 2.13. Example axis system of ellipsoid.

The quadrupole interaction is a product of *eQ* which is a nuclear constant for the isotope, and *eq* which is a function of its chemical environment. The sign of e^2qQ is an important factor in discovering the origin of the electric field gradient, however this cannot be determined from spectral line positions alone with ^{57}Fe Mössbauer spectroscopy due to there being only one transition, $3/2 \rightarrow 1/2$. To overcome this, a point charge model of the electric field gradient can be considered in order to calculate the relative magnitude of the electric field gradient [28], [29].

The energy change ΔeQ caused by the quadrupole interaction can be expressed as [2], [7];

$$\Delta E_Q = \frac{e^2qQ}{4I(2I-I)}[3I_I^2 - I(I+1)] \tag{68}$$

Where the quantum number I_z can take the 2I+1 values of I, I-1… -I. When I = 3/2, as in ^{57}Fe, there are two resulting energy levels at $+e^2qQ/4$ for m = ±3/2 and $-e^2qQ/4$ for m = ±1/2. If the asymmetry parameter, η, is greater than 0 an exact expression can be given only for I = 3/2;

$$\Delta E_Q = \frac{e^2qQ}{4I(2I-I)}[3I_I^2 - I(I+1)]\left(1+\frac{\eta^2}{3}\right)^{1/2} \tag{69}$$

Which results in energy levels at $\pm(e^2qQ/4)(1+\eta^2/3)^{1/2}$. For ^{57}Fe studying an isotropic powdered sample, this interaction will result in a spectrum of two lines of equal intensity, as both $m_I \pm 1/2$ and m_I 3/2 are allowed with equal probability, separated by $|(e^2qQ)|$. The centre of the two energies corresponds to the energy of the γ-ray transition in the absence of a quadrupole interaction; the chemical isomer shift.
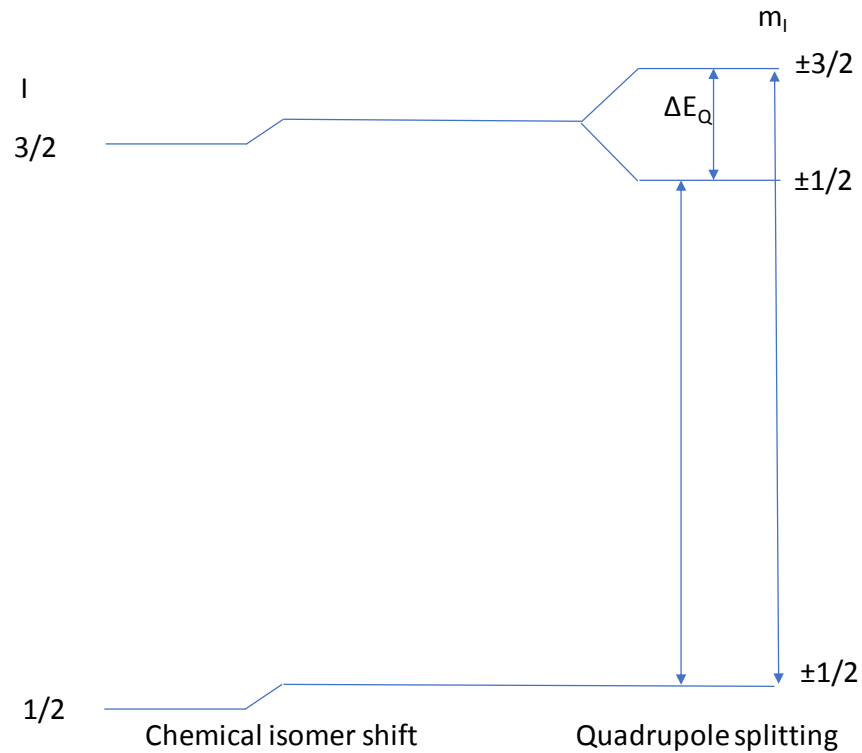
Figure 2.14. Energy level scheme of I = 3/2 to I = 1/2 transition with chemical isomer shift and quadrupole splitting influences. (Not to scale).

2.5.3 Magnetic hyperfine interaction (B_eff)

The partial loss of degeneracy caused by an electric field gradient, as shown in Figure 2.14, results in m_I states that are not distinguishable as being positive or negative. These states can be further split into positive or negative states by the presence of a magnetic field either within the atom, the crystal, or through the application of a strong external magnetic field. A nucleus with a spin quantum number, I, greater than 0 has a magnetic moment, μ. The magnetic hyperfine interaction is an interaction between the nuclear magnetic moment and any magnetic field. Because of this interaction the energy levels are shifted by a quantity, E_m, which can be expressed by;

$$E_m = \frac{-\mu B m_I}{I} = -g\mu_N B m_I \qquad (70)$$

Where m_I is the quantum magnetic number (I, I-1… -I), μ_N is the Bohr magneton (5.04929 x10^{-27} J T^{-1}), g is the nuclear g-factor $[g = \mu/(I\mu_N)]$, and B is the magnetic field flux density. This causes equidistant, non-degenerate energy splitting of the nuclear energy level of spin I into ($2I +1$) sub-states. As seen for the quadrupole splitting, Mössbauer transitions can only occur for $\Delta m_I = 0$ or ± 1; for ^{57}Fe, this results in six possible transitions, as illustrated in Figure 2.15. The splitting of the spectral lines is directly proportional to the magnetic field experienced by the nucleus, making Mössbauer spectroscopy an effective method to measure the magnetic field. Similar to the chemical isomer shift and quadrupole interaction, the magnetic hyperfine interaction is the product of a nuclear term which is constant for a given isotope, and a magnetic field which is dependent on the electronic structure of the material being studied. The origin of the internal magnetic field acting on the nucleus in a solid can be expressed as a sum of contributions from the motion of electrons within the material [30]–[32];

$$H \;=\; H_0 \,-\, DM \;+\; \frac{3}{4\pi M} + H_S \;+\; H_L \;+\; H_D \tag{71}$$

Where H_0 is the contribution of an external magnet on the nucleus; -DM the is specimen shape dependent demagnetizing field; +3/4πM is the Lorentz field; H_S is a result of the interaction of the nucleus with an imbalance in the s-electron spin density; H_L is a result of the orbital magnetic moment of the parent atom being non-zero; H_D is from the nuclear dipolar interaction with spin moment of the atom. The H_S, H_L and H_D terms are considered as the internal magnetic field, as H_0 is zero in the absence of an external magnetic field, the Lorentz field is only applicable for cubic symmetry and the demagnetising field is a generally negligible value [7], [32]. In compounds with two or more discrete magnetic lattices, the resulting Mössbauer spectra can differentiate the internal fields at each site.
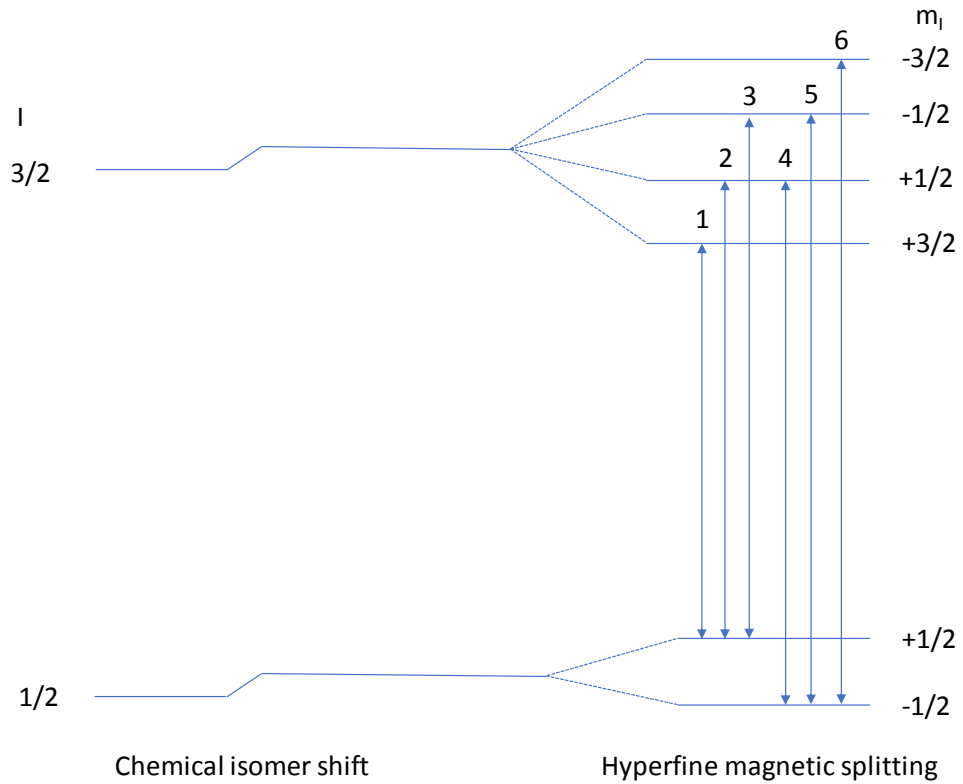
Figure 2.15. Magnetic splitting for 3/2 to 1/2 transition.

The energy level splitting caused by only a hyperfine magnetic field results in the absorption lines being equally spaced, and any chemical isomer shift will result in all absorption lines being shifted uniformly along the velocity axis. Both the magnetic and quadrupole interactions are direction dependent and result in spectra with non-equidistant absorption lines. Providing the electric field gradient is axially symmetric and its principle axis makes an angle θ with the magnetic axis, a simple solution exists if $e^2qQ \leq \mu H$;

$$E = -g\mu_N H m_I + (-1)^{|m_I|+\frac{1}{2}}\frac{e^2qQ}{4}\left(\frac{3cos^2\theta - 1}{2}\right) \tag{72}$$

This approach may not always be suitable, in which case more complex descriptions may be necessary.

2.5.4 Relative absorption line intensities

The relative intensity of an absorption line in a Mössbauer spectrum is directly related to the probability of that transition occurring, relative to the probability of the other transitions. In a complex spectrum with multiple components, knowing the relative intensity of each absorption line can make the interpretation much simpler. It is most common that the centroid of the doublet or sextet will act as a line of symmetry, both for two-line and six-line spectra, however this may not always be the case. The γ-ray transition, as illustrated in Figure 2.14, is between two levels of nuclear spin, I_1 and I_2, and between two sub-states, m_1 and m_2. The intensity of a transition between quantised sub-levels can be determined by the coupling of the two nuclear angular momentum states. For a particular hyperfine transition, the intensity can be expressed as a product of two terms, one angular dependent and one angular independent, however for a randomly orientated polycrystalline material (i.e. not single crystal), the angular dependent term averages to unity as all orientations are equally probable. In this case, the intensity of a transition can be presented as [7];

$$Intensity \propto \langle I_1 \mathbf{J} - m_1 m \,|\, I_2 m_2 \rangle^2 \tag{73}$$

Where $\mathbf{J}$ is the sum vector $I_1 + I_2$ and m is the sum vector $m_1 + m_2$. In most cases, including ^{57}Fe, the Mössbauer isotope decay is a dipole transition whereby $\mathbf{J} = 1$ ($\mathbf{J} = 2$ in the case of quadrupole transitions). The relative probabilities of these transitions has been well documented [2], [33] and are presented in Table 2.3. In the event of a quadrupole spectrum, where the degeneracy is unresolved, the probabilities are presented in Table 2.4. From these, one can see that for angular independent spectra, a sextet should appear to have relative intensities for 3:2:1:1:2:3, and a doublet to be symmetrical.

For an absorber that is angular dependent, the term ϕ(J, m) is expressed as a radiation probability in a direction at an angle θ to the magnetic field axis (V_{zz}). In most cases, and in all cases of the spectra presented herein, the absorbing materials are randomly orientated, polycrystalline materials, and as such there will be no more consideration given to this situation. It is, however, worth noting that special considerations need to be taken if this is the case.

Magnetic spectra							
m_2	$-m_1$	m	C	C^2	Φ (J, m)	θ= 90°	Θ = 0°
+ 3/2	+ 1/2	+1	1	3	$1+\cos^2\theta$	3	6
+ 1/2	+ 1/2	0	√2/3	2	$2\sin^2\theta$	4	0
- 1/2	+ 1/2	-1	√1/3	1	$1+\cos^2\theta$	1	2
- 3/2	+ 1/2	-2	0	0	0	0	0
+ 3/2	- 1/2	+2	0	0	0	0	0
+ 1/2	- 1/2	+1	√1/3	1	$1+\cos^2\theta$	1	2
- 1/2	- 1/2	0	√2/3	2	$2\sin^2\theta$	4	0
- 3/2	- 1/2	-1	1	3	$1+\cos^2\theta$	3	6

Table 2.3. Relative probabilities for a dipole 3/2, 1/2 transition, reproduced from T. C. Gibb's *Principles of Mössbauer Spectroscopy* page 41.[2]

Quadrupole spectra		
Transition	C^2	Φ (J, m)
±1/2, ±1/2	1/2	$1/2 + 3/4\sin^2\theta$
±3/2, ±1/2	1/2	$3/4(1+ \cos^2\theta)$

Table 2.4. Relative intensities of quadrupole spectra, reproduced from T. C. Gibb's *Principles of Mössbauer Spectroscopy* page 41.[2]

2.6 Mössbauer data analysis

The collection of data from a Mössbauer spectrometer is typically carried out by a data collection module separate from the computer's power supply, and with an internal memory. This is to ensure that there is continuous data collection and that the accumulated data will not be lost due to computer restarts or corrupted by improper file handling. For the data collected using the room temperature spectrometer, a WissEl CMCA-550 module was used to collect data which would be converted to a .dat file, readable in the *Recoil* data fitting software, and Microsoft Excel. The low temperature spectrometer uses a *SeeCo* Gamma-Ray Spectrometer Model W202 and W304, connected to software set to save the data as a .t file at user defined intervals (60 minutes). Both for the .dat and .t file formats, data is presented as single columns where each row corresponds to the counts recorded for that channel, where each channel corresponds to a velocity point. In collecting a Mössbauer spectrum in constant acceleration mode, each triangle waveform passes the positive and negative region twice, as shown in Figure 2.16.
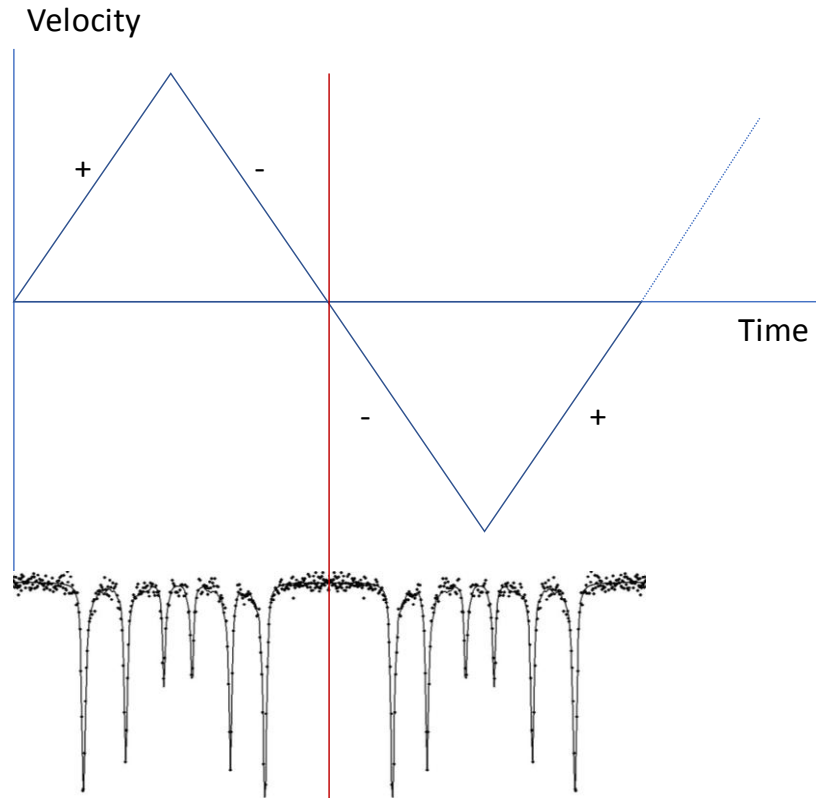
Figure 2.16. Triangle waveform of constant acceleration velocity profile. Mirror line of produced spectrum in red.

The resulting data is 'folded' along the mirror line, which in a data set containing 512 channels would be 256 and 257; folding being to sum 1 and 512, 2 and 511 etc. The folded data will have a higher signal to noise ratio, being the average of the two summed points. This data can then have 'sites' assigned using various software packages; works herein were analysed using the *Recoil* package. Different fitting methods operate by allowing different variables to be varied; Lorentzian fitting being the most common, considers the basic three hyperfine interactions, area and linewidth ratios between absorption lines, and the areas of each. More complicated fitting styles can be used where necessary, such as an extended Voigt based fit which often yields a better overall fit in amorphous materials where the sites are less well defined than in crystalline materials.

2.6.1 Spectrometer calibration

Calibrating a Mössbauer spectrometer is to ensure that the velocity range heliport position is consistent throughout the sample measurements. A new calibration data set is collected either on changing the velocity range, or after a long time at a given velocity range. The heliport, an analogue dial control that displays a value directly proportional with the velocity range, is prone to slight misplacements; a value of 2.04 translating to $\pm$ 12 mm s^{-1} may be slightly off-centre, resulting in a slightly increased or decreased velocity range. A suitable calibrant standard is measured at room temperature, about which the hyperfine parameters are well-known. A common calibrant was previously sodium nitroprusside [34] (SNP) [$Na_2Fe(CN)_5NO.2H_2O$], however more recently the ferro-magnetic, low spin, body-centred cubic α-Fe is used as the calibrant, with a single sextet with a hyperfine field of 33 T. The position of the absorption lines of α-Fe are well known, allowing the velocity axis to be scaled against the absorption lines presented to the software. The centre of the calibration spectrum is set as the zero-velocity point against which all sample centre shifts can be quoted. Calibration data should be routinely processed as sample data to verify that the calibrant used has not degraded over time through oxidation or hydration.

2.6.2 Spectrometer optimisation

As with any spectroscopic technique, regular equipment maintenance and routine benchmarking are necessary to ensure the highest quality data is being collected, accurately and reliably. For a typical Mössbauer spectrometer the most important optimisations are through ensuring the detector has sufficient gas pressure, bias voltage and distance from the radioactive source. Proper energy range selection is almost paramount, and is achieved using the *pulse height analysis* mode of the spectrometer. In this mode the energy profile of the source is observed and the spectroscopist can define the region of the profile that the detector should count, where anything outside of this region is omitted. This ensures a high signal to noise ratio, as anything outside of the defined region, which should be centred around the 14.41 keV peak, will contribute only to the background noise. With the *Janis* cryogenic spectrometer used, the optimisation and maintenance are often the same. Part of the vibration isolation is through air-filled pads at the feet of the table legs, these need to be regularly refilled with air to maintain pressure, otherwise the table will begin to sag. If this occurs, the sample holder shaft will sink lower into the chamber, reducing the count rate as the sample is no longer in-line with the source and detector, and can ultimately contact the cold finger, potentially causing irreversible damage. The sample chamber, which can be under vacuum or at ambient pressure with helium, should only be filled with helium at or below 100 ˚C. This is due to the permeability of helium through Mylar, which is the γ-transparent material in-line with the source, sample and detector – having helium in the chamber at room temperature can damage the Mylar and cause the chamber to leak. With increased time in service the radioactive sources will slowly become less active, resulting in slower data collection, and will need to be replaced.

2.6.3 Sheffield Hallam University Mössbauer Spectrometers
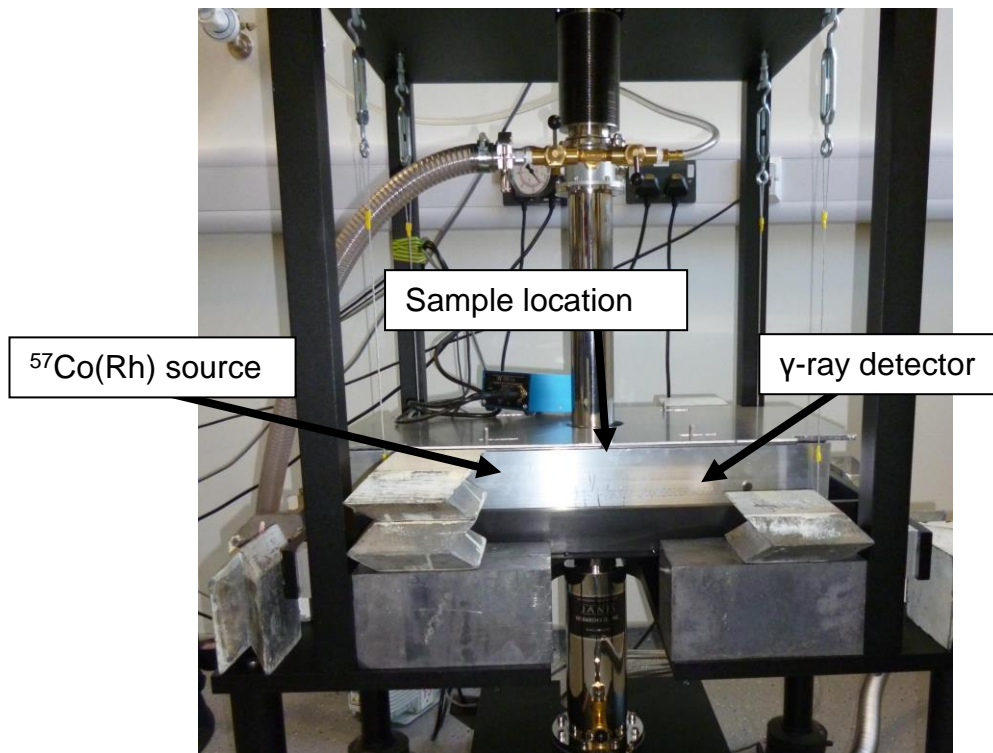

Figure 2.17. SHU low temperature Mössbauer spectrometer. Model CCS-850 10 K Cryocooler from Janis Research Cryogenics. Location indicated are within the suspended casing. Electronics and control system not included.
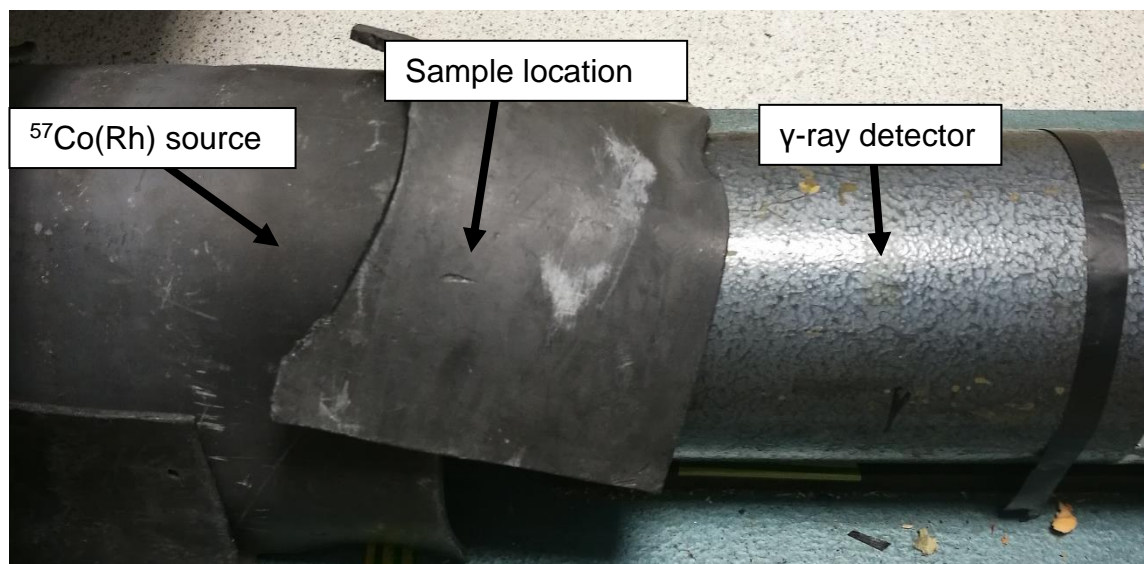

Figure 2.18. SHU room temperature Mössbauer spectrometer. Locations indicated are under lead shielding. Electronics and control system not included.

References

[1]   R. L. Mössbauer, "Kernresonanzfluoreszenz von Gammastrahlung in Ir191," *Zeitschrift für Phys.*, vol. 151, no. 2, pp. 124–143, Apr. 1958.

[2]   T. C. Gibb, *Principles of Mössbauer spectroscopy*. Chapman and Hall, 1976.

[3]   J. Kestin and J. R. Dorfman, *A Course in Statistical Thermodynamics*. New York: Academic Press, 1971.

[4]   RSC, "Introduction to Mössbauer Spectroscopy: Part 1," 2017. [Online]. Available: http://www.rsc.org/membership/networking/interestgroups/mossbauerspect/intro part1.asp. [Accessed: 23-Oct-2018].

[5]   D. P. E. Dickson and F. J. Berry, *Mössbauer Spectroscopy*. Cambridge University Press, 2005.

[6]   H. G. Karge and J. Weitkamp, *Characterization I*. Berlin: Springer-Verlag, 2004.

[7]   N. N. Greenwood and T. C. Gibb, *Mössbauer spectroscopy*. London: Chapman and Hall, 1971.

[8]   H. J. Lipkin, "Some simple features of the Mössbauer effect," *Ann. Phys. (N. Y).*, vol. 9, no. 2, pp. 332–339, 1960.

[9]   H. Frauenfelder, *The Mössbauer Effect*. New York: W. A. Benjamin, Inc., 1962.

[10]   F. E. Wagner, H. Spieler, D. Kucheida, P. Kienle, and R. Wäppling, "Mössbauer studies and nuclear quadrupole moments of 186, 188, 189, 190 Os," *Zeitschrift für Phys. A Hadron. Nucl.*, vol. 254, no. 2, pp. 112–126, Apr. 1972.

[11]   L. Aldon, A. Perea, M. Womes, C. M. Ionica-Bousquet, and J. C. Jumas, "Determination of the Lamb-Mössbauer factors of $LiFePO_4$ and $FePO_4$ for electrochemical in situ and operando measurements in Li-ion batteries," *J. Solid State Chem.*, vol. 183, no. 1, pp. 218–222, 2010.

[12]   S. C. Parida, S. K. Rakshit, and Z. Singh, "Heat capacities, order-disorder transitions, and thermodynamic properties of rare-earth orthoferrites and rare-earth iron garnets," *J. Solid State Chem.*, vol. 181, no. 1, pp. 101–121, 2008.

[13]   S. M. Dubiel, J. Cieślak, I. V. Alenkina, M. I. Oshtrakh, and V. A. Semionkin, "Evaluation of the Debye temperature for iron cores in human liver ferritin and its pharmaceutical analogue, Ferrum Lek, using Mössbauer spectroscopy," *J. Inorg.*

Biochem., vol. 140, pp. 89–93, 2014.

[14]   Ritverc, "Mössbauer Sources: Cobolt-57 / Co-57," 2017. [Online]. Available: http://www.ritverc.com/products/detail.php?ID=1691. [Accessed: 28-Oct-2018].

[15]   W. Sturhahn and A. Chumakov, "Lamb-Mössbauer factor and second-order Doppler shift from inelastic nuclear resonant absorption," *Hyperfine Interact.*, vol. 123, p. 809, 1999.

[16]   M. D. Dyar, D. G. Agresti, M. W. Schaefer, C. A. Grant, and E. C. Sklute, "Mössbauer Spectroscopy of Earth and Planetary Materials," *Annu. Rev. Earth Planet. Sci.*, vol. 34, no. 1, pp. 83–125, 2006.

[17]   V. Rusanov, S. Stankov, V. Angelov, and V. Schünemann, "Line width of single-crystal Mössbauer absorption," *Nucl. Instruments Methods Phys. Res. Sect. B Beam Interact. with Mater. Atoms*, vol. 170, pp. 443–453, 2000.

[18]   S. M. Qiam and S. M. Qaim, "Recoil-free fractions of the 14.4 keV Mossbauer gamma line of 57Fe in various host lattices," *J. Phys. F Met. Phys.*, vol. 1, pp. 320–327, 1971.

[19]   Janis, "Janis Research Company Products Overview," 2017. [Online]. Available: https://www.janis.com/Products/productsoverview.aspx. [Accessed: 11-Oct-2018].

[20]   Janis, "Janis 10 K Closed Cycle Refrigerator Systems," 2017. [Online]. Available: https://www.janis.com/Products/productsoverview/10KelvinCryocoolers/10Kelvin CryocoolerMossbauerSpectroscopy.aspx#. [Accessed: 11-Oct-2018].

[21]   R. H. Herber, *Chemical Mössbauer Spectroscopy.* Springer US, 2012.

[22]   R. V. Pound, G. B. Benedek, and R. Drever, "Effect of hydrostatic compression on the energy of the 14.4-kev gamma ray from Fe57 in iron," *Phys. Rev. Lett.*, vol. 7, no. 11, pp. 405–408, 1961.

[23]   Y. Hazony, "Effect of Zero-Point Motion on the Mössbauer Spectra of $K_4Fe(CN)_6$ and $K_4Fe(CN)_6.3H_2O$," *J. Chem. Phys.*, vol. 45, no. 7, pp. 2664–2668, 1966.

[24]   G. K. Shenoy and F. E. Wagner, *Mössbauer isomer shifts.* North-Holland Pub. Co., 1978.

[25]   H. Wegener, *Der Mössbauer-Effekt und seine Anwendungen in Physik und Chemie.* Mannheim: Bibliographisches Institut, 1966.

[26] X. Ma, S. Ran, H. Pang, F. Li, P. C. Canfield, and S. L. Bud'Ko, "[57]Fe Mössbauer study of $Lu_2Fe_3Si_5$ iron silicide superconductor," *J. Phys. Chem. Solids*, vol. 83, pp. 58–63, 2015.

[27] K. A. Stroud, *Engineering Mathematics*, 7th ed. New York: Industrial Press Inc.,U.S., 1990.

[28] R. V. Parish, *NMR, NQR, EPR and Mössbauer spectroscopy in inorganic chemistry*. Ellis Horwood Ltd, 1990.

[29] R. V. Parish and R. H. Platt, "Studies in mössbauer spectroscopy. Part II. The structures of some organotin halides, and a test of the point-charge model," *Inorganica Chim. Acta*, vol. 4, pp. 65–72, Jan. 1970.

[30] W. Marshall and C. E. Johnson, "Hyperfine field in metals and alloys," *J. Phys. Le Radium*, vol. 23, no. 10, pp. 733–737, 1962.

[31] W. Marshall, "Orientation of nuclei in ferromagnets," *Phys. Rev.*, vol. 110, no. 6, pp. 1280–1285, 1958.

[32] C. E. Johnson, "The Mössbauer Effect in Iron Alloys," vol. 81, 1963.

[33] J. J. Spijkerman, *Mössbauer spectroscopy standard for the chemical shift of iron compounds*. U.S. Dept. of Commerce, National Bureau of Standards: for sale by the Supt. of Docs., U.S. Govt. Print. Off., 1967.

[34] J. W. Niemantsverdriet *et al.*, "Behavior of metallic iron catalysts during Fischer-Tropsch synthesis studied with Moessbauer spectroscopy, X-ray diffraction, carbon content determination, and reaction kinetic measurements," *J. Phys. Chem.*, vol. 84, pp. 3363–3370, 1980.

3 Material Synthesis and Characterisation

3.1 Material synthesis

3.1.1 Solid state sintering - ball milling

Solid-state sintering describes the process whereby oxide precursors are mixed, reacted and usually densified, in the context of ceramic synthesis. Ball milling is a common method used in this type of synthesis [1]–[3]. Oxide precursors are dried to remove any physical hydration, typically for a minimum of 24 hours at 120 °C. Once dried the precursors can be batched in accordance to the required stoichiometry and loaded into the milling vessel, along with a suitable milling media. Ball milling can be carried out in different ways, depending on the required outcome; high energy ball milling uses a planetary ball mill at high speeds, using small milling media while the use of a rotary mill with larger milling media is considered low energy. The higher energy ball milling will result in smaller particle sizes, as the greater energy is spent creating a higher surface area. The milling process can also be carried out either 'wet' or 'dry', where wet milling is carried out in the presence of a solvent which does not play a part in the milling process, but keeps the reactants in suspension [4]. After the milling process, which can be from minutes to hours, the mixture is calcined / sintered at an elevated temperature; a wet milled material will need time beforehand for the solvent to evaporate. While the milling step is designed to physically force the oxide precursors together, the calcination / sintering process is to have them react to form the desired phase(s). In the context of solid-state ball milling, calcination is also to decompose carbonates and crystalline water, and to remove any volatile materials and carbon, causing the evolution of carbon dioxide and water. The milling and calcination steps may be carried out more than once to ensure full homogeneity. After being fully milled and calcined, and evaporation where appropriate, the resulting powder is pressed into pellets using a pellet press, where the compression pressure and dwell time are important considerations to ensure proper densification. These green body pellets are then sintered at a temperature above the calcination temperature, wherein the individual particles are densified into a single monolithic body of greater mechanical strength than the unfired green body pellets. These sintered pellets can then be analysed for

their composition, crystal phase identification, density, and any other characterisations required.
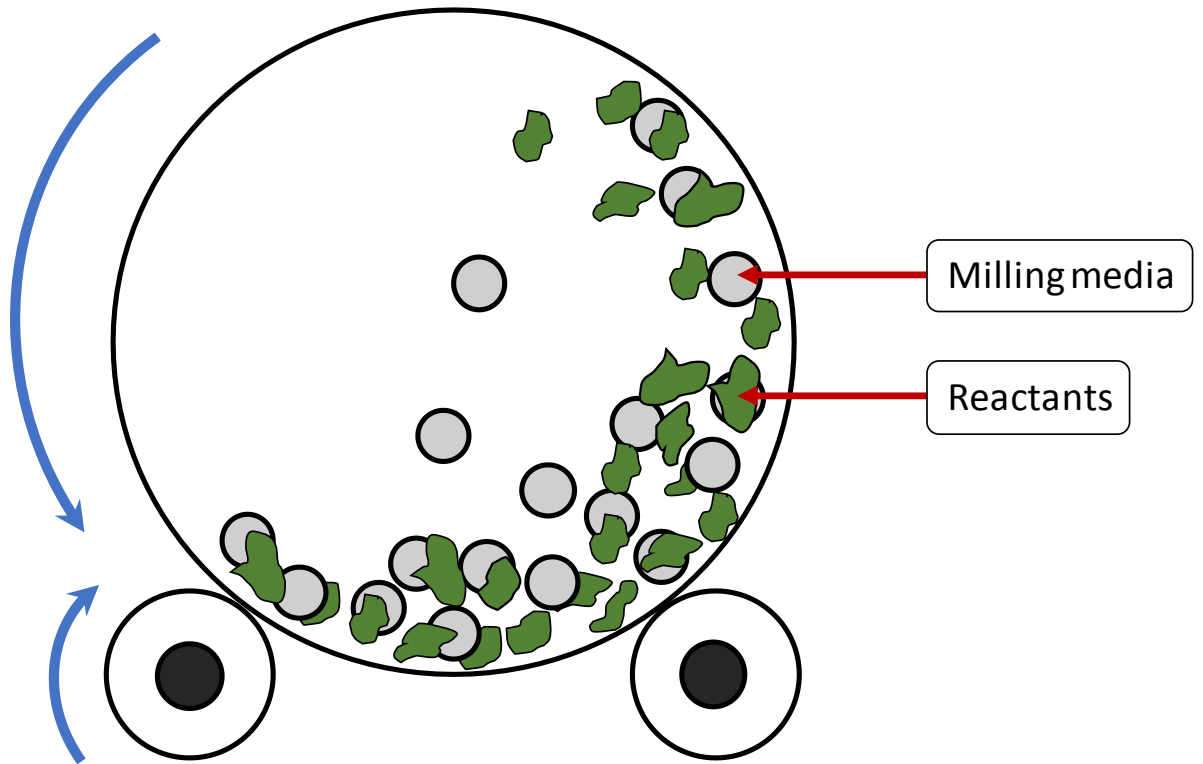
Figure 3.1. Horizontal cross-section of ball mill in motion.
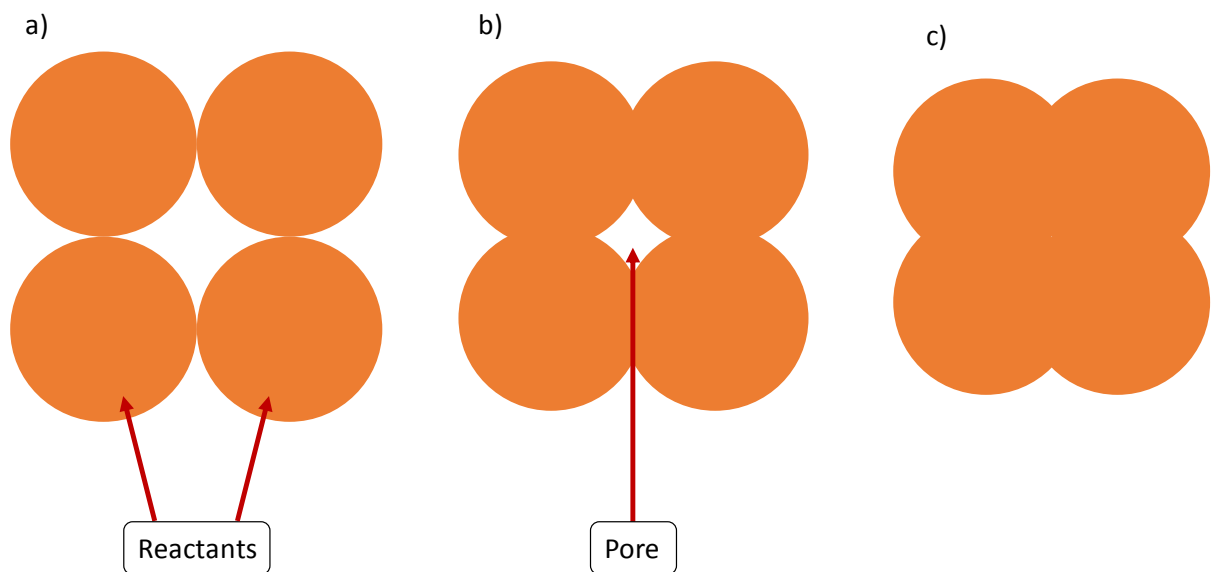

Figure 3.2. Three stages of sintering, starting from, a) loose particles in mutual contact, b) porous body and c) finally fully sintered, densified monolith.

3.1.2 Citrate-nitrate auto-combustion

Combustion synthesis can produce monophasic, homogenous nanoparticles through a thermally induced redox reaction between oxidant and fuel [5]. The citrate-nitrate auto-combustion method (CNAC) is very similar to sol-gel combustion synthesis routes, such as the Pechini method [6]–[8]. In CNAC, the fuel is often citric acid and metal nitrates are the oxidant. Stoichiometric amounts of high purity metal nitrates are dissolved with the minimum amount of distilled water for a clear solution. Aqueous citric acid is added to the nitrate solution in a variable citrate: nitrate ratio, as necessary for the reaction. The pH of the solution can be controlled through the addition of an ammonia solution as needed. The citrate-nitrate solution is then heated on a hot plate to, and held at, 80 °C to evaporate the water from solution, leaving a sticky, viscous gel. The temperature of the gel is then raised, causing the gel to decompose, and eventually auto-combust. The combustion results in an aerogel structure which can be easily ground into a fine powder. The powder can then be calcined, as detailed for the solid-state sintering process. For CNAC materials, pelletizing is not necessary as this route is used to produce nanomaterials, and not dense monoliths [9].

3.1.3 Flame spray pyrolysis

One synthesis route used to produce very small nanoparticles (< 20 nm) is flame spray pyrolysis (FSP) [10], [11], however the equipment necessary for this method requires high level of investment and maintenance. The synthesis method producing nanoparticles is due to the rapid quenching after synthesis as the heat loss by radiation and convection is at such a high rate that sintering is limited [12]. As illustrated in the schematic by Teoh, Amal and Mädler in Figure 3.3, the precursor solution is fed directly into the main flame where it is dispersed into small droplets as it is ejected. Oxygen is fed around the nozzle of the precursor capillary tube to fuel the combustion that is initiated by the surrounding methane-oxygen flamelets. At the base of the flame, as the precursor is

dispersed, it is decomposed as temperatures can exceed 2000 K, causing complete combustion of organic compounds, leaving metallic and semi metallic components [10], [12]. These remaining components will then nucleate to form the primary particles of pure metals or oxides, which can then aggregate in the high-temperature region of the flame to produce the end product. Due to the short time spent in the high temperatures the sintering time is so minimal that the resulting particles have incredibly small sizes. The final particles, after agglomeration, are collected by back-pressure or suction from above a collection filter. The properties of the product of FSP synthesis are heavily influenced by many factors that can be predetermined by the operator. For example, the stoichiometric ratios of the precursors and solvents will influence the flame temperature, the pressure of the precursor solution will affect the droplet size of the dispersion and the size of the flame. Proper control of all the variables requires highly trained operators using large amounts of equipment.
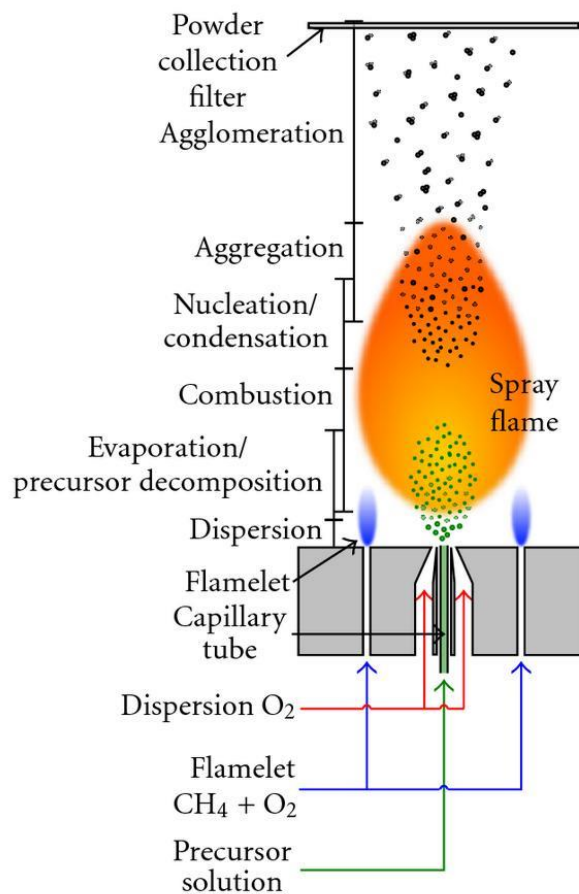

Figure 3.3. Cross-section of a flame-spray pyrolysis equipment arrangement, and different processes through the flame. Originally presented by Teoh et al. [10].

3.1.4 Wet chemistry

The phrase 'wet chemistry' is a rather vague term, referring to synthesis methods wherein reactions occur in a liquid phase. Reaction rates in wet chemistry are controlled through the temperature, environment, aggitation and presence of catalysts. In the scope of materials being studied for these works, the main wet chemistry routes are co-precipitation, through which some of the perovskites were synthesised; and some more complex routes for producing iron carbide nanoparticles.

Two complex processes which pertain to the materials herein, namely the nanoparticles of two iron carbides, are the decomposition of iron(III) acetate in gelatin, and the thermal decomposition of iron pentacarbonyl in the presence of cetyltrimethylammonium bromide (CTAB), for the synthesis of Fe_3C and Fe_5C_2 respectively. A biopolymer route for synthesising Fe_3C has been presented by Schnepp and colleagues [13] wherein carefully prepared solutions of ammonium alginate and ammonium hydroxide were combined with a gelatin gel and iron(II)acetate. The product of combining the iron component to the biopolymer solution mixture was cast into petri dishes, dried and heated at 2 °C per minute to 650 °C in lidded crucibles for calcination under nitrogen, and rapidly cooled. A facile synthesis route for nanoparticles of Fe_5C_2 was relatively recently presented by Yang, Zhao, Hou and Ma from China in 2012 [14]. This synthesis is carried out in a four-neck round-bottom flask in which octadecylamine and CTAB are mixed and degassed under N_2. After heating to 393 K, iron pentacarbonyl [$Fe(CO)_5$] is injected through one of the necks of the flask via a septa plug and the solution is heated to 453 K at 10 K per minute. The decomposition of $Fe(CO)_5$ and nucleation of iron nanoparticles is accompanied by a colour change of the solution from orange to black. The solution is heated at 10 K per minute to 623 K and held for 10 minutes to allow carbon atoms to occupy the interstices between the larger, closely-packed iron atoms to form the Fe_5C_2. The flask is cooled to room temperature and the product is washed in ethanol and hexane to remove any unreacted precursor. Iron pentacarbonyl is a highly toxic, flammable material,

meaning thorough washing is necessary. The retrieved nanoparticles can either be stored in ethanol and hexane, or under Ar to avoid contact with air.

Several of the perovskite samples studied were synthesised by co-precipitation, wherein an anion solution and cation solution are mixed causing the precipitation of a substance that would ordinarily be soluble [15]–[17]. For the materials produced, namely various $LaFeO_3$ perovskites, precursor salts (hydrated $La(NO)_3$ and $Fe(NO)_3$) were dissolved in a KOH solution and the titration of ammonia water caused the precipitation of $LaFeO_3$ which may then be washed and calcinated. The exact process parameters of this synthesis route are proprietary to Johnson Matthey, regarding precursor ratios, concentrations, titration rate and other parameters.

3.2 Supplementary Characterisation Techniques

Mössbauer spectroscopy is an isotope specific technique that can accurately detail the chemical environment around the nucleus, yielding information about its oxidation state, bonding environment and magnetic structure. As powerful a tool as it can be, Mössbauer spectroscopy can rarely be used as a stand-alone phase identification technique, and it is best utilised in combination with other, complementary characterisation techniques. Elemental analysis can indicate the ideal amount of sample to load into a Mössbauer absorber, as well as indicate any contaminations or losses through synthesis. X-ray fluorescence (XRF) and inductively coupled plasma spectrometry (ICP) are common bulk elemental analysis techniques, while scanning electron microscopy (SEM) with energy dispersive X-ray (EDX) is useful for more localised areas of interest. For phase identification, X-ray diffraction (XRD) utilises the relationship between the wavelength of an X-ray and the spacing between atoms to allow identification of phases against a database of known materials. Identifying phases through XRD, which is made much more facile with the use of an elemental analysis technique beforehand, can suggest the phases contributing to a Mössbauer spectrum. A weakness of XRD is that it cannot distinguish between different amorphous, or non-crystalline phases, whereas Mössbauer

spectroscopy can, and XRD may not be sensitive or discriminating enough to identify the less abundant phases of interest. Vibrational analyses using Raman spectroscopy and Fourier transform infrared (FTIR) spectroscopy can yield useful information about the bonding in a material, which can be particularly useful when analysing the silicate network of glasses for example. Interpretation of vibrational spectra can aid in identifying the phases in a material, crystalline or amorphous, through the identification of vibrational modes between atoms, with the aid of elemental and structural analyses. Scanning electron microscopy (SEM) uses a high-energy electron beam moving in a raster scan pattern which interacts with the sample to produce a number of signals that can yield information about sample topography, such as grain or crystal size. SEM microscopes are often equipped with the ability to analyse the x-rays emitted from the sample, which will have characteristic energy levels for each element, allowing compositional analysis (energy dispersive x-rays; EDX). With the combination of these techniques, and Mössbauer spectroscopy, materials can be thoroughly characterised and studied for their applications thereafter.

Materials studied in this project have been split into catalytic and battery material groups, with the catalysts consisting of $LnFeO_3$ perovskites, iron molybdates and iron carbides, while battery materials are cathodic $LiFePO_4$ and some anodic candidates. Once thoroughly characterised, these materials can be studied as a function of their intended application, through carefully planned electrochemical or catalytic testing processes. The type of catalyst determines the way it is tested, as the test needs to suitably simulate the service environment of the catalyst, regarding factors such as temperature, pressure and reactants. Electrochemical analyses most commonly used to measure the response of the material to a constant, such as constant current or voltage. These analyses can give useful information regarding material resistivity, charge density or how it can be expected to perform over time. Two common methods are electrochemical impedance spectroscopy (EIS), which produces Nyquist plots and yield information regarding the materials resistance mechanisms, and constant current, charge/discharge cycles which can indicate the cyclic stability of a material.

3.2.1 X-ray Fluorescence Spectroscopy (XRF)

Bombarding a material with high energy X-rays can cause shell electrons to be displaced from their orbit [18]. The displacement of an electron from its shell will result in an electron vacancy, making the atom unstable. In order to stabilise the atom, an electron from a higher orbit can move into the vacancy, such as a K-shell vacancy being filled by an L-shell electron [18]. The binding energy of electrons is greater the further away from the nucleus they are, meaning that for an L-shell electron to fill a K-shell vacancy the electron must lose energy, which is achieved through the emission of an X-ray. The energy lost will be equivalent to the difference in energy between the two electron shells, which is determined by the distance between the shells, which is itself a unique characteristic of each element [19]. The detection and analysis of these characteristic X-rays allows for the identification and semi-quantification of the elements present in a material. To calculate the wavelength of the generated, fluorescent electron we turn to Planck's law, equation 1, as;

$$\lambda = hc/E \tag{1}$$

The conversion of energy to wavelength allows for wavelength dispersive XRF, where the generated X-rays are diffracted from a single crystal towards the detector [18]. In WD-XRF the crystal, or monochromator, is used to vary the incident and take-off angles of the photon, where a single X-ray wavelength can be selected by Bragg's law, as in equation 2, where d is the interatomic spacing of atoms in the crystal (constant) and θ is the angle between the incident and take-off paths. In WD-XRF there are multiple incident wavelengths of photons, each can be isolated and detected at certain θ angles; this differs from X-ray diffraction where the incident photons are monochromatic and the d-spacing is identified by varying the θ angle [20]. More than one crystal is used to diffract the generated X-rays to ensure a full coverage of wavelengths. The spectrometer used at SHU is a PANalytical MagiX Pro equipped with Rhodium anode.

$$n\lambda = 2d\sin(\theta) \tag{2}$$
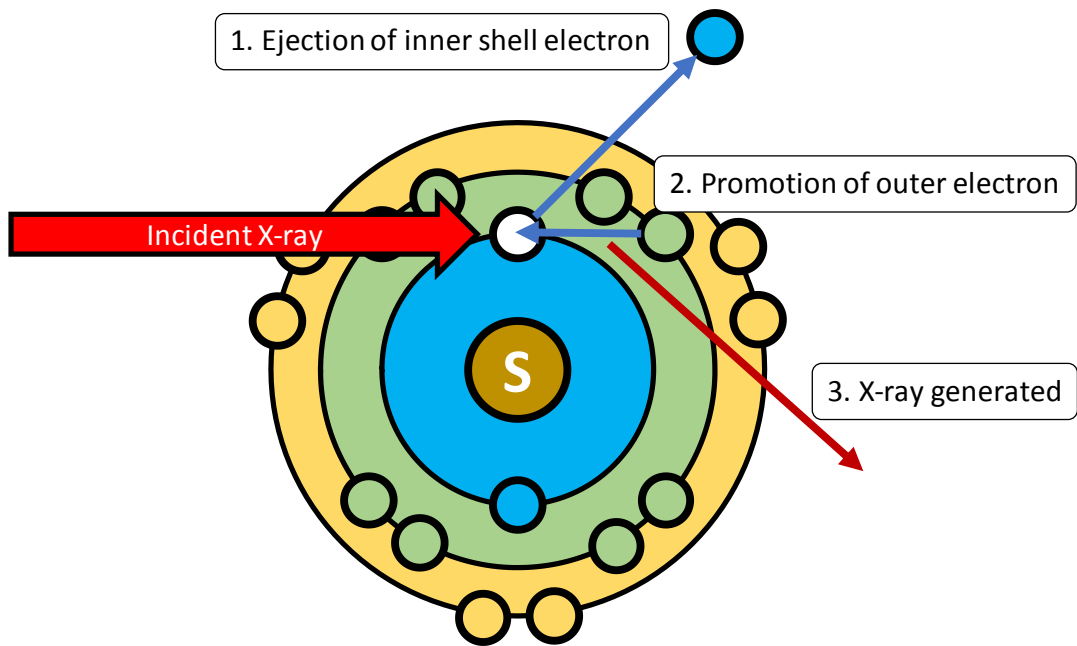
Figure 3.4. Atomic schematic of characteristic X-ray generation by XRF.
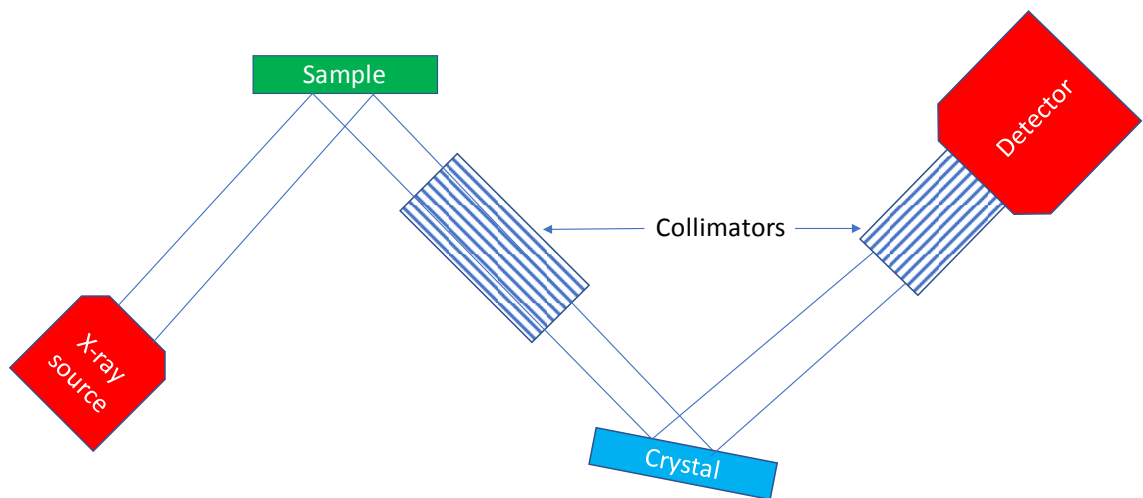
Figure 3.5. Schematic of internal components of wavelength dispersive x-ray fluorescence spectrometer in Bragg-Brentano geometry.

In order to quantify the abundance of elements in a material, the sample preparation for XRF analysis involves diluting the sample material with a predetermined ratio of flux binder [18], [19]. This can involve embedding the sample into a cellulose binder or forming a glass bead using light elements as the flux such as lithium tetraborate, both methods resulting in a flat disc, a

necessary standardisation of the sample preparation to ensure repeatability [19]. In either case, for flux elements (C, H, Li, B, O), the energy of the X-rays generated are too low to escape from the sample without being absorbed, making them difficult to be detected by the spectrometer, and by informing the software of the flux material and the flux to sample ratio, it is able to quantify the elements present in the sample [18]. This is semi-quantification as the abundances are relative to one another and are taken as a percentage of the total. XRF can produce fully quantitative results, however this requires the analysis of calibration materials with known concentrations of the elements of interest to create calibration curves and relating sample peak heights to these curves. This process is more time consuming and not always necessary, particularly in samples with few elements.

Detectors for the generated X-ray photons operate using the same detection principle as discussed for the proportional counters in the chapter *2. Mössbauer Spectroscopy*. For wavelength dispersive XRF, as only a single wavelength radiation is being diffracted by the monochromatic crystal at a given angle, a photomultiplier detector can be used [18]. As the incoming photon ionises atoms inside of the detector a charge is generated on the cathodic detector wall, the energy of which is proportional to the energy of the photon on entry. Amplification of the signal results in an accumulating count of photons, which is processed and synchronised with the angle of the crystal to produce analytical data [21]. The raw data produced consist the count rate as a function of crystal angle (as y and x-axes respectively), the peaks from which can be analysed by the spectroscopist and relevant software to assign the peaks to an electron transition from an element (M to K shell transition of element X, X K_β) [19]. After the peaks have all been assigned, the software (PANalytical SuperQ™ at SHU) can output the relative abundances of the elements present in the sample material. Appropriate calibrants are used to inform the software of the expected peak intensities of different elements, as some may fluoresce more intensely than others. There is the necessity of a human element in the analysis of XRF data, such as understanding the elements which can realistically be expected in a material, as some elements can present spectral peaks that

overlap; the K$_\alpha$ of one element around the same angle as the K$_\beta$ or L$_\alpha$ of another element, for example [22].

Figure 3.6. PANalytical MagiX Pro XRF spectrometer at SHU.

3.2.2 X-ray diffraction

The working principle of an X-ray diffractometer are closely related to those of an X-ray fluorescence spectrometer; both exploit Bragg's law of diffraction, as given in equation 2 [20].

For XRF, the wavelengths are the unknown parameter, the d-spacing of the crystal(s) are known and the relative angle between the crystal and detector are modulated to allow selective detection of individual wavelengths. X-ray diffraction (XRD) uses monochromatic X-rays (constant λ) to determine the interatomic distances (d-spacing) in the sample material by varying the angle between the sample and detector [20].
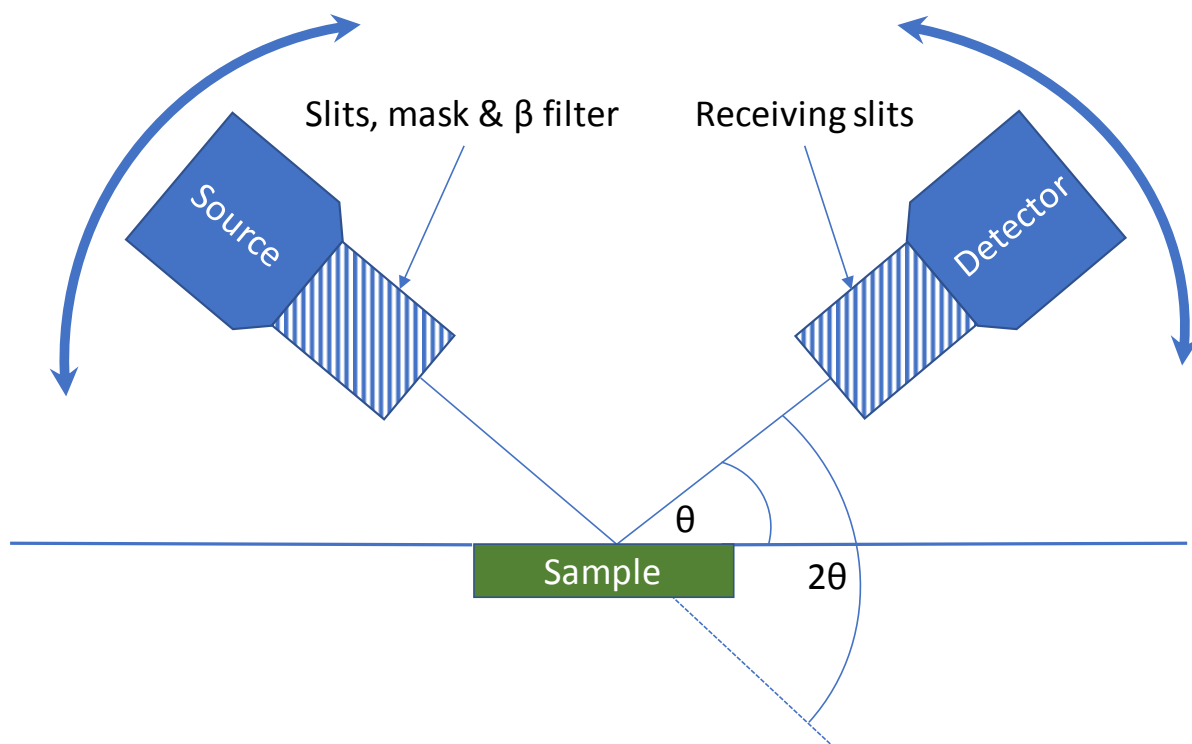
Figure 3.7. X-ray diffractometer components in Bragg-Brentano geometry.

The X-ray diffractometer used at SHU during this work is a PANalytical Empyrean with PIXcel^{3D} detector and was always used in Bragg-Brentano geometry as shown in Figure 3.7. This diffractometer can be equipped with different X-ray sources depending on the material being studied. The wavelength of the source X-rays would be different between the different source anodes (Cu λ = 1.5406 Å; Co λ = 1.7890 Å) [23], and to change the source between measurements of materials to be compared would require the data produced to be converted from the usual 2θ scale to one of d-spacing. Directly following the X-ray source is a β filter which is to block the β emissions from the X-rays and allow only α emissions [24]. The importance of this is that the α emissions are more intense than β, are of the order of magnitude of the lattice spacing in a crystalline solid. Filtering the β X-rays allows for only the more intense α X-rays to reach the detector for analysis, simplifying the resulting data. For a source of cobalt, the filter used is iron, and for a copper source the filter is nickel [23]. For the diffraction patterns presented herein, collected on the diffractometer at SHU, the Cu Kα source was used (40kV, 40 mA); while Cu Kα radiation can caused fluorescence in high iron materials. In short, fluorescence is caused by the Cu Kα

X-rays, with an energy of 8.04 keV, being able to eject a K shell electron from iron (ionization energy of Fe K-shell electron ≈ 7keV) [25], [26]. After the filter, the X-rays pass through *Soller slits*, which are essentially thin plates stacked together with a fixed spacing in between, which prevent angular divergence of the beam out of the θ/2θ plane, resulting in a narrower distribution of X-ray energies [20]. The X-rays then pass through a divergence slit, which restricts the vertical (as the instrument is observed) passage of X-rays, and then a mask, which restricts the horizontal passage. These restrictions are to only allow X-rays to pass through that will be on the sample area, and thereby avoid the detector registering signals from anything else [23], [27]. After these slits is an anti-scattering slit, which further improves the definition of the final X-ray beam by eliminating any scattering caused by the passage of X-rays through the slits, as shown in Figure 3.8.
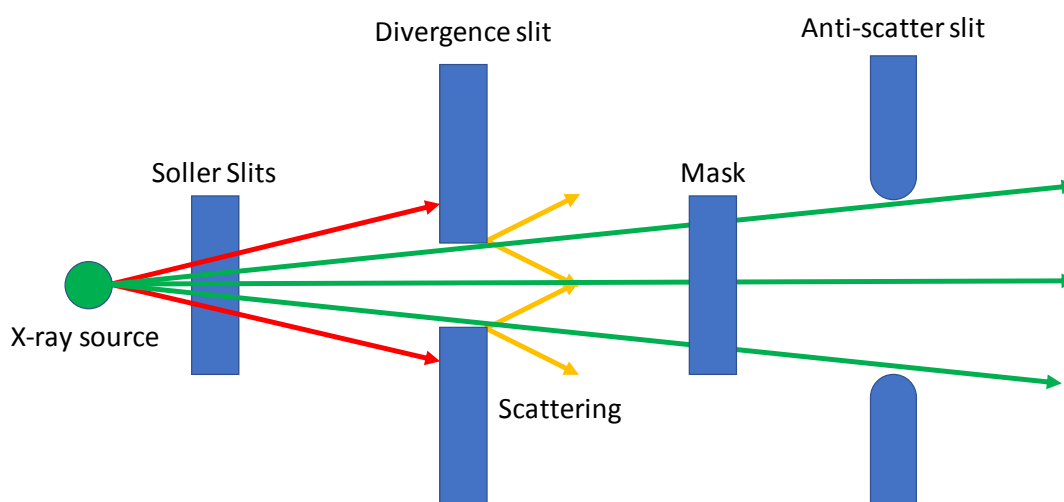
Figure 3.8. Schematic overview of X-ray diffractometer source filtering and focusing system.

After interacting with the sample material, the diffracted X-rays pass through another set of soller slits before reaching the detector, which in the PIXcel[3D] is a microchip consisting of 255 individual detectors. The detector is akin to a digital camera with discrete pixel detectors, except instead of detecting light, the PIXcel[3D] detects X-rays [28].

Upon reaching the sample material, the X-rays may penetrate a few layers into the crystal structure (depending on factors including material density, mass

absorption coefficient and incident angle [20], [26], [29]), resulting in scattering of the incident X-rays. Depending on the interatom spacing of the crystal layers the X-rays may be diffracted towards the detector. This relationship between the X-ray wavelength, interatom spacing and the relative angle is the basis of Bragg's law of diffraction. Schematically show in Figure 3.9, the satisfaction of Bragg's law, results in the X-ray pathways being in-phase upon detection, causing constructive interference, at a particular 2θ [30]. We observe Bragg's law here as the extra distance that wave *b* has travelled to reach the detector is 2(dsinθ), meaning that if *a* and *b* are in-phase then there must be an integer of wavelengths in this distance.
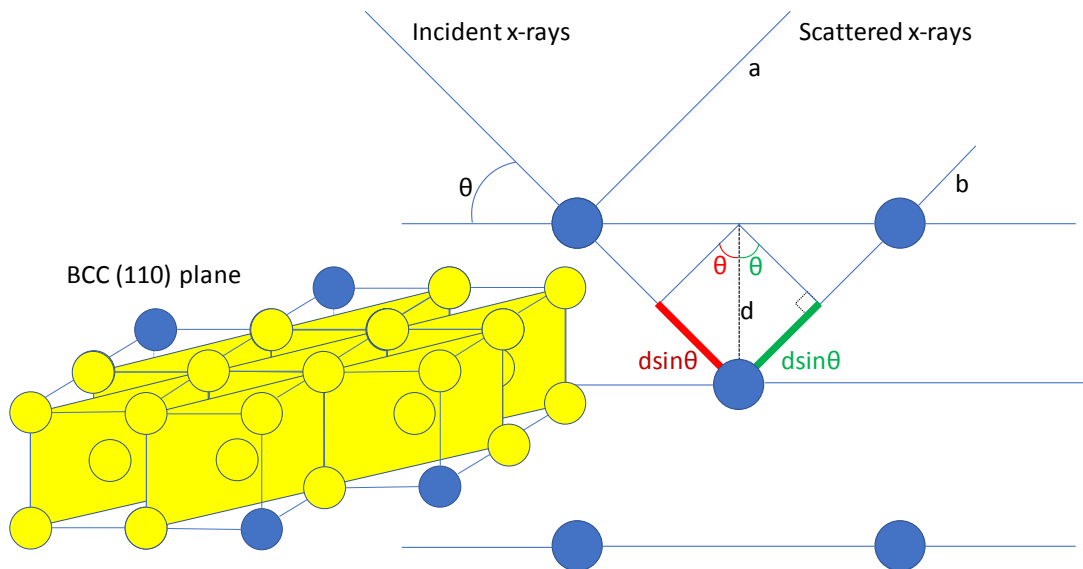
Figure 3.9. X-ray diffraction of BCC (110) plane.

As diffracted X-rays are detected as a function of 2θ, the position of diffraction peaks is directly related to the interatomic distance in the crystal for a particular plane. Because of this, a single phase material can show multiple diffraction peaks, one for each of the crystallographic planes. Once the diffraction pattern has been measured, the positions and relative intensities can be compared with data from databases of known minerals in order to identify the crystal phase(s) present in the material.
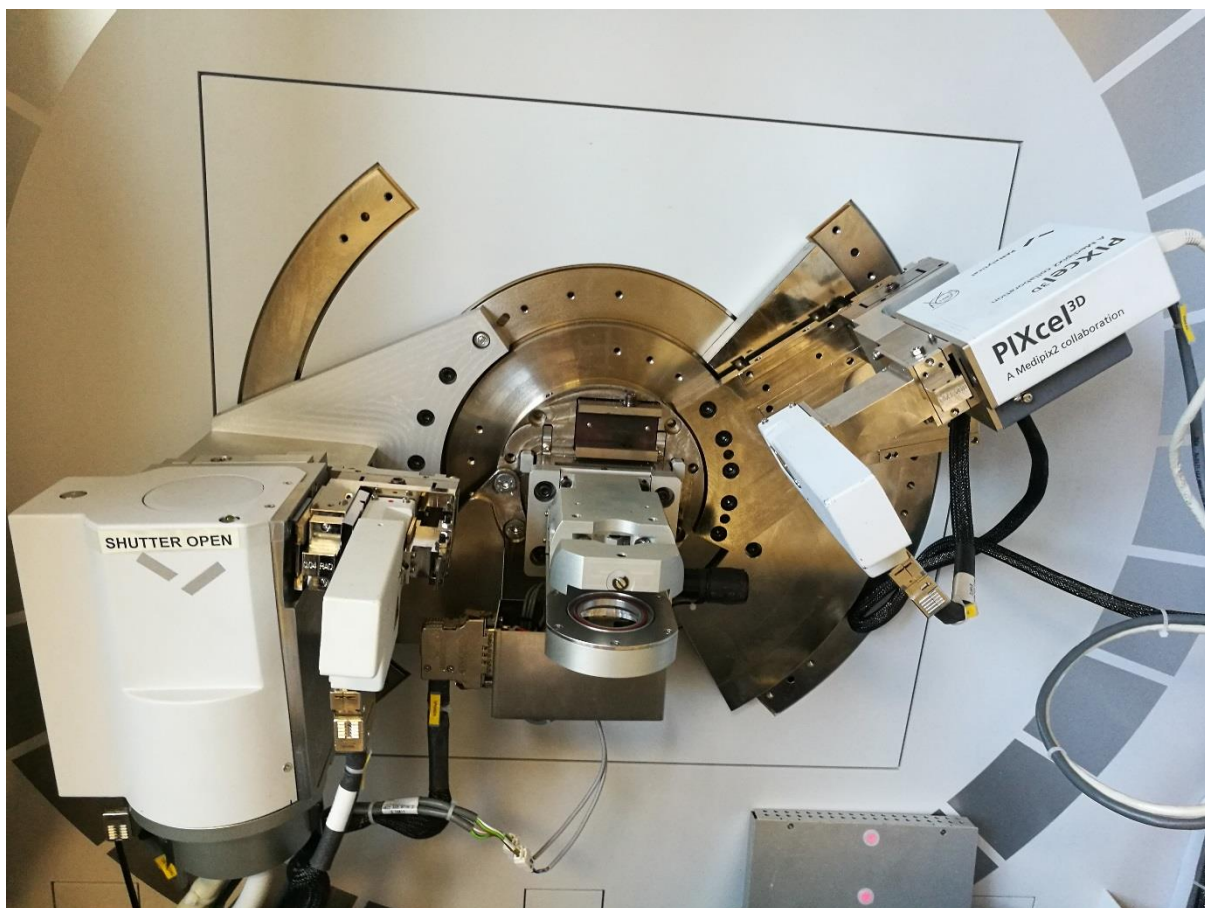
Figure 3.10. X-ray diffractometer, PANalytical Empyrean.

For all measurements herein, powders with particle sizes of ≈ 100 μm were used as the sample materials. To avoid any influence of the texture of the sample, and any preferential orientation of the crystals (non-random orientation), powdered samples should be slow rotating horizontally during the data collection. One main reason for this is that when the data is being compared with published data in the databases the relative intensities of the lines can differ, resulting in incorrect phase identification – phase identification was carried out through comparison of experimental data with the ICSD database of known materials using the *HiScore Plus* software. It is also advantageous for the particles of the powdered samples to be small and consistent in size, as this will further reduce any uneven textures on the surface – this is also why a flat based sample is preferred for XRF. XRD measurements carried out at JMTC by their analytical department were on a Bruker AXS D8 diffractometer with Cu Kα radiation, 40 kV 40 mA tube voltage and current from 10 to 130˚ 2θ at a 0.044˚ step size.

3.2.3 Raman spectroscopy

A molecular bond between atoms, at temperatures above 0 K, will vibrate in at least one mode, with a particular energy and frequency [31]. For a simple triatomic molecule there are three different ways in which atoms can vibrate in relation to each other, as depicted in Figure 3.11. The vibrational energy of a bond can be described by Planck's Law as a function of the vibrational frequency, and as a function of the wavelength [32].

$$E = hV_{vib} = \frac{hc}{\lambda} \qquad (3)$$

Where E is the vibrational energy, h is Planck's constant, V_{vib} is the vibrational frequency, c is the speed of light and λ the wavelength.

| Symmetric Stretching | Asymmetric Stretching | Bending / Scissoring |
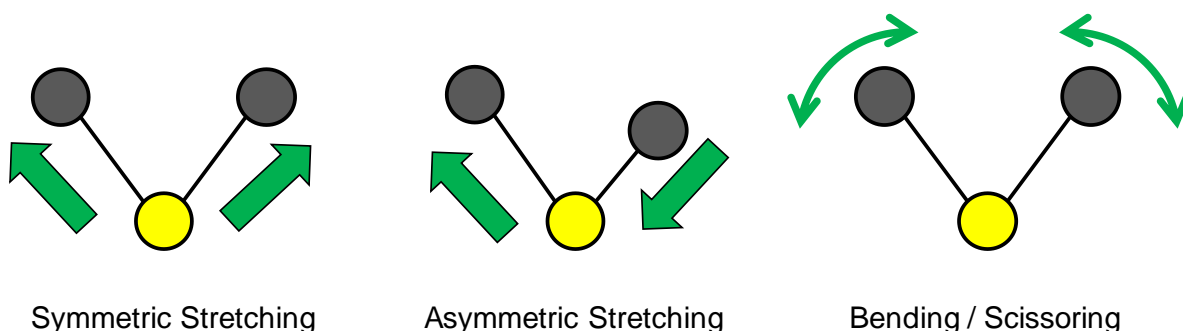
Figure 3.11. Vibrational modes in nonlinear molecules.

The same is true of photons; they too have discrete energy levels, *h(Vphoton)*, the energy of which is directly proportional to the frequency of the electromagnetic field it generates [33]. For convention, we can refer to the photon frequency as V_0 and the frequency of the molecular vibrations as V_{vib}. If a photon is fired into a molecule, the EM field it generates ($E = hV_0$) will polarise the EM field generated by the vibrations of the molecule, sinusoidally. This induced dipole will vibrate at some new frequency, $V_f = V_{vib} \pm V_0$ [32]. This can best be represented as a Jablonski diagram, as in Figure 3.12. In either Stokes or Anti-Stokes, where there is a loss or gain in photon energy, the change in energy is caused by either constructive or destructive interference with the EM field of the

molecule vibration. As described by Planck's Law, the new energy of the photon also presents a change to the frequency and wavelength [32].
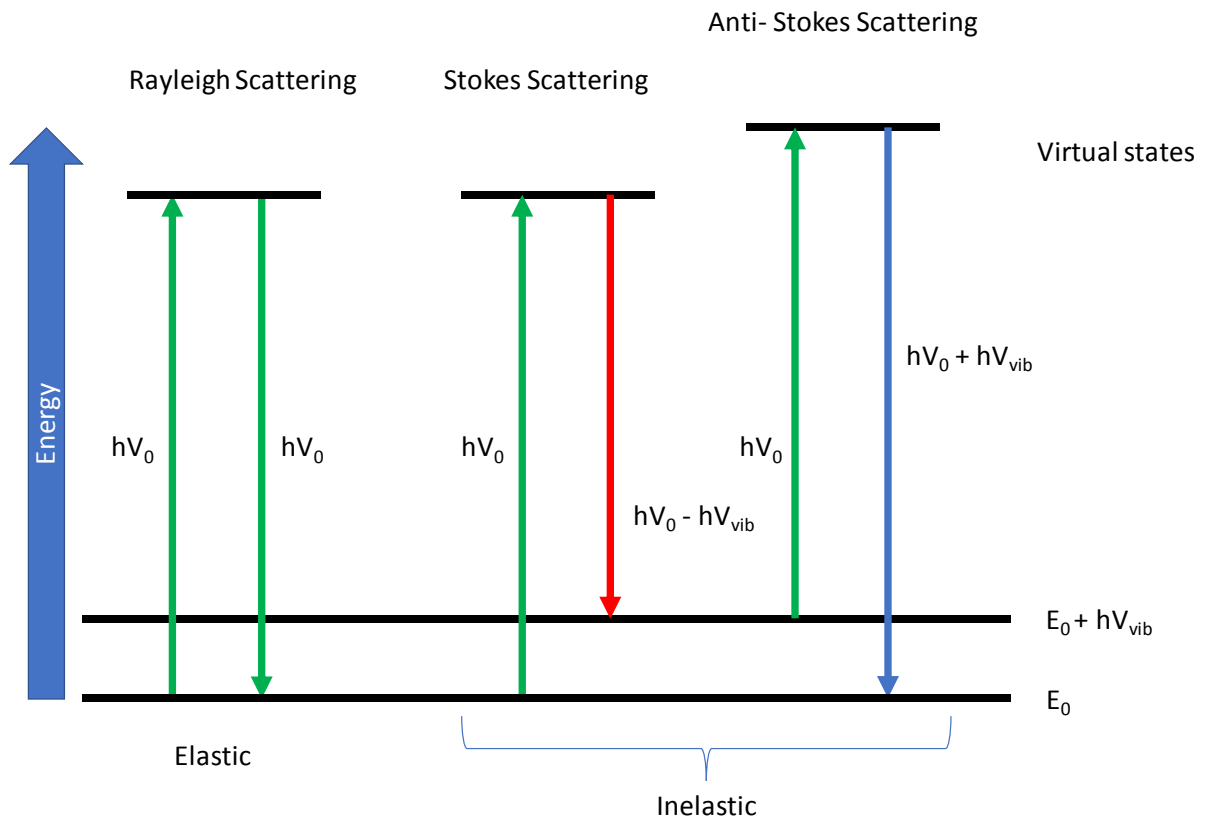
Figure 3.12. Jablonski diagram of elastic and inelastic quantum energy transitions.

The change of photon wavelength can be detected as a change in the wavenumber, *w*, a number of waves per unit distance, which is the reciprocal of the wavelength, such that;

$$\Delta w \ (nm^{-1}) = {}^{1}/_{\lambda_0} - {}^{1}/_{\lambda_{vib}} \ (nm) \tag{4}$$

To make an example; an incident photon with a wavelength 758 nm may induce a wavelength of EM radiation, caused by interactions with the molecules EM field and vibration energy, of 861.13 nm. This would result in a change in wavenumber of 1580 cm^{-1} [34], [35]. This is the working principle of Raman spectroscopy, wherein a monochromatic laser irradiates a select area of the sample material and the wavelengths of the returning photons are detected. Before reaching the detector, the photons are dispersed by concave lenses and a grating, which causes spatial separation of the photons of different energies.

The photons are separated by adjusting the spacing of the grooves in the grating where narrower spacing results in dispersion. The data collecting software will synchronise the incoming intensity of photons with the wavenumber associated with the dispersion, which is somewhat synonymous with the function of the diffracting crystal in XRF. A Raman spectrum would present the intensity of photons as a function of their wavenumber, as the y and x-axes respectively. The resulting peaks in a Raman spectrum can then be related to the frequencies of particular modes of vibration within the sample material; this is done by research and not by a direct fingerprinting process as with XRD [35]. Not all vibrational modes are *Raman active*, meaning that they are not detected by Raman spectroscopy, but these may be visible using Fourier Transform Infrared Spectroscopy, another form of vibrational spectroscopy. Raman spectroscopy can observe modes that result in a change in polarizability, while FTIR observes changes in the dipole moments; considering linear CO_2 symmetric stretching is Raman active and not FTIR active while for asymmetric stretching the inverse is true [31], [32], [36]. To fully characterise the vibrational nature of a molecule, both methods would need to be employed. To properly characterise the materials studied in this work, Raman bands were assigned to vibrational modes within the structure through cross-referencing with available, relevant literature, as presented in Table 4.3.

The vibrations between atoms within a molecule can be conceptualised as springs and masses, where the masses represent the atoms and the springs represent the bonds [37]. When considering an atomistic model in such terms, the strength of the bond can be represented as a spring constant, K, as per Hooke's law, as expressed in equation 6 [35], [38], whereby v is the vibrational frequency, and m_r is the reduced mass of the participating atoms, as defined in equation 7, in which m_x are the masses of the atoms. From equations 6 and 7, increasing the mass of the atoms will reduce the vibrational frequency, and increasing the spring constant, K, which is representing the strength of the bond, increases the frequency. In this simplified conceptualisation of molecular bonds, these two factors are accurately described using Hooke's law, although these are not the only factors to influence vibrational frequency. As Raman shift is related to the vibrational frequency of a bond, as described in equation 5, the atomic

masses and the bond strength will influence the position of Raman bands observed [37]. Depending on the amount of valence electrons being shared, carbon can form single, double or triple bonds to other carbon atoms, increasing in bond strength from single to double; the Raman bands for these bonds typically appears at ≈ 800 to 1,300 cm^{-1} for a single C-C bond, ≈ 1,550 to 1,950 cm^{-1} for a double C=C bond, and ≈ 2,000 to 2,300 cm^{-1} for a triple C≡C bond [33].

$$v = \frac{1}{2\pi} \sqrt{K/m_r} \tag{5}$$

$$m_r = \frac{m_1 m_2}{m_1 + m_2} \tag{6}$$
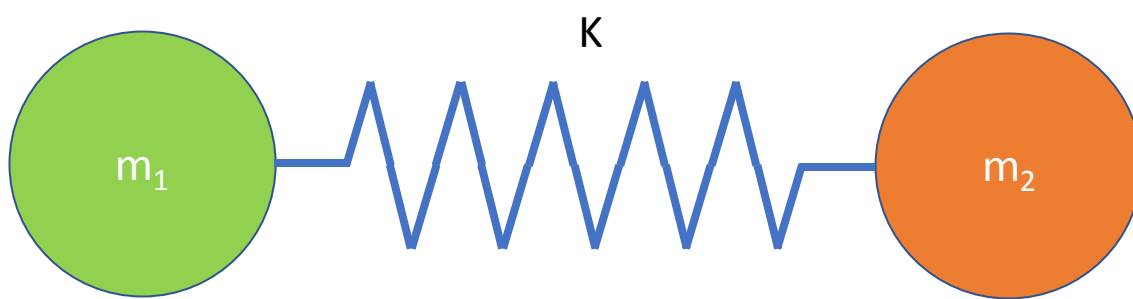
Figure 3.13. Illustration of diatomic model represented as masses on a spring.

When collecting data with Raman spectroscopy, there are a number of experimental parameters that influence the position of the Raman bands, and the quality of the output data. Primarily, the wavelength of the laser being used will have the most profound effect on the position of the bands, as this changes the λ_0 value, and therefore the change in wavenumber [35]. Calibration before collecting data will also help to ensure that the band positions are accurate, this is done by collecting data for a well-known material, such as the single band crystalline silicon [32]. Regarding data quality, the power of the incident beam plays an important role, particularly if the power is set too high as this can cause damage to the sample material. The working distance between the objective lens and the sample surface is also an important consideration, as such the spectroscopist should ensure the sample is well focused using the optical microscope portion of the instrument. The laser spot size can also be adjusted as desired, as can the duration of the measurement and amount of accumulations

that each measurement consists of. Due to the site-specific nature of Raman spectroscopy, focusing on a discrete location on the sample surface, the resulting data is accurate only for that location and not necessarily for the material as a whole. This can be advantageous as it allows for areas of the material surface to be mapped, either in one direction, or as an x-y grid, which can be useful when studying materials that may be inhomogeneous in crystallization or composition. Data of this nature should be accompanied by optical micrographs of the area with the area(s) of interest properly displayed for reference.

For the works herein, the instrument used was a *Thermo Scientific DXR2 Raman Microscope* operating with a 532 nm laser and a charge-coupled device (CCD) detector. The instrument was controlled, and data collected by the *Omnic™ Spectra* software. The data are output as two columns of values, corresponding to the wavenumber and the counts, and can be processed using programmes such as Microsoft Excel, Origin, or in the Omnic™ software itself. For the purposes for which Raman spectroscopy was used in these works the theory provided is sufficient, however a more thorough summary would discuss the selection rules beyond the rule regarding polarizability that was provided, and methods to assign observed Raman bands to specific molecular bonds. A more thorough summary would also discuss the effects of relevant variables used in the study, which may include temperature, the state of matter, or the presence of on-going chemical reactions.

3.2.4 Electrochemical testing

Electrochemistry is a branch of physics that is concerned with the relationships between chemical changes and electricity. The simplest form of electrochemistry is galvanic, or bimetallic, corrosion where the different metals possess different corrosion potentials are in direct contact and are in regular contact with a conductive electrolyte solution [39]. The electrolyte solution enables ion mobility out of the more anodic metal into solution, while the direct metal-metal contact enables the movement of electrons. This is a redox reaction, as the cathodic metal is gaining electrons (reduced) and the anodic metal is losing

electrons and being released as ions (oxidised), and the movement of electrons results in an electric current [40]. The same basic principles apply in a battery cell; there is a movement of ions and electrons resulting in, or caused by, an electronic current [41], [42]. For the purposes of this work, only the routine electrochemical testing procedures for a rechargeable battery electrode material will be discussed, as the entire field or electrochemistry is vast and would be largely irrelevant to the aims of this work.

Once a cell has been fabricated (see *7 Energy Storage and Lithium Iron Phosphate*) they are allowed time for the electrolyte to fully wet the electrodes [43] before being tested; typically 24 hours at least. The main purpose of the initial tests is to ensure, primarily that the cell is functioning and is not short-circuiting, to quantify the open circuit potential of the cell, and finally to monitor the cell during its first few charge / discharge cycles [44].

The initial testing procedure for the $LiFePO_4$ cells used in these studies consisted of; potentiostatic electrical impedance spectroscopy (PEIS), open circuit potential (OCV) for a 10-hour dwell period, a second PEIS, four charge and discharge cycles followed by a 30 minutes OCV dwell before a final PEIS. The PEIS measurements produce Nyquist plots, which can give information regarding the internal resistances of the cell as a function of frequency, and from where they are arising [45], [46]. OCV simply leaves the cell at rest and the difference in electrical potential between the two terminals of the device is measured. For the charge / discharge cycles the current required to charge / discharge the device over a desired amount of time is first calculated, as a function of the active mass [44], [45]. During the cell fabrication process the weight and thickness of the electrodes is recorded in order to calculate the amount of active material, which is used to calculate the specific capacity. Data gathered from the charge / discharge cycling is most commonly presented as Voltage (V) / Specific capacity (mAh/g) and is used primarily to observe how the specific capacity changes over the first few cycles [40], [47].

In terms of analysing these electrochemical data the most useful points are quite simple to ascertain. From a Nyquist plot from PEIS we are able to determine the internal resistances of the device and whether they are from the

current collector, the active material to electrolyte interface, or the structure of the electrodes [45]. For our needs, we simply observe the value of the charge transfer resistance (R_{ct}) which relates to the electrode : electrolyte interface, and can be seen as the diameter of the semi-circle produced [48]. A smaller semi-circle reflects a smaller resistance value, which is more desired. We are also concerned with the angle of the linear region of the plot to the x-axis; we expect an angle of around 45° which is indicative of a diffusion limited system [44].

3.2.5 Catalytic performance testing

In order to nominate a candidate as a potential catalyst for a particular application, it must first be evaluated for its ability to catalyse the reactions necessary. The process of evaluating a catalyst is so in-depth and involved that entire companies exist for this purpose alone, where they may look at the preparation of catalysts, the activation, passivation, characterisation and may also consider the support matrix for the active material. To properly evaluate the performance of a catalyst is to simulate the active service environment of the reactions and to analyse the products as a function of time, temperature, pH, or any other relevant environmental factors [49].

To consider a gaseous reaction process, such as the heterogeneous catalysis of petrol vehicle emissions, NO_x is reduced, and CO and unburnt hydrocarbons are oxidised [50]–[52]. To evaluate these catalysts, they must be subjected to the relevant operating temperatures, with realistic gas flow rates of a representative composition for a typical combustion emission. The performance of the catalyst will be qualified as a function of the conversion or temperature. For these types of catalysts, the most commonly seen metric for performance is the light-off temperature [53], which is the temperature necessary to achieve 50% conversion, often presented as T_{50}. Should a static temperature be desired then the stationary conversion at a nominal temperature may be preferred, where the conversion is presented as a function of that temperature, X_{300} for example. One of the main differences with heterogeneous catalysts is that the intake gases can either be oxygen rich or oxygen lean [52], [54], [55]. This depends on which point

in the combustion cycle is being experienced, which can be simulated by adjusting the CO and O_2 contents of the stream at regular intervals, the frequency of which will relate to the RPM of the simulated engine. By analysing the output gases, the activity and selectivity of the catalyst candidate can be quantified and compared to reference samples. The exact equipment used for this characterisation cannot be divulged, however there are several manufacturers of commercial catalyst testing equipment. The general operating principle of the automotive catalyst testing is widely similar to other catalyst testing methods, where the intake is controlled, and the outputs are monitored as a function of the environment around the reaction site [51].
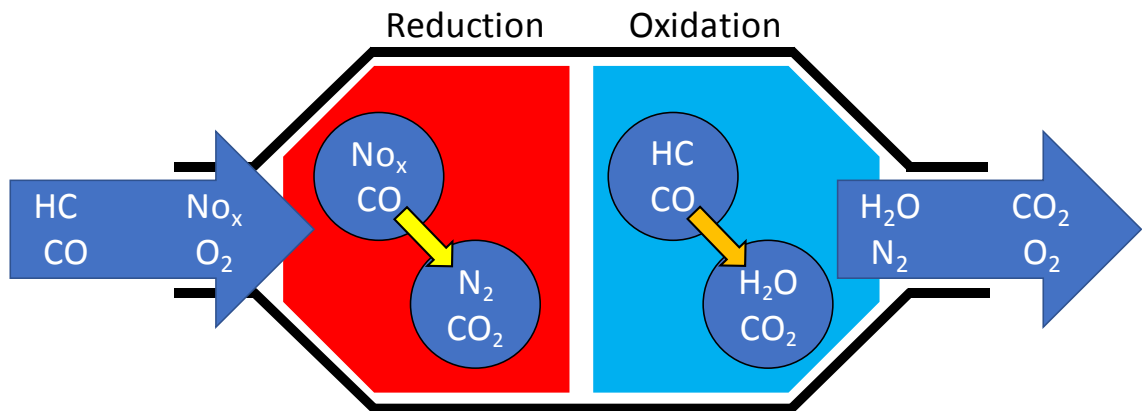
Figure 3.14. Schematic representation of a three-way automotive catalyst.

References

[1]   H. J. Tan, J. L. Dodd, and B. Fultz, "Thermodynamic and Kinetic Stability of the Solid Solution Phase in Nanocrystalline Li_xFePO_4," *J. Phys. Chem. C*, vol. 113, pp. 20527–20530, 2009.

[2]   A. M. Bolarín-Miró, F. Sánchez-De Jesús, C. A. Cortés-Escobedo, R. Valenzuela, and S. Ammar, "Structure and magnetic properties of $Gd_xY_{1-x}FeO_3$ obtained by mechanosynthesis," *J. Alloys Compd.*, vol. 586, no. SUPPL. 1, pp. 90–94, 2014.

[3]   S. Okada, T. Yamamoto, Y. Okazaki, J. I. Yamaki, M. Tokunaga, and T. Nishida, "Cathode properties of amorphous and crystalline $FePO_4$," *J. Power Sources*, vol. 146, no. 1–2, pp. 570–574, 2005.

[4]   G. W. Huber, S. Iborra, and A. Corma, "Synthesis of transportation fuels from biomass: Chemistry, catalysts, and engineering," *Chem. Rev.*, vol. 106, pp. 4044–4098, 2006.

[5]   F. Deganello, G. Marcì, and G. Deganello, "Citrate-nitrate auto-combustion synthesis of perovskite-type nanopowders: A systematic approach," *J. Eur. Ceram. Soc.*, vol. 29, no. 3, pp. 439–450, 2009.

[6]   M. Popa, J. Frantti, and M. Kakihana, "Lanthanum ferrite $LaFeO_{3+d}$ nanopowders obtained by the polymerizable complex method," *Solid State Ionics*, vol. 154–155, pp. 437–445, 2002.

[7]   X. Li, C. Tang, M. Ai, L. Dong, and Z. Xu, "Controllable Synthesis of Pure-Phase Rare-Earth Orthoferrites Hollow Spheres with a Porous Shell and Their Catalytic Performance for the CO + NO Reaction," *Chem. Mater.*, vol. 22, no. 17, pp. 4879–4889, Sep. 2010.

[8]   A. M. Huízar-Félix, T. Hernández, S. de la Parra, J. Ibarra, and B. Kharisov, "Sol-gel based Pechini method synthesis and characterization of $Sm_{1-x}Ca_xFeO_3$ perovskite $0.1 \leq x \leq 0.5$," *Powder Technol.*, vol. 229, pp. 290–293, 2012.

[9]   X. Qi, J. Zhou, Z. Yue, Z. Gui, and L. Li, "Auto-combustion synthesis of

nanocrystalline LaFeO$_3$," *Mater. Chem. Phys.*, vol. 78, pp. 25–29, 2003.

[10] W. Y. Teoh, R. Amal, and L. Mädler, "Flame spray pyrolysis: An enabling technology for nanoparticles design and fabrication," *Nanoscale*, vol. 2, no. 8, p. 1324, 2010.

[11] B. Hannoyer, A. A. M. Prince, M. Jean, R. S. Liu, and G. X. Wang, "Mössbauer study on LiFePO$_4$ cathode material for lithium ion batteries," *Hyperfine Interact.*, vol. 167, no. 1–3, pp. 767–772, 2006.

[12] R. Strobel and S. E. Pratsinis, "Flame aerosol synthesis of smart nanostructured materials," *J. Mater. Chem.*, vol. 17, no. 45, pp. 4743–4756, 2007.

[13] Z. Schnepp, S. C. Wimbush, M. Antonietti, and C. Giordano, "Synthesis of highly magnetic iron carbide nanoparticles via a biopolymer route," *Chem. Mater.*, vol. 22, no. 18, pp. 5340–5344, 2010.

[14] C. Yang, H. Zhao, Y. Hou, and D. Ma, "Fe$_5$C$_2$ nanoparticles: A facile bromide-induced synthesis and as an active phase for Fischer-Tropsch synthesis," *J. Am. Chem. Soc.*, vol. 134, no. 38, pp. 15814–15821, 2012.

[15] S. Nakayama, "LaFeO$_3$ perovskite-type oxide prepared by oxide-mixing , co-precipitation and complexsynthesis methods," *J. Mater. Sci.*, vol. 6, no. 36, pp. 5643–5648, 2001.

[16] V. Bedekar, O. D. Jayakumar, J. Manjanna, and a. K. Tyagi, "Synthesis and magnetic studies of nano-crystalline GdFeO$_3$," *Mater. Lett.*, vol. 62, pp. 3793–3795, 2008.

[17] K. S. Park, K. T. Kang, S. B. Lee, G. Y. Kim, Y. J. Park, and H. G. Kim, "Synthesis of LiFePO$_4$ with fine particle by co-precipitation method," *Mater. Res. Bull.*, vol. 39, no. 12, pp. 1803–1810, 2004.

[18] H. Bennett, *XRF analysis of ceramics, minerals, and allied materials* . Chichester: Wiley, 1992.

[19] R. Jenkins, *X-ray fluorescence spectrometry* . Wiley, 1988.

[20] M. Ermrich and D. Opper, *X-ray Powder Diffraction XRD for the analyst.*

2013.

[21]   P. Brouwer, *Theory of XRF*. 2010.

[22]   R. Jenkins, *An Introduction to X-ray Spectrometry*. Wiley & Sons, 1983.

[23]   O. H. Seeck, *X-ray diffraction : modern experimental techniques* . Boca
       Raton, Florida: Pan Stanford Publishing, 2014.

[24]   B. D. Cullity, *Elements of X-ray diffraction* , 3rd ed. Upper Saddle River,
       NJ: Prentice Hall, 2001.

[25]   J. Emsley, *The Elements*. Clarendon Press, 1998.

[26]   C. Suryanarayana and M. G. Norton, *X-Ray Diffraction: A Practical
       Approach*. Springer US, 2013.

[27]   B. D. Cullity, *Elements of X Ray Diffraction - Scholar's Choice Edition*.
       Scholar's Choice, 2015.

[28]   Malvern Panalytical, "PIXcel3D," 2018. [Online]. Available:
       https://www.malvernpanalytical.com/en/products/category/x-ray-
       components/detectors/pixcel3d. [Accessed: 08-Nov-2018].

[29]   E. Zolotoyabko, *Basic concepts of X-ray diffraction* . Weinheim: Wiley-
       VCH, 2014.

[30]   Y. Waseda, E. Matsubara, and K. Shinoda, *X-Ray Diffraction
       Crystallography: Introduction, Examples and Solved Problems*. Springer
       Berlin Heidelberg, 2011.

[31]   J. G. Grasselli, *Chemical applications of Raman spectroscopy* . Wiley,
       1981.

[32]   D. J. Gardiner, *Practical Raman Spectroscopy* . Springer, 1989.

[33]   P. Larkin, *Infrared and Raman Spectroscopy : principles and spectral
       interpretation*, Second edi. Amsterdam: Elsevier, 2018.

[34]   N. B. Colthup, *Introduction to infrared and Raman Spectroscopy* , 2nd ed.
       Academic P., 1975.

[35]   Royal Society of Chemistry, *Industrial analysis with vibrational*

spectroscopy. Royal Institute of Chemistry, 1997.

[36] O. N. Shebanova and P. Lazor, "Raman spectroscopic study of magnetite ($FeFe_2O_4$): A new assignment for the vibrational spectrum," *J. Solid State Chem.*, vol. 174, no. 2, pp. 424–430, 2003.

[37] N. Colthup, *Introduction to Infrared and Raman Spectroscopy*. Elsevier Science, 2012.

[38] Y. Hemberger, N. Wichtner, C. Berthold, and K. G. Nickel, "Quantification of yttria in stabilized zirconia by Raman spectroscopy," *Int. J. Appl. Ceram. Technol.*, vol. 13, no. 1, pp. 116–124, 2016.

[39] P. Vanýsek, "Electrochemical series," in *Handbook of Chemistry and Physics*, 2010, p. 8.20-8.29.

[40] P. H. Rieger, *Electrochemistry* , 2nd ed. Chapman and Hall, 1994.

[41] Y. P. Wu, E. Rahm, and R. Holze, "Carbon anode materials for lithium ion batteries," *J. Power Sources*, vol. 114, no. 2, pp. 228–236, 2003.

[42] N. Nitta, F. Wu, J. T. Lee, and G. Yushin, "Li-ion battery materials: Present and future," *Mater. Today*, vol. 18, no. 5, pp. 252–264, 2015.

[43] M. Z. Bazant, "Theory of Chemical Kinetics and Charge Transfer based on Nonequilibrium Thermodynamics," 2012.

[44] P.-L. Taberna and P. Simon, "Electrochemical Techniques," in *Supercapacitors: Materials, Systems and Applications*, Wiley-VCH Verlag GmbH & Co. KGaA, 2013, pp. 111–130.

[45] V. F. Lvovich, *Impedance spectroscopy applications to electrochemical and dielectric phenomena* . Hoboken, N.J.: Wiley, 2012.

[46] B. A. Mei, O. Munteshari, J. Lau, B. Dunn, and L. Pilon, "Physical Interpretations of Nyquist Plots for EDLC Electrodes and Devices," *J. Phys. Chem. C*, vol. 122, no. 1, pp. 194–206, 2018.

[47] D. Hibbert, *Dictionary of electrochemistry* , 2nd ed. Macmillan, 1984.

[48] X. Li, Z. Shao, K. Liu, Q. Zhao, G. Liu, and B. Xu, "Effect of F-doping on the properties of $LiFePO_{4-x}/3F_x/C$ cathode materials via wet mechanical

agitation-assisted high-temperature ball milling method," *J. Solid State Electrochem.*, pp. 1–7, 2018.

[49]   J. R. H. Ross, *Heterogeneous catalysis*. Amsterdam ; Elsevier, 2012.

[50]   G. C. Bond, *Heterogeneous catalysis : principles and applications* , 2nd ed. Oxford UP, 1987.

[51]   Society of Automotive Engineers, *Emissions and emissions control.* Society of Automotive Engineers, 1996.

[52]   J. D. Halderman, *Automotive fuel and emissions control systems* . Upper Saddle River, N.J.: Prentice Hall, 2006.

[53]   N. Kruse, A. Frennet, and J. M. Bastin, *Catalysis and Automotive Pollution Control IV*. Elsevier Science, 1998.

[54]   J. Kašpar, P. Fornasiero, and N. Hickey, "Automotive catalytic converters: Current status and some perspectives," *Catal. Today*, vol. 77, no. 4, pp. 419–449, 2003.

[55]   Y. Chen, V. Sima, W. Lin, J. Sterniak, and S. V. Bohac, "Lean HCCI/Rich SACI Gasoline Combustion Cycling and Three-Way Catalyst for Fuel Efficiency and NO_x Reduction," *Jounal Eng. Gas Turbines Power*, vol. 137, no. 12, p. V001T04A005, 2015.

4 Rare-Earth Orthoferrite Perovskites

First discovered in the Ural Mountains in 1839 by Gustav Rose, and named after Russian mineralogist Lev Aleksevich Perovski, *perovskite* is the mineral name of calcium titanate, $CaTiO_3$ [1]. The name *perovskite* has since been used to describe compounds with the structure of $CaTiO_3$, such as $SrTiO_3$ as illustrated in Figure 4.1. This structural classification includes materials with an overall ABX_3 composition, where in A and B are cations of which B is smaller than A in terms of ionic radius, and X is an anion that is smaller still, most commonly oxygen. In these materials, B cations are co-ordinated to 6 oxygen in BX_6 octahedra, with the A cations situated in the interstices, co-ordinated to the 12 nearest oxygen. In a cubic perovskite, such as $SrTiO_3$, bonds between titanium and oxygen atoms are always at either 90° or 180°, resulting in octahedra that are all in-line with one another, and strontium atoms in equidistant parallel lines. Where the bonds between titanium and oxygen atoms are not linear (Ti-O-Ti ≠ 180°) the octahedra will be tilted in relation to each other, causing distortion to the overall structure of the material. The tilting of octahedra in perovskites has been investigated thoroughly; Patrick Woodward presented 23 possible tilt systems in 1997, denoting relative octahedral tilts in terms of *a*, *b* and *c*, with superscript signage to denote in- or out-of-phase tilts [2]. This type of structural distortion is typically realised when the A-site cation is too small for the corner-sharing, BX_6 octahedral network to remain in cubic symmetry, and when this distortion results in a lower energy state for the crystal [3]. The ability of the perovskite structure, and its distorted derivatives, to host a wide variety of elements leads to their utilisation in many applications, including catalysis, energy storage device components, solar energy devices, multiferroics, chemical sensors and more [4]–[11].
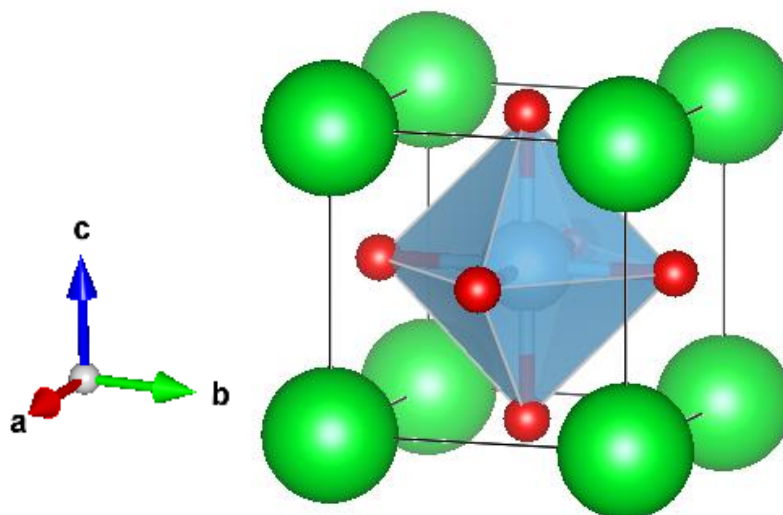
Figure 4.1. Polyhedral representation of $SrTiO_3$ cubic perovskite unit cell rendered in VESTA © from Meyer, Nelmes & Hutton, 1978 [12], [13].

As a structural classification of materials, perovskites encompass materials with an overall stoichiometry of ABX_3, although A, B and X may be composed of more than one element. As illustrated in Figure 4.1 the crystal structure of $SrTiO_3$ consists of corner-sharing TiO_6 octahedra, with Sr atoms 12 co-ordinated with the nearest oxygen of these octahedra. In $SrTiO_3$, strontium is present with a charge of 2, titanium a charge of 4, and a total of negative 6 from the three oxygen atoms. The charge balance provided by the A and B sites is one deciding factor in the formation of perovskite phases; where X = oxygen, A + B = 6 can be achieved by ($\square$ + 6), (1 + 5), (2 + 4) or (3 + 3) as in the examples of ReO_3 [14], $NaNbO_3$ [15], [16], $SrTiO_3$ [15] and $LaFeO_3$ [17] ($\square$ denoting a vacant A-site). Experimentally speaking this becomes important when selecting precursor materials, as the element being sought must be presented in the same charge state as is required for the desired perovskite, in the absence of non-ambient conditions. That is to say that if Mn^{3+} is required for a B site, then Mn_2O_3 would be appropriate and MnO inappropriate, unless oxidised in the process. The relative ionic radius of each element, in its desired co-ordination, is also important when predicting if a proposed composition can form a perovskite structure. A-site cations are co-ordinated with 12 neighbouring X anions, and B with 6. In his 1926 article in Natural Sciences [18], Victor Goldschmidt presented the *Goldschmidt Tolerance Factor* which can be used to predict the crystal structure of a material based on the relative ionic radii sizes;

$$t = \frac{r_A + r_X}{\sqrt{2}(r_B + r_X)} \tag{1}$$

A tolerance factor of greater than 1 would predict hexagonal or tetragonal perovskite structures, such as $BaNiO_3$, with relatively over-sized A cation size [19]. 0.9 to 1 predicts a perovskite structure with cubic symmetry, such as $SrTiO_3$ as depicted in Figure 4.1, where A and B are ideally sized relative to each other. The original perovskite, $CaTiO_3$ and rare earth orthoferrites, such as La or $GdFeO_3$ have tolerance factors between 0.7 and 0.9, which encompasses the range of orthorhombic or rhombohedral structures, where A is too small by comparison to B. Below 0.7, the Goldschmidt tolerance factor would predict more close-packed structures such as ilmenite ($FeTiO_3$) and Bixbyite (Mn_2O_3) [20].

The range of possible A, B and X site combinations is so wide-reaching that perovskites have found potential, or proven application in an equally wide range of fields. Perovskite solar cells have been a leading field of interest driving the synthesis of new compositions and structures. Organolead halide perovskites ($RPbX_3$ R = monovalent organic cation; X halide anion) with varied site occupancies and support matrices have increased in power conversion efficiency from 3.8% in 2009 with $CH_3NH_3PbI_3$ on TiO_2 [21] to 22.1% in 2017 using formamidinium ($[R_2N\text{-}CH\text{=}NR_2]^+$) containing, multi-cation, mixed halide thin films on nano-crystalline TiO_2 [22]. In these types of perovskites, the organic molecules occupy the A sites, Pb on the B sites and I on the X sites. Additional applications of perovskite materials include the dielectric $BaTiO_3$ that can be used in capacitors and sensing applications [23], piezoelectric $PbTiO_3$ has been used in acoustic transducers [24] and $(BaK)BiO_3$ exhibits superconducting properties [25]. A specific group of this broad category of materials, lanthanide metal oxide perovskites ($LnMeO_3$) have attracted considerable attention for a number of potential applications. $(La, Sm)FeO_3$ films have proven to have chemical sensing properties [6], [26], $La(Mn, Cr)O_3$ have found use as components in solid-oxide fuel cells [5], [27], many have multiferroic properties $(Nd, Sm, Gd, Tb)FeO_3$ [11], [28]–[30], $(La, Sm, Eu, Gd)FeO_3$ can be used as photocatalysts [9], [31] and more importantly for upcoming sections of this chapter, $LaFeO_3$ can be used as a heterogenous catalyst in petrol cars [7], [32], [33].

4.1 LnFeO$_3$ orthoferrite perovskites where Ln = La, Sm, Nd, Eu, Gd

4.1.1 Introduction

Rare earth orthoferrite perovskites have found viability for a range of industrial applications and are found to exhibit scientifically interesting properties. In this work five such materials are focused upon; La, Sm, Nd, Eu and GdFeO$_3$, all synthesised through bulk, solid state ball milling and sintering. All of these materials exhibit orthorhombic symmetry, with Goldschmidt tolerance factors between 0.9 (Gd) and 0.96 (La) [19], [34]. Structurally similar, with corner-sharing FeO$_6$ octahedra forming one 'pore' in a cube of 8 such octahedra, in which the rare earth cation is situated. The ionic radii of the rare earths decrease from La to Gd, causing the reduction in tolerance factor as the cations become smaller, and smaller than ideal, as previously discussed in the primary introduction to this chapter.

LaFeO$_3$ is discussed in greater depth during the 4.2 section of this chapter for its catalytic properties, and other applications were mentioned, including its superparamagnetism, and multiferroicity. LnMeO$_3$, lanthanide metal oxide perovskites, have attracted considerable attention for a wide variety of potential applications. To highlight a few examples, (La, Sm, Eu, Gd)FeO$_3$ exhibit photocatalytic properties [9], [31]; LaFeO$_3$ can be a heterogeneous catalyst [7], [8], [32]; (La, Sm)FeO$_3$ thick films have chemical sensing properties [26], [35]; and La(Mn,Cr)O$_3$ has been used for cathodes and interconnects in solid-oxide fuel cells [5]. Fundamental studies of these materials utilising synchrotron techniques have been recently conducted, for example neutron diffraction of TbFeO$_3$ to understand its' multiferroic nature [28]; and of NdFeO$_3$ to understand temperature induced spin reorientation and structural changes [36]. In recent years there have been a number of lengthy review articles of perovskite oxides in the interests of ferroelectricity [16], piezoelectricity [37], environmental catalysts [38] and for solar cell applications [39], [40]. Advantages of perovskite ceramics over conventional materials are often cited as their lower price, facile synthesis routes and ability to be compositionally tailored to suit the application.

In this body of work these five rare earth orthoferrites are studied for their crystallographic, vibrational and hyperfine structures through X-ray diffraction, Raman spectroscopy and [57]Fe Mössbauer spectroscopy. Synthesised through the solid-state sintering process, the materials studied are representative of bulk materials, a distinction of import in the later section of this chapter, 4.2, where particle size becomes more relevant. This section does not consider the applications of these materials, and focuses on characterising them principally through low temperature [57]Fe Mössbauer spectroscopy to approximate their Debye temperatures and recoil-free fractions, information which is useful for quantifying the abundance of these materials in mixed-phase systems. There have been studies conducted prior to this work to understand the hyperfine structure of these materials, as summarised in Table 4.1, and the novelty of this work comes from the range of materials studied, and the Debye temperature calculations. This work also provides insightful baselines for comparison used in the 4.2 section that follows, where $LaFeO_3$ is studied in detail as a three-way catalyst material for petrol vehicle emission control.

Material	CS (mm s^{-1})	ε (mm s^{-1})	B$_{eff}$ (T)	Reference
$LaFeO_3$	0.36	-0.09	52.7	[7]
	0.36	-0.09	52.7	[41]
$SmFeO_3$	0.36	-0.10	50.8	[42]
	0.36	-0.05	50.1	[43]
$NdFeO_3$	0.36	-0.01	51.1	[43]
	0.39	-0.01	50.1	[44]
$EuFeO_3$	0.38	-0.02	50.4	[45]
	0.37	0.01	50.5	[46]
$GdFeO_3$	0.37	0.02	50.7	[47]

Table 4.1. Summary of hyperfine parameters of $LnFeO_3$ from literature. CS relative to α-Fe.

4.1.2 Material Characterisation

Conventional solid-state ceramic synthesis of $LnFeO_3$ (Ln = La, Nd, Sm, Eu, Gd) materials was carried out, using Fe_2O_3 (98%, Alfa Aesar) and either La_2O_3 (>99.9%, Arcos Organics), Nd_2O_3 (>99.9%, Arcos Organics), Sm_2O_3 (>99.9%, Alfa Aesar) Eu_2O_3 (>99.9% Alfa Aesar), or Gd_2O_3 (99.99%, Strem Chemicals). Other synthesis routes have been reported for $LnFeO_3$ perovskite oxides, including flame spray pyrolysis, microwave crystallisation and auto combustion [32], [47], [48], and the physical properties of the perovskites are known to be dependent on the synthesis method [38], [49]. Solid-state sintering was utilised for this work to produce dense monoliths and to avoid particle-size induced variables. To prepare 100 g of $LnFeO_3$, dried (>48 h, 120 °C), Ln_2O_3 and Fe_2O_3 precursors were weighed in the required 1:1 molar ratios. These powders were placed in a 250 ml polyethylene bottle with ≈ 500 g of 10 mm spheres of yttrium-stabilised zirconia (YSZ) milling media and ≈ 100 ml of propan-1-ol, and then were milled using a roller ball mill for 24 hours. The resultant slurries were air dried and subsequently calcined in an electric furnace in air at 800 °C for 24 hours before being sieved through a 75 µm mesh. The process, from milling, was repeated for a second time, after which 10 mm diameter green compacts were made by uniaxial pressing under applied pressure of ≈ 3 tonnes for 90 seconds. Green compact pellets were then fired in an electric furnace in air using a controlled heating rate of 5 °C /min, followed by holding for 4 hours at a temperature of 1200 °C, following which the pellets were cooled inside the furnace. After sintering, the pellets were powdered using a manual pestle and mortar and sieved to a particle size < 75 µm.

Elemental analysis was performed using a PANalytical MagiX Pro X-ray Fluorescence (XRF) spectrometer equipped with a Rh anode. Powdered samples were mixed with cellulose binder and pressed into pellets using a 20 tonne force in a Retsch PP40 hydraulic press. For this XRF spectrometer, Na is usually the lightest element detectable, and any unexpected Rh lines observable are attributed to the anode x-ray source. Accuracies of the resultant data in this study are estimated to be ± 0.2 % of the values provided by the analysis.

Phase identification was performed using room temperature powder X-ray diffraction on powdered pellets using an Empyrean PANalytical diffractometer in Bragg-Brentano geometry. Samples were mounted on a reflection / transmission spinner stage rotating at 15 rpm, irradiated with Cu K$_\alpha$ radiation (λ = 1.5406 Å) over a °2θ range of 20 to 80 degrees, with step size 0.013 °2θ and step time 68.59 seconds, 10 mm incident mask, 1° anti-scatter and divergence slits, and a nickel beta filter. X-rays were detected using a PIXCEL-3D area detector. Phases were identified by fingerprinting against the ICDD database using the PANalytical software, X'Pert HighScore Plus. Crystal structures of the $LnFeO_3$ perovskites were refined by the Rietveld method [50] using FULLPROF software [51].

Raman spectroscopy measurements were carried out using a Thermo Scientific DXR2 spectrometer with a depolarised 10 mW 532 nm laser, on powdered samples of the synthesised materials, between 200 and 2000 cm^{-1}. Calibrations with the proprietary Thermo alignment tool were carried out before, during and after each sample measurement.

For transmission [57]Fe Mössbauer spectroscopy measurements, acrylic absorber discs with a sample area of 1.767 cm^2 were loaded to present 2.16 x 10^{-3} g/cm^2 of Fe to achieve a Mössbauer thickness of 1 [52]. Sample weights of 0.013 g were homogeneously mixed with graphite to achieve this level of loading. The 14.4 keV γ-rays were supplied by the cascade decay of 25 mCi [57]Co in Rh matrix source, oscillated at constant acceleration by a SeeCo W304 drive unit, and detected using a SeeCo 45431 Kr proportional counter operating with 1.745 kV bias voltage applied to the cathode. All measurements were carried out over a velocity range of +/- 12 mm s^{-1} due to the presence of high-field magnetic splitting, and were calibrated relative to α-Fe foil. Spectral data were fitted using the Recoil software package [53], using Lorentzian line shapes. Sub-ambient temperatures were maintained using a Janis 10 K CCR cytostatic spectrometer (Model CCS-800/204N) and Lakeshore 335 temperature controller.
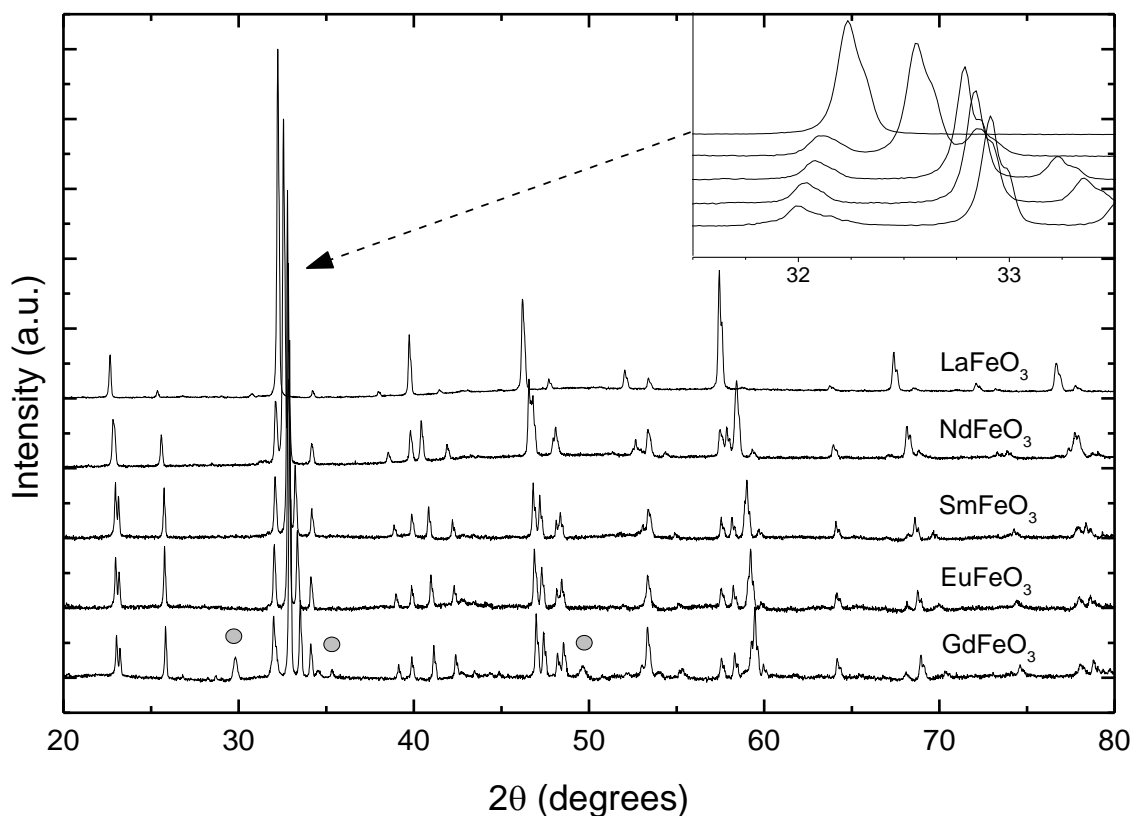
Figure 4.2. X-ray diffraction patterns of LnFeO$_3$ perovskites; Cu K$_\alpha$ radiation. Circles indicate second phase in GdFeO$_3$ only. PDF numbers – LaFeO$_3$ 00-037-1493; NdFeO$_3$ 01-088-0477; SmFeO$_3$ 01-070-7772; EuFeO$_3$ 01-074-1475; GdFeO$_3$ 01-072-9906.

Table 4.2. Lattice parameters of LnFeO$_3$ perovskites refined by Reitveld refinement from referenced starting structures.

LnFeO$_3$	LaFeO$_3$	NdFeO$_3$	SmFeO$_3$	EuFeO$_3$	GdFeO$_3$
a (Å)	5.55531(16)	5.45509(8)	5.40201(8)	5.37715(8)	5.35188(9)
b (Å)	5.5602(2)	5.57756(9)	5.59063(8)	5.59319(9)	5.59788(10)
c (Å)	7.85114(19)	7.76423(12)	7.71054(12)	7.68806(12)	7.67091(14)
Vol. (Å^3)	242.511(13)	236.235(6)	232.863(6)	231.222(6)	229.814(7)
R$_p$	27.9	25.8	31.7	33.0	43.3
R$_{wp}$	17.5	16.8	18.8	17.6	23.2
R$_{exp}$	6.77	7.55	10.36	11.18	11.37
χ^2	8.281	5,724	3.856	2.853	4.205
Reference	[54]	[36]	[55]	[56]	[57]
Bond Lengths (Å)					
Fe-O1	1.997(12)	1.985(3)	2.020(5)	2.000(3)	1.979(4)
Fe-O2	1.99(5)	1.968(15)	2.002(16)	1.964(11)	1.969(16)
Fe-O2	1.99(5)	2.016(13)	2.009(16)	2.058(11)	2.064(16)
FeO$_6$ Volume	10.53 Å^3	10.50 Å^3	10.82 Å^3	10.77 Å^3	10.72 Å^3
Bond Angles (°)					
Fe-O1-Fe	158.7	155.94	145.28	147.96	151.37
Fe-O2-Fe	162.3	156.5	151.4	149.3	147.5
O – Fe – O	180	180	179.9	180	180
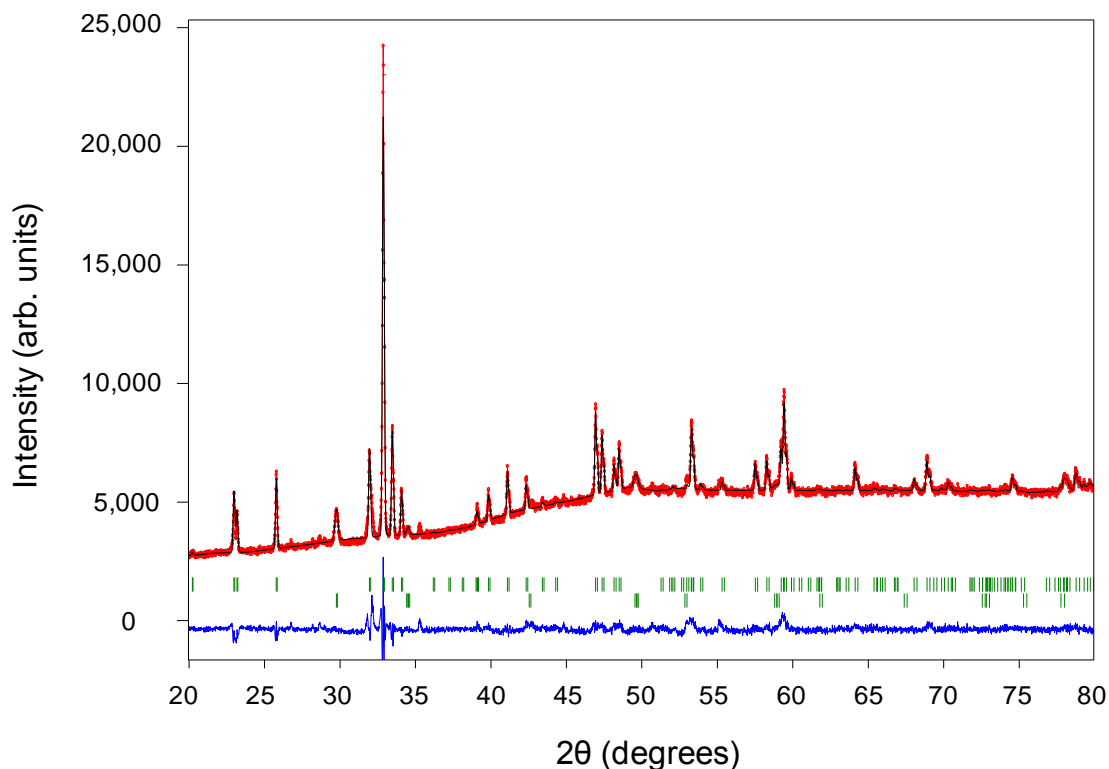
Figure 4.3. X-ray diffractogram of $GdFeO_3$ with Rietveld refinement using $GdFeO_3$ and $ZrO_{1.97}$ starting structures. Red line indicates observed data, black line indicates calculated data, blue line shows difference between observed and calculated data. Green lines indicate the positions for $GdFeO_3$ (upper) and $ZrO_{1.97}$ (lower).
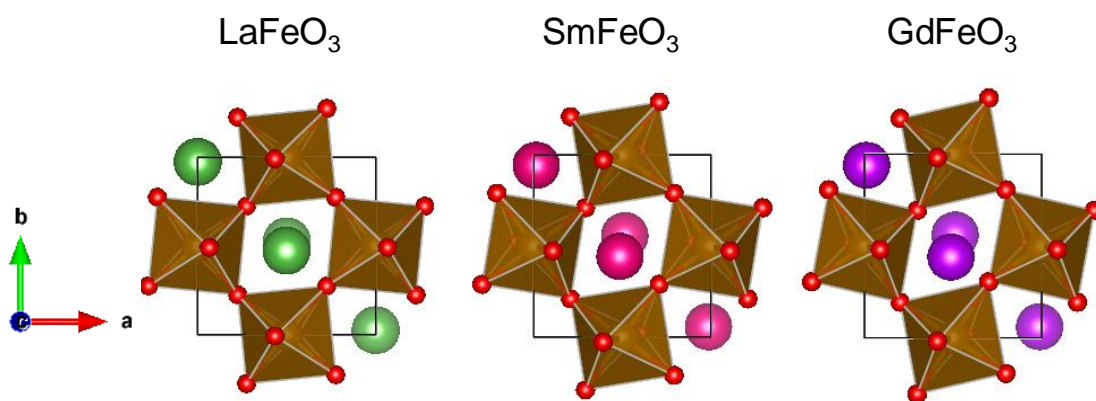
Figure 4.4. Polyhedral schema of $(La, Sm, Gd)FeO_3$ orthorhombic perovskites along axis c, rendered in VESTA © [13]. Lattice parameters are shown in Table 4.2.

XRD analysis confirmed the presence of single-phase $LnFeO_3$ for all rare-earth orthoferrites, except for $GdFeO_3$, as shown in Figure 4.2, using the HighScore Pro software. Low levels of mechanical contamination from the milling media were identified by XRD and XRF, however, as this is a mechanical mixture of two materials it would have no appreciable effect on the measured Mössbauer spectrum for this sample since the second phase is iron-free. As the ionic radius of the rare earth cation decreases from 1.36 Å for 12 co-ordinated La^{3+} to 1.22 Å for 12 co-ordinated Gd^{3+} [58], a decrease in unit cell volume is observed by XRD as summarised in Table 4.2, resulting in a line shift to higher diffraction angles. For all but the $GdFeO_3$ sample, single-phase Rietveld refinements were carried out using isostructural *Pbnm* crystal structures. For $GdFeO_3$ a 2-phase refinement was carried out with $GdFeO_3$ as the main phase [57] and $ZrO_{1.97}$ from the milling media included as a minor phase (7.6(3))% by refinement [59]). Table 4.2 shows the refined lattice parameters for the $LnFeO_3$ phases, together with the R-factors from the FULLPROF refinements. Figure 4.3 shows the Rietveld plot of the $GdFeO_3$ sample material, indicating the presence of this second phase and the assignment of diffraction peaks. The phase identification of tetragonal $ZrO_{1.97}$, which is not a stable polymorph of zirconia at room temperature [59], suggests that this structure is being stabilised by a secondary component, most likely Y_2O_3, due to the use of yttrium stabilised zirconia milling media.

From the structures of the $LnFeO_3$ series determined by Rietveld refinement, the largest cell volume is present for $LaFeO_3$, with a consistent decrease in cell volume as the ionic radius of the rare earth decreases from Ln = La to Gd. As the cell volume reduces by ≈ 5.2% from $LaFeO_3$ to $GdFeO_3$, FeO_6 octahedra volume does not vary linearly. We observe that the bonds in the direction of c, or in the [010] plane, connecting FeO_6 octahedra do tend away from 180° from La to Sm, however Eu and $GdFeO_3$ exhibit and bonds closer to 180°, while the O – Fe – O bonds remain essentially 180° inside of the octahedra. An inverse relation can be observed between the FeO_6 volume and the bond angles of Fe – O_1 – Fe, while the Fe – O_2 – Fe bond angles reduce almost linearly from 180° as the rare earth cation radius decreases. Figure 4.4 shows the polyhedral schematic of $LaFeO_3$, $SmFeO_3$ and $GdFeO_3$ along the c axis, where the octahedra tilting can clearly be observed.
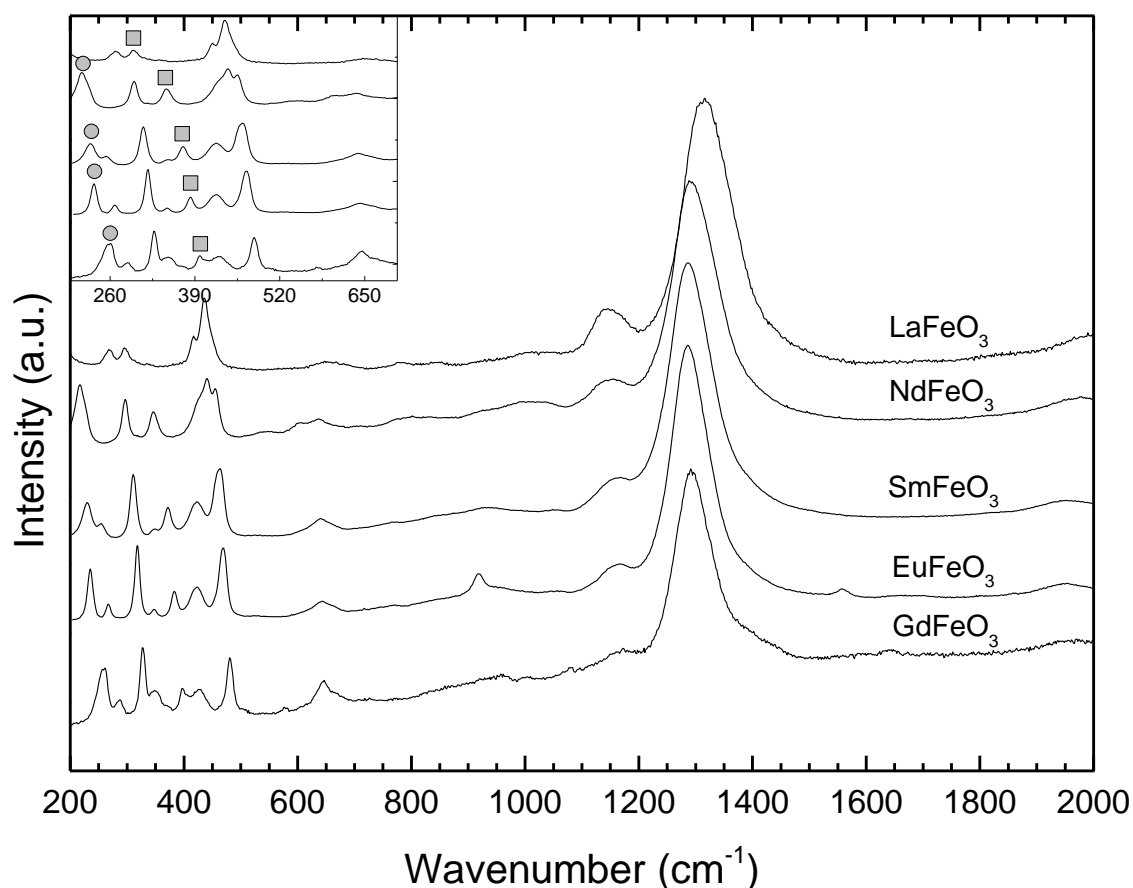
Figure 4.5. Raman spectra of LnFeO$_3$ series (LaFeO$_3$ to GdFeO$_3$, top to bottom) from 200 to 2000 cm^{-1}, with inset of 200 to 700 cm^{-1}; circles indicate A$_g$(3) mode and squares indicate A$_g$(5).

Table 4.3. Raman vibrational peak centres (in cm^{-1}) for LnFeO$_3$ perovskites (Ln = La, Nd, Sm, Eu, Gd) measured using a 532 nm laser.

LaFeO$_3$			NdFeO$_3$		SmFeO$_3$		EuFeO$_3$		GdFeO$_3$	
Present Study	[60]	[47]	Present Study	[61]	Present Study	[42]	Present Study	[62]	Present Study	[47]
105	-	101	106	103	229	225	-	140	111	103
140	-	151	140	142	254	260	235	218	158	152
160	154	-	151	153	311	310	267	291	260	246
181	176	173	216	-	349	-	318	-	287	275
268	-	264	297	297	372	375	347	362	328	316
295	284	288	346	349	423	420	383	-	350	-
436	432	431	441	441	464	460	423	445	396	386
651	653	650	455	458	637	630	470	-	430	412
1145	1154	1143	602	-	1166	-	643	-	480	469
1315	1315	1310	637	-	1287	-	917	-	581	-
			1155	-			1166	-	647	623
			1288	-			1287	-	962	-
			1975	-			1556	-	1084	-
									1173	-
									1291	1280

Raman spectra for all $LnFeO_3$ perovskites present bands consistent with those expected from literature as shown in Table 4.3. They also show agreement with the detailed Raman scattering study by Weber and colleagues [63]. There are 24 Raman-active modes in the space group *Pbnm* for rare-earth orthoferrites, which can be described by the representation $\gamma_{Raman,Pbnm}$: $7A_g+5B_{1g}+7B_{2g}+5B_{3g}$ [64]. Peaks at Raman shifts greater than ca. 700 cm^{-1} are reportedly not due to active modes, but rather to other phenomena; those at 1150 – 1200 and 1300 cm^{-1} are attributable to second order excitations of active modes [47], [65], one-phonon scattering or two-phonon scattering [60], [66]. Peaks observed around 650 cm^{-1} are believed to be caused by impurity scattering [66], [67] or second-order Raman scattering [68]. Concerning the second phase in $GdFeO_3$, the main Raman peaks for yttria-stabilised zirconia (YSZ) appear around 266 ($Zr-O_{II}$ bending) and 645 cm^{-1} ($Zr-O_I$ stretching) [69], both of which can also be attributed to $GdFeO_3$ itself. We observe a greater intensity of the 647 cm^{-1} Raman peak, which may be caused by the low level of YSZ contamination in this sample.

From the crystal structures of these perovskites, and the refined lattice parameters in Table 4.2, a change is observed in the angles of bonds through which the FeO_6 octahedra connect by corner-sharing oxygen atoms, indicating that their relative tilts vary. Vibrational modes $A_g(3)$ and $A_g(5)$ are associated with the [010] and [101] rotations respectively, i.e. in the direction of *c* and of *a* and *b*. Weber and colleagues, in 2016 [63], presented the Raman band positions for these vibrational modes, as illustrated in Table 4.4. Weber comment on the linear trends between the band positions of these vibration modes, and the angle octahedra rotational angle.

Table 4.4. Raman band positions for $A_g(3)$ and $A_g(5)$ from this work, and read from graphs presented by Weber et al. [63]

	This work (cm $^{-1}$)		Weber et al. (cm $^{-1}$) [63]	
	$A_g(3)$ [010]	$A_g(5)$ [101]	$A_g(3)$ [010]	$A_g(5)$ [101]
LaFeO₃	140 (5)	295 (5)	130 (10)	300 (10)
NdFeO₃	216 (5)	346 (5)	210 (10)	340 (10)
SmFeO₃	229 (5)	372 (5)	230 (10)	380 (10)
EuFeO₃	235 (5)	383 (5)	230 (10)	390 (10)
GdFeO₃	260 (5)	396 (5)	250 (10)	400 (10)

## 4.1.3 Mössbauer Spectroscopic Study of LnFeO₃ orthoferrites
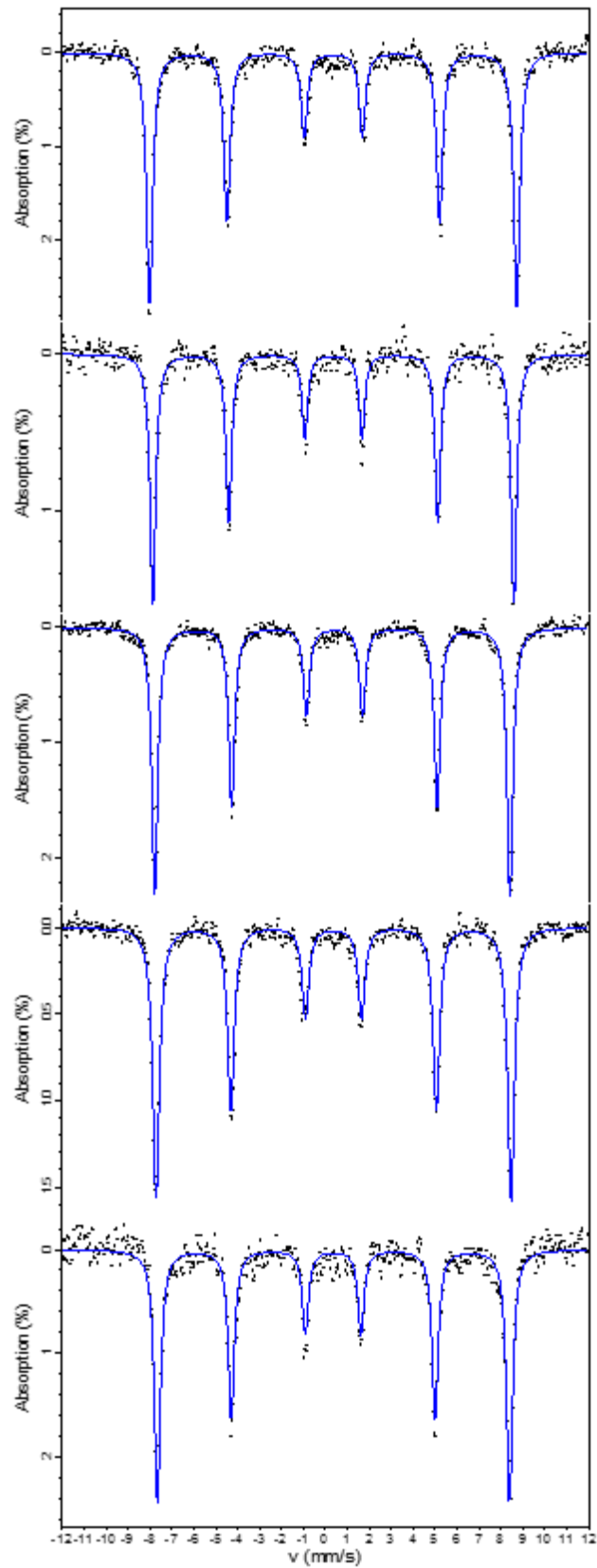
Figure 4.6. Mössbauer spectra of LnFeO₃ perovskites **at 293 K**, relative to α-Fe. Top to bottom; La, Nd, Sm, Eu, GdFeO₃.
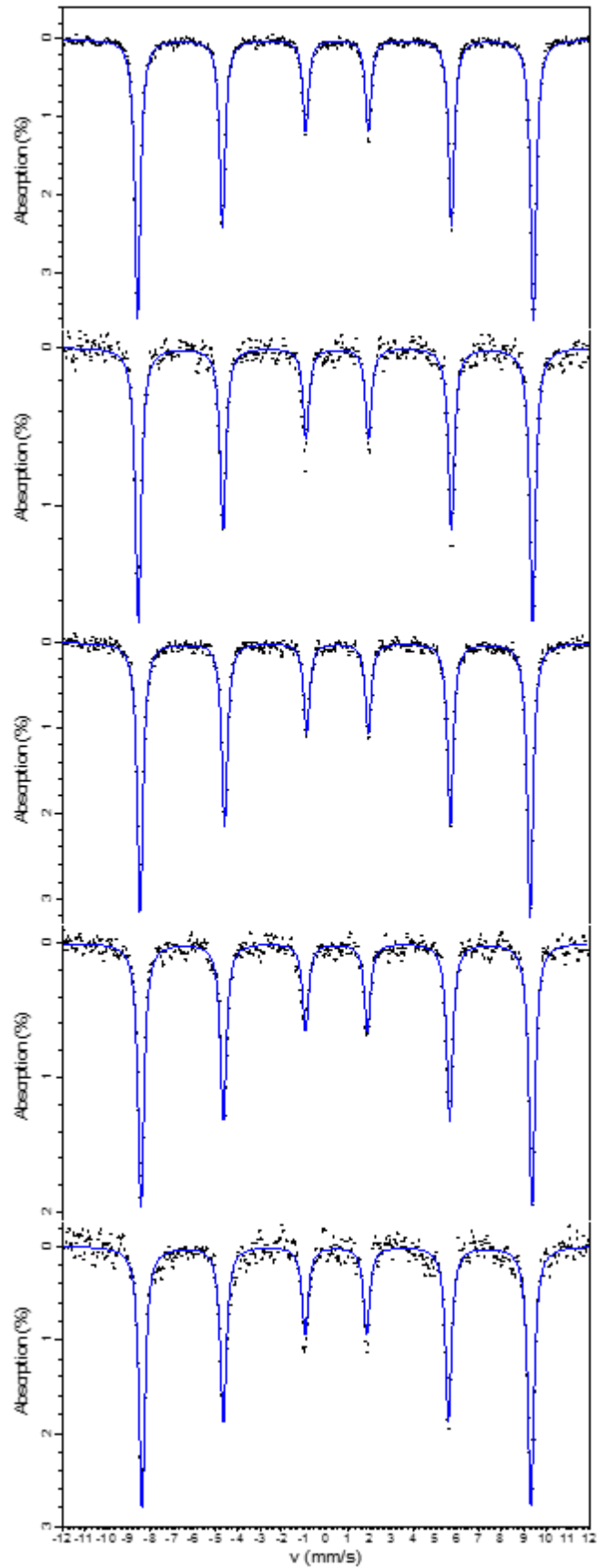
Figure 4.7. Mössbauer spectra of LnFeO$_3$ perovskites **at 10 K**, relative to α-Fe. Top to bottom; La, Nd, Sm, Eu, GdFeO$_3$.

Table 4.5. Hyperfine parameter of single Lorentzian sextets fit for $LnFeO_3$ perovskites. CS given relative to thin α-Fe foil.

Ferrite	Temperature (K)	CS (mm s^{-1})	B_{eff} (T)	$\Gamma/2$ (mm s^{-1})	Reduced X^2
Uncertainty	[± 1 K]	[± 0.02 mm s^{-1}]	[± 0.5 T]	[± 0.02 mm s^{-1}]	
LaFeO$_3$	293	0.37	51.9	0.16	1.35
	250	0.39	53.1	0.16	1.38
	200	0.42	54.3	0.21	0.78
	150	0.45	55.1	0.16	1.42
	100	0.46	55.6	0.16	1.35
	80	0.47	55.7	0.15	1.57
	50	0.47	55.8	0.14	1.41
	10	0.48	55.8	0.15	1.43
NdFeO$_3$	293	0.37	51.0	0.15	0.74
	250	0.39	52.5	0.16	0.69
	200	0.42	53.8	0.17	0.87
	150	0.45	54.8	0.16	0.86
	100	0.47	55.3	0.15	0.79
	10	0.48	55.6	0.16	0.82
SmFeO$_3$	293	0.37	50.2	0.16	0.78
	250	0.39	51.7	0.17	0.69
	200	0.43	53.4	0.17	0.47
	150	0.45	54.5	0.15	0.63
	100	0.47	55.1	0.15	0.51
	50	0.48	55.4	0.14	0.65
	10	0.48	55.0	0.16	0.63
EuFeO$_3$	293	0.38	50.2	0.18	1.41
	250	0.40	51.8	0.17	0.97
	200	0.43	53.2	0.18	0.95
	150	0.46	54.3	0.17	0.89
	100	0.48	54.9	0.17	1.16
	50	0.49	55.1	0.16	1.66
	10	0.49	55.2	0.16	0.87
GdFeO$_3$	293	0.36	49.8	0.17	0.80
	250	0.39	51.3	0.18	0.68
	200	0.41	52.8	0.17	0.61
	150	0.44	53.9	0.17	0.64
	100	0.46	54.5	0.15	0.92
	50	0.47	54.8	0.15	0.63
	10	0.47	54.9	0.17	0.69

4.1.4 Results, Interpretation and Discussion

The temperature dependence of Centre Shift (CS) in Mössbauer spectra can be predicted by the Debye model for a given material, allowing variable temperature Mössbauer spectroscopy studies to approximate the Debye temperature [70], and by extension, the recoil-free fraction [71]–[73]. The recoil-free fraction, f factor, or Lamb-Mössbauer factor, is the temperature-dependent ratio of the recoilless γ absorption of a material, therefore the greater the f factor, the greater the Mössbauer spectral area by comparison with a material with a smaller f factor. Ascertaining the recoil-free fraction of Fe within a particular phase enables quantification of its abundance in a mixed-phase material, which can be vital for studying materials that undergo phase changes, redox reactions or other forms of dynamic in-application, such as catalysis [71]. The Debye temperature of a material can also be used in further approximations of properties reliant on its thermal behaviour, such as specific heat capacity [74]. Debye temperatures for $LnFeO_3$ perovskites have been obtained previously through the temperature dependence of the Mössbauer Centre Shift [75] and through specific heat methods [76].

The Mössbauer spectra for all studied perovskites can be reliably fitted using a single sextet, indicating their magnetic nature as antiferromagnetic [77] with Centre Shift values consistent with octahedral Fe^{3+} [52], [71]. The room temperature Centre Shifts for the $LnFeO_3$ series show little change as a function of the rare earth cation. A decrease in the magnitude of the internal magnetic field is observed, wherein B_{hf} is greatest for $LaFeO_3$ and decreases towards $GdFeO_3$, a trend shown to continue to $LuFeO_3$ by Eibschütz, Shtrikman and Treves [75]. which can be linked to the known decrease in Néel temperature of $LnFeO_3$ perovskites from La to Lu. From the refined structural data of the materials studied here, Fe-O bond lengths, and FeO_6 volumes, do not reflect the near-linear trend in B_{hf}, suggesting that these bond lengths are not a deciding factor in the magnitude of B_{hf}. The structural data of several $LnFeO_3$, from Pr to $LuFeO_3$ by Marezio, Remeika and Dernier in 1970 [56] show that through this series, the average distance between iron and rare earth atom decreases from Pr to Lu, as

the Ln ionic radius decreases, and the difference in individual distances becomes greater. This could suggest that the proximity of Ln and Fe atoms, and the interactions between them, is influencing the magnitude of the hyperfine field of the iron. Links have also been made between the hyperfine field and the angles between magnetic domains [75].

Centre Shift and hyperfine magnetic field for all studied $LnFeO_3$ samples show non-linear increases with decreasing temperature. Increases in the hyperfine magnetic fields are due to the removal of thermal vibrations with reduced temperature, while the increases in the centre shift values can be explained using equations from the Debye model [75], [78]. The stated centre shift values differ from the intrinsic isomer shift values as the centre shift is affected by temperature while isomer shift is an inherent parameter for a given material. The different values are brought about through the Second Order Doppler Shift (SODS) such that [70], [79], [80];

$$CS(\Theta_D, T) = IS + SODS(\Theta_D, T) \tag{2}$$

The Centre Shift (CS) is the experimentally observed outcome, while the Isomer Shift (IS) is temperature independent and a characteristic of the material, and the SODS is the temperature dependent term of this equation. The SODS can be related to the Debye temperature, and measured temperature by:

$$SODS = -\frac{3}{2}\frac{k\,\Theta_D}{Mc}\left[\frac{3}{8} + 3\left(\frac{T}{\Theta_D}\right)^4 \int_0^{\frac{\Theta_D}{T}} \frac{x^3 dx}{e^x - 1}\right] \tag{3}$$

where k is the Boltzmann constant; E_γ is the energy of the gamma ray (14.41 keV); c is the speed of light; θ_D is the Debye temperature; M is the mass of the iron, taken as 57 amu (multiplied by Avogadro's constant for conversion to mass). From this, the Debye temperature can be used to calculate the recoil-free fraction;

$$Lnf = -\frac{3E\gamma^2}{Mc^2 k\,\Theta_D}\left[\frac{1}{4} + \left(\frac{T}{\Theta_D}\right)^2 \int_0^{\frac{\Theta_D}{T}} \frac{x dx}{e^x - 1}\right] \tag{4}$$

In approximating the Debye temperature of a material, through the use of variable temperature Mössbauer spectroscopy, it is necessary to consider all temperature points simultaneously. A self-feeding program was constructed, in

which a Debye temperature and an isomer shift would be simulated, resulting in theoretical SODS and Centre Shift. The objective of the program was to minimise the difference between the theoretical centre shift using simulated Debye temperatures and Isomer Shifts, for all measured temperatures simultaneously. The Debye temperature and Isomer Shift stipulated by the program, with the minimal difference between theoretical and experimental values, are those presented herein. This is the Debye temperature used in equation (3) to ascertain the recoil-free fraction of each material at a given temperature. Using these equations, by inputting a range of Debye temperatures, several trends were drawn to compare the values gathered in this study to theoretical values as illustrated in Figure 4.8. This process is not to fit the data presented against a theoretical line from Figure 4.8, and these lines are principally to guide the approximation procedure. Approximating the Debye temperature in this manner has been shown to reliably produce accurate values by Dubiel and colleagues previously [73], [81], and here, summarised in Table 4.6 are corroborating Debye temperatures from other research groups' data Mössbauer spectroscopy data using the present method. The material presented by Aldon was $LiFePO_4$, by Cieślak was σ-phase $Fe_{54}Cr_{46}$ and by Kim was $CoFe_2O_4$.

Table 4.6. Validation of Debye temperature and recoil-free fraction calculation method using third-party published data.

|	θ_D (K) (This work)	θ_D Ref.	f_{293} (This work)
Aldon $LiFePO_4$ [72]	336 (10)	336	0.69 (2)
Cieślak $Fe_{54}Cr_{46}$ [81]	435 (10)	437 (7)	0.80 (2)
Kim $CoFe_2O_4$ Site A [82]	738 (10)	734 (5)	0.92 (2)
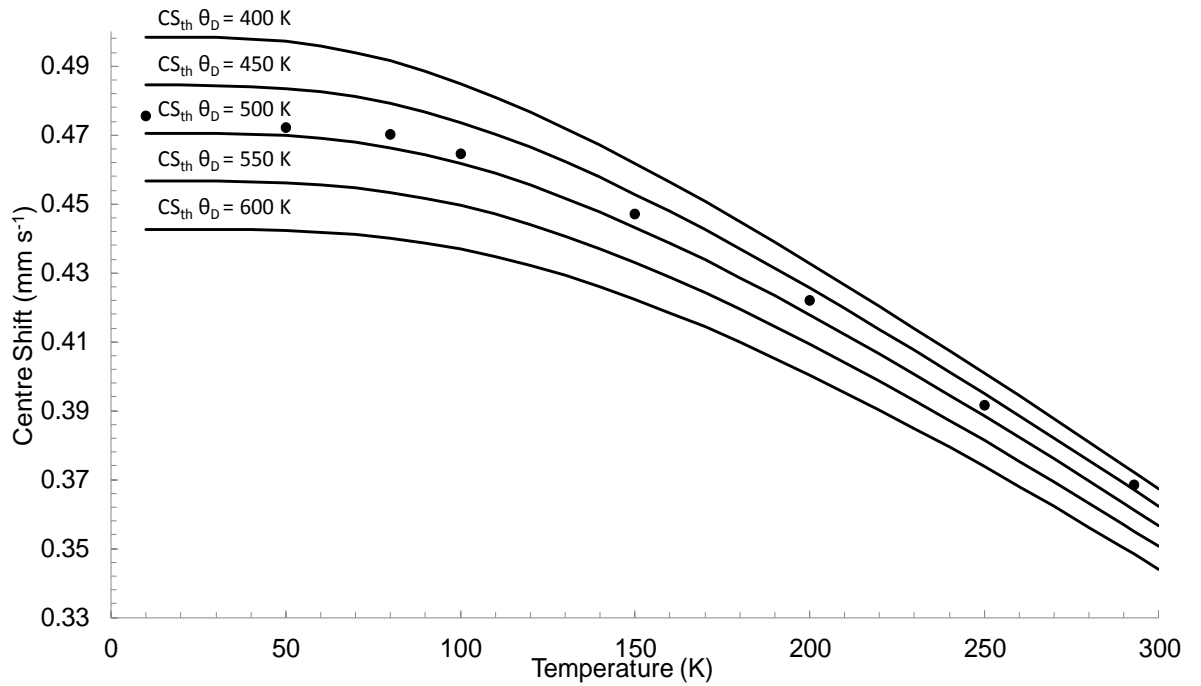
Figure 4.8. Theoretical trend lines of Centre Shifts for given θ_D (solid lines) and experimental data for LaFeO$_3$ (circles)with intrinsic Isomer Shift = 0.61 mm s^{-1}.

Table 4.7. Debye temperatures and recoil-free fractions for LnFeO$_3$ series with previously published data for comparison.

	θ_D / K (This work)	θ_D / K [75] (Eibshütz)	θ_D / K [76] (Parida)	θ_D / K [83] (Romero)	θ_D / K [84] (Morishita)	θ_D / K [85] (Yoon)
Method	Temp shift	Temp shift	Heat capacity	Elastic modulus	Heat capactiy	Temp shift
LaFeO$_3$	474 (20)	800 (50)	582	415	479	610
NdFeO$_3$	459 (20)	770 (50)	574	-	-	-
SmFeO$_3$	457 (20)	730 (50)	-	-	-	-
EuFeO$_3$	452 (20)	730 (50)	-	505	-	-
GdFeO$_3$	473 (20)	770 (50)	555	-	-	-

The calculated Debye temperatures for the $LnFeO_3$ series are consistently ca. 300 K lower than those reported by Eibshütz [75], and are closer in value with values ascertained by other methods as shown in Table 4.7. When considering the differences observed between sources in Table 4.7, it is important to consider the methods by which the Debye temperatures were determined. It is known that the value of the Debye temperature depends on the method used to approximate it [81], [86], and such comparisons of Debye temperatures are ideally made with values obtained using the same method and within the same temperature range. When using the data presented by Eibshütz [75] in the approximation program used in the present work, we obtain Debye temperatures considerably lower than the Debye temperatures reported by Eibshütz and closer to those obtained in this work, as shown in Table 4.8. Data for $EuFeO_3$ and $GdFeO_3$ were not used here as only two of Eibshütz's measured temperatures were within our measured range. The discrepancies in values that remain may be attributable to the improvements in spectroscopy equipment in the last 50 years that allow for more accurate measurements of the Centre Shift. It is certainly conceivable that the spectral noise of the data Eibshütz analysed and published, combined with their methodology of using a ruler to obtain Centre Shift values from spectra printed with chart recorder, could have introduced uncertainties into their data. Despite these differences, the overall trend in Debye temperatures from Ln = La to Gd, for our data, do follow the trend shown by Eibshütz wherein there is a reduction in Debye temperature from $LaFeO_3$ to $EuFeO_3$, and an increase for $GdFeO_3$.

Table 4.8. Debye temperature values obtained using the present method for $LnFeO_3$ materials using centre shift values from this work and from Eibshütz [75].

	θ_D K (This work)	θ_D K [75] (Eibshütz)
$LaFeO_3$	474 (10)	603 (10)
$NdFeO_3$	459 (10)	599 (10)
$SmFeO_3$	457 (10)	605 (10)

From these Debye temperatures, we find the recoil-free fractions for the $LnFeO_3$ perovskites from equation (3) as presented in Table 4.9. These values are not relative to α-Fe, as is often presented, and are the recoil-free fractions of these phases alone. The recoil-free fractions of these materials has been found to be greater than that of α-Fe previously, by comparing the spectral areas of

suitable Mössbauer absorbers [43]. An *f*-factor that is greater than that of α-Fe implies that the iron nucleus is more strongly embedded, allowing for the recoilless absorption of γ-rays. It is suggested that the structure of these materials, wherein the iron is octahedrally co-ordinated in FeO_6 by ionic bonds, should be more thermally stable than α-Fe which is packed densely in planes bound by metallic bonds that allow for heat transfer more readily.

Table 4.9. Room temperature recoil-free fractions of $LnFeO_3$ series where Ln = La, Nd, Sm, Eu, Gd.

Orthoferrite	Room temperature recoil-free fraction ($f_{293\,K}$)
$LaFeO_3$	0.827 (20)
$NdFeO_3$	0.817 (20)
$SmFeO_3$	0.816 (20)
$EuFeO_3$	0.812 (20)
$GdFeO_3$	0.826 (20)

The simplest form of presenting the Debye temperature can be seen in equation (5) [78] In this form we see both Planck's and Boltzmann's constant, and only the variable Debye frequency, which is expressed in equation (6) [87].

$$\theta_D = \frac{h v_m}{k} \tag{5}$$

$$v_m = \left(\frac{3N}{4\pi V}\right)^{1/3} v_s \tag{6}$$

Through equations (5) and (6) it is shown that the Debye temperature of a crystal is related to the number density (N) of, and speed of sound (V) through, the crystal. The Debye frequency (v_m) is the characteristic frequency of a material, the maximum vibrational frequency, achieved due to a single normal vibration. The Debye temperature is the temperature of the crystals highest normal mode of vibration [78], [87]. As the recoil-free fraction relies on the ability of the nucleus to absorb and fluoresce γ-rays, we find that an increase in v_m, and therefore an increase in the Debye temperature, resulting in an increase in *f* is to be expected. An increase in Debye temperatures reflects an increase in the rigidity of the FeO_6 octahedra in the $LnFeO_3$. This can be taken from the relationship observed between FeO_6 octahedra volumes and Fe-O bond lengths, and Debye temperatures. The approximated Debye temperatures in this work show an overall trend where θ_D decreases from $LaFeO_3$ to $EuFeO_3$, and $GdFeO_3$ sharply

increases to a value near that of LaFeO$_3$, which agrees with the overall trend observed by Eibshütz and colleagues [75].

4.1.5 Conclusions

A series of LnFeO$_3$ perovskite oxides was synthesised through stoichiometric ball milling of oxide precursors, where Ln = La, Nd, Sm, Eu and Gd. ^{57}Fe Mössbauer spectroscopy measurements were taken at temperatures from 10 to 293 K. Debye temperatures and recoil free fractions were calculated using equations relating the temperature dependence of the second order Doppler shift and the CS of the Mössbauer spectra. The accuracy in temperature control and data processing allowed for the Debye temperatures calculated by this method to be consistent with heat capacity and relative Mössbauer spectral area methods, while allowing the observation of potential transitions that may occur over the temperature range. The calculated Debye temperatures were complemented by translatable trends observed in Raman spectra, wherein greater intensities of Ln–O vibrations were presented by perovskites with lower Debye temperatures. This work provides suitable reference data on these rare earth orthoferrites which should prove useful in further studies investigating their structures, whether crystallographic or hyperfine, at ambient temperature or below, when studying their multitude of potential applications.

4.2 Lanthanum orthoferrite as three-way catalyst

4.2.1 Introduction

A three-way catalyst, otherwise called a catalytic convertor, is the catalyst found as part of the exhaust system on petrol powered cars, as depicted in Figure 4.9, responsible for reducing the levels of harmful pollutants emitted through the exhaust pipe. Eugene Houdry, informally referred to as *'Mr. Catalysis'* [88] after a history of war-driven catalysis research in hydrocarbon cracking was issued the first patent for a catalytic converter for exhaust gases in 1954 [89]. Houdry describes the issue of "carbon monoxide, a deadly poison" which at the time "averages 4.5 % by volume and at certain times reached 9 %", "approximately six pounds per hour". A typical exhaust gas under normal engine operation is nominally 0.5 volume % carbon monoxide, 350 vppm unburnt hydrocarbons and 900 vppm nitrogen oxides, NO_X [90]. The first European emission control standard, *Euro 1*, set limits on the emission of carbon monoxide, particulate matter, and a combined limit for unburnt hydrocarbons and nitrogen oxides from 1992 [91]. As of 2018 the current emission standards are set by *Euro 6*, which is predominantly a diesel-focused amendment on Euro 5 related to NO_x trapping and conversion [92]. Over the 22 years between Euro 1 and Euro 6, summarised in Table 4.11, the allowable amount of pollutants has reduced (Euro 3 increase in CO due to change in test procedure), resulting in a continued effort to improve the catalytic performance of the catalytic converters to meet the new and upcoming legislation. These improvements have been through optimising the design of the catalyst bed, the form the catalyst materials are in, and through the development of new materials. A three-way catalyst is defined by the ability of one catalyst to simultaneously reduce NO_X and oxidise both CO and unburnt hydrocarbons, while a two way catalyst does not reduce NO_X [93], as the reactions shown in Table 4.10 illustrate.

Figure 4.9. Illustration of three-way catalytic converter [94].

Table 4.10. Summary of simplified reactions of automotive exhaust gases by two and three way catalysts [93]. * denotes unbalanced reactions.

Two way	$2CO + O_2 \rightarrow 2CO_2$
	$HC + O_2 \rightarrow CO_2 + H_2O$ *
Three way	$2CO + 2NO \rightarrow 2CO_2 + N_2$
	$HC + NO \rightarrow CO_2 + H_2O + N_2$ *
	$2H_2 + 2NO \rightarrow 2H_2O + N_2$

Table 4.11. Euro 1 to 6 emission standards of pollutants for petrol passenger cars, by year implemented. CO carbon monoxide, HC hydrocarbon, NO_x nitrogen oxides, PM particulate matter, NMHC non-methane hydrocarbons. Data collected from European Commission directives [91], [92], [95]–[97].

	Analyte (g km^{-1})						Date introduced
	CO	HC + NO_x	HC	NO_x	PM	NMHC	
Euro 1	2.72	0.97	-	-	0.14	-	1992
Euro 2	2.20	0.50	-	-	-	-	1996
Euro 3	2.30	-	0.2	0.15	-	-	2000
Euro 4	1.00	-	0.1	0.08	-	-	2005
Euro 5	1.00	-	0.1	0.06	0.005	0.068	2009
Euro 6	1.00	-	0.1	0.06	0.005	0.068	2014

Platinum group metals (PGMs) have been the active components of automotive catalysts since they were discovered to be able to catalyse the necessary reactions in the late 1970s [98]. The challenges found following this discovery was how to optimise the materials, their shapes, support systems, and

the gas composition. Pt and Rh have primarily been used together as the active components, where the former would oxidise, and the latter would reduce the CO / hydrocarbons and NO_x respectively [99]–[101]. A platinum to rhodium ratio of around 8 was reported by Helmers in 1998 for automotive catalysts, however the exact compositional ratios of components is often not public knowledge [102]. Ceria (CeO_2) can be used as a minor component to improve the oxygen storage capacity of the catalyst, and zirconia (ZrO_2) can improve the thermal stability [103]–[105]. The support material of the catalyst and the shape of the support is usually a ceramic monolith with pathways for air to travel through the catalyst, often a honeycombed shape of edge-sharing hexagons. Some main design elements for the support include low thermal expansion, high thermal stability, high surface area, moderate strength, and be compatible with the method of applying the catalyst, which is commonly wash-coating. Cordierite, a magnesium-alumino-silicate ceramic ($Mg_2Al_4Si_5O_{18}$), is widely used as the support substrate, onto which the catalyst is wash coated [32], [38], [90], [104]. This kind of support system is relatively inexpensive compared to metal supports [105] and can be prepared through industrially scalable processes. The importance of thermal properties for the substrate stems from the temperatures at which the catalysts require to convert the exhaust components, one method of comparing these temperatures is to compare the temperature at which 50% conversion occurs, referred to as the *light-off temperature*, denoted as t_{50}. A candidate material for the replacement of PGMs should exhibit T_{50} values equal to or lower than the current PGM catalysts in order to be competitive – Johnson Matthey PGM-based catalysts have T_{50} values of $\approx$ 370 °C for unburnt hydrocarbons and NO_x [106].

Petroleum is composed of numerous hydrocarbons of varying C-chain lengths, with minor constituents containing nitrogen, sulphur and some trace amounts of metals such as copper and vanadium [107]. A simplified view of the consumption of petroleum to release energy can be viewed as the combustion of octane;

$$25\ O_2 + 2\ C_8H_{18} \rightarrow 16\ CO_2 + 18\ H_2O + energy$$

Due to the oscillatory nature of the internal combustion engine, this stoichiometric reaction will fluctuate between being oxygen rich, and fuel rich, at

a frequency related to the rpm of the engine. Controlling the ratio of air and fuel (A/F) being fed into the combustion chamber will affect the stoichiometry of the above reaction, resulting in exhaust gases that are more oxidising or reducing with increased or decreased A/F ratio. By weight, 400 amu of oxygen is required to oxidise 132 amu of octane, and as oxygen is approximately 23% of the total mass of air, an air to fuel ratio, by weight, of ≈13:1 would provide stoichiometric combustion conditions of pure octane. In commercial fuels, the stoichiometric A/F ratio is found around 14.6:1, as illustrated in Figure 4.10 from J Kašpar [93] and given by K C Taylor in 1993 [108]. A reduced A/F ratio, where the composition is fuel lean, causes NO_X reduction to peak; an increased A/F ratio, in fuel rich conditions, causes oxidation of hydrocarbons and CO to maximise, at the expense of NO_X conversion. The ratio of air to fuel being fed into the combustion chamber is controlled by the on-board diagnostics, consisting of the three-way catalyst, sensors before and after the catalyst, air flow meters and fuel injectors. This system analyses the exhaust gas pre- and post-catalyst and the on-board computer adjusts the ratio of air and fuel to maintain optimal conditions for the catalyst.

When the catalyst is operating under fuel rich conditions there is a deficit of oxygen in the exhaust gas, which would be in excess during fuel lean conditions. The ability to adsorb excess oxygen during fuel lean operation and liberate it during fuel rich enables the catalyst to convert the pollutants over an increased range of A/F ratios by mitigating the effect of the momentary perturbations in air to fuel; this is referred to as the oxygen storage capacity (OSC). In PGM-based three-way catalyst, CeO_2 is commonly used as a component in the catalyst wash-coat, primarily for its OSC capability [103], [105]. Ceria also plays a role in stabilising the platinum against sintering, and has a positive effect on the kinetics for CO oxidation [98], [109]. The thermal stability, CO oxidation kinetics and oxygen exchange rate of ceria is improved on by incorporating zirconia into the ceria structure [109], [110]. Modern three-way catalysts consist of a ceramic, cordierite monolith support structure, with a high surface area and gas flow rate design, treated with a coating of active platinum group metals, ceria and zirconia.
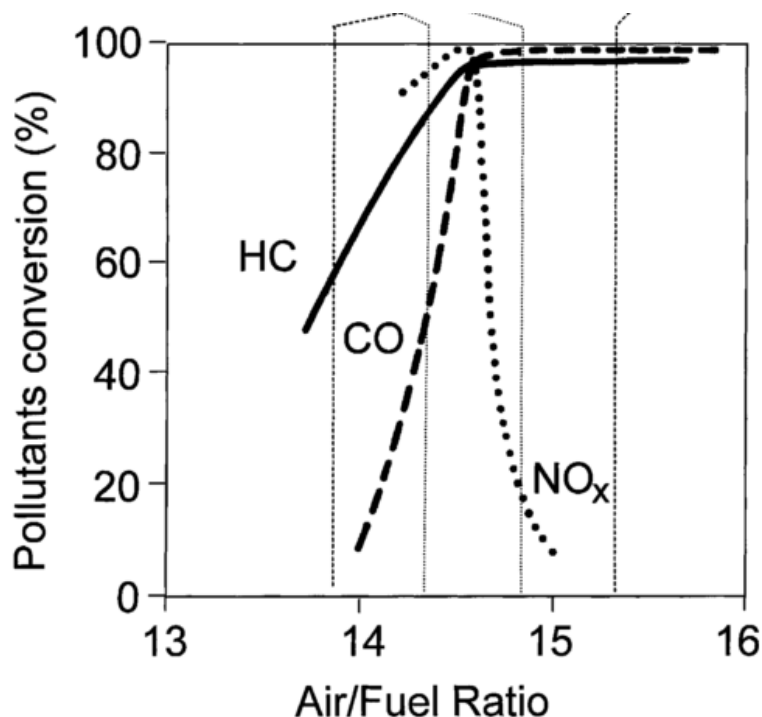
Figure 4.10. Effect of air to fuel ratio on the conversion of efficiency of three-way catalysts. Reproduced directly from [93].

Platinum group metal catalysts are very effective for the treatment of petrol vehicle emissions and adhering to the increasingly restrictive European emission standards [92], [106]. PGMs are found in low concentrations naturally, however in increased concentrations can cause such ailments as dermatitis, pregnancy issues, asthma, nausea, and more serious issues with even greater concentration [111]. Barbante et al. analysed snow and ice samples from different depths in Greenland, relatable to different years, finding increased concentrations of platinum, palladium and rhodium in recent history, due to the release of PGMs from the catalysts over time [112]. The high working temperature, chemical and physical stresses, and mechanical abrasion on the catalyst wash coat all contribute to the emission of PGM particles from the catalyst, and into the environment [111].

Candidates for the replacement of PGMs in three-way catalysts must be able to address all the previously outlined factors; competitive light-off temperatures and conversion rates, OSC, thermal and chemical stability, ability to be applied through wash coat for easier assimilation with existing technology, and less harmful. In order to be industrially competitive, candidates would also be easy and cheap to synthesise, using readily available materials. One group of

materials garnering much scientific focus for potential candidates are rare-earth orthoferrites, more specifically lanthanum ferrite, $LaFeO_3$. Rare earth orthoferrites more widely, have been found viable for various heterogenous catalyst applications, including methane oxidation [113], [114], water depollution [115] and the elimination of volatile organics such as alkanes and alcohols [38], [116]. In 2010, Xun Li and colleagues presented a complete series of $LnFeO_3$ perovskites (omitting $CeFeO_3$) indicating $LaFeO_3$ to have the second lowest T_{50} for NO conversion (second to $GdFeO_3$), and second highest N_2 selectivity (second to $NdFeO_3$) [117]. Shen, Colonna and Varma, in 1998, 2002 and 2003, each studied $LaFeO_3$ for catalysis synthesised through co-precipitation, citric acid complexation and solid-state synthesis respectively [118]–[120], each of which influenced particle size, morphology, surface area and other physicochemical properties. The A and B sites have co-hosted a variety of elements including; Sr on the A site to influence the charge state of the iron from Fe^{3+} to a combination of Fe^{3+} and Fe^{4+} [121], the B site has been occupied by numerous metals, and combinations of metals, including Fe, Mn, Co and Cu [9], [32], [113]. Aside from the application of interest herein, $LaFeO_3$, doped or undoped, has garnered interest in gas sensing [35] and for its superparamagnetic [17] and multiferroic properties [10].

4.2.2 Research Objectives

Mössbauer spectroscopy has been used in this work to study lanthanum ferrites and to investigate the effects of varying synthesis routes, including solid state, citrate-nitrate auto-combustion, flame spray pyrolysis and co-precipitation. Synthesis parameters within methods have been varied and studied, such as calcination or sintering temperatures. Changes to the nominal composition and stoichiometry of $LaFeO_3$ have been investigated, primarily through studying lanthanum deficient $La_{0.8}FeO_3$, whereby 20% of lanthanum sites are vacant, which exhibits promising activity and selectivity at relatively low temperatures [122], [123]. The material selection of the perovskites studied was influenced by their catalytic properties, and changes in catalytic behaviour as a function of one or more of these variables discussed. In one instance it was found that to change the calcination temperature in the citrate-nitrate process, keeping all other variables constant, there was an observable difference in catalytic behaviour, and no other spectroscopic techniques employed to understand why this was the case had yielded any answers. Here we use Mössbauer spectroscopy to support the characterisation by complementary techniques, to investigate further where these techniques are not sufficient, and with the aims to improve the existing understanding on how these materials function, why those performing better are doing so, and to use this information to guide the next iteration of perovskite three-way catalysts.

Research questions directly posed by the industrial scientists for these studies include;

- Are there any iron-bearing impurity phases, such as nano-Fe_2O_3?
- Can the surface and bulk phases be distinguished?
- Can the oxidation states and environments be determined for the active iron species for the catalytic reactions?

4.2.3 Materials Characterisation

4.2.3.1 Synthesis and Characterisation

There were four different synthesis routes used to produce the lanthanum ferrite materials used in this study; high energy ball milling, citrate-nitrate auto combustion (CNAC), precipitation and flame spray pyrolysis. Outlines of each of these procedures can be found in chapter 2, *Materials Synthesis and Characterisation*. All the materials studied in this sub-chapter were synthesised at JMTC, Sonning Common, and as such the details of the synthesis methods used are not disclosable. Any specific information that can be published will be included in the appropriate locations in the following sub-sections. A summary of the materials studied can be found in Table 4.12, below.

Table 4.12. Summary of lanthanum ferrite catalyst samples studied.

Synthesis method	Material
Ball milling	$LaFeO_3$, $La_{0.8}FeO_3$
Citrate-nitrate (CNAC)	$LaFeO_3$ calcined at 500, 700 and 900 °C, $La_{0.8}FeO_3$
Precipitation	$La_{0.8}FeO_3$
Flame spray	$La_{0.8}FeO_3$
	$La_{0.8}FeO_3$ that has been acid washed
	$La_{0.8}FeO_3$ that has been impregnated with 5 wt% Fe
	$La_{0.8}FeO_3$ that has been catalytically aged

The ball milled samples were made using a single calcination step after milling at 600 °C. Each of the ball milled samples were identified as phase pure by XRD, either as $LaFeO_3$ – The X-ray diffraction pattern of $LaFeO_3$ is presented in Figure 4.11. Their surface areas were measured by liquid N_2 BET at 18.2 m^2 g^{-1} for $LaFeO_3$ and 9.9 m^2 g^{-1} for $La_{0.8}FeO_3$. H_2-TPR (temperature-programmed reduction) analysis showed that the La deficient material resulted in more easily reducible iron ($Fe^{3+} \rightarrow Fe^{2+}$). Total oxygen storage capacity at 450 °C of the three materials were measured at 27% and 46% for $LaFeO_3$ and $La_{0.8}FeO_3$ respectively, as determined by the bespoke catalyst testing equipment at JMTC.
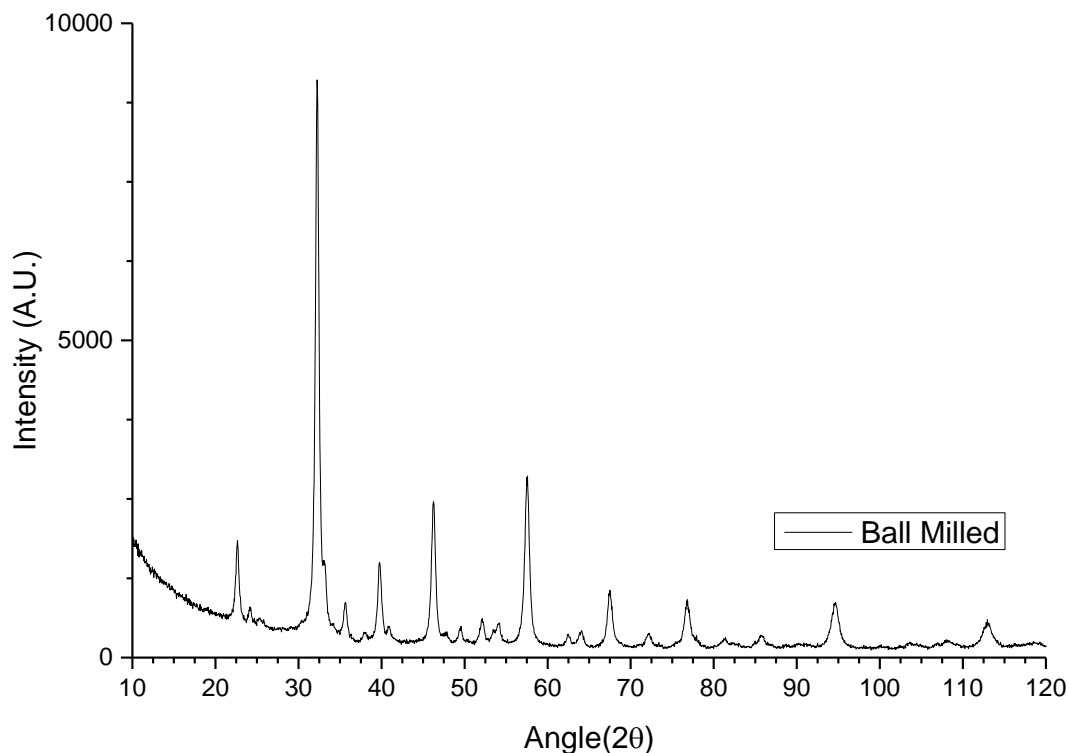
Figure 4.11. X-ray diffraction pattern of ball milled $LaFeO_3$. Identified as single phase, PDF 00-037-1493.

All three stoichiometric citrate-nitrate materials were made through identical synthesis routes and calcined at 500, 700 and 900 °C as the final step. All were identified as single phase through XRD, as shown in Figure 4.12, with no unique diffraction peaks, or peak shifts through the series. An increase in the calcination temperature causes the diffraction peaks to become narrower and more intense, indicating increased crystallinity. Rietveld refinement of the data gave average crystallite sizes of 18, 44 and 150 nm for calcination temperature 500, 700 and 900 °C respectively, indicating that the greater the calcination temperature the larger the particles formed. The exact surface areas of these materials cannot be disclosed, however it can be said that the surface area decreased dramatically with increased calcination, to < 1 m^2 g^{-1} when calcined at 900 °C. The $La_{0.8}FeO_3$ material was calcined at 700 °C and was also identified as single phase by XRD. Its surface area is comparable to the stoichiometric material.

118
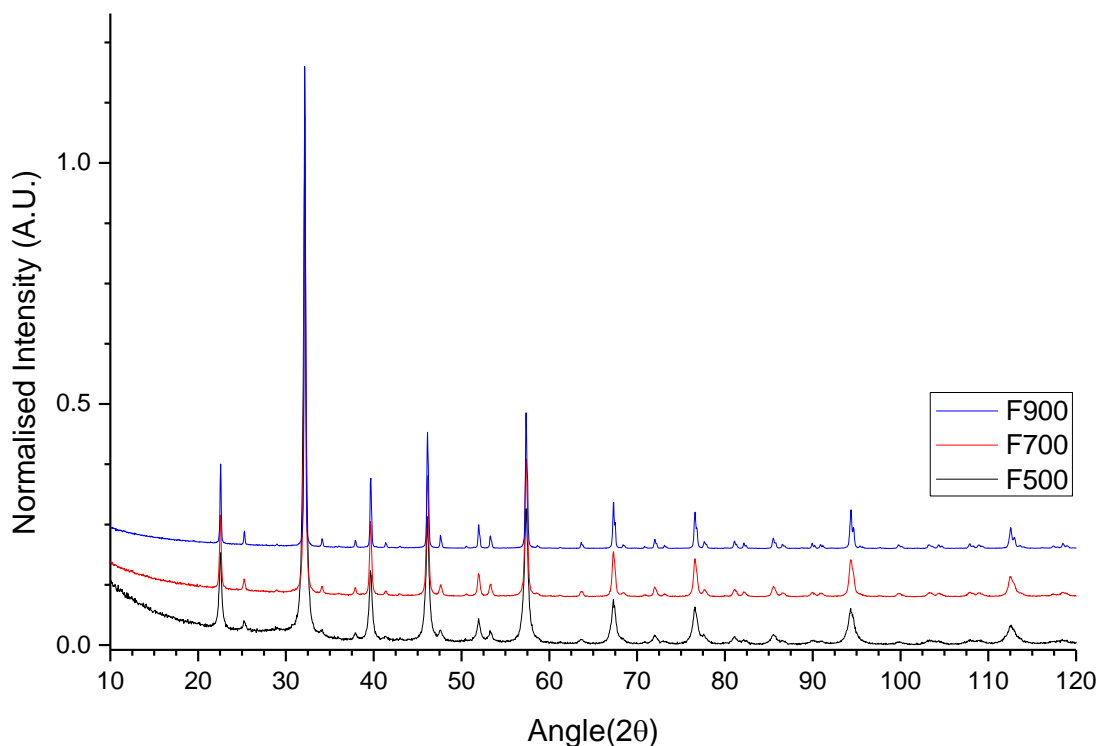
Figure 4.12. X-ray diffraction patterns of $LaFeO_3$ samples produced through CNAC synthesis, calcined at 500, 700 and 900 °C. All samples identified as single phase PDF 00-037-1493.

Details pertaining to the synthesis of the precipitated $La_{0.8}FeO_3$ material cannot be disclosed, however it was identified as single phase by XRD, and its surface area determined by BET as 24 m^2 g^{-1}.

A single batch of $La_{0.8}FeO_3$ was used in all flame-spray related studies, the details of the synthesis parameters cannot be disclosed in any more detail than was discussed in the *Material Synthesis and Characterisation* chapter. All samples prepared through this route were calcined at 650 °C. Four materials synthesised through flame spray pyrolysis were studied, one being $La_{0.8}FeO_3$ direct from the synthesis, another after being used for catalytic testing, details of which to follow. Two of the samples were subject to post-synthesis treatments of acid washing and surface iron impregnation. The surface impregnation was achieved through incipient wetness impregnation using iron nitrate nonahydrate (mass equivalent to 5 wt% Fe) in distilled water. The mixture was dried at 105 °C until dry, and subsequently calcined at 500 °C for 2 hours. XRD of the resulting material showed no change in crystal phases while X-ray photoelectron spectroscopy (XPS) analysis indicated a La / Fe ratio of 0.70 (compared to the

1.07 ratio of the as-prepared material) – the X-ray diffraction pattern of the untreated $La_{0.8}FeO_3$ material is presented in Figure 4.13. The acid wash treatment was carried out using dilute (2M) acetic acid, 5 grams of $La_{0.8}FeO_3$ was added to 50 mL of the solution whilst maintaining the solution's pH. The solution was decanted after 60 minutes, washed with deionized water and dried at 105 °C until dry. The purpose of this treatment was to etch the surface of the particles, selectively removing lanthanum, exposing more iron sites. More information on the process and rationale behind this acid wash treatment can be found in the 2014 article presented by Huang and colleagues who used this treatment on $La_{0.5}Sr_{0.5}MnO_3$ [124]. XRD analysis of the resulting material revealed no structural changes, and XPS analysis indicated a lanthanum to iron ratio of 0.89. The effect these treatments had on the catalytic performance of the material is discussed in the following section. The untreated $La_{0.8}FeO_3$ was identified as single phase by XRD with an 'amorphous hump' between 25 and 35° 2θ, as seen in Figure 4.13, and its surface area was measured by BET at 112 m^2 g^{-1}. Transmission electron microscope (TEM) image analysis showed an average particle size of 10.4 nm with a range from 5 to 15+ nm as depicted in Figure 4.14.
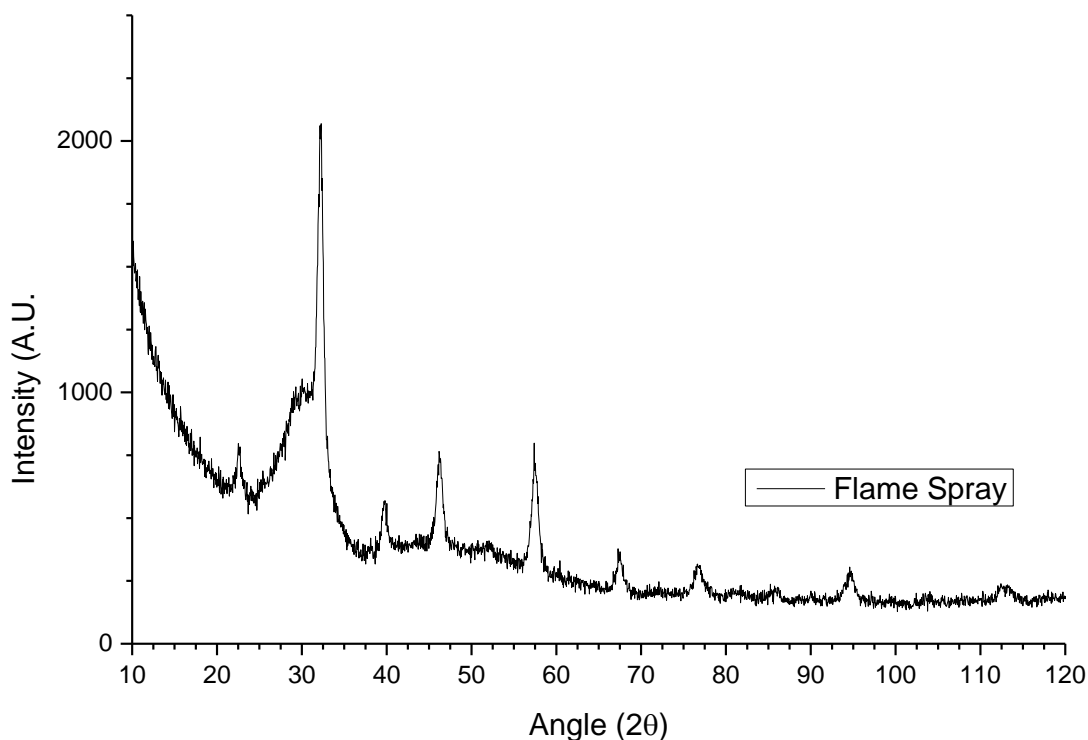

Figure 4.13. X-ray diffraction pattern of $La_{0.8}FeO_3$ produced by flame spray pyrolysis. Identified as single phase, PDF 00-037-1493.
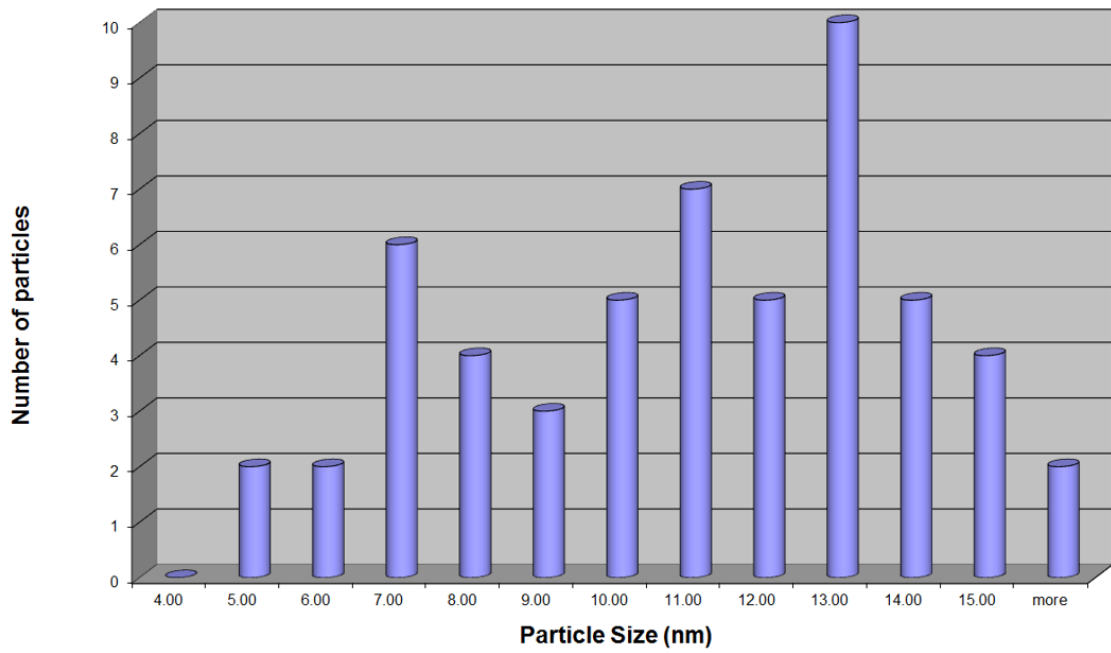
Figure 4.14. Particle size distribution of FSP $La_{0.8}FeO_3$ from TEM analysis. Errors approximated at ± 0.2 nm, from TEM image analysis.

4.2.3.2 Three-Way Catalyst (TWC) Testing

The testing of TWC catalyst candidate materials is conducted on bespoke equipment at JMTC Sonning Common, under controlled temperature and gas environment conditions. The inlet gases are controlled by the operator to imitate nominal exhaust gases while monitoring the outlet gas composition as a function of catalyst temperature. All the materials tested as part of this study were analysed up to 600 °C. The inlet gas composition is monitored and continually fluctuating between a fuel-rich and fuel-lean condition. As discussed in this chapter's introduction, three-way catalysts operate most efficiently within a narrow window around the stoichiometric air-to-fuel ratio in the engine ($\approx$ 14.6). The stoichiometric mixture of air and fuel in the engine has the correct amount of both air and fuel to produce complete combustion. Where the stoichiometric ratio is $\lambda = 1$, the testing of these materials was conducted at $\lambda = 0.99 \pm 0.05$, with the median composition being fuel-lean. The air to fuel ratio is monitored rapidly by the voltage response from an O_2 sensor that is greater during rich operation and reduced in the lean. During lean operation the inlet of the catalyst bed adsorbs oxygen by TWC and the outlet reduces NO_x; conversely, during rich operation the inlet adsorbed oxygen reacts with the reducing species and NO_x reduction occurs here also [32], [125]. The exhaust gases of the test process are monitored to determine the conversion rates of intake gases to their reacted products. The main indicators for the catalyst performance are the temperatures at which 20% and 50% of the reactant gases have been converts, known as T_{20} and T_{50}. The T_{20} and T_{50} temperatures of some of the studied materials for CO, NO and total hydrocarbons (THC) are presented in Table 4.13. The values of T_{20} and T_{50} cannot be disclosed for the ball milled materials, however the following can be said. For the $LaFeO_3$ material, 50% conversion of neither CO nor NO occurred before 600 °C. $La_{0.8}FeO_3$ achieved 50% conversion of CO at 450 °C and plateaued at around 45% NO conversion from 550 °C. No TWC data of the citrate-nitrate materials calcined at 700 or 900 °C is held at present.

Table 4.13. Summary of TWC test data of lanthanum ferrites.

		NO		THC		CO	
		T_{50} (°C)	T_{20} (°C)	T_{50} (°C)	T_{20} (°C)	T_{50} (°C)	T_{20} (°C)
Flame Spray	$La_{0.8}FeO_3$	591	577	565	434	591	524
	+5 wt% Fe	595	494	532	432	501	431
	Acid Wash	502	436	502	401	**442**	384
Precipitation	$La_{0.8}FeO_3$	569	497	522	463	466	433
Citrate-Nitrate	$La_{0.8}FeO_3$ F500	**484**	**367**	**440**	**366**	480	**331**

From the TWC test data presented the citrate-nitrate produced $La_{0.8}FeO_3$ calcined at 500 °C has the lowest T_{20} for NO, THC and CO, and the lowest T_{50} for NO and THC while the acid washed flame sprayed material has the lowest CO T_{50}. These conversion temperatures are all greater than those for platinum-group metal catalysts [100], [126], however these candidate materials do not represent the culmination of all possible research in the field of non-PGM, perovskite-based three-way catalysts. The low-to-nil oxygen storage capacity of these materials is one known drawback at present.

The wide range of T_{20} and T_{50} temperatures between the five materials disclosed was one reason for which a Mössbauer spectroscopy study was desired. All of the materials studied in this chapter were identified as single phase $La_{0.8}FeO_3$ by XRD, however their catalytic performance varied significantly.

Of the materials synthesised through FSP, the material that had been acid washed with acetic acid to remove surface lanthanum gave consistently lower T_{20} and T_{50} for all the reactants observed. The iron impregnated material has lower, or similar, T_{20} and T_{50} compared with the untreated material. The La / Fe ratio for the acid washed sample was almost exactly between that of the untreated and the impregnated material (1.07, 0.89, 0.7), indicating that the amount of surface iron is not itself an indicator for performance. The reason for this observation is still unclear and would require further investigation before conclusions are drawn, to avoid speculation.

4.2.3.3 Mössbauer Spectroscopy

In addition to the catalysis samples mentioned thus far, a number of rare-earth orthoferrites were synthesised at Sheffield Hallam University which have been studied extensively in Section 4.1 including $LaFeO_3$. The lanthanum ferrite prepared at SHU was synthesised through oxide precursor, solid-state sintering with two milling and calcination steps to ensure a homogenous, well crystalline material was produced. The room temperature Mössbauer spectrum of this material is seen in Figure 4.15, and the hyperfine parameters of the fit provided in Table 4.14. The hyperfine parameters of the fit provided are in good agreement with established literature, as introduced in 4.1, and will be used as the parameters of $LaFeO_3$ in the spectra collected for JMTC catalyst materials [17], [41], [127].
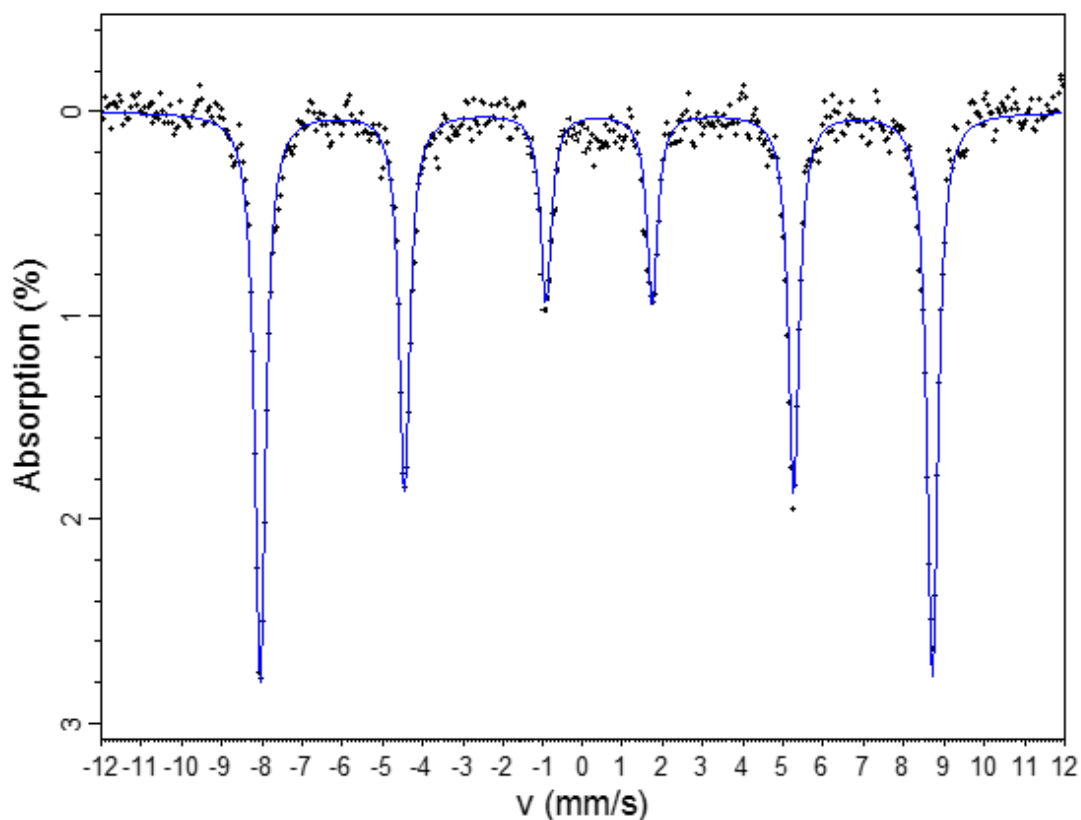

Figure 4.15. Room temperature Mössbauer spectrum of $LaFeO_3$ perovskite synthesised at SHU.

Table 4.14. Hyperfine parameters of SHU $LaFeO_3$ at 293 K.

| CS (mm s^{-1})	ε (mm s^{-1})	B$_{eff}$ (T)	Γ/2 (mm s^{-1})
0.37	-0.03	51.9	0.16
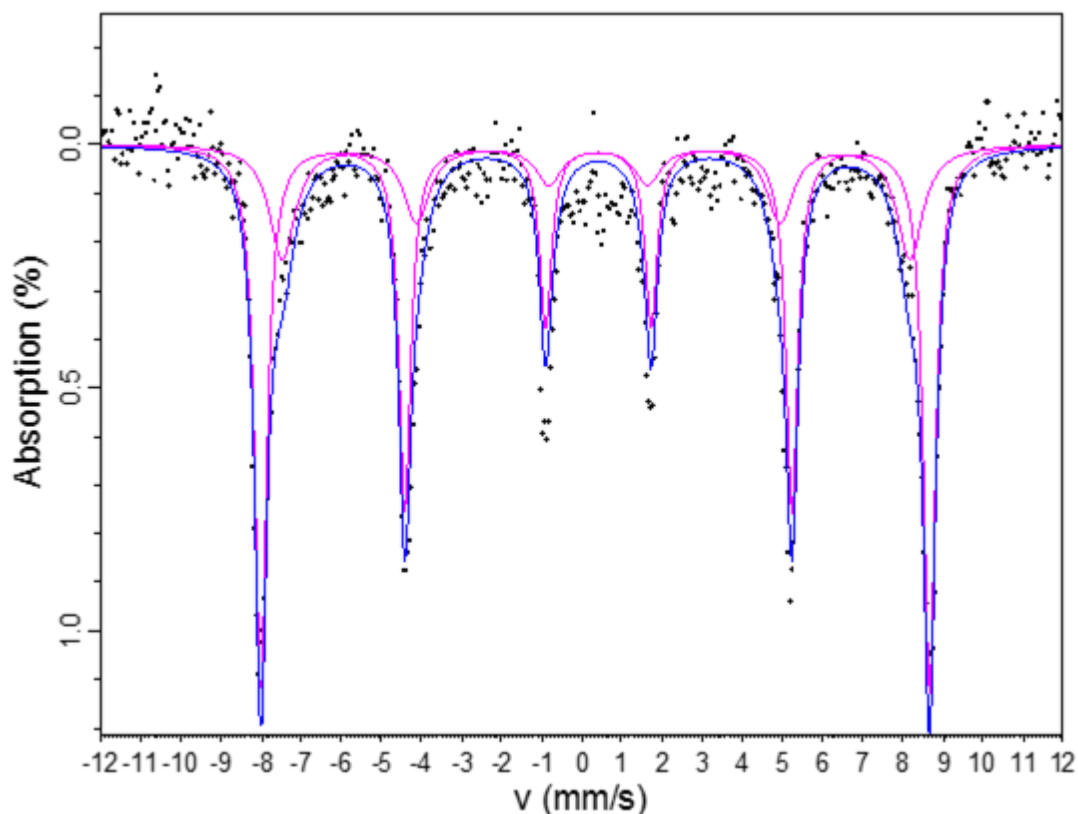
Figure 4.16. Room temperature Mössbauer spectrum of ball milled LaFeO$_3$ synthesised at JMTC.

Table 4.15. Hyperfine parameters of JMTC ball milled LaFeO$_3$ at 293 K.

	CS (mm s^{-1})	ε (mm s^{-1})	B$_{eff}$ (T)	Γ/2 (mm s^{-1})	Area (%)
Sextet 1	0.37	-0.04	51.7	0.18	69.2
Sextet 2	0.38	-0.03	48.5	0.39	30.8

Sextet 1 of Figure 4.16 can be assigned to the LaFeO$_3$ phase as seen in the SHU LaFeO$_3$ material [17], [41]. Due to the relatively high spectral area of sextet 2, the similarities in parameters to sextet 1 other than the hyperfine field, and the absence of unassigned diffraction peaks through XRD, this iron site is believed to be the result of a second species of LaFeO$_3$. As the SHU LaFeO$_3$ ball milled material spectrum was fit using one site this second phase may be due to differences in the synthesis procedure. Firstly, the iron precursor at SHU was Fe$_2$O$_3$, and FeOOH at JMTC, secondly the milling and calcination steps were conducted twice at SHU, and only once at JMTC; the SHU material was also pelletized and sintered at 1200 °C. From the diffraction patterns of FeOOH, the most intense diffraction peak for α-FeOOH is at 21.2 2θ (Cu K$_α$) [128]; γ-FeOOH

has its most intense peak at 14.2 2θ and second most intense at 36.2 2θ (Cu K$_\alpha$) [129] – these diffraction peaks would not be superimposed onto peaks from LaFeO$_3$, eliminating the possibility of unreacted precursor remaining from an incomplete synthesis. If the LaFeO$_3$ was present as a different crystal structure then this would result in similar diffraction lines, particularly considering the high Mössbauer spectral area associated with this site. The reduced synthesis steps of this materials compared to the SHU LaFeO$_3$ may suggest that, while the reaction is complete, that the degree of crystallinity in this material is lower. A spectral fitting site associated with a less-crystalline material would typically present with a higher linewidth, as seen in this instance. Whether this "less crystalline" phase would be present as discrete particles or as a surface phase is unclear with the interpretation of this spectrum alone.
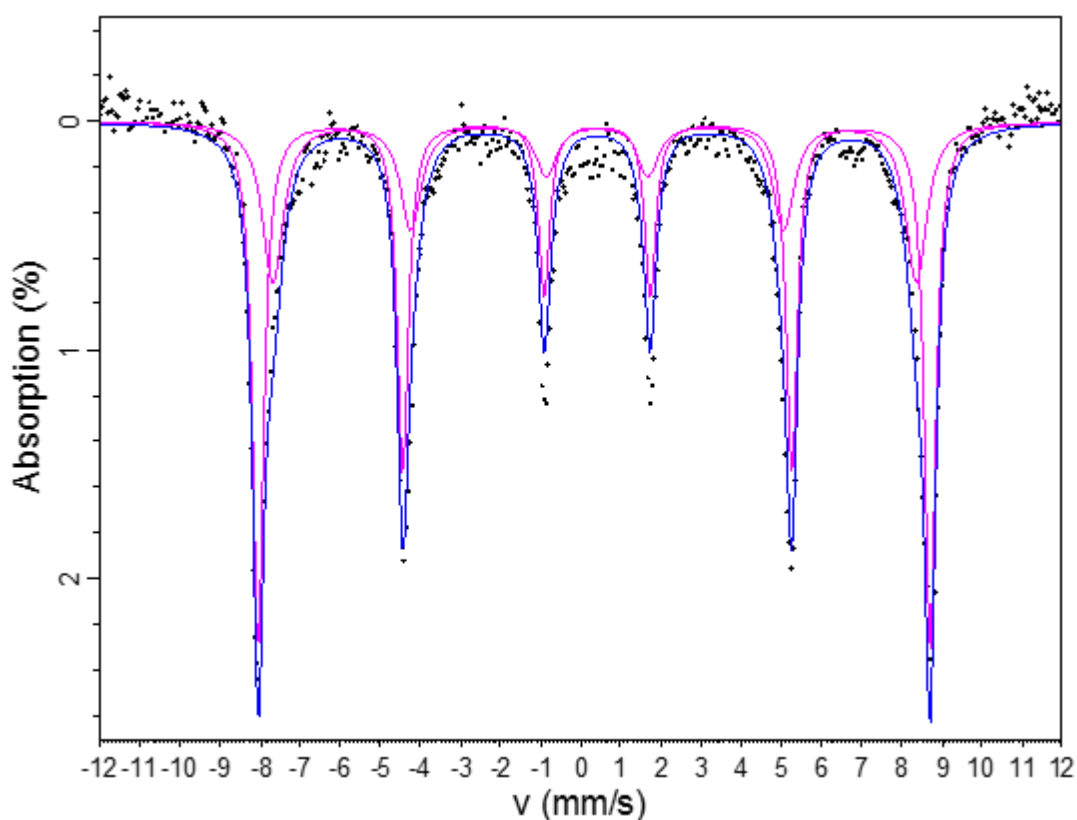

Figure 4.17. Room temperature Mössbauer spectrum of ball milled La$_{0.8}$FeO$_3$ synthesised at JMTC.

Table 4.16. Hyperfine parameters of JMTC ball milled La$_{0.8}$FeO$_3$ at 293 K.

	CS (mm s^{-1})	ε (mm s^{-1})	B$_{eff}$ (T)	Γ/2 (mm s^{-1})	Area (%)
Sextet 1	0.37	-0.04	52.0	0.17	68
Sextet 2	0.37	-0.03	49.8	0.32	32

Sextet 1 in Figure 4.17, of the lanthanum deficient ($La_{0.8}FeO_3$), material can be assigned to the same $LaFeO_3$ phase as previously observed. The second sextet may be caused by the same iron species as seen in the stoichiometric materials, or due to the lanthanum deficiency – it is difficult to be certain due to the similarities between the hyperfine parameters of the second sextets present in Figure 4.16 and Figure 4.17. If the second sextet is of the same structural origin as in Figure 4.16 then the lanthanum deficiency has had no appreciable effect on the iron environments of the material. Due to the iron-rich nature of this material, the formation of Fe_2O_3 may be expected as a consequence, however the high relative spectral area of sextet 2 would indicate sufficient abundance to result in distinct diffraction lines. As discussed previously, the tilt system in a perovskite material can be predicted using the Goldschmidt tolerance factor which is a function of the ionic radii of the A and B site cations, and X site anion. Where an A site is vacant, as with 20% of the lanthanum sites in this material, some form of localised distortion would be expected, whether as a deviation from the tilt system of the crystal, distortion of the FeO_6 octahedra, or in oxygen vacancies to compensate for the charge imbalance. Tilt system deviations and octahedral distortion would influence the nature of O-Fe-O intra-octahedra and Fe-O-Fe inter-octahedral bonds in terms of their strength, lengths and angles. Either of these possibilities would affect the s-electron density around the iron nucleus, resulting in a change to the magnitude of the hyperfine magnetic field. Alternatively, in the event of oxygen vacancies, the lack of the sixth Fe-O ligand in the FeO_6 octahedra would have similar effects on the iron atom. The second sextet observed in this spectrum may be due to these localised crystal deviations due to the lanthanum deficiency or may be due to some of the material being less well crystalline than the bulk, or a surface phase. If this were due to a surface phase, then it would be expected that increasing the surface area of the particles would result in an increased abundance of this phase.
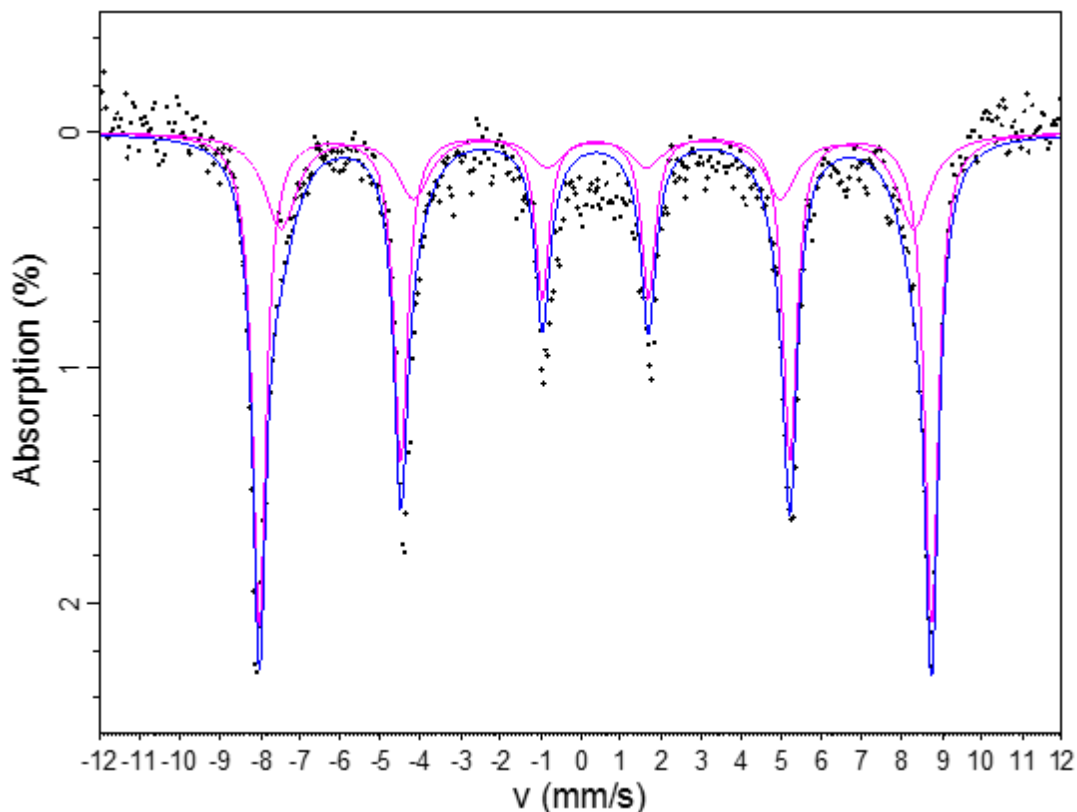
Figure 4.18. Room temperature Mössbauer spectrum of CNAC $La_{0.8}FeO_3$.

Table 4.17. Hyperfine parameters of CNAC $La_{0.8}FeO_3$ at 293 K.

	CS (mm s^{-1})	ε (mm s^{-1})	B_{eff} (T)	Γ/2 (mm s^{-1})	Area (%)
Sextet 1	0.36	0	52.0	0.21	63
Sextet 2	0.40	0	49.0	0.49	37

The hyperfine parameters of sextet 1 in Figure 4.18 of this CNAC material are consistent with $LaFeO_3$ as presented in Table 4.1 [7], [41]. Unlike the ball milled $La_{0.8}FeO_3$, the spectrum of this material can be fit sensibly using only two sites. The surface area of this material is known to be less than 20 m^2 g^{-1}, and was characterised as single phase by XRD. It is most likely that the second sextet used in this fit has the same origin as the second sextet in the ball milled $La_{0.8}FeO_3$ as they have the same composition and phase identification through XRD. The increased linewidth of the sextet in this spectrum by comparison to that of the ball milled material indicates that it is less crystalline as a result of the CNAC synthesis than the ball milling. The magnitude of the hyperfine magnetic field that the second is associated with has decreased by 0.9 T by comparison with the ball milled material. There appears to be some under-fitting occurring

around the centre of the sextets that may suggest a weak paramagnetic component that is not intense enough to be acknowledged.
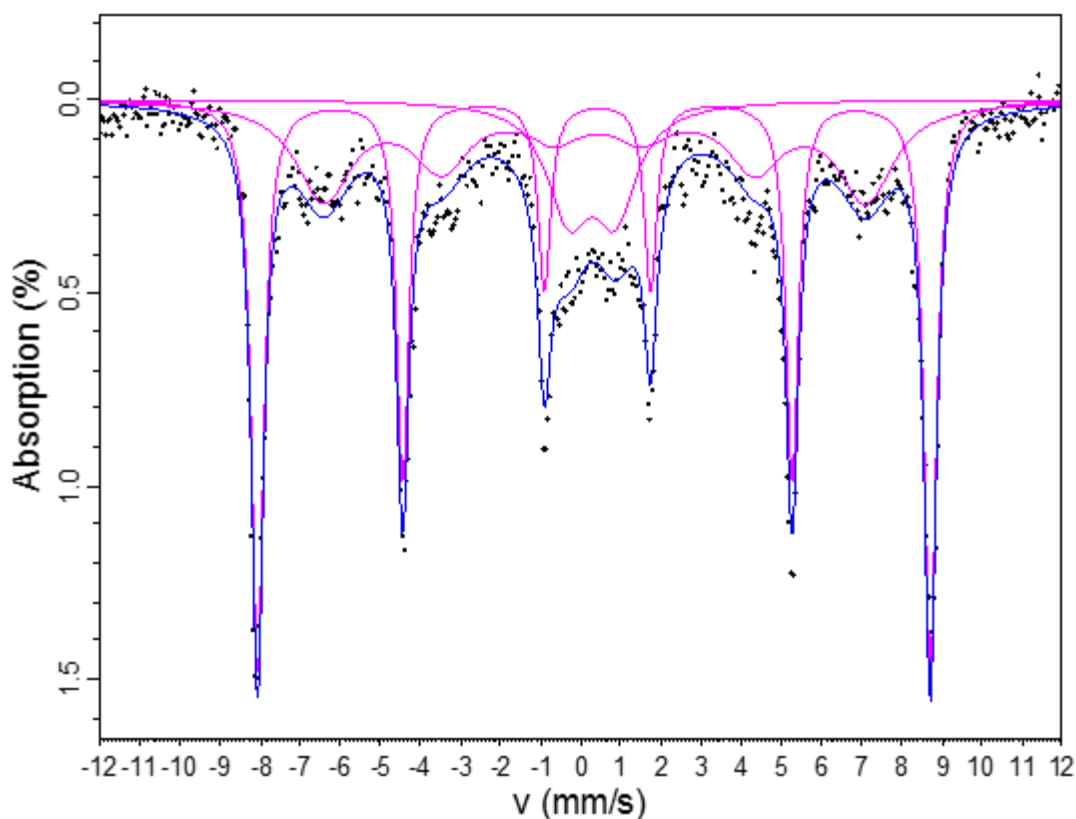

Figure 4.19. Room temperature Mössbauer spectrum of $La_{0.8}FeO_3$ synthesised by precipitation.

Table 4.18. Hyperfine parameters of precipitation $La_{0.8}FeO_3$ at 293 K.

	CS (mm s^{-1})	ε (mm s^{-1})	B$_{eff}$ (T)	Γ/2 (mm s^{-1})	Area (%)
Doublet 1	0.27	1.17	0	0.66	15.4
Sextet 1	0.37	-0.04	52.0	0.19	47.7
Sextet 2	0.39	-0.04	41.9	0.85	36.9

In the spectrum in Figure 4.19, sextet 1 can be attributed to the bulk $LaFeO_3$ phase as in previously presented spectra. The outer-most absorption lines are well fit using one sextet indicating that the second sextet seen previously, for ball milling and CNAC, is no longer necessary. The second sextet presented in this fit has a greatly reduced magnetic splitting by comparison of either the ball milled or the CNAC material. This reduction in the magnitude of the second magnetic field and the presence of the paramagnetic doublet suggests that the phase that is associated with the second sextet is losing its magnetic

ordering as the surface area of the materials increase (24 m^2 g^{-1} for precipitation). As the second phase is decreasing in magnetic ordering it simultaneously increases in abundance, with the main LaFeO$_3$ phase associated with < 50 % of the spectrum for this material. It is reasonable to believe that the second phase is therefore due to a surface phase, as between the materials discussed thus far the principal difference is their surface area, and by extension their particle size. The SHU LaFeO$_3$ should have a low surface area, due to the sintering process at 1200 °C and is readily fit using one sextet.
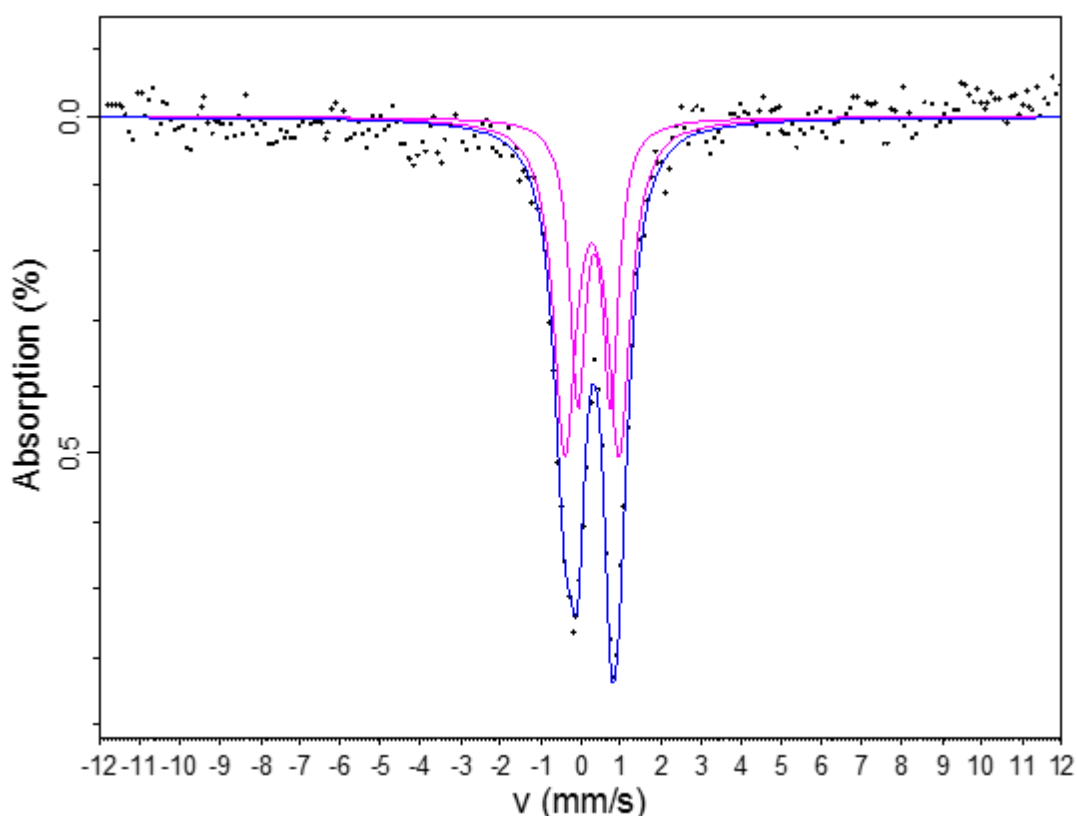

Figure 4.20. Room temperature Mössbauer spectrum of La$_{0.8}$FeO$_3$ synthesised by flame spray pyrolysis.

Table 4.19. Hyperfine parameters of FSP La$_{0.8}$FeO$_3$ at 293 K.

	CS (mm s^{-1})	QS (mm s^{-1})	Γ/2 (mm s^{-1})	Area (%)
Doublet 1	0.27	1.35	0.34	62
Doublet 2	0.33	0.82	0.24	38

The spectrum for La$_{0.8}$FeO$_3$, produced through flame spray pyrolysis in Figure 4.20 is no longer fit using a sextet, as seen in the previous spectra. Doublet 1 in this fit a is most consistent with the paramagnetic site fit in the previous

spectra, however it may be that the paramagnetic sites fit in previous spectra are a combination of both these doublets undistinguishable due to the two sextets causing absorption around the same area. As the paramagnetic site in the previous spectra was a result of the collapsing second magnetic component, doublet 1 in this spectrum can be assigned to the same iron site. If doublet 1 is attributed to the surface phase of the particles, as reasoned by its increasing abundance with increasing surface-to-bulk ratio, then doublet 2 must be associated with the bulk phase. In such small particles ($\approx$ 10.4 nm average) materials that are magnetically ordered in bulk form can become paramagnetic, as explained by Simmons; "when the particle volume is small, the relaxation time for [the] change in magnetization direction approaches the lifetime of the nuclear excited state" [130], and as shown by Vasundhara et al. with $CoFe_2O_4$ [131]. In bulk materials the direction of the magnetic spins align by interacting with one another resulting in the observed magnetic ordering, where in such small particles where the spins do not align the directions average to a net-zero field, this effect being known as superparamagnetic relaxation. Simmons was referring to work by Kündig et al. where Fe_2O_3 was studied at particles sizes < 10 nm, 13.5 nm, 15 nm and 18 nm where the reduction in particle size resulted in a transition from a single, well defined sextet reducing in magnitude, to include an Fe^{3+} doublet at intermediate particle sizes, and a single doublet at < 10 nm [132]. The same work by Kündig found that the magnetic ordering of small particles can be re-established at low temperatures, by studying the 13.5 nm materials from temperatures between 440 K and 12 K.
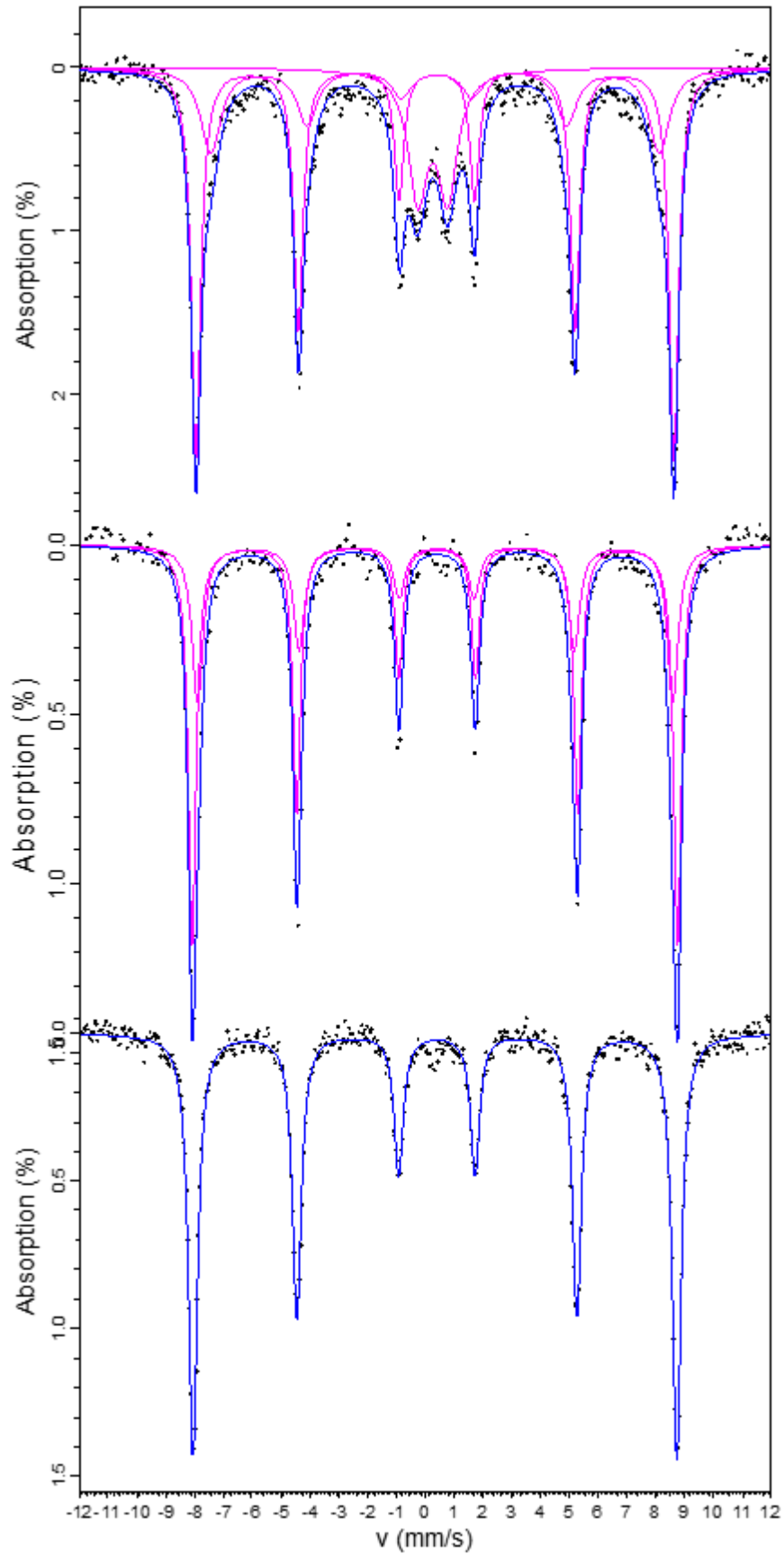
Figure 4.21. Room temperature Mössbauer spectra of LaFeO$_3$ synthesised by CNAC. F500, F700, F900, top to bottom.

Table 4.20. Hyperfine parameters of CNAC $LaFeO_3$ materials, F500, F700 and F900 at 293 K.

	CS (mm s^{-1})	ε (mm s^{-1})	B$_{eff}$ (T)	Γ/2 (mm s^{-1})	Area (%)
F500	0.26	1.03	0	0.41	18.2
	0.37	-0.03	51.4	0.20	56.2
	0.38	-0.03	48.3	0.42	25.6
F700	0.38	-0.04	52.2	0.16	65
	0.37	-0.03	51.1	0.23	35
F900	0.36	-0.04	52.1	0.20	100

When considering the samples prepared by various synthesis routes there were multiple variables to consider, including but not limited to the precursor materials, particle size, morphology, calcination temperatures, and any crystal defects as a result of the specific process. In comparing these three CNAC materials the synthesis routes were identical, apart from the final calcination temperatures of 500, 700 and 900 °C, avoiding much of the variability between synthesis routes. In the CNAC process the formation of $LaFeO_3$ is achieved in the initial reaction process between the citrate and nitrate precursors and the calcination thereafter is to improve crystallinity and grain growth, a primary reason for electing this process for a single-synthesis route study.

Through the series from F500 to 900 the particle sizes were determined by Reitveld refinement from XRD data as 18 nm, 44 nm and 150 nm, and the respective cell volumes calculated at 243.8, 243.1 and 242.9 Å. The single sextet in Figure 4.21 for F900, and the sextet with the highest magnitude in F500 and F700 are consistent with the bulk $LaFeO_3$ phase as previously observed. As the particle size increased from F500 to 900 there is a slight observable increase in the magnitude of B$_{eff}$ from 51.4 to 52.1 T. The second magnetic phase in F500 and F700 have similar parameters to that observed in the CNAC lanthanum deficient material that was calcined at 700 °C, and the paramagnetic site of F500 is similar to that in the precipitated material, however both show reduced linewidths in the F500 and F700 materials. The second sextet of the F700 spectrum has a higher B$_{eff,}$ and reduced linewidth in comparison to F500, suggesting that the increased calcination temperature causes this phase to become increasingly magnetically ordered with a greater degree of crystallinity. The 2 T increase in B$_{eff}$ between the lanthanum deficient and stoichiometric

materials, calcinated at 700 °C, suggests that the lanthanum deficiency causes a reduction in the magnitude of the magnetic field. The linewidth for the $LaFeO_3$ is consistent in all spectra indicating that the main crystal structure is not largely affected by the lanthanum deficiency or by the synthesis route. The primary differences between spectra is in the second phase which is more abundant and with a greater linewidth in materials with smaller particle size / larger surface area.
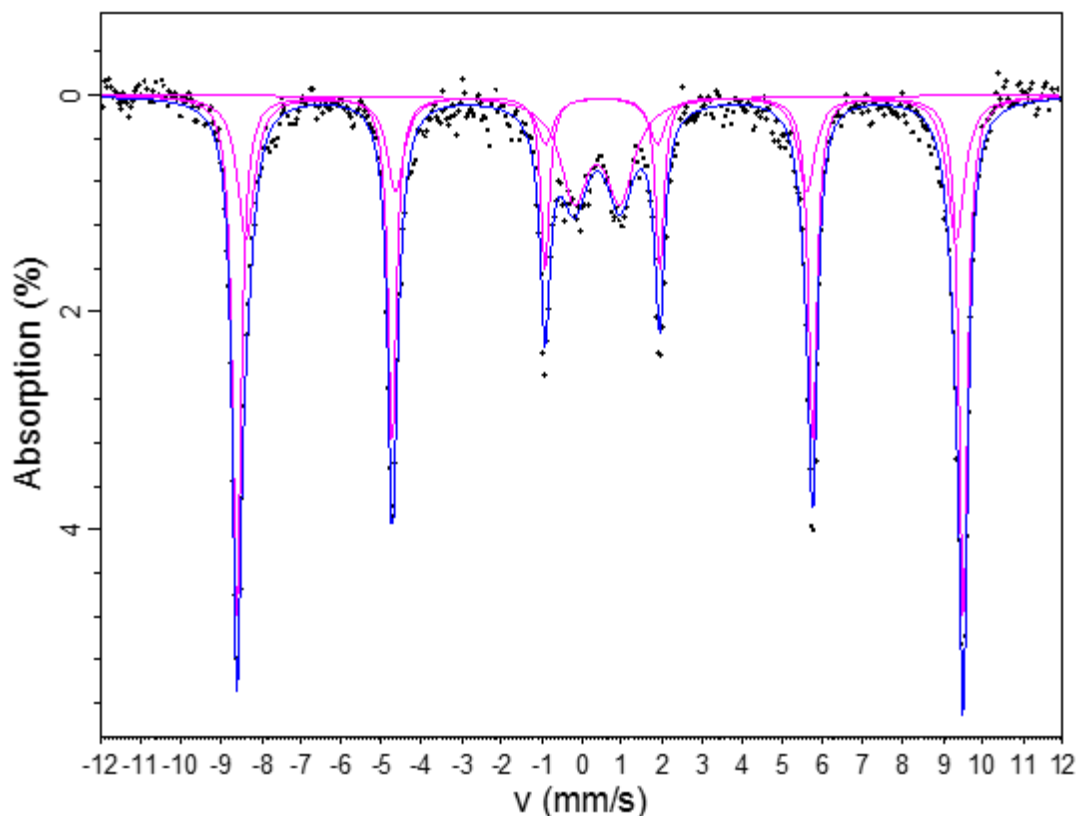

Figure 4.22. Room temperature Mössbauer spectrum of CNAC F500.

Table 4.21. Hyperfine parameters of CNAC F500 at 50 K.

	CS (mm s^{-1})	ε (mm s^{-1})	B$_{eff}$ (T)	Γ/2 (mm s^{-1})	Area (%)
Doublet 1	0.38	1.15	0	0.42	16.6
Sextet 1	0.48	-0.03	56.2	0.13	53.9
Sextet 2	0.48	0	54.9	0.26	29.5

The positive shift in CS in Table 4.21 for the spectrum in Figure 4.22 is consistent with expectations from the Debye model where CS increases non-linearly with reduced temperature [78], [83], [133]. Measuring F500 at 50 K was intended to ensure that there were no additional phases superimposed under the observed data, as different phases would shift independent of each other. The

slight decrease in spectral area associated with the paramagnetic site, and increase in the second magnetic phase may indicate that some of the paramagnetism is not observed magnetically, as expected with superparamagnetism [130], [134], however, the change in areas of these phases is small and one must take care to not over-interpret the data. The similarity between the 293 and 50 K spectra of F500 indicate that the phases fit at 293 K are accurate, and that the paramagnetic phase has not magnetically ordered into a third sextet, further suggesting that this phase, and that attributed to the second sextet, are the same, in different magnetic states. The second phase becomes more abundant with reduced particle size / increased surface area, in both the lanthanum deficient materials and the CNAC stoichiometric materials, indicating that it is a surface phase that is not observed in larger particle materials as the surface to bulk ratio is too low.

Considering the relationship between the TWC data and the presence and abundance of the second phase would indicate that the greater the surface to bulk ratio, the higher the 50% conversion temperatures which would suggest that the larger, more crystalline particles are preferential for this form of catalysis. This relationship may be due to the increased oxygen availability in larger particles, and the ability to replenish the active surface layer more readily [32]. It may be expected that a higher surface area, exposing more active surface sites, would result in greater catalytic activity, with the inverse appearing true in this instance, it would indicate that the bulk of the particles plays an important role to facilitate the surface catalysis. In service these materials would be supported on a ceramic monolith, typically composed of materials including alumina, ceria and zirconia, which provide oxygen to the catalyst as well as providing structural stability [93], [103], [109], [126].
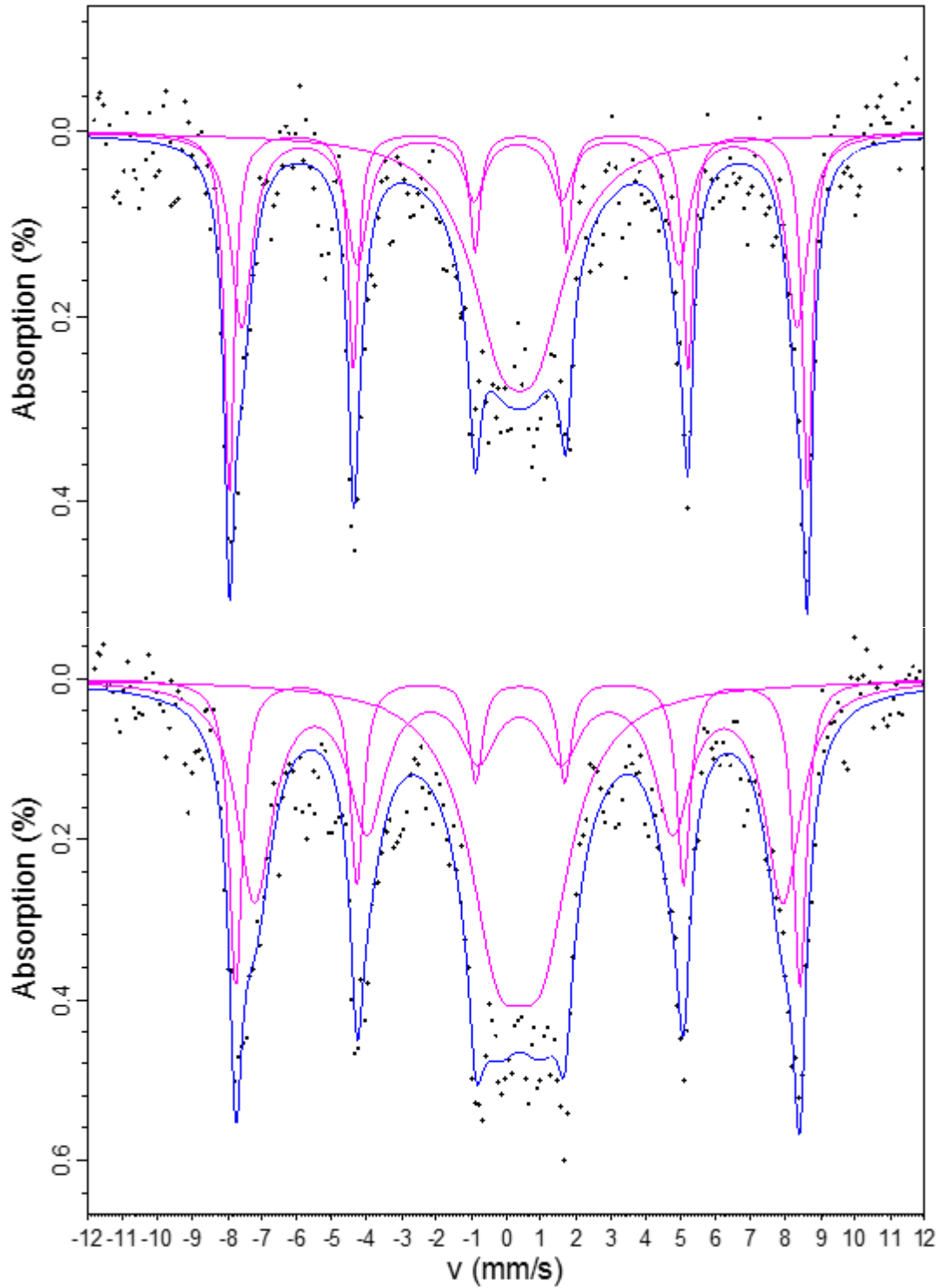
Figure 4.23. Room temperature Mössbauer spectra of FSP $La_{0.8}FeO_3$ with +5 wt% iron impregnation (top) and following an acid wash (bottom).

Table 4.22. Hyperfine parameters for FSP $La_{0.8}FeO_3$ with post-synthesis treatments, at 293 K.

	CS (mm s^{-1})	ε (mm s^{-1})	B_{eff} (T)	Γ/2 (mm s^{-1})	Area (%)
+5% Fe	0.37	1.05	0	1.08	39.3
	0.38	-0.03	51.4	0.17	28.3
	0.36	0.02	49.4	0.37	32.4
Acid wash	0.38	1.24	0	1.02	35.8
	0.37	-0.04	50.2	0.23	22
	0.38	-0.02	47.0	0.6	42

Sextet 1 presented in Table 4.22, of data presented in Figure 4.23, is considered the $LaFeO_3$ phase, and sextet 2 appears consistent with the second magnetic phase previously observed for these materials (such as the F500 material in Figure 4.21), typically having a slightly lower B_{eff}. The B_{eff} of both sextets are lower than observed previously, and linewidths are larger, suggesting that these phases are more distorted, or that the magnetic fields are not fully realised. The paramagnetic doublet applied to these fits are consistent with the paramagnetic behaviour observed for untreated FSP $La_{0.8}FeO_3$ – only one site is used here due to the increases velocity range used, and the presence of additional absorption lines from the two sextets. The iron impregnated sample presents magnetic sites with increased magnitude and reduced linewidths, compared to the acid washed material. Of the magnetic phases observed, the acid washed material has almost twice the relative spectral area attributed to the phase with the lower B_{eff}, while the iron impregnated material has these sextets with near-equal spectral area. Overall, the acid washed material appears to be less crystalline than the iron impregnated material (as evidenced by the increased linewidths and decreased B_{eff}), however both materials appear to present similar iron-bearing phases, neither presenting unique spectral features.
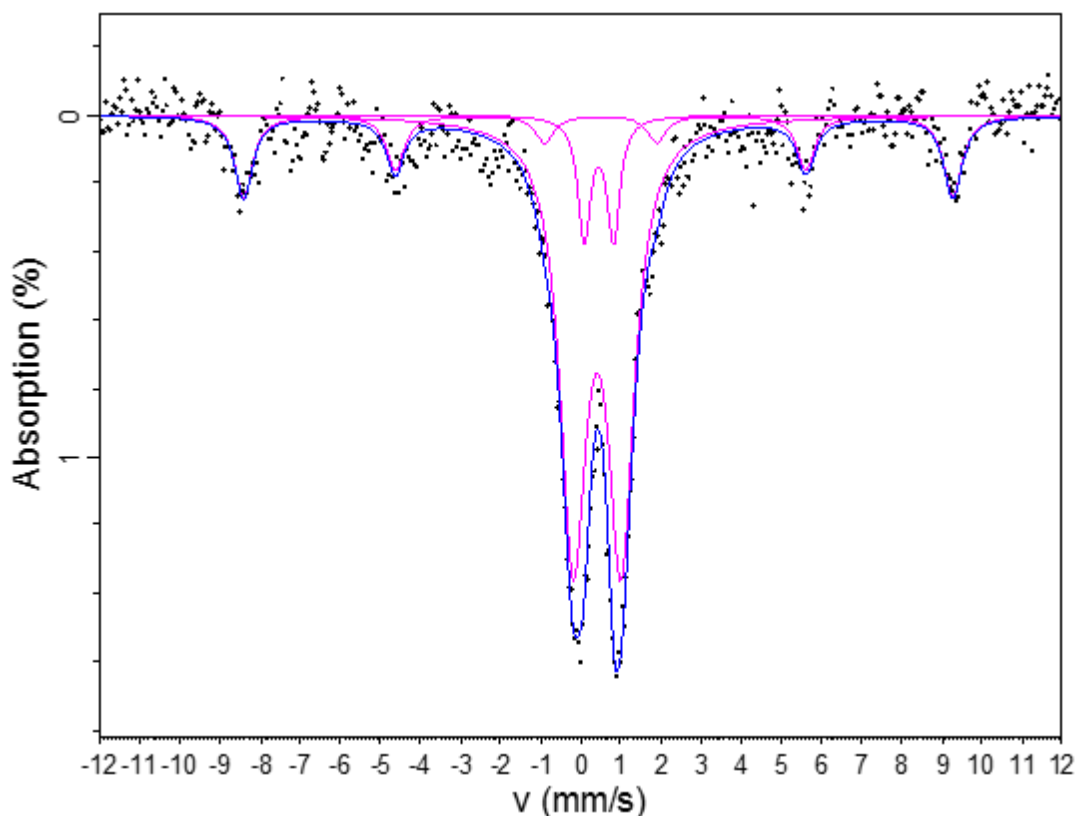
Figure 4.24. Mössbauer spectrum of FSP $La_{0.8}FeO_3$ at 50 K.

Table 4.23. Hyperfine parameters of FSP $La_{0.8}FeO_3$ at 50 K.

	CS (mm s^{-1})	ε (mm s^{-1})	B$_{eff}$ (T)	Γ/2 (mm s^{-1})	Area (%)
Doublet 1	0.41	1.20	0	0.40	71
Doublet 2	0.45	0.73	0	0.19	10
Sextet 1	0.46	-0.03	54.9	0.28	19

The hyperfine parameters of the two doublets used to fit the FSP $La_{0.8}FeO_3$ at 293 K, in Figure 4.24, (CS 0.27; 0.33 mm s^{-1}; QS 1.35, 0.82 mm s^{-1}) correspond to both doublets observed at 50 K. Both centre shifts show an increase consistent with the Debye model. It would be reasonable to assign doublets 1 and 2 in both spectra to be associated with the same iron environment, and same structural origin. Doublet 2 from the 293 K data has reduced greatly in spectral area at 50 K, where the sextet appears, consistent with bulk $LaFeO_3$, indicating that it is the phase that is magnetically ordering. If these two doublets are indicative of surface and bulk phases then it would be reasonable to believe that doublet 2, and the sextet, are associated with the bulk phase that would become magnetically ordered before the surface due to the bulk phase iron atoms being surrounded by a greater number of other iron atoms than the surface.
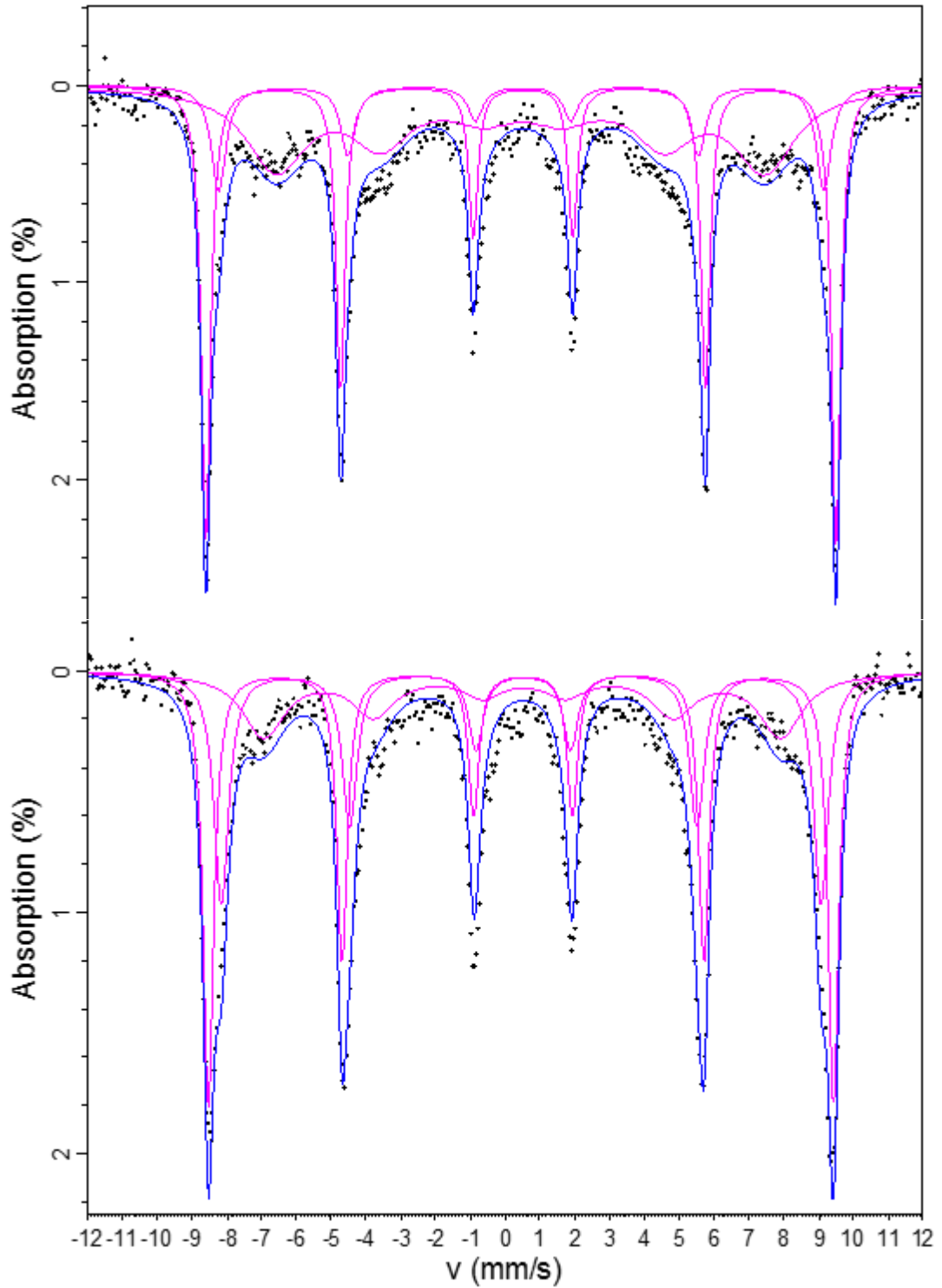
Figure 4.25. Mössbauer spectra of FSP $La_{0.8}FeO_3$ with +5 wt% iron impregnation (top) and following an acid wash (bottom), at 50 K.

Table 4.24. Hyperfine parameters for FSP $La_{0.8}FeO_3$ with post-synthesis treatments, at 50 K.

	CS (mm s^{-1})	ε (mm s^{-1})	B_{eff} (T)	Γ/2 (mm s^{-1})	Area (%)
+5% Fe	0.48	-0.03	56.1	0.16	39.2
	0.49	-0.03	53.9	0.26	14.5
	0.47	-0.03	43.5	1.06	46.2
Acid wash	0.48	-0.03	55.7	0.18	42.5
	0.49	-0.03	53.4	0.26	31.6
	0.51	-0.02	46.0	0.76	25.9

In comparing the spectra in Figure 4.25, sextets 1 and 2 are largely consistent between the two materials and are attributed to the bulk $LaFeO_3$ phase and the second sextet that has appeared in previous data. The increase in B_{eff} and CS, and reduction in linewidths are consistent with the reduced temperature. These two sextets account for 54% of the spectral area for the iron impregnated material, and 74% in the acid washed material, indicating increased abundance in the acid washed material. There are no paramagnetic sites observed for either material, which is in stark contrast to the untreated material at 50 K, presented in Figure 4.24, which was fit with 81% of its spectral area attributed to paramagnetic phases. All of the FSP materials were calcined at 650 °C, suggesting that the post-treatment calcination at 500 °C is not responsible for the differences observed in the Mössbauer spectra. Both treatments have had profound effects on the Mössbauer spectra, by comparison with the untreated material, however the differences between the spectra for the two treatments are subtle. From these data there is the suggestion that the increased abundance of sextets 1 and 2, which have been attributed to $LaFeO_3$ and the unidentified, but previously observed, second phase, may be related to the increased catalytic performance. However as these are the only two materials studied for post-synthesis treatments of FSP $La_{0.8}FeO_3$, such a claim may be speculation and further studies would be required with more materials that had been treated post-synthesis.
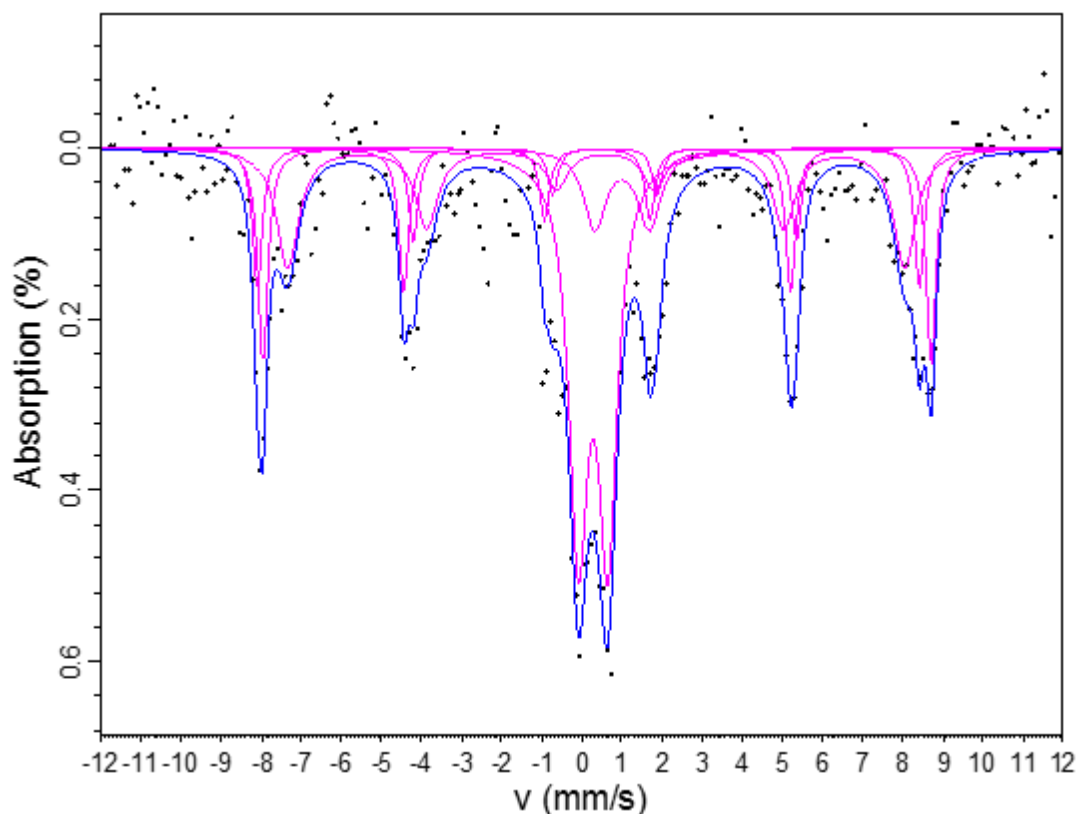
Figure 4.26. Room temperature Mössbauer spectrum of FSP $La_{0.8}FeO_3$ post-catalytic aging.

Table 4.25. Hyperfine parameters of FSP $La_{0.8}FeO_3$ post-catalytic aging, 293 K.

	CS (mm s^{-1})	ε (mm s^{-1})	B_{eff} (T)	Γ/2 (mm s^{-1})	Area (%)
Doublet 1	0.28	0.74	0	0.29	34
Doublet 2	1.00	1.35	0	0.34	8
Sextet 1	0.38	0	51.7	0.15	20
Sextet 2	0.47	-0.12	47.7	0.34	25
Sextet 3	0.37	-0.20	51.2	0.14	13

From the hyperfine parameters presented in Table 4.25, doublet 1 can be attributed to the nominal $La_{0.8}FeO_3$ paramagnetic phase previously observed as in Figure 4.20, due to this being an aged sample of the same material and the similarities between the hyperfine parameters of the two data. Doublet 2 is a previously unobserved Fe^{2+} phase that has been produced through the ageing of this catalyst material, evidencing some degree of reduction. This site may be questionable, due to the high spectral noise in this data. The hyperfine parameters of sextet 3 are consistent with those expected of α-Fe_2O_3 (CS 0.37 mm s^{-1}, ε -0.20 mm s^{-1}, B_{eff} 51.1 T [135]). Sextets 1 and 2 are not consistent with iron oxide or hydroxide phases and are consistent with the sextets observed for

similar material (see Table 4.22). This data indicates that the ageing process has caused some reduction of paramagnetic iron, and the formation of α-Fe_2O_3, in addition to some sintering of $La_{0.8}FeO_3$ resulting in sextets 1 and 2.

4.2.4 Conclusions

The materials studied as part of this work were all identified as single phase $LaFeO_3$ by X-ray diffraction, however there were significant differences observed in their catalytic performance. The aims of this work were to identify whether Mössbauer spectroscopy could impart new information into the causes of these materials' differences. By studying various materials, prepared through a number of synthesis routes, there were significant differences observed in their hyperfine structures observed with Mössbauer spectroscopy. A relationship was observed between the presence of paramagnetic iron species and the particle size of the material, suggesting the observation of surface and bulk phases. This was further supported by the study into the calcination temperatures for materials produced through one synthesis route, resulting in the observation of paramagnetic iron for the material calcined at the lowest temperature, which had the smallest particles, and wholly magnetically ordered phases in those calcined at higher temperatures, with larger particles.

Collectively, these studies were able to provide answers to some industrially relevant questions posed by the partnered industrial scientists. It has been shown that there are no iron bearing impurities, or nanoparticle iron oxides present in these materials (omitting the catalytically aged FSP $La_{0.8}FeO_3$ materials in Figure 4.26). The oxidation states and environments of the iron species of these materials have been determined, and there is evidence that surface and bulk species can be distinguished between. The relationships between these data and how they pertain to the catalytic performance has been discussed, although only lightly reported here due to confidentiality. The usefulness of Mössbauer spectroscopy for studying these catalyst materials has been realised, and further studies may be required to determine the exact nature of the active phase for catalysis.

References

[1]   G. Rose, "Beschreibung einiger neuen Mineralien des Urals," *Ann. der Phys. und Chemie*, vol. 124, no. 12, pp. 551–573, Jan. 1839.

[2]   P. M. Woodward, "Octahedral Tilting in Perovskites. I. Geometrical Considerations," *Acta Crystallogr. Sect. B Struct. Sci.*, vol. 53, no. 1, pp. 32–43, 1997.

[3]   J. B. Goodenough, "Crystallographic and magnetic properties of perovskite and perovskite-related compounds," in *Magnetic and Other Properties of Oxides and Related Compounds*, 1970, pp. 126–314.

[4]   F. J. Berry, S. Jobson, T. Zhang, and J. F. Marco, "In Situ Characterisation of Heterogeneous Catalysts by Mössbauer Spectrosopy," *Catal. Today*, vol. 9, pp. 137–143, 1991.

[5]   N. Q. Minh, "Ceramic Fuel Cells," *J. Am. Ceram. Soc.*, vol. 76, no. 3, pp. 563–588, 1993.

[6]   M. C. Carotta, G. Martinelli, Y. Sadaoka, P. Nunziante, and E. Traversa, "Gas-sensitive electrical properties of perovskite-type $SmFeO_3$ thick films," *Sensors Actuators B Chem.*, vol. 48, no. 1–3, pp. 270–276, 1998.

[7]   F. J. Berry, X. Ren, and J. F. Marco, "Reduction properties of perovskite-related rare earth orthoferrites," *Czechoslov. J. Phys.*, vol. 55, no. 7, pp. 771–780, 2005.

[8]   N. Russo, D. Mescia, D. Fino, G. Saracco, and V. Specchia, "N_2O Decomposition over Perovskite Catalysts," *Ind. Eng. Chem. Res.*, vol. 46, no. 12, pp. 4226–4231, Jun. 2007.

[9]   I. N. Sora *et al.*, "Photoelectrochemical properties of doped lanthanum orthoferrites," *Electrochim. Acta*, vol. 109, no. 3, pp. 710–715, 2013.

[10]   K. Mukhopadhyay, A. S. Mahapatra, and P. K. Chakrabarti, "Multiferroic behavior, enhanced magnetization and exchange bias effect of Zn substituted nanocrystalline $LaFeO_3$ ($La_{(1-x)}Zn_xFeO_3$, x=0.10, and 0.30)," *J. Magn. Magn. Mater.*, vol. 329, pp. 133–141, 2013.

[11]   C. Zhang *et al.*, "Multiferroicity in $SmFeO_3$ synthesized by hydrothermal method," *J. Alloys Compd.*, vol. 665, pp. 152–157, 2016.

[12]   G. M. Meyer, R. J. Nelmes, and J. Hutton, "High-resolution (direct space) studies of anharmonic motion associated with the structural phase transition in $SrTiO_3$," *Ferroelectrics*, vol. 21, pp. 461–462, 1978.

[13]   K. Momma and F. Izumi, "VESTA: A three-dimensional visualization system for electronic and structural analysis," *J. Appl. Crystallogr.*, vol. 41, no. 3, pp. 653–658, 2008.

[14]   T. Chatterji, T. C. Hansen, M. Brunelli, and P. F. Henry, "Negative thermal

expansion of ReO_3 in the extended temperature range," *Appl. Phys. Lett.*, vol. 94, no. 24, pp. 92–95, 2009.

[15] H. Xu, A. Navrotsky, Y. Su, and M. Lou Balmer, "Perovskite solid solutions along the $NaNbO_3$-$SrTiO_3$ join: Phase transitions, formation enthalpies, and implications for general perovskite energetics," *Chem. Mater.*, vol. 17, no. 7, pp. 1880–1886, 2005.

[16] M. Tyunina *et al.*, "Concurrent bandgap narrowing and polarization enhancement in epitaxial ferroelectric nanofilms," *Sci. Technol. Adv. Mater.*, vol. 16, no. 2, 2015.

[17] T. Fujii, I. Matsusue, M. Nakanishi, and J. Takada, "Formation and superparamagnetic behaviors of $LaFeO_3$ nanoparticles," *Hyperfine Interact.*, vol. 205, no. 1–3, pp. 97–100, 2012.

[18] V. M. Goldschmidt, "Die Gesetze der Krystallochemie," *Naturwissenschaften*, vol. 14, no. 21, pp. 477–485, May 1926.

[19] T. Sato, S. Takagi, S. Deledda, B. C. Hauback, and S. I. Orimo, "Extending the applicability of the Goldschmidt tolerance factor to arbitrary ionic compounds," *Sci. Rep.*, vol. 6, no. April, pp. 1–10, 2016.

[20] A. Hossain, P. Bandyopadhyay, and S. Roy, "An overview of double perovskites $A2B'B''O_6$ with small ions at A site: Synthesis, structure and magnetic properties," *J. Alloys Compd.*, vol. 740, pp. 414–427, 2018.

[21] A. Kojima, K. Teshima, Y. Shirai, and T. Miyasaka, "Organometal Halide Perovskites as Visible- Light Sensitizers for Photovoltaic Cells," *J. Am. Ceram. Soc.*, vol. 131, no. October, pp. 6050–6051, 2009.

[22] W. S. Yang, B. Park, E. H. Jung, and N. J. Jeon, "Iodide management in formamidinium-lead-halide – based perovskite layers for efficient solar cells," *Science (80-.).*, vol. 356, no. 6345, pp. 1376–1379, 2017.

[23] G. Vasta, T. J. Jackson, and E. Tarte, "Electrical properties of $BaTiO_3$ based ferroelectric capacitors grown on oxide sacrificial layers for micro-cantilevers applications," *Thin Solid Films*, vol. 520, no. 7, pp. 3071–3078, 2012.

[24] S. Zhang, F. Li, X. Jiang, J. Kim, J. Luo, and X. Geng, "Advantages and challenges of relaxor-$PbTiO_3$ ferroelectric crystals for electroacoustic transducers - A review," *Prog. Mater. Sci.*, vol. 68, pp. 1–66, 2015.

[25] D. S. Lee, M. H. Hsieh, H. E. Horng, H. C. Yang, and H. C. Chen, "Some superconducting properties of $(BaK)BiO_3$ system," *Phys. B Condens. Matter*, vol. 165–166, pp. 1561–1562, 1990.

[26] T. Arakawa, H. Kurachi, and J. Shiokawa, "Physicochemical properties of rare earth perovskite oxides used as gas sensor material," *J. Mater. Sci.*, vol. 20, no. 4, pp. 1207–1210, Apr. 1985.

[27] S. P. Simner *et al.*, "Development of lanthanum ferrite SOFC cathodes," *J. Power Sources*, vol. 113, no. 1, pp. 1–10, 2003.

[28] S. Artyukhin *et al.*, "Solitonic lattice and Yukawa forces in the rare-earth orthoferrite TbFeO₃," *Nat. Mater.*, vol. 11, no. 8, pp. 694–699, 2012.

[29] G. H. Hu, I. Umehara, X. Shuang, S. Yuan, and S. X. Cao, "Pressure Effect in Multiferroic Phase Transition of Perovskite Ferrite Crystals NdFeO₃ and ErFeO₃," *J. Phys. Conf. Ser.*, vol. 400, p. 032023, 2012.

[30] A. Panchwanee, V. R. Reddy, A. Gupta, and V. G. Sathe, "Study of spin-phonon coupling and magnetic field induced spin reorientation in polycrystalline multiferroic GdFeO₃," *Condens. Matter Mater. Sci.*, pp. 1–8, 2016.

[31] X. Niu, H. Li, and G. Liu, "Preparation, characterization and photocatalytic properties of REFeO₃ (RE=Sm, Eu, Gd)," *J. Mol. Catal. A Chem.*, vol. 232, pp. 89–93, 2005.

[32] D. Duprez, F. Can, X. Courtois, C. Batiot-dupeyrat, S. Laassiri, and H. Alamdari, "Perovskites as Substitutes of Noble Metals for Heterogeneous Catalysis : Dream or Reality," *Chem. Rev.*, vol. 114, pp. 10292–10368, 2014.

[33] N. Afifah and R. Saleh, "Synthesis, Characterization and Catalytic Properties of Perovskite LaFeO₃ Nanoparticles," *J. Phys. Conf. Ser.*, vol. 710, p. 012030, 2016.

[34] E. Haye *et al.*, "Properties of rare-earth orthoferrites perovskite driven by steric hindrance," *J. Alloys Compd.*, vol. 657, pp. 631–638, 2016.

[35] X. Wang *et al.*, "Sensing performances to low concentration acetone for palladium doped LaFeO₃ sensors," *J. Rare Earths*, vol. 34, no. 7, pp. 704–710, 2016.

[36] W. Sławiński, R. Przeniosło, I. Sosnowska, and E. Suard, "Spin reorientation and structural changes in NdFeO₃," *J. Phys. Condens. Matter*, vol. 17, pp. 4605–4614, 2005.

[37] K. Uchino, "Glory of piezoelectric perovskites," *Sci. Technol. Adv. Mater.*, vol. 16, no. 4, 2015.

[38] N. Labhasetwar *et al.*, "Perovskite-type catalytic materials for environmental applications," *Sci. Technol. Adv. Mater.*, vol. 16, no. 3, 2015.

[39] S. Yang, W. Fu, Z. Zhang, H. Chen, and C.-Z. Li, "Recent advances in perovskite solar cells: efficiency, stability and lead-free perovskite," *J. Mater. Chem. A*, vol. 5, no. 23, pp. 11462–11482, 2017.

[40] M. Kubicek, A. H. Bork, and J. L. M. Rupp, "Perovskite oxides – a review on a versatile material class for solar-to-fuel conversion processes," *J. Mater. Chem. A*, vol. 5, no. 24, pp. 11983–12000, 2017.

[41] M. M. Abou-Sekkina, M. M. El-Kersh, and O. A. Shalma, "Thermophysical properties of gamma-irradiated LaFeO₃ and YFeO₃ orthoferrites," *J. Radioanal. Nucl. Chem.*, vol. 241, no. 1, pp. 15–24, 1999.

[42]   I. B. Usman, "Synthesis and characterization of Sm-based orthoferrite compounds, $SmFe_{1-x}Mn_xO_3$," 2010.

[43]   L. A. Morales, G. Sierra-Gallego, C. A. Barrero, and O. Arnache, "Relative recoilless F-factors in $REFeO_3$ (RE = rare-earth La, Pr, Nd and Sm) orthoferrites synthesized by self-combustion method," *Mater. Sci. Eng. B Solid-State Mater. Adv. Technol.*, vol. 211, pp. 94–100, 2016.

[44]   A. Bashir *et al.*, "Structural, magnetic and electronic structure studies of $NdFe_{1-x}Ni_xO_3$ ($0 \leq x \leq 0.3$)," *J. Phys. Condens. Matter*, vol. 21, no. 32, p. 325501, 2009.

[45]   L. Li, X. Song, W. Su, Q. Wei, and Z. Kang, "The influence of substitution of Mn ions on quadrupole splitting of $EuFeO_3$ perovskite oxide," vol. 116, pp. 167–172, 1998.

[46]   S. Z. Li, Y. J. Huang, J. B. Zhu, Y. Zhang, N. Chen, and Y. F. Hsia, "XRD and Mössbauer investigation of phase segregation in $Eu_{1-x}Sr_xFeO_3$," *Phys. B Condens. Matter*, vol. 393, no. 1–2, pp. 100–104, 2007.

[47]   M. Romero, R. W. Gómez, V. Marquina, J. L. Pérez-mazariego, and R. Escamilla, "Synthesis by molten salt method of the $AFeO_3$ system (A = La , Gd) and its structural , vibrational and internal hyper fi ne magnetic fi eld characterization," vol. 443, no. Figure 1, pp. 90–94, 2014.

[48]   P. Tang, J. Zhang, M. Fu, F. Cao, and C. Lv, "Characterization and Preparation Nanosized $CeFeO_3$ by a Microwave Process," *Integr. Ferroelectr.*, vol. 146, no. July 2015, pp. 99–104, 2013.

[49]   V. Bedekar, O. D. Jayakumar, J. Manjanna, and a. K. Tyagi, "Synthesis and magnetic studies of nano-crystalline $GdFeO_3$," *Mater. Lett.*, vol. 62, pp. 3793–3795, 2008.

[50]   H. M. Rietveld, "A profile refinement method for nuclear and magnetic structures," *J. Appl. Crystallogr.*, vol. 2, no. 2, pp. 65–71, 1969.

[51]   J. Rodriguez-carvajal, "Recent advances in magnetic structure determination by neutron powder diffraction," *Phys. B*, vol. 192, pp. 55–69, 1993.

[52]   T. a. Kovats and J. C. Walker, "Mössbauer absorption in Fe57 in metallic iron from the curie point to the γ-δ Transition," *Phys. Rev.*, vol. 181, no. 1963, pp. 610–618, 1969.

[53]   D. Rancourt, "Recoil Mössbauer Spectral Analysis Software." 1998.

[54]   S. V Tsybulya, A. N. Shmakov, G. N. Kryukova, I. S. Yakovleva, and L. A. Isupova, "High temperature studies of $La_{1-x}Sr_xFeO_{3-d}$ solid solutions using synchrotron radiation," *J. Struct. Chem.*, vol. 48, no. 6, pp. 1170–1174, 2007.

[55]   C. Y. Kuo *et al.*, "K = 0 magnetic structure and absence of ferroelectricity in $SmFeO_3$," *Phys. Rev. Lett.*, vol. 113, no. 21, pp. 1–5, 2014.

[56] M. Marezio, J. P. Remeika, and P. D. Dernier, "The crystal chemistry of the rare earth orthoferrites," *Acta Crystallogr. Sect. B Struct. Crystallogr. Cryst. Chem.*, vol. 26, no. 12, pp. 2008–2022, 1970.

[57] P. Coppens and M. Eibschütz, "Determination of the crystal structure of yttrium orthoferrite and refinement of gadolinium orthoferrite," *Acta Crystallogr.*, vol. 19, no. 4, pp. 524–531, 1965.

[58] R. D. Shannon, "Revised effective ionic radii and systematic studies of interatomic distances in halides and chalcogenides," *Acta Crystallogr. Sect. A*, vol. 32, no. 5, pp. 751–767, 1976.

[59] U. Martin, H. Boysen, and F. Frey, "Neutron powder investigation of tetragonal and cubic stabilized zirconia, TZP and CSZ, at temperatures up to 1400 K," *Acta Crystallogr. Sect. B*, vol. 49, no. 3, pp. 403–413, 1993.

[60] W. Y. Lee, H. J. Yun, and J. W. Yoon, "Characterization and magnetic properties of $LaFeO_3$ nanofibers synthesized by electrospinning," *J. Alloys Compd.*, vol. 583, no. 3, pp. 320–324, 2014.

[61] S. Chanda, S. Saha, A. Dutta, and T. P. Sinha, "Raman spectroscopy and dielectric properties of nanoceramic $NdFeO_3$," *Mater. Res. Bull.*, vol. 48, no. 4, pp. 1688–1693, 2013.

[62] L. Ju, Z. Chen, L. Fang, W. Dong, F. Zheng, and M. Shen, "Sol-gel synthesis and photo-fenton-like catalytic activity of $EuFeO_3$ nanoparticles," *J. Am. Ceram. Soc.*, vol. 94, no. 10, pp. 3418–3424, 2011.

[63] M. C. Weber *et al.*, "Raman spectroscopy of rare-earth orthoferrites $RFeO_3$ (R = La, Sm, Eu, Gd, Tb, Dy)," *Condens. Matter Mater. Sci.*, vol. 3, pp. 1–9, 2016.

[64] H. C. Gupta, M. Kumar Singh, and L. M. Tiwari, "Lattice dynamic investigation of Raman and infrared wavenumbers at the zone center of orthorhombic $RFeO_3$ (R = Tb, Dy, Ho, Er, Tm) perovskites," *J. Raman Spectrosc.*, vol. 33, no. 1, pp. 67–70, 2002.

[65] S.-H. Shim and T. S. Duffy, "Raman spectroscopy of Fe_2O_3 to 62 GPa," *Am. Mineral.*, vol. 87, pp. 318–326, 2001.

[66] M. Popa, J. Frantti, and M. Kakihana, "Lanthanum ferrite $LaFeO_{3+d}$ nanopowders obtained by the polymerizable complex method," *Solid State Ionics*, vol. 154–155, pp. 437–445, 2002.

[67] N. Koshizuka and S. Ushioda, "Inelastic-light-scattering study of magnon softening in $ErFeO_3$," *Phys. Rev. B*, vol. 22, no. 11, pp. 5394–5399, Dec. 1980.

[68] V. B. Podobedov, A. Weber, D. B. Romero, J. P. Rice, and H. D. Drew, "Effect of structural and magnetic transitions in $La_{1-x}M_xMnO_3$ single crystals in Raman scattering," *Phys. Rev. B*, vol. 58, no. 1, pp. 43–46, Jul. 1998.

[69] Y. Hemberger, N. Wichtner, C. Berthold, and K. G. Nickel, "Quantification of yttria in stabilized zirconia by Raman spectroscopy," *Int. J. Appl. Ceram. Technol.*, vol. 13, no. 1, pp. 116–124, 2016.

[70] R. H. Herber, "Structure, Bonding, and the Mossbauer Lattice Temperature," in *Chemical Mössbauer Spectroscopy*, R. H. Herber, Ed. Boston, MA: Springer US, 1984, pp. 199–216.

[71] M. D. Dyar, D. G. Agresti, M. W. Schaefer, C. A. Grant, and E. C. Sklute, "Mössbauer Spectroscopy of Earth and Planetary Materials," *Annu. Rev. Earth Planet. Sci.*, vol. 34, no. 1, pp. 83–125, 2006.

[72] L. Aldon, A. Perea, M. Womes, C. M. Ionica-Bousquet, and J. C. Jumas, "Determination of the Lamb-Mössbauer factors of $LiFePO_4$ and $FePO_4$ for electrochemical in situ and operando measurements in Li-ion batteries," *J. Solid State Chem.*, vol. 183, no. 1, pp. 218–222, 2010.

[73] S. M. Dubiel, J. Cieślak, I. V. Alenkina, M. I. Oshtrakh, and V. A. Semionkin, "Evaluation of the Debye temperature for iron cores in human liver ferritin and its pharmaceutical analogue, Ferrum Lek, using Mössbauer spectroscopy," *J. Inorg. Biochem.*, vol. 140, pp. 89–93, 2014.

[74] C. Kittel, "Phonons II. Thermal Properties," in *Introduction to Solid State Physics*, Wiley India Pvt. Limited, 2007.

[75] M. Eibschütz, S. Shtrikman, and D. Treves, "Mössbauer Studies of Fe^{57} in Orthoferrites," *Phys. Rev.*, vol. 156, no. 2, pp. 562–577, 1967.

[76] S. C. Parida, S. K. Rakshit, and Z. Singh, "Heat capacities, order-disorder transitions, and thermodynamic properties of rare-earth orthoferrites and rare-earth iron garnets," *J. Solid State Chem.*, vol. 181, no. 1, pp. 101–121, 2008.

[77] E. Niwa *et al.*, "Dependence of crystal symmetry , electrical conduction property and electronic structure of $LnFeO_3$ (Ln : La , Pr , Nd , Sm) on kinds of Ln^{3+}," *J. Ceram. Soc. Japan*, vol. 3, pp. 501–506, 2015.

[78] T. L. Hill, "The Debye Approximation," in *An Introduction to Statistical Thermodynamics*, Dover Publications, 2012.

[79] R. H. Herber, A. E. Smelkinson, M. J. Sienko, and L. F. Schneemeyer, "Lattice dynamics in covalent solids: Sn in $SnS_{2-x}Se_x(0 \leq x \leq 2)$," *J. Chem. Phys.*, vol. 68, no. 8, pp. 3705–3712, 1978.

[80] J. J. Quinn and K. S. Yi, "Lattice Vibrations," in *Solid State Physics: Principles and Modern Applications*, Springer Berlin Heidelberg, 2009.

[81] J. Cieślak, S. Dubiel, J. Żukrowski, M. Reissner, and W. Steiner, "Determination of the Debye temperature of the σ-phase Fe-Cr alloys," *Phys. Rev. B*, vol. 65, no. 21, pp. 1–3, 2002.

[82] S. J. Kim, S. W. Lee, and C. S. Kim, "Mössbauer Studies on Exchange Interactions in $CoFe_2O_4$," *Jpn. J. Appl. Phys.*, vol. 40, no. Part 1, No. 8, pp. 4897–4902, 2001.

[83] M. Romero, R. Escamilla, V. Marquina, and R. Gómez, "Structural and mechanic properties of $RFeO_3$ with R = Y, Eu and La perovskites: a first-principles calculation," *Eur. Phys. J. D*, vol. 69, no. 7, 2015.

[84] M. Morishita and H. Yamamoto, "Heat capacity of $La_{1-x}Sr_xFeO_{3-delta}$ from 2 K to 1340 K," *Mater. Trans.*, vol. 48, no. 12, pp. 3109–3117, 2007.

[85] S. H. Yoon, S. J. Choi, D. J. Cha, B. K. Min, and C. S. Kim, "Effects of Ga substitution in $LaFe_{1-x}Ga_xO_3$ (x = 0, 0.1, 0.3, 0.5 and 0.7)," *J. Magn.*, vol. 7, no. 2, pp. 40–44, 2002.

[86] R. H. Wilson, E. F. Skelton, and J. L. Katz, "Measurement of the thermal variation of the X-ray Debye temperature of pure nickel and chromium," *Acta Crystallogr.*, vol. 21, no. 5, pp. 635–638, Nov. 1966.

[87] J. Kestin and J. R. Dorfman, *A Course in Statistical Thermodynamics*. New York: Academic Press, 1971.

[88] C. G. Moseley, "Eugene Houdry, catalytic cracking and World War II aviation gasoline," *J. Chem. Educ.*, vol. 61, no. 8, p. 655, 1984.

[89] E. J. Houdry, "Catalytic Converter for Exhaust Gases," 2,742,437, 1954.

[90] R. M. Heck and R. J. Farrauto, "Automobile exhaust catalysts," *Appl. Catal. A Gen.*, vol. 221, no. 1–2, pp. 443–457, 2001.

[91] European Commission, "Council Directive 91/441/EEC of 26 June 1991 amending Directive 70/220/EEC on the approximation of the laws of the Member States relating to measures to be taken against air pollution by emissions from motor vehicles," *Off. J. Eur. Communities*, vol. 242, no. L, pp. 1–106, 1991.

[92] European Commission, "Amendment No 459/2012 as regards emissions from light passenger and commercial vehicles (Euro 6)," *Off. J. Eur. Union*, vol. 2012, no. 459/2012, pp. 16–24, 2012.

[93] J. Kašpar, P. Fornasiero, and N. Hickey, "Automotive catalytic converters: Current status and some perspectives," *Catal. Today*, vol. 77, no. 4, pp. 419–449, 2003.

[94] M. Lessard, "New Reduced Platinum Catalyst for Catalytic Converters," *Thermo Fisher Scientific*, 2018. [Online]. Available: https://www.thermofisher.com/blog/metals/new-reduced-platinum-catalyst-for-catalytic-converters/. [Accessed: 03-Nov-2018].

[95] European Commission, "DIRECTIVE 98/69/EC OF THE EUROPEAN PARLIAMENT AND OF THE COUNCIL of 13 October 1998 relating to measures to be taken against air pollution by emissions from motor vehicles and amending Council Directive 70/220/EEC," *Off. J. Eur. Communities*, vol. 350, 1998.

[96] European Commission, "DIRECTIVE 2002/51/EC OF THE EUROPEAN PARLIAMENT AND OF THE COUNCIL of 19 July 2002 on the reduction of the level of pollutant emissions from two- and three-wheel motor

vehicles and amending Directive 97/24/EC," *Off. J. Eur. Communities*, vol. 252, no. June, 2002.

[97]   European Commission, "REGULATION (EC) No 715/2007 OF THE EUROPEAN PARLIAMENT AND OF THE COUNCIL of 20 June 2007 on type approval of motor vehicles with respect to emissions from light passenger and commercial vehicles (Euro 5 and Euro 6) and on access to vehicle repair and mai," *Off. J. Eur. Union*, vol. L171, no. December 2006, pp. 1–16, 2007.

[98]   R. J. Farrauto and R. M. Heck, "Catalytic converters: state of the art and perspectives," *Catal. Today*, vol. 51, no. 3–4, pp. 351–360, 1999.

[99]   B. I. Whittington, C. J. Jiang, and D. L. Trimm, "Vehicle exhaust catalysis: I. The relative importance of catalytic oxidation, steam reforming and water-gas shift reactions," *Catal. Today*, vol. 26, no. 1, pp. 41–45, 1995.

[100]   S. Golunski, H. A. Hatcher, R. R. Rajaram, and T. J. Truex, "Origins of low-temperature three-way activity in Pt/CeO_2," *Appl. Catal. B, Environ.*, vol. 5, no. 4, pp. 367–376, 1995.

[101]   P. B. Kettler, "Platinum group metals in catalysis: Fabrication of catalysts and catalyst precursors," *Org. Process Res. Dev.*, vol. 7, no. 3, pp. 342–354, 2003.

[102]   E. Helmers and N. Mergel, "Platinum and rhodium in a polluted environment: studying the emissions of automobile catalysts with emphasis on the application of CSV rhodium analysis," *Fresenius. J. Anal. Chem.*, vol. 362, no. 6, pp. 522–528, Nov. 1998.

[103]   A. F. Diwell, R. R. Rajaram, H. A. Shaw, and T. J. Truex, "The role of ceria in three-way catalysts," *Stud. Surf. Sci. Catal.*, vol. 71, no. C, pp. 139–152, 1991.

[104]   L. Lan, S. Chen, Y. Cao, M. Zhao, M. Gong, and Y. Chen, "Preparation of ceria-zirconia by modified coprecipitation method and its supported Pd-only three-way catalyst," *J. Colloid Interface Sci.*, vol. 450, pp. 404–416, 2015.

[105]   C. Wang, T. Zheng, J. Lu, X. Wu, H. Hochstadt, and Y. Zhao, "Three-way catalytic reactions on Rh-based catalyst: Effect of Rh/ceria interfaces," *Appl. Catal. A Gen.*, vol. 544, no. June, pp. 30–39, 2017.

[106]   J. Cooper and J. Beecham, "A study of platinum group metals in three-way autocatalysts," *Platin. Met. Rev.*, vol. 57, no. 4, pp. 281–288, 2013.

[107]   C. Barker, "Origin, Composition and Properties of Petroleum," *Dev. Pet. Sci.*, vol. 17, no. PA, pp. 11–45, Jan. 1985.

[108]   K. C. Taylor, "Nitric Oxide Catalysis in Automotive Exhaust Systems," *Catal. Rev.*, vol. 35, no. 4, pp. 457–481, Dec. 1993.

[109]   J. Kašpar, P. Fornasiero, and M. Graziani, "Use of CeO_2-based oxides in the three-way catalysis," *Catal. Today*, vol. 50, no. 2, p. 285, 1999.

[110] G. Li, B. Wu, and L. Li, "Surface-structure effect of nano-crystalline CeO_2 support on low temperature CO oxidation," *J. Mol. Catal. A Chem.*, vol. 424, pp. 304–310, 2016.

[111] K. Ravindra, L. Bencs, and R. V Grieken, "Platinum group elements in the environment and their health risk," *Sci. Total Environ.*, vol. 318, no. 1–3, pp. 1–43, 2004.

[112] C. Barbante *et al.*, "Greenland snow evidence of large scale atmospheric contamination for platinum, palladium, and rhodium," *Environ. Sci. Technol.*, vol. 35, no. 5, pp. 835–839, 2001.

[113] M. Alifanti, N. Blangenois, M. Florea, and B. Delmon, "Supported Co-based perovskites as catalysts for total oxidation of methane," *Appl. Catal. A Gen.*, vol. 280, no. 2, pp. 255–265, 2005.

[114] H. Wang, C. Tablet, T. Schiestel, S. Werth, and J. Caro, "Partial oxidation of methane to syngas in a perovskite hollow fiber membrane reactor," *Catal. Commun.*, vol. 7, no. 11, pp. 907–912, 2006.

[115] J. Faye, E. Guélou, J. Barrault, J. M. Tatibouët, and S. Valange, "$LaFeO_3$ perovskite as new and performant catalyst for the wet peroxide oxidation of organic pollutants in ambient conditions," *Top. Catal.*, vol. 52, no. 9, pp. 1211–1219, 2009.

[116] T. Asada, T. Kayama, H. Kusaba, H. Einaga, and Y. Teraoka, "Preparation of alumina-supported $LaFeO_3$ catalysts and their catalytic activity for propane combustion," *Catal. Today*, vol. 139, no. 1, pp. 37–42, 2008.

[117] X. Li, C. Tang, M. Ai, L. Dong, and Z. Xu, "Controllable synthesis of pure-phase rare-earth orthoferrites hollow spheres with a porous shell and their catalytic performance for the CO + NO reaction," *Chem. Mater.*, vol. 22, no. 17, pp. 4879–4889, Sep. 2010.

[118] S.-T. Shen and H.-S. Weng, "Comparative Study of Catalytic Reduction of Nitric Oxide with Carbon Monoxide over the $La_{1-x}Sr_xBO_3$ (B = Mn, Fe, Co, Ni) Catalysts," *Ind. Eng. Chem. Res.*, vol. 37, no. 7, pp. 2654–2661, Jul. 1998.

[119] S. Colonna, S. De Rossi, M. Faticanti, I. Pettiti, and P. Porta, "XAS characterization and CO oxidation on zirconia-supported $LaFeO_3$ perovskite," *J. Mol. Catal. A Chem.*, vol. 187, no. 2, pp. 269–276, 2002.

[120] S. Varma, B. N. Wani, and N. M. Gupta, "Redox behavior and catalytic activity of La–Fe–V–O mixed oxides," *Appl. Catal. A Gen.*, vol. 241, no. 1, pp. 341–348, 2003.

[121] A. A. Leontiou, A. K. Ladavos, and P. J. Pomonis, "Catalytic NO reduction with CO on $La_{1-x}Sr_x(Fe^{3+}/Fe^{4+})O_{3\pm\delta}$ perovskite-type mixed oxides (x = 0.00, 0.15, 0.30, 0.40, 0.60, 0.70, 0.80, and 0.90)," *Appl. Catal. A Gen.*, vol. 241, no. 1, pp. 133–141, 2003.

[122] A. P. E. York, C. S. Cooper, K. Simmance, and S. K. Wilkinson, "Performance of a Non-Platinum Group Metal Perovskite Catalyst for Gasoline Emissions Control : Kinetics , Reaction Mechanism and Catalyst Sizing Study," in *The 25th International Symposium on Chemical Reaction Engineering*, 2018, pp. 1–2.

[123] National Centre for Scientific Research "Demokritos," "Final Report Summary - NEXT-GEN-CAT," 2016.

[124] K. Huang *et al.*, "Engineering the surface of perovskite $La_{0.5}Sr_{0.5}MnO_3$ for catalytic activity of CO oxidation," *Chem. Commun.*, vol. 50, no. 65, pp. 9200–9203, 2014.

[125] Y. Chen, V. Sima, W. Lin, J. Sterniak, and S. V. Bohac, "Lean HCCI/Rich SACI Gasoline Combustion Cycling and Three-Way Catalyst for Fuel Efficiency and NO_x Reduction," *Jounal Eng. Gas Turbines Power*, vol. 137, no. 12, p. V001T04A005, 2015.

[126] H.-Y. Chen and H.-L. R. Chang, "Development of Low Temperature Three-Way Catalysts for Future Fuel Efficient Vehicles," *Johnson Matthey Technol. Rev.*, vol. 59, no. 1, pp. 64–67, 2015.

[127] a. a. Leontiou, a. K. Ladavos, T. V. Bakas, T. C. Vaimakis, and P. J. Pomonis, "Reverse uptake of oxygen from $La_{1-x}Sr_x(Fe^{3+}/Fe^{4+})O_{3\pm\delta}$ perovskite-type mixed oxides (x = 0.00, 0.15, 0.30, 0.40, 0.60, 0.70, 0.80, 0.90)," *Appl. Catal. A Gen.*, vol. 241, pp. 143–154, 2003.

[128] E. Zepeda-Alarcon *et al.*, "Magnetic and nuclear structure of goethite (α-FeOOH): A neutron diffraction study," *J. Appl. Crystallogr.*, vol. 47, no. 6, pp. 1983–1991, 2014.

[129] H. Christensen and A. N. Christensen, "Hydrogen Bonds of γ-FeOOH," *Acta Chem. Scand.*, vol. 32, pp. 87–88, 1978.

[130] R. L. Cohen, *Applications of Mossbauer Spectroscopy*. Elsevier Science, 2012.

[131] K. Vasundhara, S. N. Achary, S. K. Deshpande, P. D. Babu, S. S. Meena, and A. K. Tyagi, "Size dependent magnetic and dielectric properties of nano $CoFe_2O_4$ prepared by a salt assisted gel-combustion method," *J. Appl. Phys.*, vol. 113, no. 19, 2013.

[132] W. Kundig and H. Bommel, "Some Properties of Supported Small alpha-Fe_2O_3 Particles Determined with the Mossbauer Effect," *Phvsical Rev.*, vol. 59, no. 1965, p. 327, 1966.

[133] A. Scrimshire *et al.*, "Determination of Debye temperatures and Lamb–Mössbauer factors for $LnFeO_3$ orthoferrite perovskites (Ln = La, Nd, Sm, Eu, Gd)," *J. Phys. Condens. Matter*, vol. 30, p. 105704, 2018.

[134] J. A. Ramos Guivar *et al.*, "Mössbauer study of intermediate superparamagnetic relaxation of maghemite (γ-Fe_2O_3) nanoparticles," *Hyperfine Interact.*, vol. 224, no. 1–3, pp. 89–97, 2014.

[135] S. J. Oh, D. C. Cook, and H. E. Townsend, "Characterization of iron oxide commonly formed as corrosion products on steel," *Hyperfine Interactions*, vol. 112. pp. 59–65, 1998.

5. Iron Carbide Catalysts for Fischer-Tropsch Synthesis

5.1. Introduction

The topics surrounding climate change, global warming and the longevity of fossil fuel use are often cause for political controversy and debate. The Yale Program on Climate Change Communication and the George Mason Center for Climate Change Communications, using public opinion data on climate change from 2008 to 2016, estimated that 70% of United States citizens believed that global warming was happening, and 12% not actively believing [1]. From the same estimations, only 53% of Americans believed that global warming was mostly caused by humans and 28% opposed this stance; 50% of Americans were estimated to have believed that global warming will personally affect them "little / not at all". The effects of climate change can be seen in many different ways, where the most commonly perceived effect is an increase in the average global temperature, which has increased 0.8 °C in 2010, since 1880, according to NASA's Goddard Institute for Space Studies [2], [3]. Arctic Climate Impact Assessment reported the greatest effect of global warming to be around the Arctic, where parts of Canada, Russia and Alaska in 2004 had witnessed an average temperature increase of twice the global average [4]. The melting of polar ice caps is synonymous with climate change, being reported by NASA, National Geographic, universities and newspapers alike. The loss of sea ice would not only see the displacement and endangering of the indigenous species, but also a rise in sea water levels and release of gaseous CO_2, CH_4 and O_2 frozen in the ice [5]. The importance of climate change is reflected in the 195 member nations (as of November 2017) signed into the Paris Climate Accord, wherein 2 °C is the upper limit of acceptable average temperature increase and the control of greenhouse gases in a primary course of action to achieve this goal [6]. The release of the most abundant major greenhouse gas, CO_2 (76% of greenhouse gas emissions in 2010 [7]), comes primarily from industrial processes, including electricity generation from burning fuels. Reduction in CO_2 emissions are focused around the reduction of energy consumption by industries and consumers, by recycling where appropriate, and by eating more locally produced foods. The United States Environmental Protection Agency states that an estimated 13% of greenhouse gas emissions is attributed to the production and transportation of

food [8]. A clear increase in the amount of N_2O, CH_4 and CO_2 being emitted can be closely tied to the turn of the 19th century, and the Industrial Revolution, as shown by the Intergovernmental Panel on Climate Change (IPCC) in their 2007 report [9], an illustration of which is shown in Figure 5.1. Analysis of the CO_2 in Antarctic ice cores in a 2012 report in Global Biogeochemical Cycles corroborate the sharp incline in CO_2 since $\approx$ 1750 – 1800 [10].
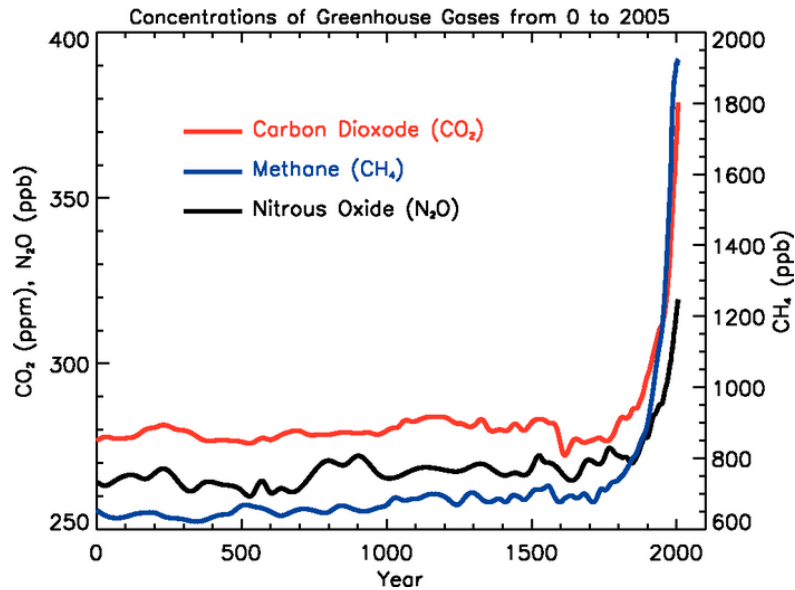

Figure 5.1. Excerpt from IPCC 2007 report on climate change; concentrations of greenhouse gases from 0 to 2005 [9].
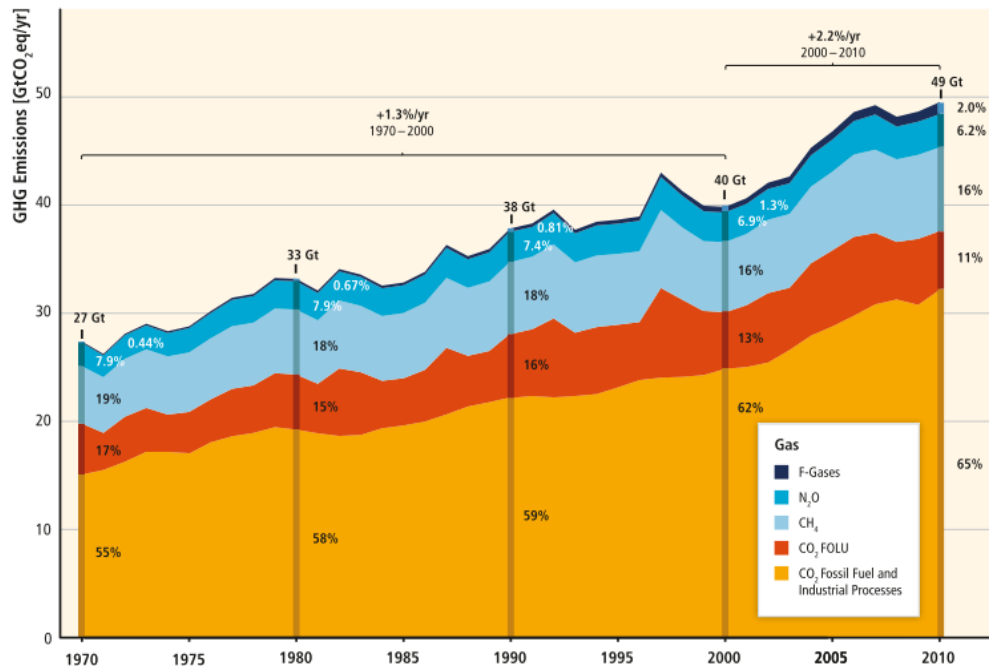
Figure 5.2. Total Annual Anthropogenic GHG Emissions by Groups of Gases 1970 – 2010, from the IPCC 2014 report [7].

The use of biodiesel is one route for reducing the overall CO_2 emissions, as the CO_2 that burning these produces is offset by the CO_2 that is absorbed by the growth of the feedstock, such as soy plants. A comprehensive study of biodiesels, by the Environmental Protection Agency in 2002 suggests that using biodiesel, either wholly or in a blended fuel with conventional diesel, causes a clear decrease in CO, unburnt hydrocarbon and particulate matter emission (to -48%, -67% and -47% respectively, at 100% biodiesel), although accompanied by a slight increase in NO_X emissions (≤ +10%) [11]. A 2014 article in *Energies* reports a 30:70 blend of biodiesel and conventional diesel to result in CO emission reduction of 83%, and a 33% reduction in particulate matter, with the increase in NO_x emissions as previously reported [12]. As a fuel source, as of 2014, conventional diesels had an energy density of ≈ 36 MJ/L, which was slightly higher than that of biodiesels at ≈ 33 MJ/L [13]. One of the more prominent reasons for an interest in biodiesels is that they are a form of renewable energy, not relying on the ever-decreasing amount of fossil fuels. The 2016 BP Statistical Review of World Energy shows that biofuel production has increased from 19.7 to 74.8 million tonnes oil equivalent from 2005 to 2015, and that approximately 14% of primary energy was produced using non-fossil fuel sources in 2015 [14]. Global consumption of biodiesel in 2014 was 8.1 billion gallons according to the U.S. Energy Information Administration, an increase from 0.3 billion gallons in 2001 [15].

Fischer-Tropsch synthesis (FTS) is one route for producing biofuels from biomass feedstocks. Historically used for the production of liquid fuels from coal or natural gas (solid-to-liquid and gas-to-liquid respectively), Fischer-Tropsch synthesis is the conversion of carbon monoxide and hydrogen to hydrocarbons and water [16]–[18]. The Fischer-Tropsch synthesis process occurs, over suitable catalysts, in the gas phase, requiring the feedstock to first be gasified to produce synthesis gas (*syngas*) which is first cleaned, and sulphur filtered. The products are separated by hydrocarbon chain length, as shorter chain products will be gaseous olefins, liquid products are of medium chain lengths and longer chains produce solid waxes. The products of the process can be controlled as a function of operating pressure and temperature, as well as the catalysts used. Greater temperatures and pressures will favour more rapid reactions, resulting in the

production of shorter hydrocarbon chains [19], and since the subsequent cracking of hydrocarbon chains is a simpler process, it is more common that longer chains are desired. A bio-gasoline has hydrocarbon chains of C_5 to C_{11}, and bio-diesels are C_{12} to C_{20}, and C_{20+} are waxy solids [20]. The overall reaction of Fischer-Tropsch synthesis can be considered as;

$$n\text{CO} + (2n+1)\text{H}_2 \rightarrow \text{C}_n\text{H}_{2n+2} + n\text{H}_2\text{O}$$
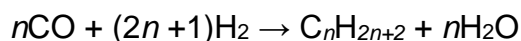
Most industrial Fischer-Tropsch catalysts are iron and cobalt based [21], [22]. Ruthenium and nickel are both also active catalysts for Fischer-Tropsch, however the cost of ruthenium and the high selectivity for methane production of nickel make these less desirable catalysts [23]. Iron catalysts are reported to be preferable over cobalt where the feedstock is biomass or coal based: where cobalt catalysts excel is when natural gas is used [24]. Of the iron-based catalysts, iron carbides have been shown to play active roles in catalysing the hydrogenation of carbon monoxide for Fischer-Tropsch synthesis [18], [25]–[29]. The exact mechanism of how these carbides catalyse the reactions is still not fully understood [23], [30]. It is believed that the Hägg carbide (Fe_5C_2) is a more active catalyst phase of the iron carbides, and that cementite (Fe_3C) is less active [18], [31]. As cementite is a more stable iron carbide phase, the high temperature, high pressure reactions of Fischer-Tropsch synthesis cause the higher carbon : iron ratio phases to form cementite over time.

Table 5.1. Characteristics of iron carbide phases [29], [32]

	Formula	Atomic ratio (C : Fe)	Crystal lattice	Interstitial occupation of carbon atoms	Wt% C
ε	Fe_2C	0.5	hcp to monoclinic	Octahedral	9.7
ε'	$Fe_{2.2}C$	0.45	hcp	Octahedral	8.9
	Fe_7C_3	0.43	Orthorhombic	Trigonal prismatic	8.4
χ	Fe_5C_2	0.4	Monoclinic	Trigonal prismatic	7.9
θ	Fe_3C	0.33	Orthorhombic	Trigonal prismatic	6.7

Aside from Fischer-Tropsch synthesis, iron carbides are important materials for applications including engineering, for steels [33] and electromagnetism [34], and in biomedicine for magnetic resonance imaging [35] and magnetic hyperthermia [36]. In this chapter we consider iron carbide FTS

catalysts, considering near phase-pure Fe_3C and Fe_5C_2 materials, their Mössbauer spectral responses to temperatures from 10K to 293 K, and how these phases appear in multi-phase industrially relevant catalyst samples.

Mössbauer spectroscopic studies of Fe_3C and Fe_5C_2 have been conducted previously, the resulting room temperature data from which is summarised in Table 5.2 and Table 5.3. The purpose of conducting our own independent studies is to allow for the temperature range mentioned to be investigated, and to provide data relevant for the particle sizes of the materials produced. Superparamagnetic doublets in nanoparticles, or ferromagnetic sextets for larger particles can be expected for Fe_3C. The nanoparticle Mössbauer spectroscopy doublet may present as a sextet with decreased temperature at or above 60 K [37]. Data for Fe_5C_2 suggests that magnetic ordering should remain, even in nanoparticles, reportedly up to its Curie temperature of 521 K [38].

Table 5.2. Summary of room temperature hyperfine parameters for Fe_3C from existing literature. (a) represents superparamagnetic nanoparticles, (b) represents ferromagnetic particles, a change induced by varied synthesis parameters. (c) after annealing amorphous product at 873 K for 2 hours.

Fe_3C

Synthesis	CS (mm s^{-1})	QS (mm s^{-1})	B_{eff} (T)	Source
Citrate-nitrate	0.45	-	21.2	[39]
Laser pyrolysis	0.18	0.42	0.0	[37] (a)
Laser pyrolysis	0.19	0.01	20.5	[37] (b)
Alloying	0.44	-	20.8	[40]
Sonochemical	0.20	-	21.1	[41] (c)
Solid-state	0.21	0.03	20.6	[42]

Table 5.3. Summary of room temperature hyperfine parameters for Fe_5C_2 from existing literature.

Fe_5C_2

Synthesis	CS (mm s^{-1})	QS (mm s^{-1})	B$_{eff}$ (T)	Source
Solid-state	0.18	0.01	17.9	[42]
Solid-state	0.18	0.01	11.2	[42]
Citrate-nitrate	0.43	-	18.9	[39]
Citrate-nitrate	0.51	-	21.8	[39]
Citrate-nitrate	0.47	-	11.0	[39]
Carburation	0.23	0.04	21.6	[38]
Carburation	0.20	0.05	18.5	[38]
Carburation	0.17	-0.12	18.5	[38]

5.2 Research Objectives

The main objectives of this work were to characterise nanoparticles of two iron carbide forms, Fe_3C and Fe_5C_2, that are of great industrial importance. In the context of this work the application of iron carbides as FTS catalysts was explored, however their applications are varied across different fields of interest including medicine and metallurgy. The aim of this work was to use Mössbauer spectroscopy to determine the hyperfine structure of these iron carbide nanoparticles, with the goal of enabling their identification in mixed-phase catalyst systems. The Fe_5C_2 iron carbide is believed to be the more active phase, and Fe_3C the less active and more thermodynamically stable [43]. Phase transformations through service, the effect of catalyst promotors and dopants, and changes to the support matrices may be viable subsequent studies, provided that these important iron carbide phases can be identified and distinguished between. The hyperfine structures of the two near phase-pure iron carbide samples, Fe_3C and Fe_5C_2 are to be thoroughly characterised by Mössbauer Spectroscopy over a temperature range of 10 to 293 K. Resulting data can be used to determine the Debye temperature and recoil-free fraction of these phases and allow for their identification in mixed phase materials. Phase changes induced by the reduced temperature can also be observed. Probing the hyperfine structure of two samples of the "state-of-the-art" JMFT material (Johnson Matthey Fischer-Tropsch), pre- and post-catalysis may yield information regarding the iron

carbide phase presence and abundance, with quantification made possible by the determination of their recoil-free fractions. Iron phases (carbide or otherwise) identified in these materials may also yield useful information regarding the ageing mechanisms of this material, with the overall objective to supply evidence for which phases are more active and which are a product of deactivation. This may provide industrially relevant information for the phases that should be promoted in these catalysts.

5.3 Material Characterisation

The synthesis routes of the Fe_3C and Fe_5C_2 near phase-pure nanoparticle samples, detailed in *Materials Synthesis and Characterisation*, were the thermal decomposition of Fe (III) acetate in gelatine [44] and the bromide-induced decomposition of iron pentacarbonyl under N_2 flow [41], [45] respectively. Both syntheses were carried out at JMTC, by the author, and subsequently characterised by the JMTC analytical department. The commercial, state-of-the-art, JMFT material was synthesised through precipitation of iron and copper salts in a sodium-containing base, as outlined in a 2013 patent application [46], and studied previously [47]–[49]. The catalyst base was precipitated, before the addition of a silica support precursor and a post-synthesis treatment of potassium. An aged sample of JMFT has also been analysed, where the aging consisted of a gas feed of H_2 and CO in a 2:1 ratio, at 210 ˚C and 20 bar pressure, for 100 hours.

The XRD data collected at JMTC for the Fe_3C and Fe_5C_2 samples, presented with theoretical XRD patterns for each phase [50], [51], are shown in Figure 5.3 and Figure 5.4.

The experimental and theoretical data for the Fe_3C sample show close agreement with each other, and with orthorhombic *pnma* space group (PDF #00-035-0772). Rietveld refinement of the Fe_3C data suggests 1.92% metallic iron. High resolution transmission electron microscope images, in Figure 5.5 and Figure 5.6 show the core-shell structure of an Fe_5C_2 nanoparticle with monoclinic

Fe_5C_2 core and a cubic Fe_3O_4 shell. The high linewidth of the Fe_5C_2 diffraction peaks is due to presence of amorphous phases of iron carbides and oxides [40]. Diffraction peaks associated with Fe_5C_2 (PDF 04-014-4562) can be observed in this diffractogram, consistent with existing literature [39], [47], [51].

The material considered "state-of-the-art" (JMFT) was synthesised with a nominal precursor composition of; Fe_2O_3 78.4 wt%, CuO 3.4 wt%, K_2O 2.6 wt%, Na_2O 0.04 wt%, SiO_2 15 wt%. XRD analysis of this material, which cannot be reproduced, revealed little about the phases present due to the highly amorphous nature of this material causing a large "amorphous hump" in the diffraction pattern, caused by diffuse scattering. This observation appears consistent with existing literature on this type of material [48], [49].
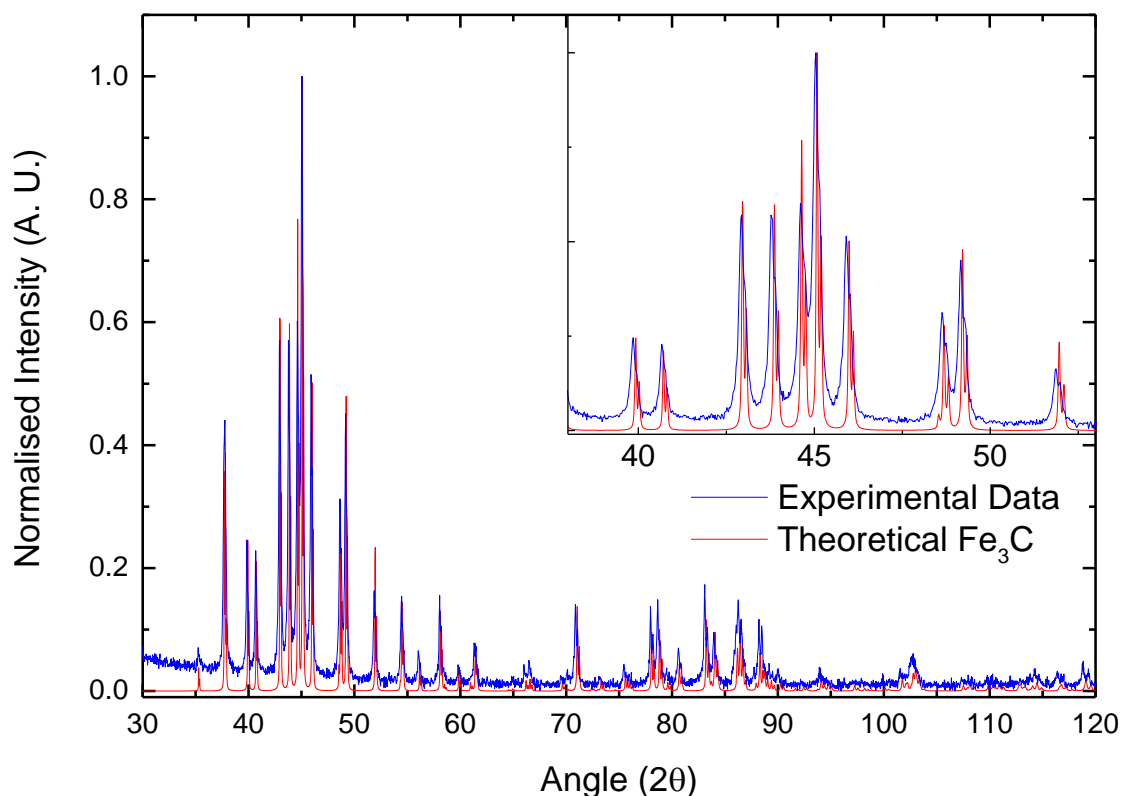
Figure 5.3. Experimental XRD data (blue) for the Fe₃C sample with theoretical pattern (red) from ICSD data [50]. (PDF 00-035-0772).
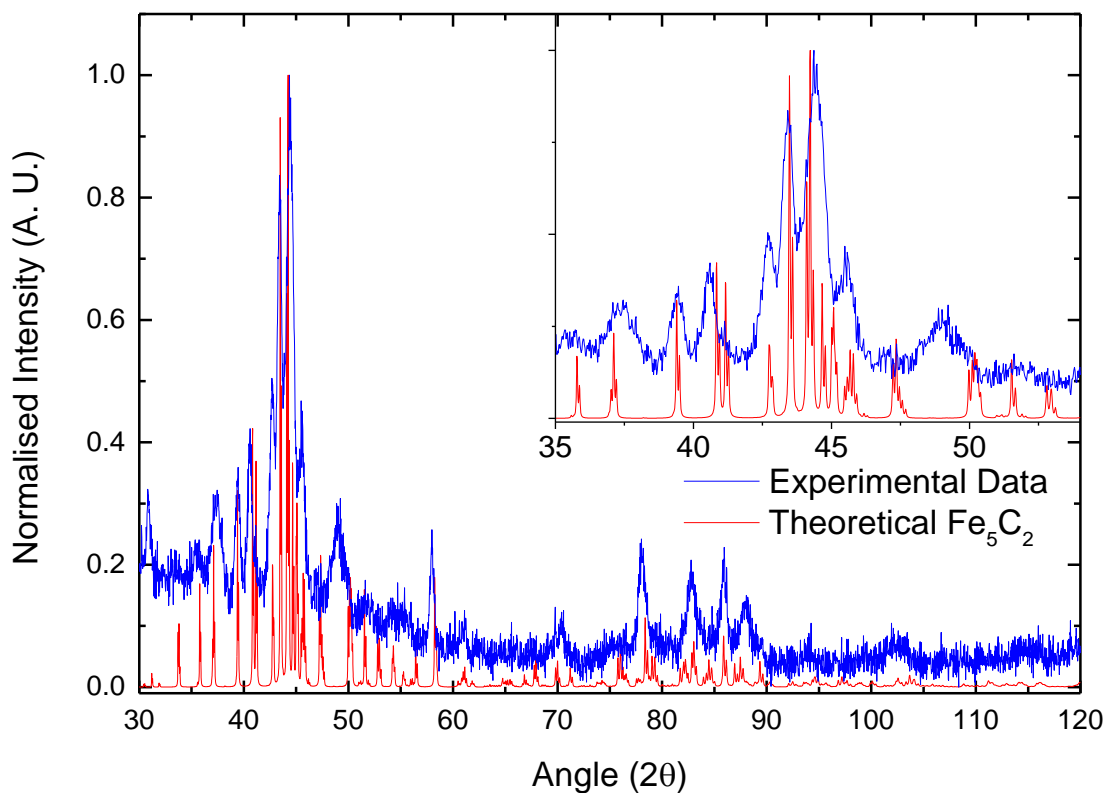
Figure 5.4. Experimental XRD data (blue) for the Fe₅C₂ sample with theoretical pattern (red) from ICSD data [51]. (PDF 04-014-4562).
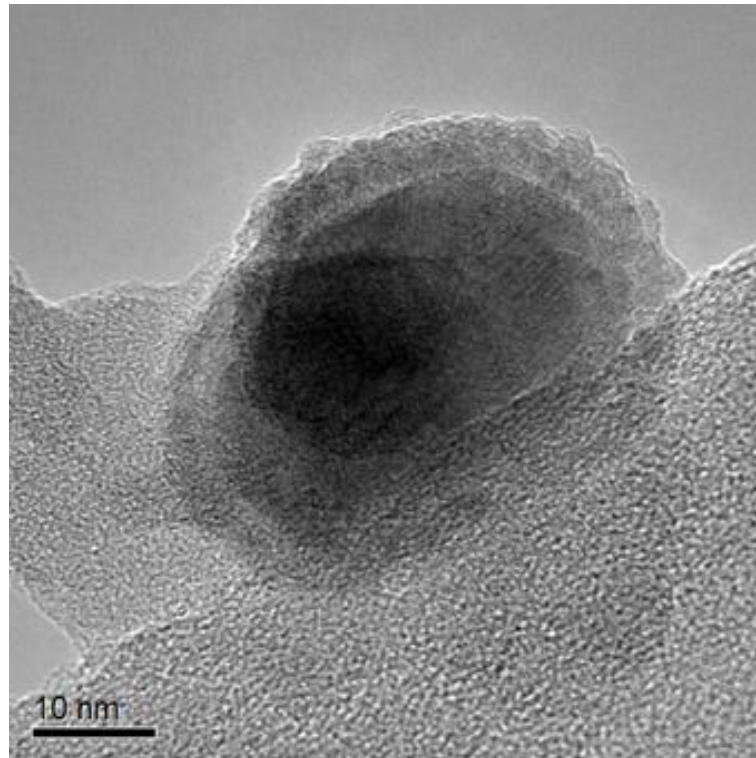
Figure 5.5. HRTEM image of supported Fe_5C_2 nanoparticle.
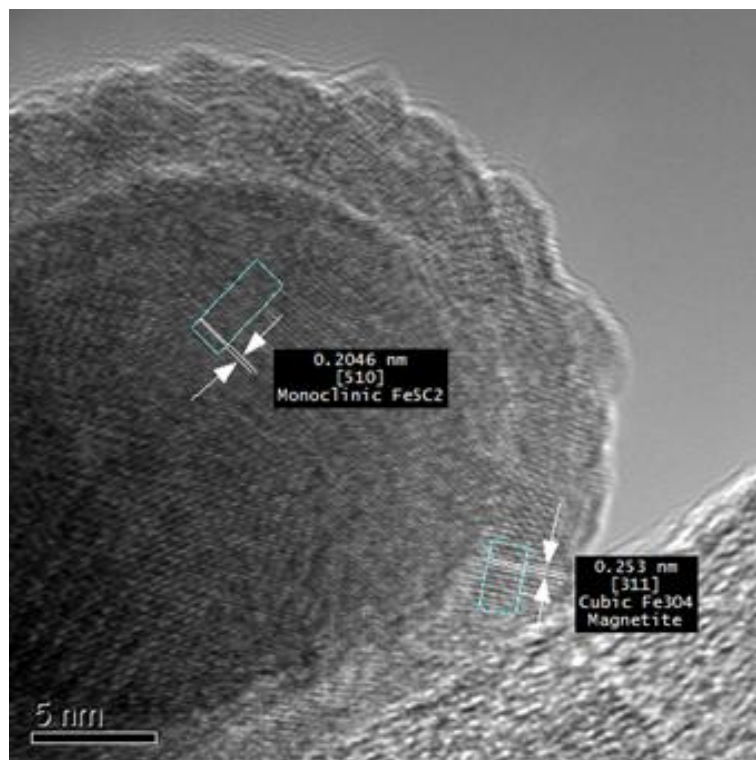
Figure 5.6. HRTEM image showing d-spacing of the core particle and shell-like structure of Fe_5C_2.

5.4 Mössbauer spectroscopy
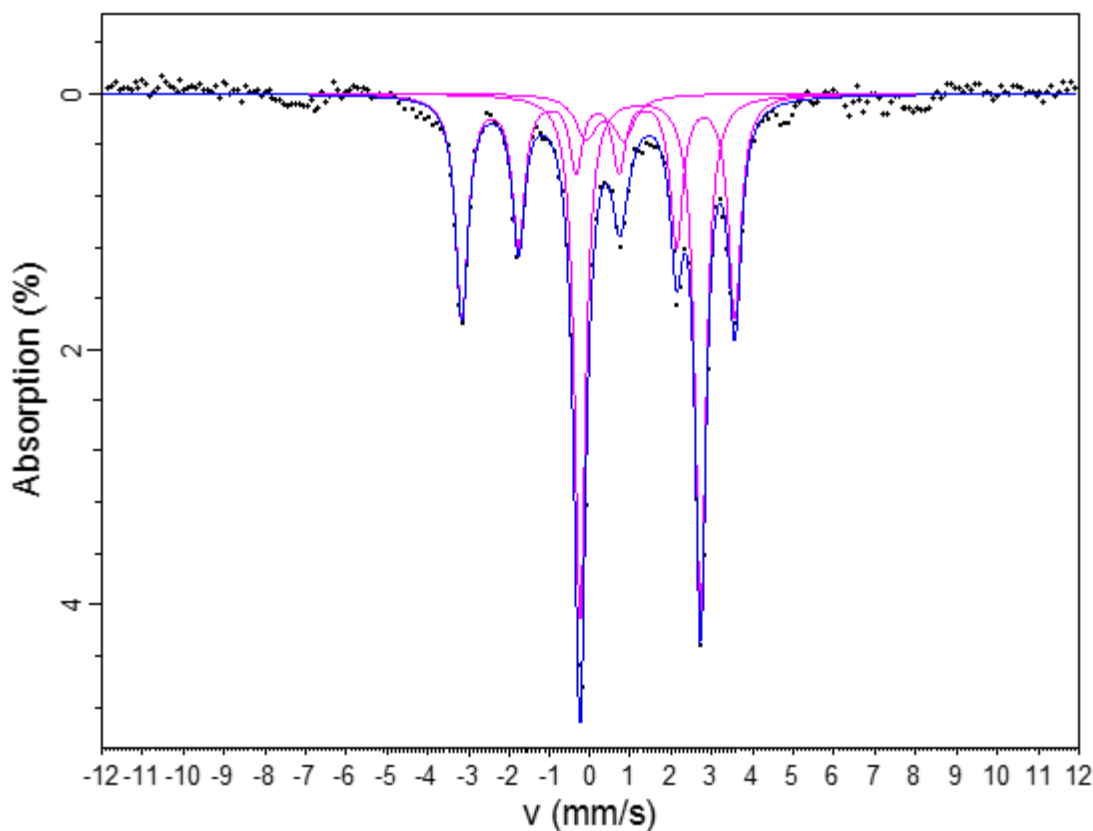
Figure 5.7. Room temperature Mössbauer spectrum of Fe_3C.

Table 5.4. Hyperfine parameters of Fe_3C at 293 K.

	CS (mm s⁻¹)	QS (mm s⁻¹)	B_{eff} (T)	Γ/2 (mm s⁻¹)	Area (%)
Doublet 1	1.23	2.96	0	0.16	46.5
Doublet 2	0.36	0.93	0	0.32	7.6
Sextet 1	0.19	0.01	20.8	0.19	45.9

The expected sextet of ferromagnetically order Fe_3C is observed, along with a ferric and ferrous doublet, as described in Table 5.4. The origin of the majority doublet, associated to Fe^{2+}, is believed to be due to residual iron(II) acetate from the synthesis route [52]. Iron(II) acetate does oxidise in air to iron(III) acetate, however if time for this was not provided, i.e. a recently opened bottle was used, then this may not have occurred. The addition of H_2O_2 to the dispersion during synthesis may overcome this issue. There are small absorption features around -7 and +8 mm s⁻¹ which may suggest a small amount of iron oxide. The

sextet associated to Fe_3C was considered to have great enough spectral area for the purposes of the study.
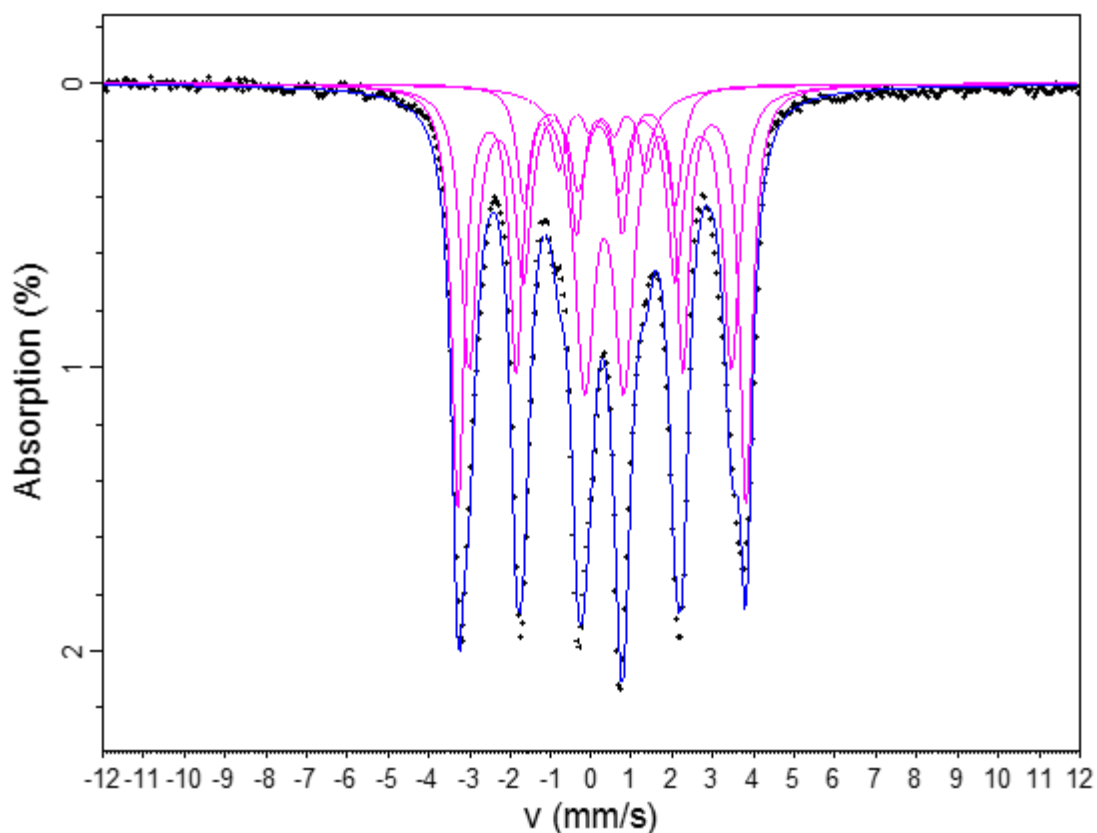

Figure 5.8. Room temperature Mössbauer spectrum of Fe_5C_2.

Table 5.5. Hyperfine parameters of Fe_5C_2 at 293 K.

	CS (mm s^{-1})	QS (mm s^{-1})	B$_{eff}$ (T)	Γ/2 (mm s^{-1})	Area (%)
Doublet 1	0.32	0.97	0	0.29	19.7
Sextet 1	0.23	0.03	21.9	0.19	37.4
Sextet 2	0.21	0.01	20.0	0.24	31.5
Sextet 3	0.24	-0.04	11.5	0.21	11.4

The parameters of the observed doublet are consistent with 'as-prepared' materials produced by the same group from which the synthesis was primarily sourced [41], where they report average particle size of 6 nm, and of other existing literature [38], [53]–[56]. The high linewidth of peaks presented in the XRD trace of the Fe_5C_2 sample analysed herein would also indicate very small particles. Fe_5C_2 is known to be magnetically ordered at room temperature, with a

Curie temperature of 521 K [38], suggesting the doublet observed is either an effect of particle size, or amorphous iron oxides / carbides.
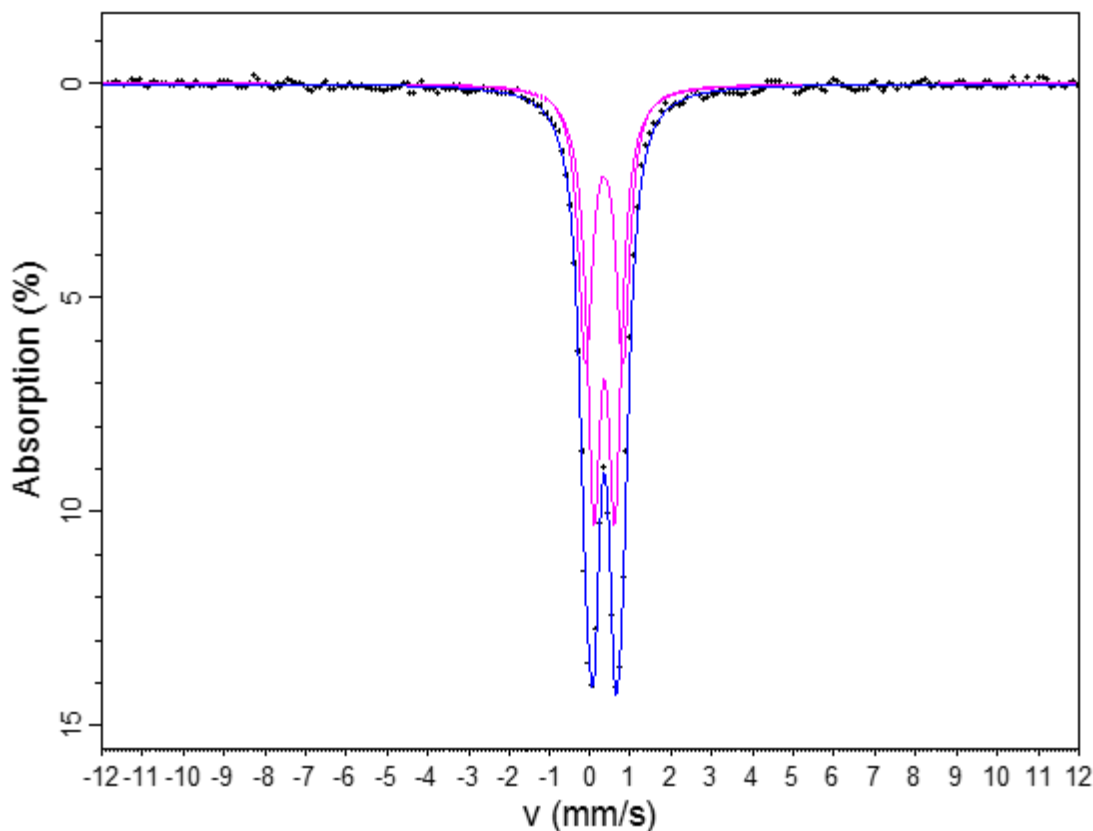

Figure 5.9. Room temperature Mössbauer spectrum of JMFT before catalysis.

Table 5.6. Hyperfine parameters of of JMFT before catalysis, at 293 K

	CS (mm s^{-1})	QS (mm s^{-1})	Γ/2 (mm s^{-1})	Area (%)
Doublet 1	0.35	0.52	0.20	58
Doublet 2	0.34	0.92	0.21	42

The doublets observed here can be associated with very small particles of α-Fe$_2$O$_3$ (< 13.5 Å average particle diameter) [57]–[59] where the average particle size is so small that the behaviour is entirely superparamagnetic [60]. It is believed that small α-Fe$_2$O$_3$ particles have iron in octahedral and tetrahedral sites [61]–[64], which is consistent with the fitted Mössbauer parameters of this material. Moreover, the spectrum observed for this precipitated Fischer-Tropsch catalyst material is consistent with what can be expected from existing literature detailing precipitated FTS iron-based catalysts [47].
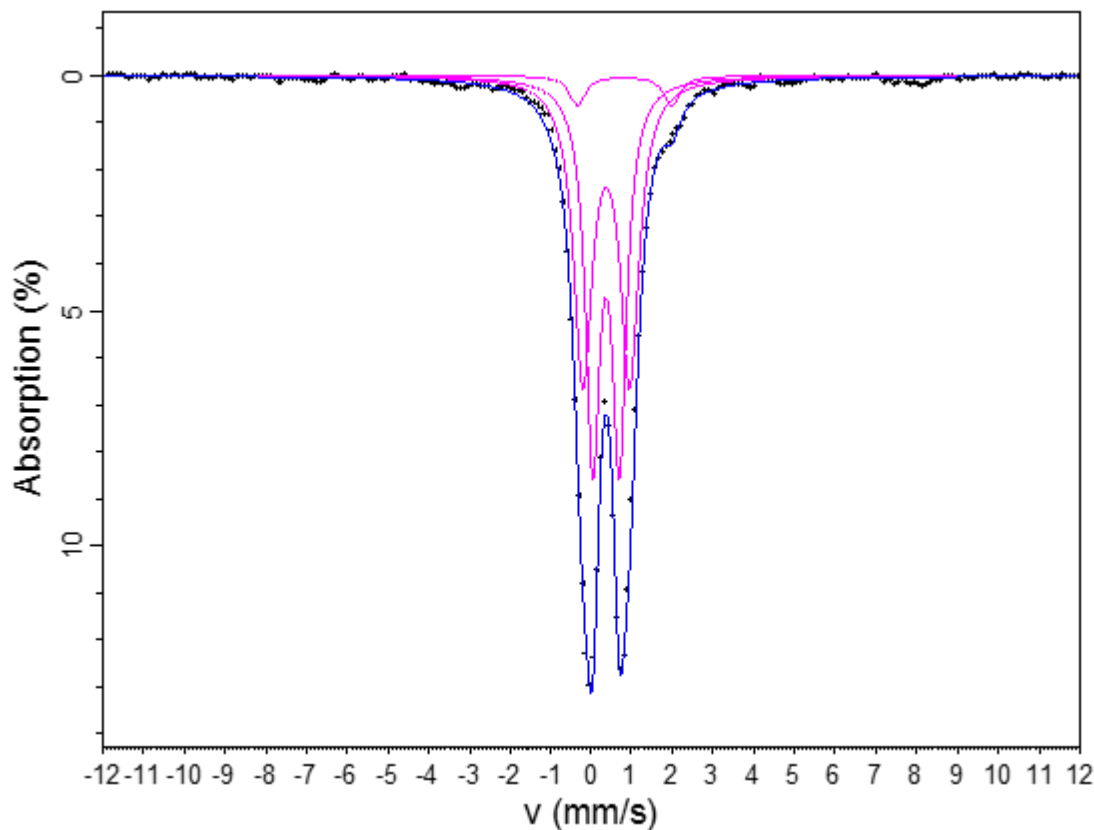
Figure 5.10. Room temperature Mössbauer spectrum of JMFT after catalysis.

Table 5.7. Hyperfine parameters of JMFT after catalysis, at 293 K.

	CS (mm s^{-1})	QS (mm s^{-1})	Γ/2 (mm s^{-1})	Area (%)
Doublet 1	0.36	0.63	0.21	48.9
Doublet 2	0.37	1.15	0.28	46.8
Doublet 3	0.83	2.32	0.23	4.3

Doublets one and two of this spectrum can be associated to the same sites as in the fresh material, with an increase in quadrupole splitting being caused by greater site asymmetry and higher distortion. The centre shift of doublet 3 is within the range expected for ferrous Fe^{2+}. The combined isomeric and quadrupole effects are consistent with tetrahedral Fe^{2+} [65], [66].
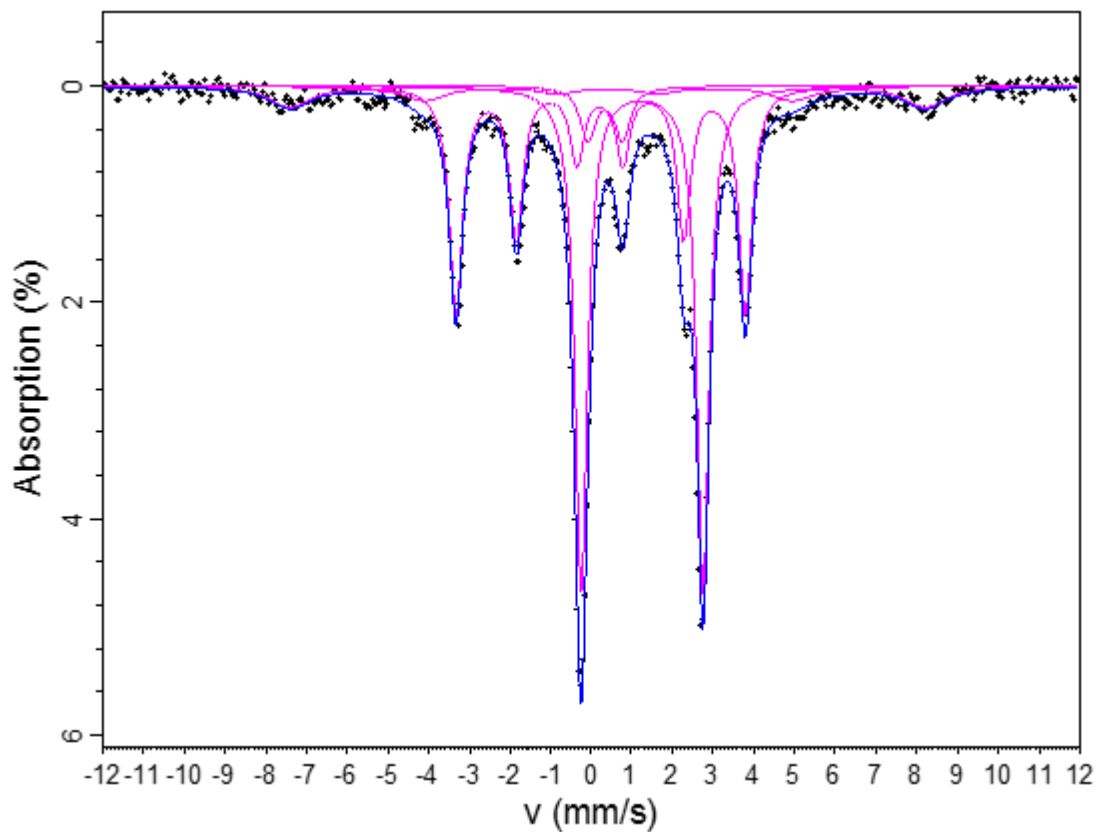
Figure 5.11. Mössbauer spectrum of Fe_3C at 250 K

Table 5.8. Hyperfine parameters of Fe_3C at 250 K

	CS (mm s^{-1})	QS (mm s^{-1})	B$_{eff}$ (T)	Γ/2 (mm s^{-1})	Area (%)
Doublet 1	0.35	0.85	0	0.23	5.5
Doublet 2	1.25	3.00	0	0.19	42.1
Sextet 1	0.22	0.01	22.0	0.20	40.7
Sextet 2	0.41	-0.01	48.5	0.62	11.6
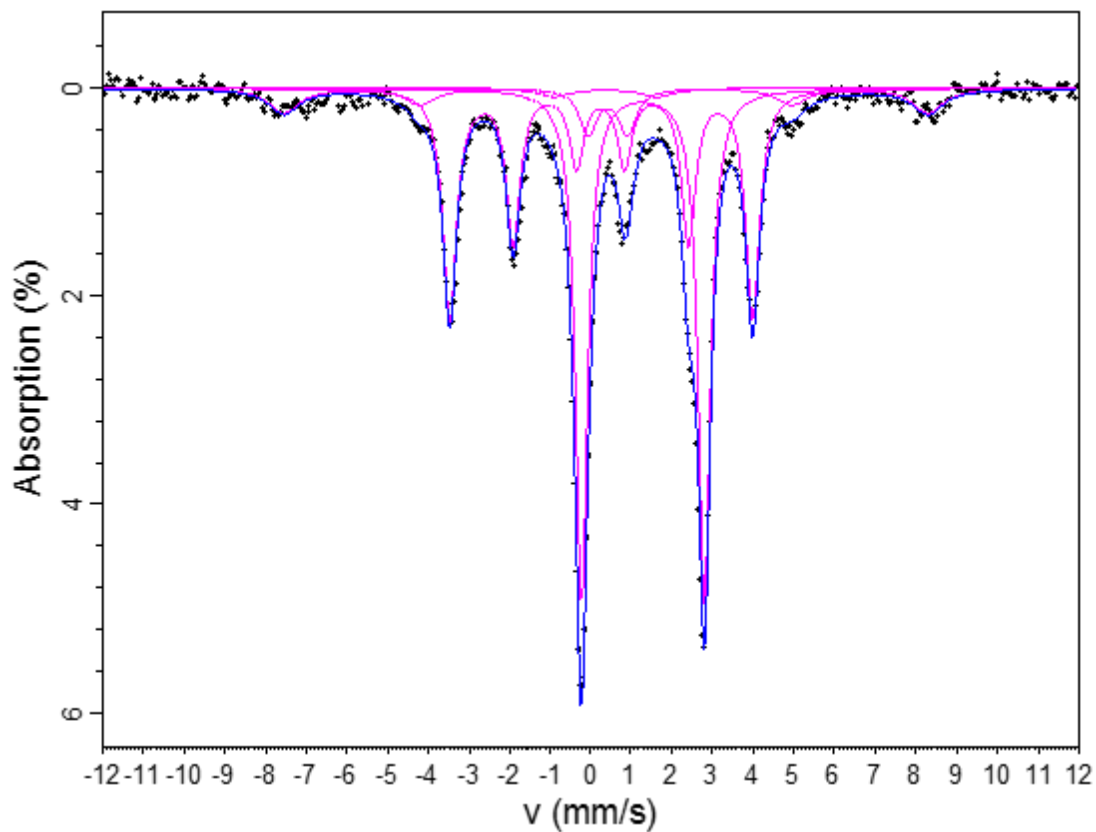
Figure 5.12. Mössbauer spectrum of Fe$_3$C at 200 K.

Table 5.9. Hyperfine parameters of Fe$_3$C at 200 K.

	CS (mm s^{-1})	QS (mm s^{-1})	B$_{eff}$ (T)	Γ/2 (mm s^{-1})	Area (%)
Doublet 1	0.43	0.96	0	0.26	5.3
Doublet 2	1.28	3.02	0	0.18	41.7
Sextet 1	0.25	0.00	23.1	0.21	42.8
Sextet 2	0.37	-0.00	49.1	0.46	10.2
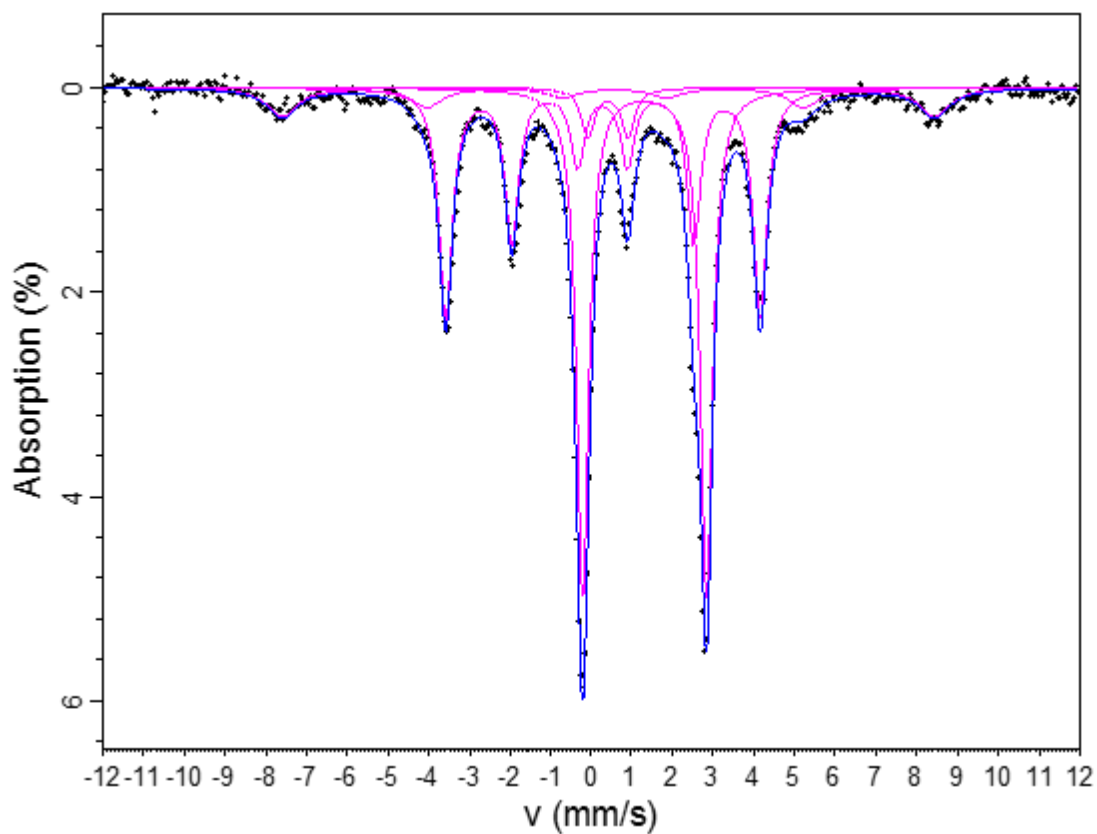
Figure 5.13. Mössbauer spectrum of Fe_3C at 150 K.

Table 5.10. Hyperfine parameters of Fe_3C at 150 K.

	CS (mm s^{-1})	QS (mm s^{-1})	B_{eff} (T)	Γ/2 (mm s^{-1})	Area (%)
Doublet 1	0.42	0.98	0	0.18	4.4
Doublet 2	1.31	3.04	0	0.20	41.6
Sextet 1	0.28	0.00	23.9	0.20	42.2
Sextet 2	0.50	-0.09	49.7	0.50	11.8
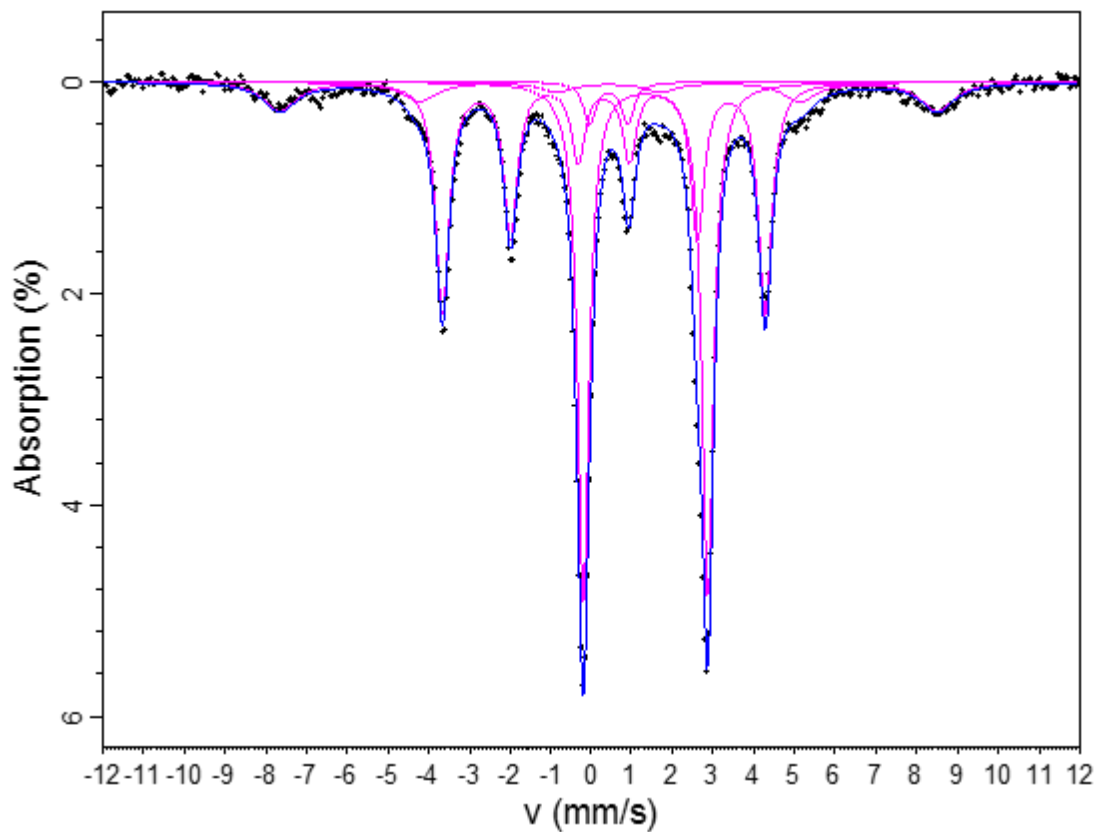
Figure 5.14. Mössbauer spectrum of Fe₃C at 100 K.

Table 5.11. Hyperfine parameters of Fe₃C at 100 K.

	CS (mm s^{-1})	QS (mm s^{-1})	B_{eff} (T)	$\Gamma/2$ (mm s^{-1})	Area (%)
Doublet 1	0.43	0.94	0	0.19	3.6
Doublet 2	1.33	3.06	0	0.17	40.6
Sextet 1	0.31	-0.00	24.6	0.20	13.4
Sextet 2	0.43	-0.01	50.12	0.50	42.5
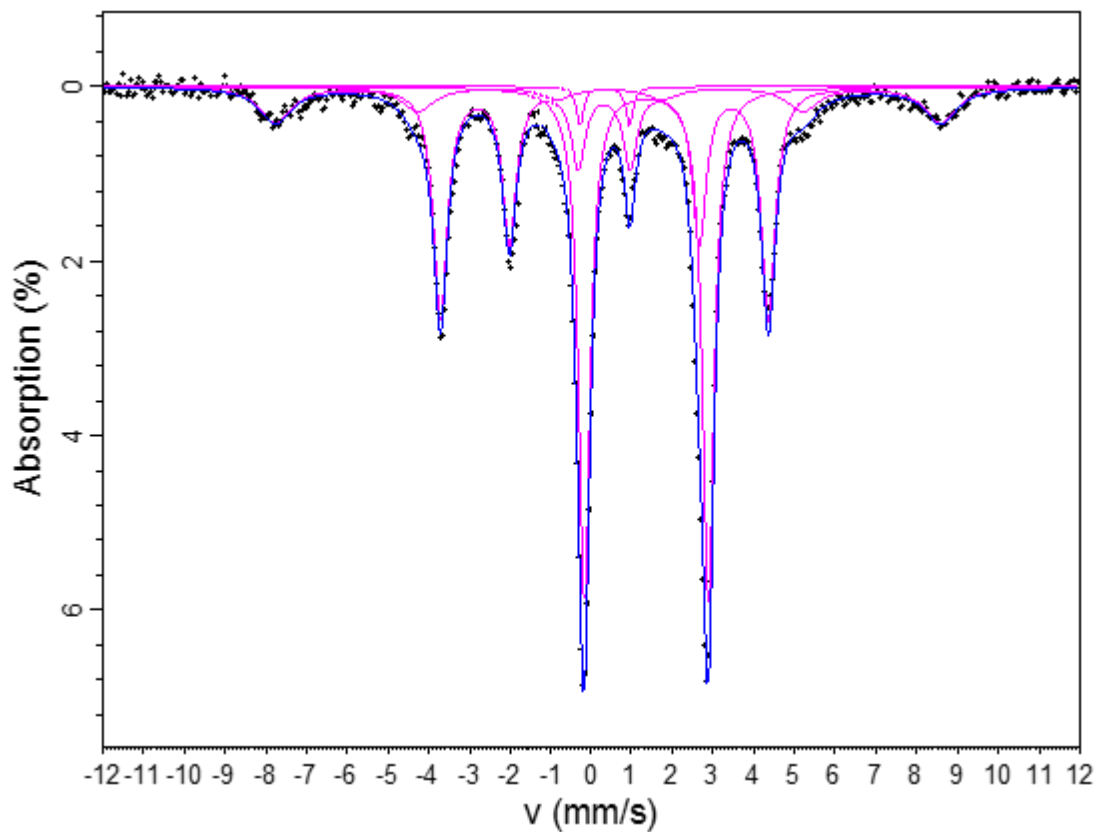
Figure 5.15. Mössbauer spectrum of Fe_3C at 52.5 K.

Table 5.12. Hyperfine parameters of Fe_3C at 52.5 K.

	CS (mm s^{-1})	QS (mm s^{-1})	B$_{eff}$ (T)	Γ/2 (mm s^{-1})	Area (%)
Doublet 1	0.33	1.21	0	0.11	1.8
Doublet 2	1.35	3.04	0	0.17	39.8
Sextet 1	0.32	0.00	25.0	0.21	43.0
Sextet 2	0.44	-0.03	50.7	0.48	15.4
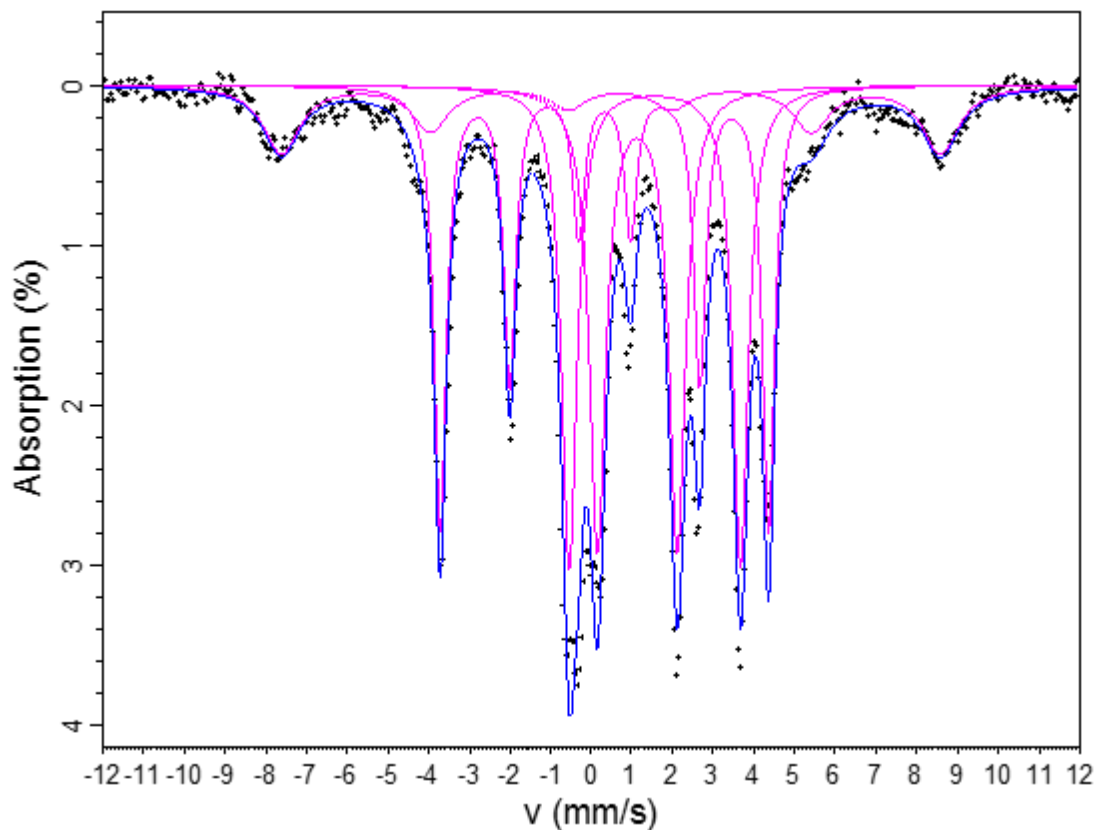
Figure 5.16. Mössbauer spectrum of Fe_3C at 50 K.

Table 5.13. Hyperfine parameters of Fe_3C at 50 K.

	CS (mm s^{-1})	QS (mm s^{-1})	B$_{eff}$ (T)	Γ/2 (mm s^{-1})	Area (%)
Doublet 1	1.13	4.21	0	0.23	24.2
Doublet 2	1.56	1.96	0	0.24	24.5
Sextet 1	0.32	-0.00	25.0	0.18	35.2
Sextet 2	0.60	-0.12	50.2	0.54	16.1

In the spectrum for Fe_3C at 50 K, the Fe^{3+} doublet is not observed. This site may still be present but in too low concentration to be observed, with the other sites occupying this region. The Fe^{2+} doublet which had been assigned to Fe(II) acetate is no longer present, and instead there are two ferrous environments. In 1996, Singh and colleagues [52] presented the structure of Fe(II)acetate, and describe two iron sites; one octahedral site that is bridged by three acetate groups to a more distorted site.
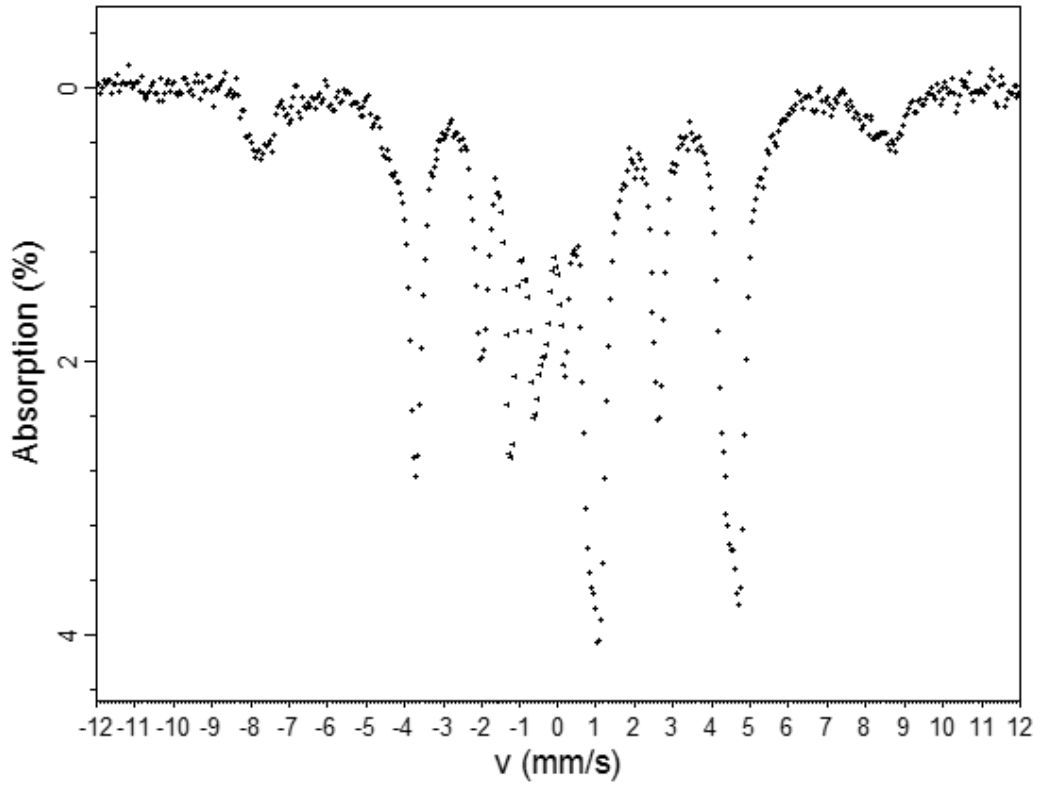
Figure 5.17. Mössbauer spectrum of Fe$_3$C at 30 K.
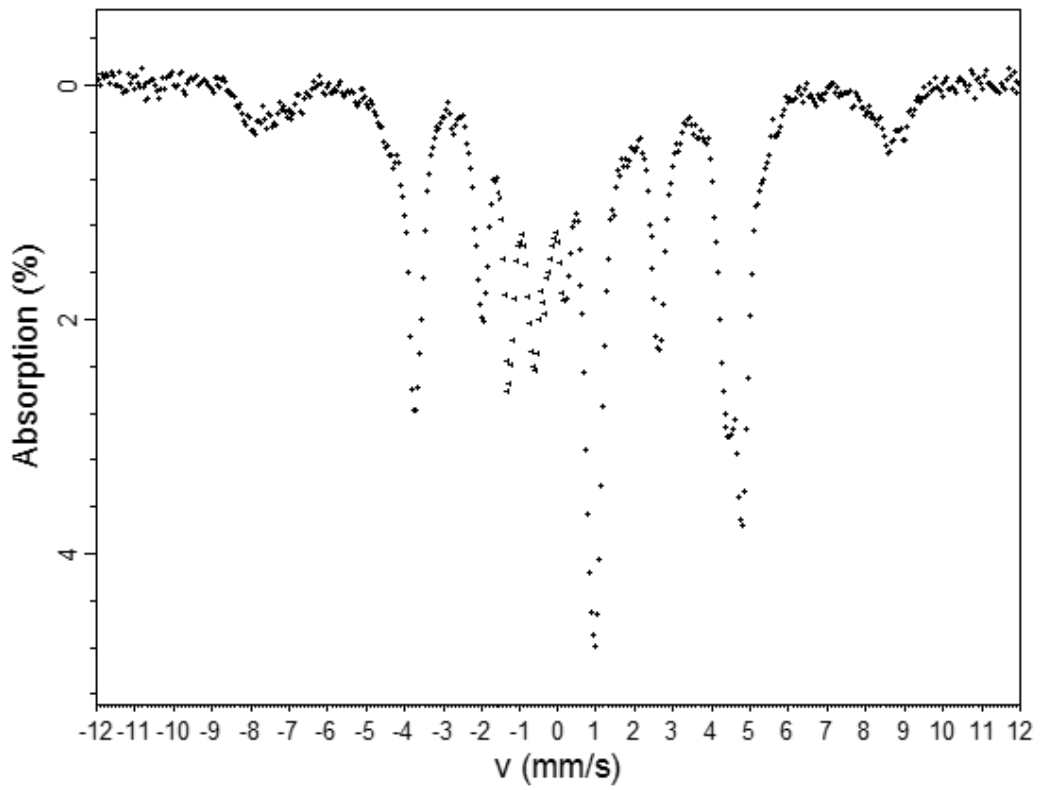

Figure 5.18. Mössbauer spectrum of Fe$_3$C at 10 K.
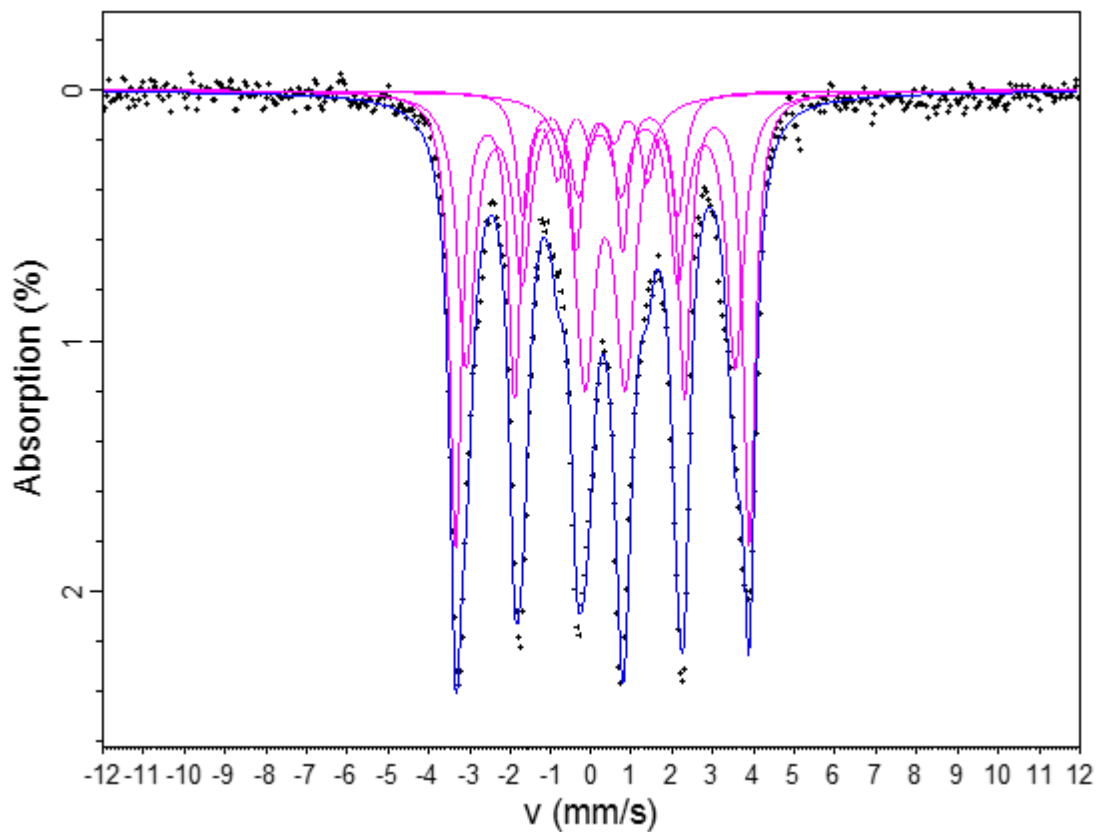
Figure 5.19. Mössbauer spectrum of Fe_5C_2 at 250 K.

Table 5.14. Hyperfine parameters of Fe_5C_2 at 250 K.

|	CS (mm s^{-1})	QS (mm s^{-1})	B_{eff} (T)	Γ/2 (mm s^{-1})	Area (%)
Doublet	0.34	0.99	0	0.30	19.2
Sextet 1	0.24	0.04	22.4	0.18	37.3
Sextet 2	0.22	0.01	20.5	0.26	32.2
Sextet 3	0.25	-0.03	11.8	0.20	11.5
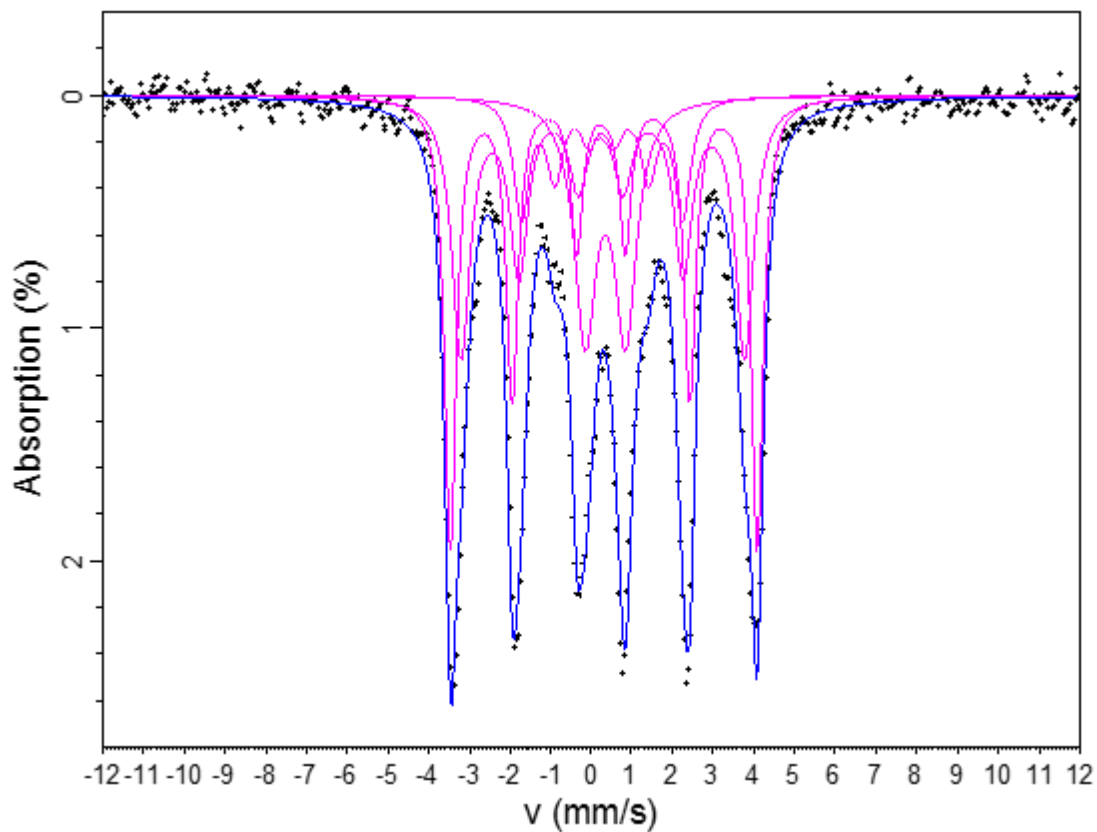
Figure 5.20. Mössbauer spectrum of Fe_5C_2 at 200 K.

Table 5.15. Hyperfine parameters of Fe_5C_2 at 200 K.

|	CS (mm s^{-1})	QS (mm s^{-1})	B_{eff} (T)	Γ/2 (mm s^{-1})	Area (%)
Doublet	0.35	0.99	0	0.32	17.5
Sextet 1	0.27	0.03	23.4	0.18	36.8
Sextet 2	0.26	0.02	21.6	0.27	32.8
Sextet 3	0.26	0.02	12.3	0.23	12.9
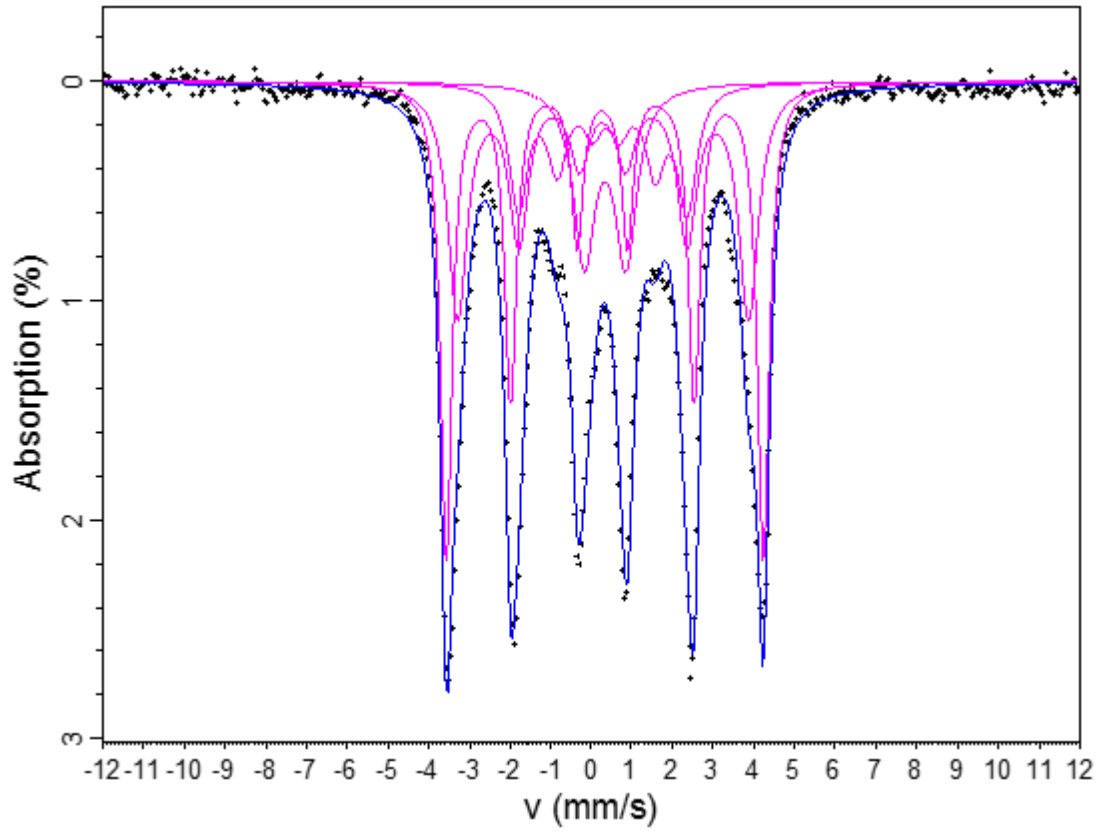
Figure 5.21. Mössbauer spectrum of Fe_5C_2 at 150 K.

Table 5.16. Hyperfine parameters of Fe_5C_2 at 150 K.

|	CS (mm s^{-1})	QS (mm s^{-1})	B$_{eff}$ (T)	Γ/2 (mm s^{-1})	Area (%)
Doublet	0.34	1.02	0	0.32	13.2
Sextet 1	0.30	0.03	24.1	0.18	39.0
Sextet 2	0.29	0.00	22.1	0.29	31.6
Sextet 3	0.32	-0.05	12.9	0.28	16.2
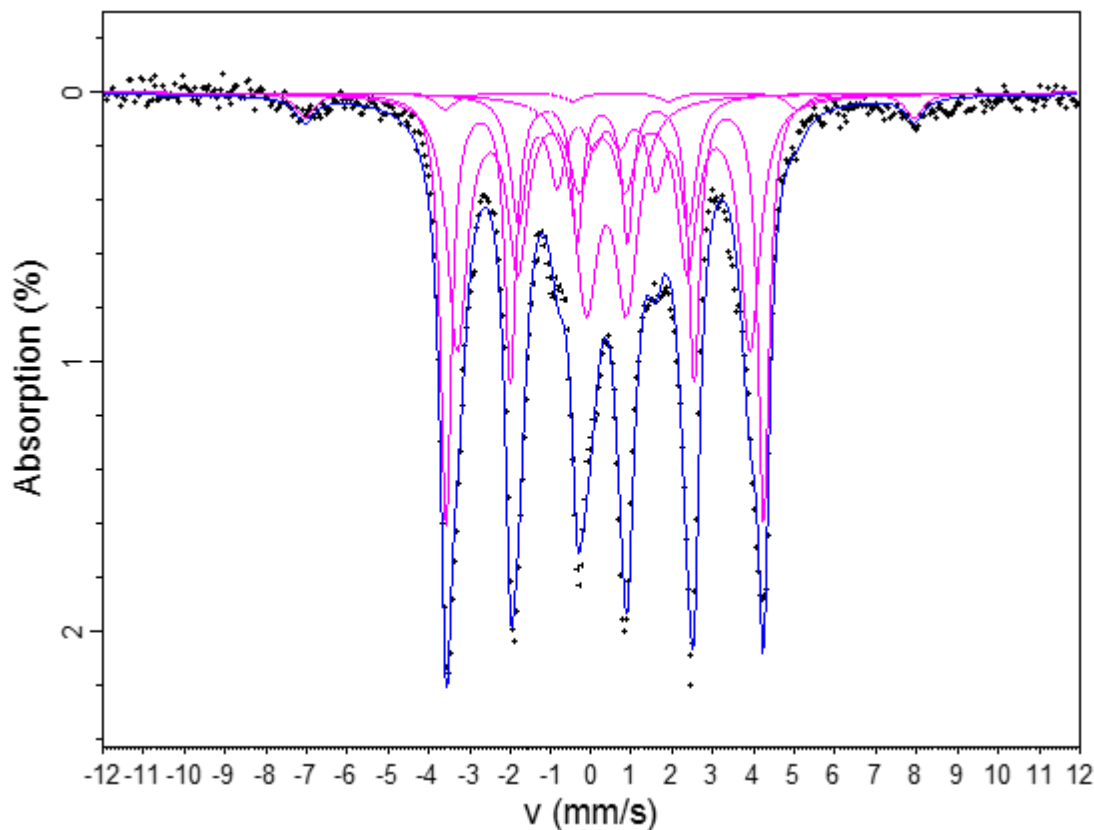
Figure 5.22. Mössbauer spectrum of Fe_5C_2 at 148.5 K.

Table 5.17. Hyperfine parameters of Fe_5C_2 at 148.5 K.

|	CS (mm s^{-1})	QS (mm s^{-1})	B_{eff} (T)	Γ/2 (mm s^{-1})	Area (%)
Doublet	0.37	0.99	0	0.35	16.1
Sextet 1	0.30	0.03	24.2	0.16	32.4
Sextet 2	0.29	0.02	22.3	0.30	34.3
Sextet 3	0.34	-0.04	12.9	0.24	14.0
Sextet 4	0.59	-0.15	46.4	0.28	3.2

Reducing the temperature from 150 to 148.5 K has caused a fourth sextet to appear in the Mössbauer spectrum of the Fe_5C_2 sample. For such a low spectral abundance, the centre shift and quadrupole splitting may not be accurate, however the magnitude of the magnetic splitting, which is directly related to the distance between the first and sixth absorption lines of a sextet, can be considered as accurate, within the uncertainty inherent with such a low spectral abundance. The magnitude of the magnetic field could suggest that sextet 4 may be attributed to some iron oxide phase(s) being resolved at low temperature.
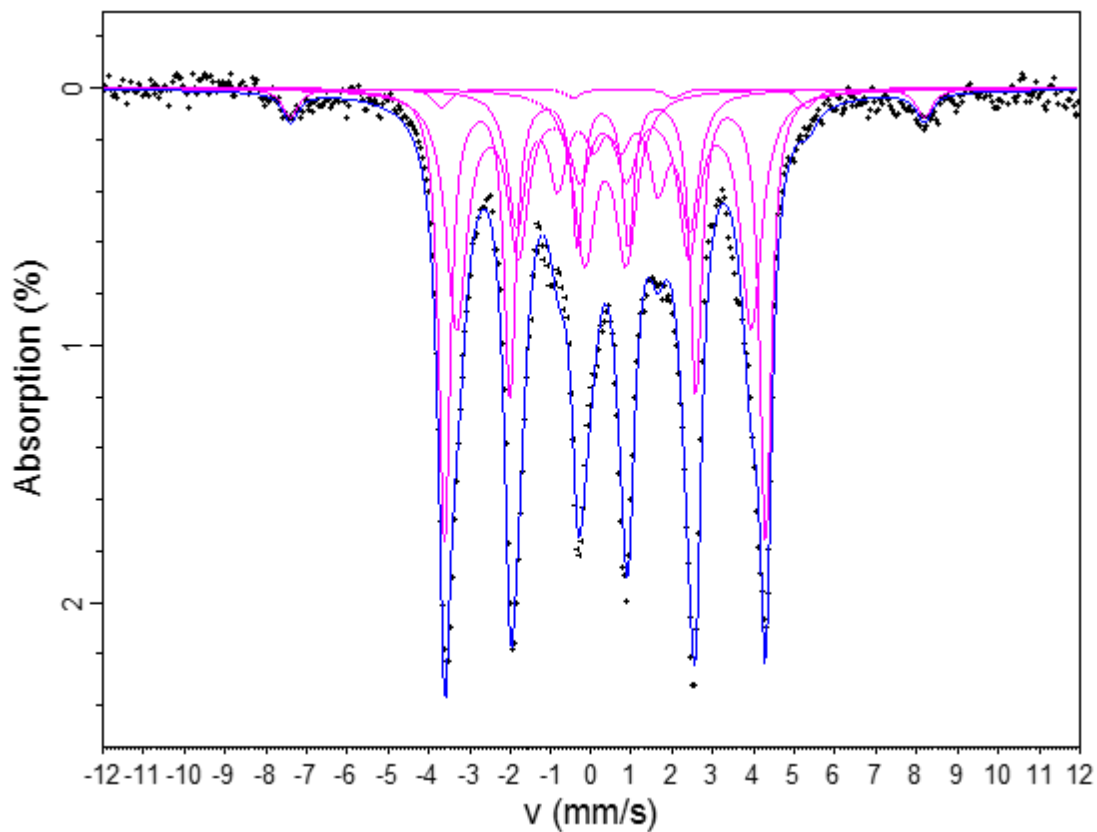
Figure 5.23. Mössbauer spectrum of Fe_5C_2 at 125 K.

Table 5.18. Hyperfine parameters of Fe_5C_2 at 125 K.

	CS (mm s^{-1})	QS (mm s^{-1})	B_{eff} (T)	Γ/2 (mm s^{-1})	Area (%)
Doublet	0.35	1.02	0	0.32	12.0
Sextet 1	0.31	0.03	24.5	0.17	35.3
Sextet 2	0.31	0.01	22.4	0.32	33.0
Sextet 3	0.35	-0.06	13.2	0.27	16.4
Sextet 4	0.60	-0.21	48.3	0.24	3.2
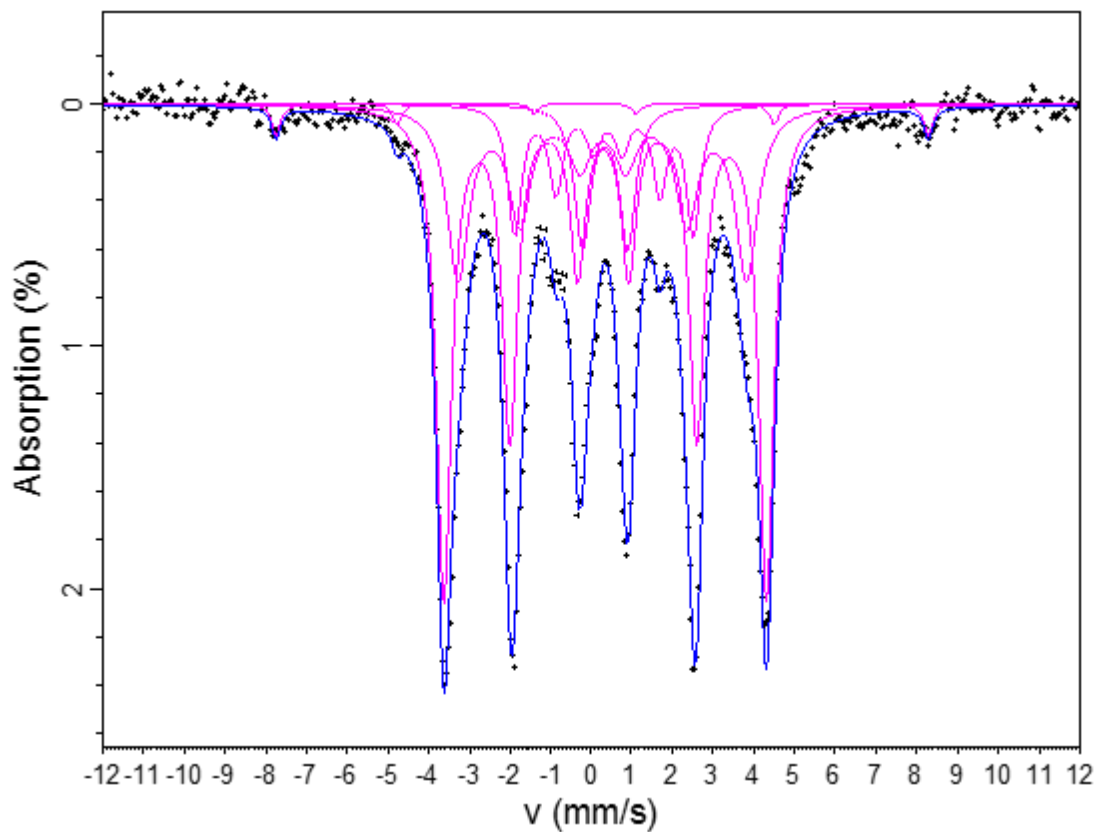
Figure 5.24. Mössbauer spectrum of Fe_5C_2 at 100 K.

Table 5.19. Hyperfine parameters of Fe_5C_2 at 100 K.

|	CS (mm s^{-1})	QS (mm s^{-1})	B$_{eff}$ (T)	Γ/2 (mm s^{-1})	Area (%)
Doublet	0.34	1.11	0	0.24	7.8
Sextet 1	0.32	0.02	24.6	0.22	51.4
Sextet 2	0.28	-0.01	22.0	0.33	26.4
Sextet 3	0.36	-0.05	13.6	0.21	12.4
Sextet 4	0.06	0.20	49.6	0.13	2.0
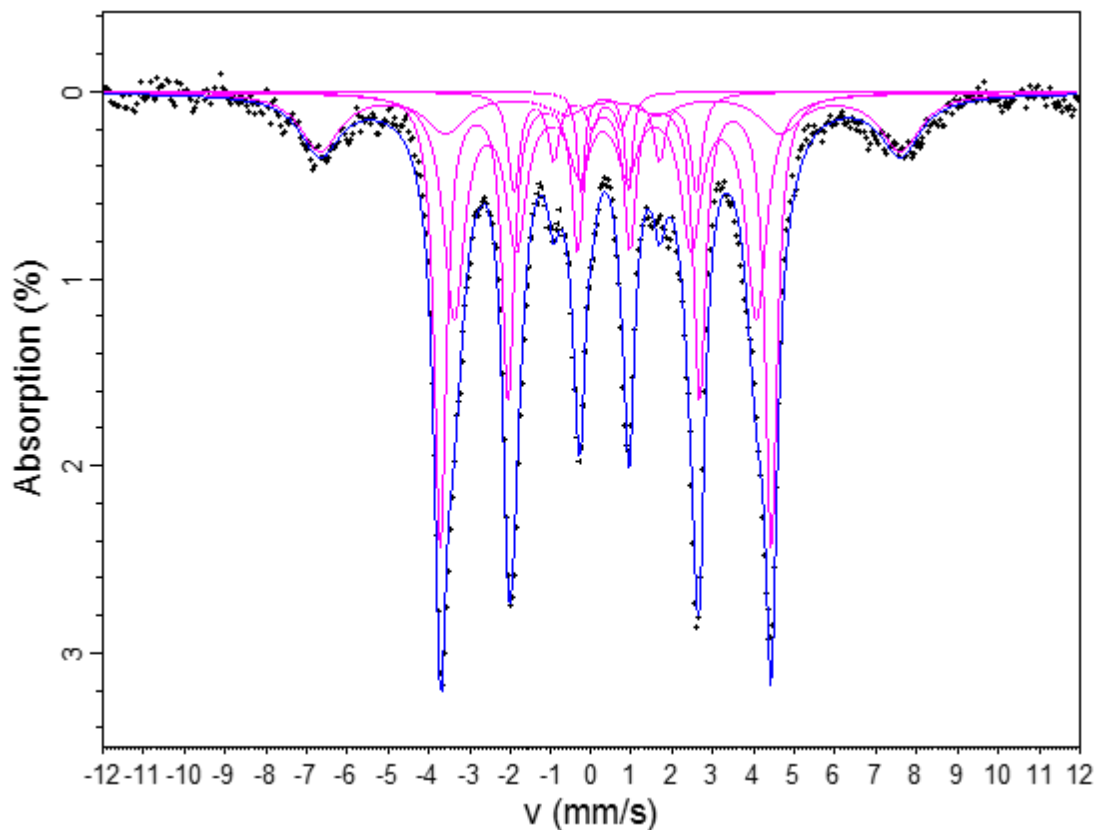
Figure 5.25. Mössbauer spectrum of Fe_5C_2 at 50 K.

Table 5.20. Hyperfine parameters of Fe_5C_2 at 50 K.

	CS (mm s^{-1})	QS (mm s^{-1})	B$_{eff}$ (T)	Γ/2 (mm s^{-1})	Area (%)
Doublet	0.33	1.17	0	0.14	2.8
Sextet 1	0.33	0.02	25.2	0.18	38.9
Sextet 2	0.32	0.02	23.0	0.30	33.1
Sextet 3	0.36	-0.02	13.9	0.17	8.1
Sextet 4	0.49	-0.03	44.2	0.60	17.1

The Néel temperature is the temperature at which an paramagnetic material becomes antiferromagnetic as temperature is reduced [67], [68]. This can be observed in Mössbauer spectra as a doublet "becoming" a sextet. The same spectral transformation can be attributed to superparamagnetism, whereby a material that is typically magnetically ordered at the measurement temperature may present as paramagnetic, this may be due to small particle size [59]. In 1966 Kündig and Bommel reported superparamagnetism of small (< 13.5 nm) particles of α-Fe_2O_3 [57]. Superparamagnetism can be observed through Mössbauer

spectroscopy with external magnetic fields that cause the single domain magnetic moments of the nanoparticles to align. Magnetic ordering is not a binary system but is governed by time-dependant fluctuations of the orientation of electronic spin, which affects the magnetic hyperfine interaction – if the magnetic moments align for sufficient times to be observed, they may be observed. This process is known as magnetic relaxation and is influenced by temperature. The energy that is required for the magnetisation vector to change direction is denoted as *2K*, and the probability that this vector will change its direction spontaneously is proportional to Exp(- *2Kv / kT*), where v is the particle volume, *k* is the Boltzmann constant and T is the temperature [57]. From this it can be seen that as temperature increases, or the particle volume decreases, the probability that the magnetisation vector would change direction increases, which results in the observed magnetic moment becoming weaker. The reduction in the spectral area attributed to the paramagnetic doublet, and the increased spectral area attributed to sextet 4 in Figure 5.25 may be caused by this relaxation effect – this trend is continued in the spectrum presented in Figure 5.26 as the temperature is further reduced.

.
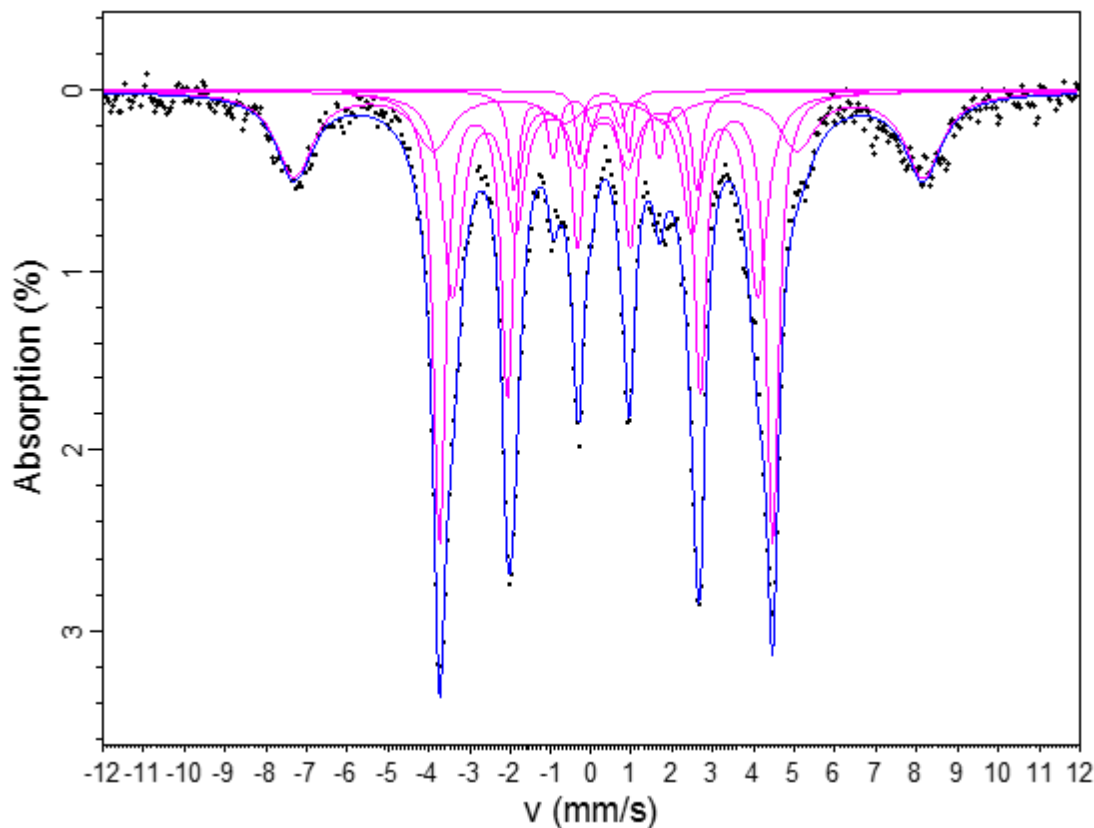
Figure 5.26. Mössbauer spectrum of Fe_5C_2 at 10 K.

Table 5.21. Hyperfine parameters of Fe_5C_2 at 10 K.

	CS (mm s^{-1})	QS (mm s^{-1})	B_{eff} (T)	$\Gamma/2$ (mm s^{-1})	Area (%)
Doublet	0.31	1.22	0	0.11	1.7
Sextet 1	0.33	0.03	25.4	0.18	39.6
Sextet 2	0.32	0.02	23.2	0.29	28.2
Sextet 3	0.36	-0.01	13.9	0.16	7.5
Sextet 4	0.51	-0.08	47.9	0.55	23.0

A reduction in the spectral area assigned to the doublet of Fe_5C_2 spectra has been observed as the temperature is reduced, and as the spectral area of the highest magnitude sextet increased since 148.5 K. The sextet that has been fit to the high absorption lines observed at around ± 8 mm s^{-1} may be considered as a superposition of multiple indistinguishable magnetic sites, due to the high linewidth reported here.

Temp (K)	CS (mm s^{-1})	B$_{eff}$ (T)	Γ/2 (mm s^{-1})	ε (mm s^{-1})
293	0.19	20.8	0.19	0.01
250	0.22	22.0	0.20	0.01
200	0.25	23.1	0.21	0.00
150	0.28	23.9	0.20	0.00
100	0.31	24.6	0.20	0.00
50	0.32	25.0	0.19	0.00

Table 5.22. Mössbauer spectral parameters of **Fe$_3$C sextet**, relative to α-Fe. CS: Centre shift (+/- 0.02 mm s^{-1}); B$_{eff}$: Magnetic splitting (+/- 0.5 T); Γ/2 = HWHM (+/- 0.02 mm s^{-1}); ε: Quadrupole shift (+/- 0.02 mm s^{-1})

Temp (K)	CS (mm s^{-1})	B$_{eff}$ (T)	Γ/2 (mm s^{-1})	ε (mm s^{-1})
293	0.23	21.9	0.19	0.03
250	0.24	22.4	0.18	0.04
200	0.27	23.3	0.18	0.03
150	0.30	24.2	0.18	0.03
100	0.32	24.6	0.22	0.02
50	0.33	25.2	0.18	0.02
10	0.34	25.4	0.17	0.03

Table 5.23. Mössbauer spectral parameters of **Fe$_5$C$_2$ sextet 1**, relative to α-Fe. CS: Centre shift (+/- 0.02 mm s^{-1}); B$_{eff}$: Magnetic splitting (+/- 0.5 T); Γ/2 = HWHM (+/- 0.02 mm s^{-1}); ε: Quadrupole shift (+/- 0.02 mm s^{-1})

Temp (K)	CS (mm s^{-1})	B$_{eff}$ (T)	Γ/2 (mm s^{-1})	ε (mm s^{-1})
293	0.21	20.0	0.23	0.01
250	0.22	20.5	0.26	0.01
200	0.26	21.6	0.27	0.02
150	0.29	22.2	0.29	0.00
125	0.31	22.4	0.32	0.01
100	0.28	22.0	0.33	-0.01
50	0.32	23.0	0.30	0.02
10	0.33	23.2	0.26	0.02

Table 5.24. Mössbauer spectral parameters of **Fe$_5$C$_2$ sextet 2**, relative to α-Fe. CS: Centre shift (+/- 0.02 mm s^{-1}); B$_{eff}$: Magnetic splitting (+/- 0.5 T); Γ/2 = HWHM (+/- 0.02 mm s^{-1}); ε: Quadrupole shift (+/- 0.02 mm s^{-1})

Temp (K)	CS (mm s^{-1})	B$_{eff}$ (T)	Γ/2 (mm s^{-1})	ε (mm s^{-1})
293	0.24	11.5	0.21	-0.04
250	0.25	11.8	0.20	-0.03
200	0.26	12.3	0.23	0.02
150	0.32	12.9	0.28	-0.05
100	0.36	13.6	0.21	-0.05
50	0.36	13.9	0.17	-0.02
10	0.36	13.9	0.16	-0.01

Table 5.25. Mössbauer spectral parameters of **Fe$_5$C$_2$ sextet 3**, relative to α-Fe. CS: Centre shift (+/- 0.02 mm s^{-1}); B$_{eff}$: Magnetic splitting (+/- 0.5 T); Γ/2 = HWHM (+/- 0.02 mm s^{-1}); ε: Quadrupole shift (+/- 0.02 mm s^{-1})

5.5 Discussion

Fe_3C and Fe_5C_2 were both identified by X-ray diffraction, however Mössbauer spectroscopy reveals the presence of additional phases that were not observed through XRD. The additional phases are believed to be unreacted iron (II) acetate precursor, or amorphous iron oxide(s), identified by the ferrous doublet and high magnetic splitting sextet respectively, through Mössbauer spectroscopy. The ability to identify the presence of all iron environments, particularly in materials where iron plays an active role, is essential in understanding any performance changes in otherwise comparable materials. The great spectral change for the Fe_3C sample, observed with the temperature decrease to 50 K has been attributed to a structural phase transition, as described, where the single octahedral site has become split into a slightly less distorted octahedral FeO_6 structure and an 8-coordinated iron site, FeO_8. While not related to the iron carbides, or Fischer-Tropsch studies, this phase change may be noteworthy nonetheless as a similar phenomenon is observed in a lithium iron phosphate material in a later chapter.

During the *Mössbauer Spectroscopy* chapter, in particular the section focusing on *Debye Model Approximation* the Centre Shift (CS) parameter was defined as the sum of the intrinsic Isomer Shift (IS) of the material and the second order Doppler shift (SODS). The Centre Shift, directly observed through Mössbauer spectroscopy, is temperature dependant, where a reduced temperature will yield a greater centre shift; this is due to the second order Doppler shift. As the main contribution for the temperature dependence of the Mössbauer centre shift, the second order Doppler shift can be approximated, as discussed, such that;

$$SODS = -\frac{3kT}{2Mc}\left(\frac{3\theta_D}{8T} + 3\left(\frac{T}{\theta_D}\right)^3 \int_0^{\theta_D/T} \frac{x^3}{e^x - 1}dx\right) \tag{1}$$

In this approximation, the Debye temperature, θ_D, is material specific, the mass of the Mössbauer isotope nucleus, M, is isotope specific, the Boltzmann constant k and speed of light c are both always constant. For this approximation, using a number of temperatures, the intrinsic isomer shift and Debye temperatures can be made the only unknown material specific variables. As with

the Fe_3C and Fe_5C_2 samples, Mössbauer spectroscopy measurements were taken at various temperatures, allowing such an approximation to be made. A program was written which takes the measurement temperatures and centre shifts of a chosen site and allows only the Debye temperature and isomer shift to vary using the previous equation, and the relation of Centre Shift = isomer shift + second order Doppler shift. By varying the Debye temperature and isomer shift, the program compares a calculated theoretical centre shift at the measurement temperature, with the experimental centre shift input. The program will continually adjust the Debye temperature and isomer shift to minimise the difference between the theoretical and experimental centre shift, for each measurement temperature simultaneously. The Debye temperature and isomer shift can be constrained within user-defined ranges, to guide the calculations to sensible values. The program displays expected trendlines for how the Centre Shift may vary with temperature for different Debye temperatures, overlaying the experimental centre shift data, as shown for the Fe_3C sextet previously identified, in Figure 5.27. By comparing these modelled centre shifts as a function of Debye temperature, the Fe_3C sextet Debye temperature can be expected to be less than 400 K due to the position of the overlaid experimental data.
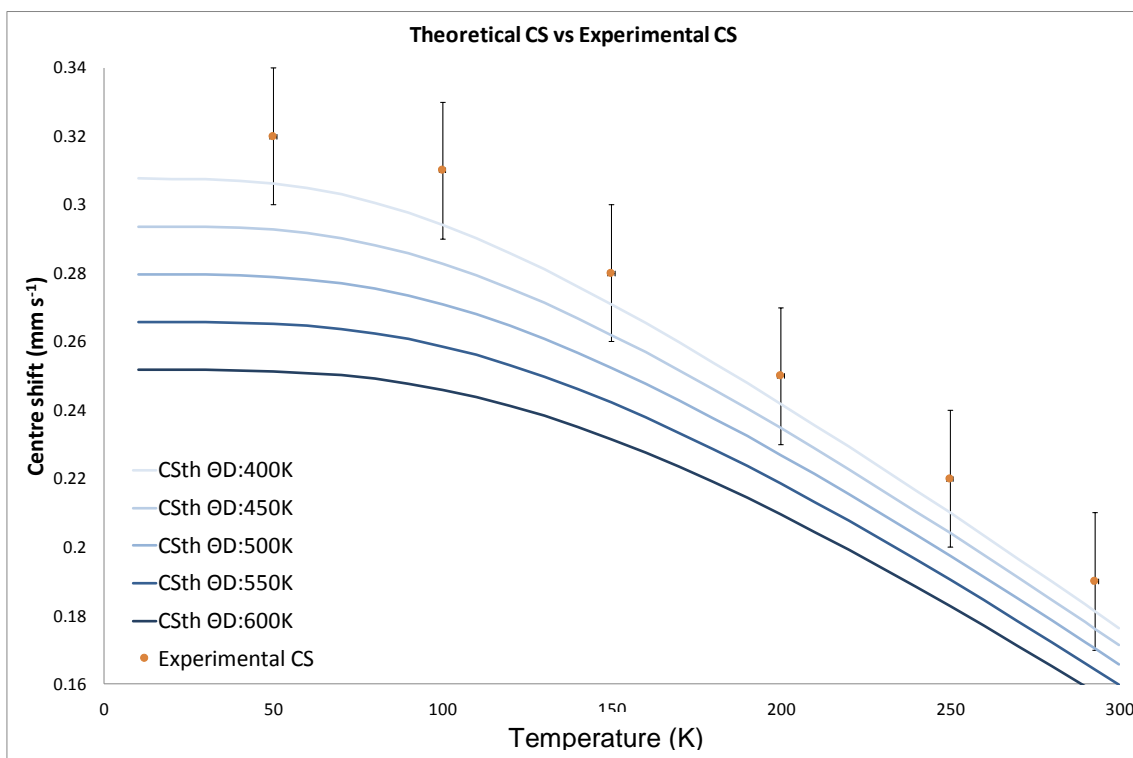
Figure 5.27. Theoretical centre shifts for modelled Debye temperatures and experimental centre shift data for Fe_3C sextet.

Using this method of approximating the Debye temperature, Fe_3C was found to have a Debye temperature of 356.9 K and an intrinsic isomer shift of 0.419 mm s^{-1}. The total sum of the differences between the theoretical centre shifts at the measured temperatures, and the experimental centre shifts was 0.0074 mm s^{-1}, suggesting good agreement between theoretical and experimental. The recoil-fee fraction can be calculated using this approximation, through the equation from *Mössbauer Spectroscopy – Debye Model Approximations*;

$$f = \exp\left[\frac{-6E_R}{k\theta_D}\left\{\frac{1}{4} + \left(\frac{T}{\theta_D}\right)^2 \int_0^{\theta_D/T} \frac{x\,dx}{e^x - 1}\right\}\right] \tag{2}$$

From this, the recoil-free fraction at 293 K is found as $f_{293} = 0.721$, at 10 K as $f_{10} = 0.908$ and at 600 K as $f_{600} = 0.522$.

Table 5.26. Debye temperatures reported for Fe₃C.

Source	Fe₃C θ_D Reported (K)	Calculation Method
This work	357	Mössbauer Spec.
Ledbetter [69]	501	Elastic Modulus
Wood [50]	604	Neutron Diffraction
Ghosh [70]	332	First Principle Calc.
Guillermet and Grimvall [71]	394	First Principle Calc.
Le Caer [38]	350	

The work in this study concerns isolated nanoparticles of Fe₃C, which is most comparable with the works of Ghosh and Guillermet [70], [71], where the Debye temperatures reported are from first principle calculations. Ledbetter used materials annealed at 773 K [69] and Wood sintered at 1.5 GPa and between 1473 – 1523 K for 30 minutes [50]. The difference in synthesis methods, producing different particle sizes, will influence the thermal stability of the product Fe₃C, and therefor the Debye temperature. The 1976 publication by Le Caer [38] reports a Debye temperature of 350 K, for cementite isolated by electrolytic extraction from heat treated iron-carbon alloys. Their method for calculating the Debye temperature utilises the temperature induced change in centre shift, similar to the method used at SHU. Ledbetter calculated their Debye temperature by extrapolating data gathered by acoustic measurements, using the relationship between the Debye temperature and sound velocity through a material [69]. Wood calculated their reported Debye temperature from neutron diffraction data, and Tsuzuki from vibrating sample magnetometry [50], [72]. The closest agreement of reported Debye temperatures and that of this work is between the works of La Caer, with small, unsintered particles, and theoretical approximations from Ghosh and Guillermet. This relationship between a decreased particle size resulting in reduced Debye temperatures has previously been reported [73]–[75] and a quantification of this relationship suggested as [76], [77];

$$\theta_D = \theta_{D\infty} \left(1 - \frac{2d}{\eta D}\right)^{1/2} \tag{3}$$

Where θ_D is the Debye temperature of the nanoparticle, $\theta_{D\infty}$ is the Debye temperature of the bulk material, D is the particle size, η is the atomic packing factor and *d* is the atomic diameter. The effect of annealing amorphous alloys has been explored by Partiti [78], [79] where annealing was found to increase the

188

Debye temperature, explained by the stiffening of atomic vibrations induced by structural relaxation. The decrease of particle size resulting in a decreased Debye temperature, and the increased Debye temperature caused by annealing are both consistent with the observations of the presently reported value for the Debye temperature of Fe_3C and comparison with previously reported values.

The same approximation procedure was carried out on the Mössbauer spectroscopy data for the Fe_5C_2 nanoparticles analysed, the outputs of which are compiled, along with those of Fe_3C, in Table 5.27.

Table 5.27. Summary of approximated isomer shifts, Debye temperatures and recoil-free fractions of Fe_3C and the three sextets of Fe_5C_2.

	Uncertainty	Fe_5C_2 S1	Fe_5C_2 S2	Fe_5C_2 S3	Fe_3C
Isomer Shift (mm s^{-1})	± 0.02	0.454	0.434	0.456	0.419
Debye Temp (K)	± 10	439	377	345	357
f_{10}	± 0.02	0.924	0.913	0.906	0.909
f_{293}	± 0.02	0.799	0.746	0.706	0.722
f_{600}	± 0.02	0.644	0.560	0.500	0.523
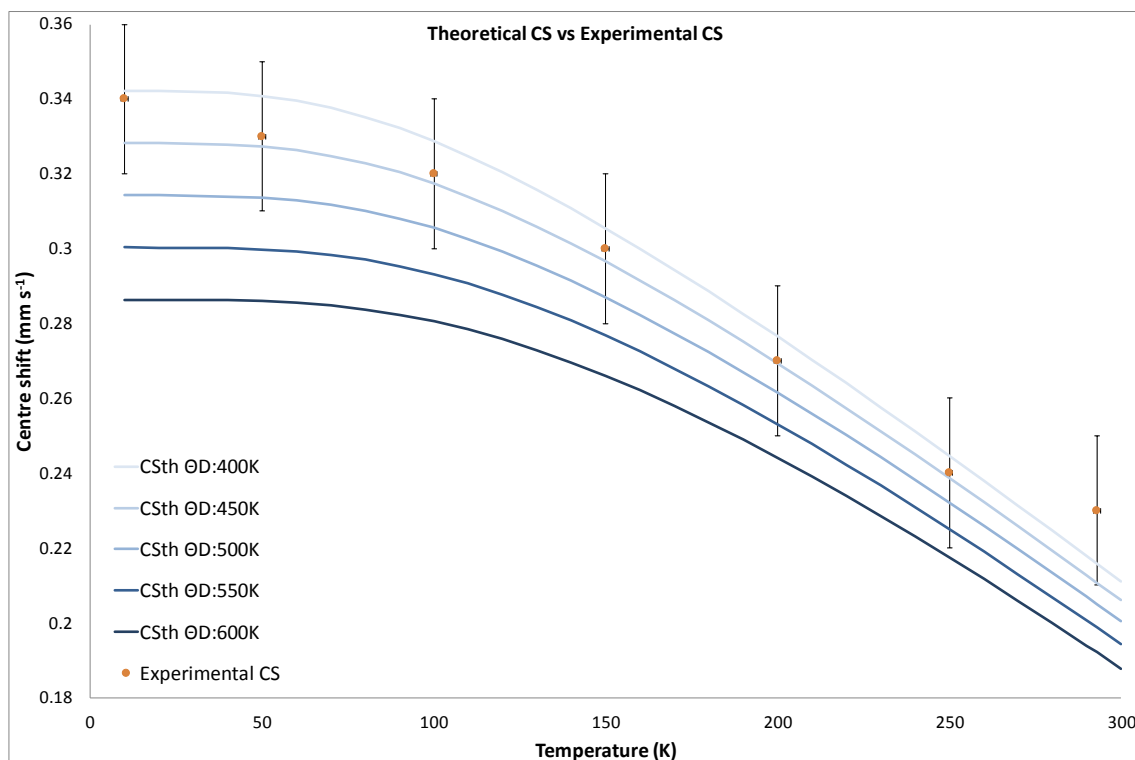
Figure 5.28. Theoretical centre shifts for modelled Debye temperatures and experimental centre shift data for Fe_5C_2 sextet 1.
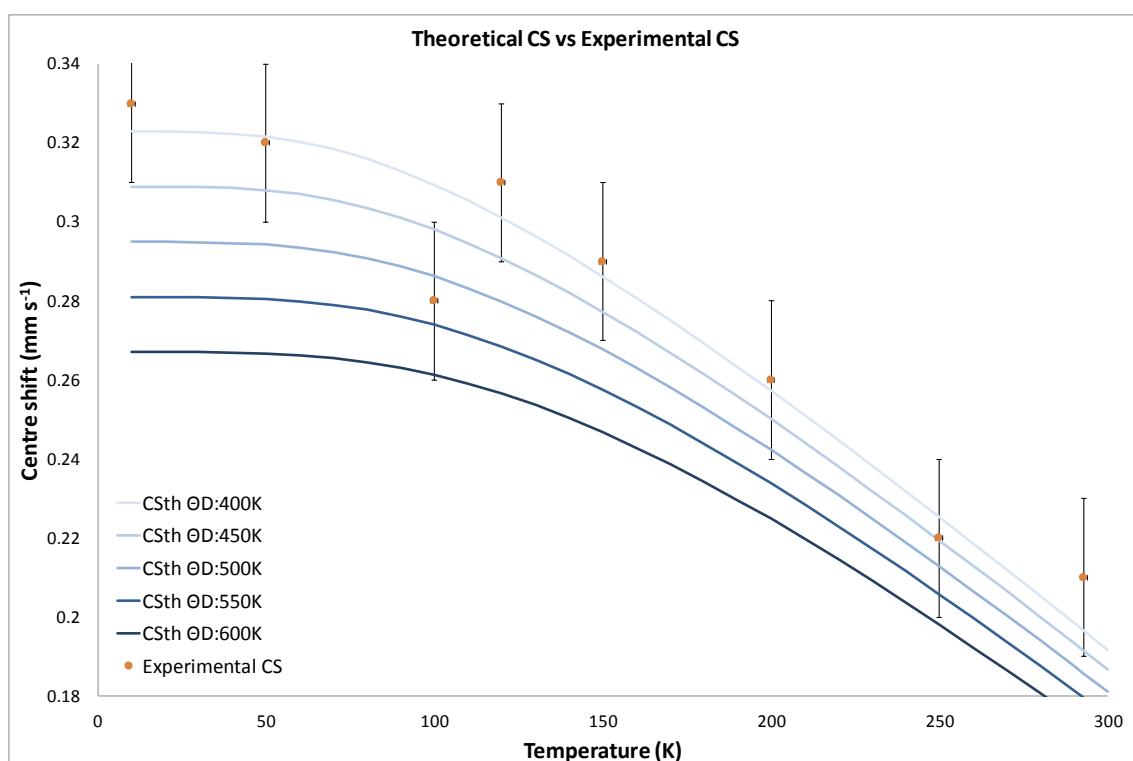

Figure 5.29. Theoretical centre shifts for modelled Debye temperatures and experimental centre shift data for Fe_5C_2 sextet 2.
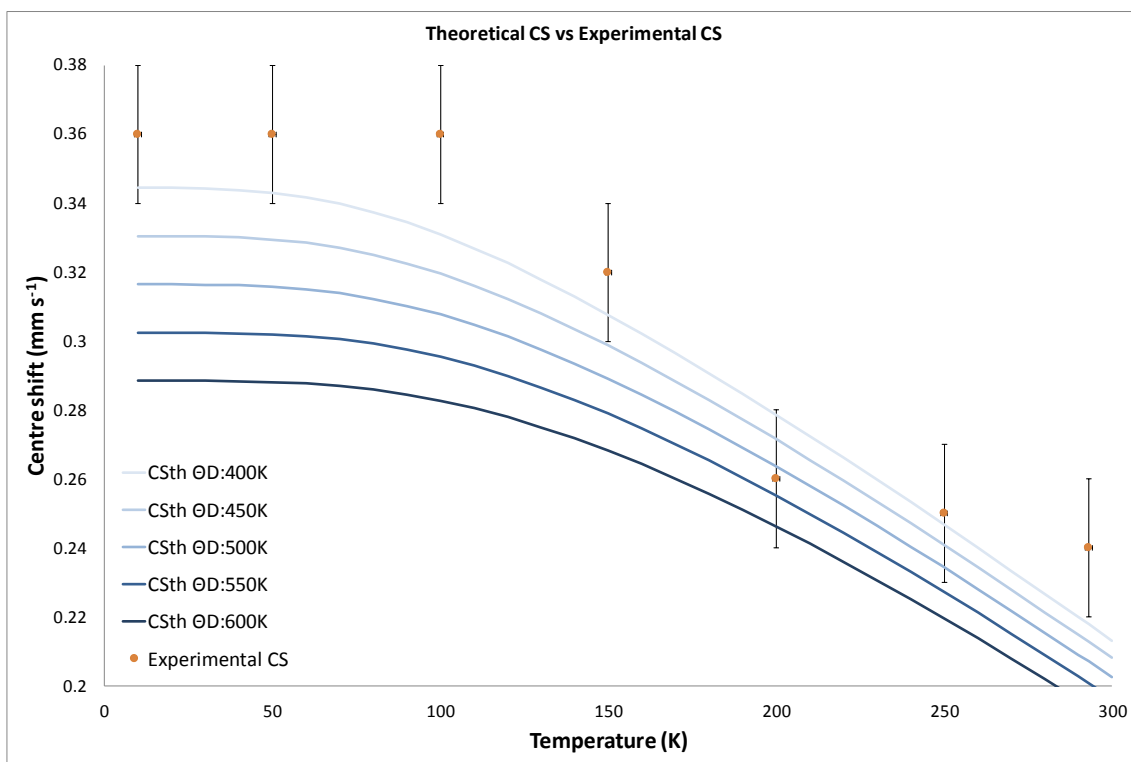
Figure 5.30. Theoretical centre shifts for modelled Debye temperatures and experimental centre shift data for Fe_5C_2 sextet 3.

Due to the Mössbauer spectra of Fe_5C_2 being more complex than that of Fe_3C the sum of the differences for between the theoretical and experimental centre shifts are greater for the three Fe_5C_2 sites analysed. As shown in figures 5.8 to 5.10, the experimental Centre Shifts do not follow the expected curves predicted by the Debye model as closely as for the single sextet analysed for Fe_3C in Figure 5.27. The centre shifts of all three Fe_5C_2 sextets are consistently greater than expected at room temperature. In Figure 5.29 it is shown that the centre shift of Fe_5C_2 sextet two is not in agreement with the expected trend at 100 K, as such this result was excluded from the approximation procedure. The reduced CS value from 150 to 100 K caused errors with the program which expects a reduction in temperature to cause either an increase in centre shift, or no change, and as such the 125 K spectral data was introduced instead. The third sextet of Fe_5C_2 is clearly present, however due to the overlapping of absorption peaks it is difficult to obtain precise hyperfine parameters for this site. This is particularly relevant with the lower temperature measurements, where the third sextet attributed to Fe_5C_2 account for < 10 % of the total spectral area. The high

difference between the experimental and theoretical Centre Shifts of this site reflects the difficulty to give precise site parameters.

Table 5.28. Debye temperatures of Fe_5C_2 iron sites.

	Site 1	Site 2	Site 3
Present work (K)	439 ± 10	377 ± 10	345 ± 10
La Caer [38] (K)	300	370	

The variable temperature Mössbauer spectra of these near phase-pure Fe_3C and Fe_5C_2, and the recoil-free fractions approximated, allow for the identification and semi-quantification of these phases in mixed-phase materials. There is limited data available regarding the Debye temperature of Fe_5C_2, with the only source found by the author first being published in 1976 [38]. In the work by La Caer, Dubois and Senateur, the Debye temperature is approximated by the variations of isomer shift with temperature, comparable with the method used in the present study. The improved spectrometer and computing capabilities of the present study allow for greater temperature resolution where T < 293 K, and more advanced computational analysis for the approximation process. The 1976 data was gathered using Fe_5C_2 obtained by the carburation of metallic iron and Fe_2O_3 at 400 °C under CO and H_2, and using only 5 temperatures, from 4 to 428 K.

For the JMFT materials, no variable temperature studies were conducted. The low degree of iron reduction that occurred from the test parameters did not provide sufficient spectral variety between the fresh material and the tested material for a more comprehensive study of this effect. The concentration of silica [16], [19] and reduction conditions [80], [81] have both been reported amongst influencing factors on the resulting Mössbauer spectra for such materials. A more complete study on these materials would involve various reaction condition, where temperature, pressure and gas flows varied. The two materials included herein may be better characterised by low temperature measurements, where the doublets may resolve into magnetically ordered components, allowing for definitive phase identification. The doublets presented can only confidently show a semi-quantitative iron redox ratio in the materials, as the support matrix, particle size and an amorphous material could all result in similarly fit doublets. A study of this nature may use the information gathered from the Fe_3C and Fe_5C_2 studies

to better identify these phases in these mixed phase systems, and the approximation of their recoil-free factors allows for their relative quantification.

5.6 Conclusions

Through these variable temperature Mössbauer spectroscopic studies the Debye temperatures and recoil-free fractions for nanoparticles of two iron carbide phases, with importance in various industrial applications, have been approximated. Comparisons between reported values and those in existing literature show good agreement where the materials studied in literature are comparable to those studied here – i.e. are nanoparticulate. Approximations of the recoil-free fractions of these materials enables their relative abundances to be quantified in mixed-phase systems, an ability that may prove useful for a number of applications, particularly catalysis. The matrix within which the carbide phases are found was found to influence the resulting Debye temperature, by comparing values found within literature and with those approximated herein. The Debye temperatures of the materials studied in this work are relevant to the forms that would be of interest for catalytic applications – i.e. nanoparticles – while the Debye temperature of Fe_3C is shown to increase for sintered or annealed materials in existing literature.

References

[1]   P. D. Howe, M. Mildenberger, J. R. Marlon, and A. Leiserowitz, "Geographic variation in opinions on climate change at state and local scales in the USA," *Nat. Clim. Chang.*, vol. 5, p. 596, Apr. 2015.

[2]   J. Hansen, R. Ruedy, M. Sato, and K. Lo, "Global surface temperature change," *Rev. Geophys.*, vol. 48, no. 4, p. RG4004, 2010.

[3]   NASA, "GISS Surface Temperature Analysis (GISTEMP)," 2017. [Online]. Available: https://data.giss.nasa.gov/gistemp/. [Accessed: 16-Nov-2017].

[4]   Arctic Climate Impact Assessment, "Impacts of a Warming Arctic," 2004.

[5]   H. Craig, Y. Horibe, and T. Sowers, "Gravitational Separation of Gases and Isotopes in Polar Ice Caps," *Am. Assoc. Adv. Sci.*, vol. 242, no. 4886, pp. 1675–1678, 1988.

[6]   UNFCCC, "Paris Agreement," *Conf. Parties its twenty-first Sess.*, vol. 21932, no. December, p. 32, 2015.

[7]   IPCC, *Climate Change 2014: Mitigation of Climate Change*. 2014.

[8]   Environmental Protection Agency, "Climate Change Indicators: Global Greenhouse Gas Emissions." [Online]. Available: http://www.epa.gov/climatechange/climate-change-waste/. [Accessed: 01-Oct-2016].

[9]   Intergovernmental Panel on Climate Change, "IPCC Fourth Assessment Report: Climate Change 2007," 2007. [Online]. Available: https://www.ipcc.ch/publications_and_data/ar4/wg1/en/faq-2-1.html. [Accessed: 16-Nov-2017].

[10]   J. Ahn *et al.*, "Atmospheric CO2 over the last 1000 years: A high-resolution record from the West Antarctic Ice Sheet (WAIS) Divide ice core," *Global Biogeochem. Cycles*, vol. 26, no. 2, pp. 1–11, 2012.

[11]   Environmental Protection Agency, "Analysis of Biodiesel Impacts on Exhaust Emissions Draft Technical Report," 2002.

[12]   S. K. Yoon, M. S. Kim, H. J. Kim, and N. J. Choi, "Effects of canola oil biodiesel fuel blends on combustion, performance, and emissions reduction in a common rail diesel engine," *Energies*, vol. 7, no. 12, pp. 8132–8149, 2014.

[13]   G. Ferrari and S. E. Esculapio, *Internal Combustion Engines*. Società Editrice Esculapio, 2014.

[14]   BP, "Statistical Review of World Energy," *BP Stat. Rev. World Energy*, no. June, pp. 1–48, 2016.

[15]   U.S. Energy Information Administration, "Biofuels: Ethanol and Biodiesel Explained. Use of Biodiesel," 2017. [Online]. Available: https://www.eia.gov/energyexplained/index.cfm?page=biofuel_biodiesel_ use. [Accessed: 17-Nov-2017].

[16]   K. Cheng *et al.*, "Support effects in high temperature Fischer-Tropsch synthesis on iron catalysts," *Appl. Catal. A Gen.*, vol. 488, pp. 66–77, 2014.

[17]   W. Ma *et al.*, "Fischer-Tropsch synthesis: Effect of ammonia in syngas on the Fischer-Tropsch synthesis performance of a precipitated iron catalyst," *J. Catal.*, vol. 326, no. x, pp. 149–160, 2015.

[18]   T. Herranz, S. Rojas, F. J. Pérez-Alonso, M. Ojeda, P. Terreros, and J. L. G. Fierro, "Genesis of iron carbides and their role in the synthesis of hydrocarbons from synthesis gas," *J. Catal.*, vol. 243, no. 1, pp. 199–211, 2006.

[19]   K. Cheng *et al.*, "Pore size effects in high-temperature Fischer–Tropsch synthesis over supported iron catalysts," *J. Catal.*, vol. 328, pp. 139–150, 2015.

[20]   D. J. McCracken, "Hydrocarbon Combustion and Physical Properties," 1970.

[21]   F. J. Berry, "Industrial applications of Mössbauer spectroscopy," *Hyperfine Interact.*, vol. 144–145, no. 1–4, pp. 381–390, 2002.

[22]   V. R. Calderone *et al.,* "De novo design of nanostructured iron-cobalt

fischer-tropsch catalysts," *Angew. Chemie - Int. Ed.*, vol. 52, no. 16, pp. 4397–4401, 2013.

[23] B. C. Enger and A. Holmen, "Nickel and Fischer-Tropsch synthesis," *Catal. Rev. - Sci. Eng.*, vol. 54, no. 4, pp. 437–488, 2012.

[24] Johnson Matthey, "Delivering world class catalysts for Gas to Liquids," 2014.

[25] T. H. Pham *et al.*, "Insights into Hagg Iron-Carbide-Catalyzed Fischer-Tropsch Synthesis: Suppression of CH_4 Formation and Enhancement of C-C Coupling on χ-Fe_5C_2 (510)," *ACS Catal.*, vol. 5, no. 4, pp. 2203–2208, 2015.

[26] J. a. Amelse, J. B. Butt, and L. H. Schwartz, "Carburization of supported iron synthesis catalysts," *J. Phys. Chem.*, vol. 82, no. 5, pp. 558–563, 1978.

[27] D. H. Chun *et al.*, "Highly selective iron-based Fischer-Tropsch catalysts activated by CO_2-containing syngas," *J. Catal.*, vol. 317, pp. 135–143, 2014.

[28] G. Le Caer, J. M. Dubois, M. Pijolat, V. Perrichon, and P. Bussiere, "Characterization by Moessbauer Spectroscopy of Iron Carbides Formed by Fischer-Tropsch Synthesis," *J. Phys. Chem.*, vol. 86, no. 24, pp. 4799–4808, 1982.

[29] E. de Smit and B. M. Weckhuysen, "The renaissance of iron-based Fischer-Tropsch synthesis: on the multifaceted catalyst deactivation behaviour.," *Chem. Soc. Rev.*, vol. 37, pp. 2758–2781, 2008.

[30] M. Sarkari, F. Fazlollahi, H. Ajamein, H. Atashi, W. C. Hecker, and L. L. Baxter, "Catalytic performance of an iron-based catalyst in Fischer-Tropsch synthesis," *Fuel Process. Technol.*, vol. 127, pp. 163–170, 2014.

[31] E. De Smit *et al.*, "Stability and Reactivity of E-X-θ Iron Carbide Catalyst Phases in Fischer - Tropsch Synthesis : Controlling μC - Supporting information," *J. Am. Chem. Soc.*, no. 5, pp. 14928–14941, 2010.

[32] A. Scrimshire, A. Lobera, R. Kultyshev, P. Ellis, S. D. Forder, and P. A.

Bingham, "Variable Temperature ^{57}Fe-Mössbauer Spectroscopy Study of Nanoparticle Iron Carbides," *Croat. Chem. Acta*, vol. 88, no. 4, pp. 531–537, 2015.

[33] J. Brown, "Foseco Ferrous Foundryman Handbook," p. 76, 2000.

[34] Q. Su, G. Zhong, J. Li, G. Du, and B. Xu, "Fabrication of Fe/Fe_3C-functionalized carbon nanotubes and their electromagnetic and microwave absorbing properties," *Appl. Phys. A Mater. Sci. Process.*, vol. 106, pp. 59–65, 2012.

[35] J. Yu *et al.*, "Multifunctional Fe_5C_2 nanoparticles: A targeted theranostic platform for magnetic resonance imaging and photoacoustic tomography-guided photothermal therapy," *Adv. Mater.*, vol. 26, no. 24, pp. 4114–4120, 2014.

[36] J. Yu *et al.*, "Iron carbide nanoparticles: an innovative nanoplatform for biomedical applications," *Nanoscale Horiz.*, vol. 2, no. 2, pp. 81–88, 2017.

[37] B. David, O. Schneeweiss, F. Dumitrache, C. Fleaca, R. Alexandrescu, and I. Morjan, "Powders with superparamagnetic Fe_3C particles studied with Mössbauer spectrometry," *J. Phys. Conf. Ser.*, vol. 217, p. 012097, 2010.

[38] G. Le Caer, J. M. Dubois, and J. P. Senateur, "Etude par spectrométrie Mössbauer des carbures de Fer Fe_3C et Fe_5C_2," *J. Solid State Chem.*, vol. 19, no. 1, pp. 19–28, 1976.

[39] J. W. Niemantsverdriet *et al.*, "Behavior of metallic iron catalysts during Fischer-Tropsch synthesis studied with Moessbauer spectroscopy, X-ray diffraction, carbon content determination, and reaction kinetic measurements," *J. Phys. Chem.*, vol. 84, pp. 3363–3370, 1980.

[40] V. A. Volkov, A. A. Chulkina, I. A. El'kin, and E. P. Elsukov, "Formation of carbide phases upon the mechanosynthesis of the $(Fe_{0.93}Cr_{0.07})_{75}C_{25}$ alloy compared with other carbide-forming processes," *Phys. Met. Metallogr.*, vol. 117, no. 2, pp. 178–187, 2016.

[41] R. Miyatani, Y. Yamada, and Y. Kobayashi, "Mössbauer study of iron

carbide nanoparticles produced by sonochemical synthesis," *J. Radioanal. Nucl. Chem.*, vol. 303, pp. 1503–1506, 2015.

[42] O. Schneeweiss, R. Zbořil, B. David, M. Heřmánek, and M. Mashlan, "Solid-state synthesis of α-Fe and iron carbide nanoparticles by thermal treatment of amorphous Fe_2O_3," *Hyperfine Interact.*, vol. 189, pp. 167–173, 2009.

[43] C. K. Ande and M. H. F. Sluiter, *First-Principles Calculations on Stabilization of Iron Carbides (Fe₃C, Fe₅C₂, and η-Fe2C) in Steels by Common Alloying Elements*, vol. 43, no. 11. 2012.

[44] Z. Schnepp, S. C. Wimbush, M. Antonietti, and C. Giordano, "Synthesis of highly magnetic iron carbide nanoparticles via a biopolymer route," *Chem. Mater.*, vol. 22, no. 18, pp. 5340–5344, 2010.

[45] C. Yang, H. Zhao, Y. Hou, and D. Ma, "Fe_5C_2 nanoparticles: A facile bromide-induced synthesis and as an active phase for Fischer-Tropsch synthesis," *J. Am. Chem. Soc.*, vol. 134, no. 38, pp. 15814–15821, 2012.

[46] D. J. Duvenhage *et al.*, "Catalyst for low temperature slurry bed fischer-tropsch synthesis," 2017.

[47] E. S. Lox, G. B. Marin, E. De Grave, and P. Bussière, "Characterization of a promoted precipitated iron catalyst for Fischer-Tropsch synthesis," *Appl. Catal.*, vol. 40, no. C, pp. 197–218, 1988.

[48] H. Hayakawa, H. Tanaka, and K. Fujimoto, "Preparation of a new precipitated iron catalyst for Fischer-Tropsch synthesis," *Catal. Commun.*, vol. 8, no. 11, pp. 1820–1824, 2007.

[49] D. J. Duvenhage, C. Schmidt, and H. W. Wright, "Precipitated iron Fischer-Tropsch catalyst manufacturing: Impact of Hematite," *J. Mater. Sci.*, vol. 49, no. 7, pp. 2810–2823, 2014.

[50] I. G. Wood *et al.*, "Thermal expansion and crystal structure of cementite, Fe_3C, between 4 and 600 K determined by time-of-flight neutron powder diffraction," *J. Appl. Crystallogr.*, vol. 37, no. 1, pp. 82–90, 2004.

[51] H. E. Du Plessis, J. P. R. De Villiers, G. J. Kruger, A. Steuwer, and M.

Brunelli, "Rietveld and pair distribution function study of Hägg carbide using synchrotron X-ray diffraction," *J. Synchrotron Radiat.*, vol. 18, no. 2, pp. 266–271, 2011.

[52] B. Singh, J. R. Long, G. C. Papaefthymiou, and P. Stavropoulos, "On the reduction of basic iron acetate: Isolation of ferrous specis mediating Gif-type oxidation of hydrocarbons," *J. Am. Chem. Soc.*, vol. 118, no. 24, pp. 5824–5825, 1996.

[53] K. Xu *et al.*, "ε -Iron carbide as a low-temperature Fischer-Tropsch synthesis catalyst," *Nat. Commun.*, vol. 5, pp. 1–8, 2014.

[54] O. Schneeweiss *et al.*, "Mössbauer and Magnetic Studies of Nanocrystalline Iron, Iron Oxide and Iron Carbide Powders Prepared from Synthetic Ferrihydrite," *AIP Conf. Proc.*, no. December 2014, pp. 106–113, 2008.

[55] J. M. Genin, C. Le G., and A. Simon, "Mössbauer spectroscopy of the transformatin of ε carbide during the tempering of iron carbide martensite - the existence of highly faulted cementite.," in *Proc. - Int. Conf. Moessbauer Spectrosc., 5th*, 1975, vol. 1–3, pp. 318–327.

[56] H. Bernas, I. A. Campbell, and R. Fruchart, "Electronic exchange and the Mössbauer effect in iron-based interstitial compounds," *J. Phys. Chem. Solids*, vol. 28, no. 1, pp. 17–24, 1967.

[57] W. Kundig and H. Bommel, "Some Properties of Supported Small alpha-Fe_2O_3 Particles Determined with the Mossbauer Effect," *Phvsical Rev.*, vol. 59, no. 1965, p. 327, 1966.

[58] M. Polikarpov, V. Cherepanov, M. Chuev, S. Shishkov, and S. Yakimov, "Mössbauer spectra of hematite and magnetite nanoparticles in polymer composites," *J. Phys. Conf. Ser.*, vol. 217, p. 012114, 2010.

[59] R. L. Cohen, *Applications of Mossbauer Spectroscopy*. Elsevier Science, 2012.

[60] B. R. Guduri and A. S. Luyt, "Structure and Mechanical Properties of Polycarbonate Modified Clay Nanocomposites," *J. Nanosci. Nanotechnol.*,

vol. 8, no. 4, pp. 1880–1885, 2008.

[61] V. A. Drits, "Structural Model for Ferrihydrite," *Clay Miner.*, vol. 28, no. 2, pp. 185–207, 1993.

[62] E. Jansen, A. Kyek, W. Schäfer, and U. Schwertmann, "The structure of six-line ferrihydrite," *Appl. Phys. A Mater. Sci. Process.*, vol. 74, no. SUPPL.II, pp. 1004–1006, 2002.

[63] T. Hiemstra and W. H. Van Riemsdijk, "A surface structural model for ferrihydrite I: Sites related to primary charge, molar mass, and mass density," *Geochim. Cosmochim. Acta*, vol. 73, no. 15, pp. 4423–4436, 2009.

[64] F. Marc Michel *et al.*, "The Structure of Ferrihydrite, a Nanocrystalline Material," *Science (80-.).*, vol. 316, no. June, pp. 1726–1729, 2007.

[65] R. G. Burns, "Mineral Mössbauer spectroscopy: Correlations between chemical shift and quadrupole splitting parameters," *Hyperfine Interact.*, vol. 91, no. 1, pp. 739–745, Dec. 1994.

[66] M. D. Dyar, D. G. Agresti, M. W. Schaefer, C. A. Grant, and E. C. Sklute, "Mössbauer Spectroscopy of Earth and Planetary Materials," *Annu. Rev. Earth Planet. Sci.*, vol. 34, no. 1, pp. 83–125, 2006.

[67] O. Clemens, F. J. Berry, J. Bauer, A. J. Wright, K. S. Knight, and P. R. Slater, "Synthesis, structural and magnetic characterisation of the fluorinated compound 15R-BaFeO$_2$F," *J. Solid State Chem.*, vol. 203, pp. 218–226, 2013.

[68] E. Zepeda-Alarcon *et al.*, "Magnetic and nuclear structure of goethite (α-FeOOH): A neutron diffraction study," *J. Appl. Crystallogr.*, vol. 47, no. 6, pp. 1983–1991, 2014.

[69] H. Ledbetter, "Polycrystalline elastic constants of in situ cementite (Fe$_3$C)," *Mater. Sci. Eng. A*, vol. 527, no. 10–11, pp. 2657–2661, 2010.

[70] G. Ghosh, "A first-principles study of cementite (Fe$_3$C) and its alloyed counterparts : Elastic constants , elastic anisotropies , and isotropic elastic moduli A first-principles study of cementite (Fe$_3$C) and its alloyed

counterparts : Elastic constants , elast," *AIP Adv.*, vol. 5, 2015.

[71] A. F. Guillermet and G. Grimvall, "Cohesive properties and vibrational entropy of 3d-transition metal carbides," *J. Phys. Chem. Solids*, vol. 53, no. 1, pp. 105–125, 1992.

[72] A. Tsuzuki, S. Sago, S.-I. Hirano, and S. Naka, "High temperature and pressure preparation and properties of iron carbides Fe_7C_3 and Fe_3C," *J. Mater. Sci.*, vol. 19, no. 8, pp. 2513–2518, Aug. 1984.

[73] G. R. Patel, N. A. Thakar, and T. C. Pandya, "Effect of size on specific heat and Debye temperature of nanomaterials," *AIP Conf. Proc.*, vol. 1728, no. 1, p. 20138, May 2016.

[74] K. Bian, W. Bassett, Z. Wang, and T. Hanrath, "The strongest particle: Size-dependent elastic strength and Debye temperature of PbS nanocrystals," *J. Phys. Chem. Lett.*, vol. 5, no. 21, pp. 3688–3693, 2014.

[75] M. Hou, M. El Azzaoui, H. Pattyn, J. Verheyden, G. Koops, and G. Zhang, "Growth and lattice dynamics of Co nanoparticles embedded in Ag: A combined molecular-dynamics simulation and Mössbauer study," *Phys. Rev. B*, vol. 62, no. 8, p. 5117, 2000.

[76] Y. D. Qu, X. L. Liang, X. Q. Kong, and W. J. Zhang, "Size-dependent cohesive energy, melting temperature, and Debye temperature of spherical metallic nanoparticles," *Phys. Met. Metallogr.*, vol. 118, no. 6, pp. 528–534, 2017.

[77] R. Kumar and M. Kumar, "Effect of size on cohesive energy, melting temperature and Debye temperature of nanomaterials," *Indian J. Pure Appl. Phys.*, vol. 50, no. 5, pp. 329–334, 2012.

[78] C. S. M. Partiti and H. R. Rechenberg, "Debye Temperature Change Induced by Structural Relaxation in $Fe_{78}B_{13}Si_9$ Metallic Glass," *Phys. status solidi*, vol. 145, no. 1, pp. K17--K20, 1994.

[79] C. S. M. Partiti, I. G. Rocha, and J. M. Gonzalez, "Mössbauer Study of the $Fe_{64.5}Co_{18}SiB_{16}C_{0.5}$ Amorphous Alloy," *Hyperfine Interact.*, pp. 21–24, 1997.

[80] V. P. Santos *et al.*, "Metal organic framework-mediated synthesis of highly active and stable Fischer-Tropsch catalysts," *Nat. Commun.*, vol. 6, p. 6451, 2015.

[81] J. W. Niemantsverdriet and W. N. Delgass, "In situ Mössbauer spectroscopy in catalysis," *Top. Catal.*, vol. 8, pp. 133–140, 1999.

6. Iron Molybdate Catalysts for Oxidation of Methanol to Formaldehyde

6.1 Introduction

Formaldehyde, otherwise known as methanal, CH_2O, consists of a central carbon atom, single bonded to two hydrogen atoms and double bonded to one oxygen atom, with all bond angles at 120°, creating a trigonal planar molecule. An *aldehyde* group is formed of the carbon atom, with the double bonded oxygen and single bonded hydrogen, formaldehyde is the simplest member of this group, where its functional *R* group is simply a second hydrogen. First synthesised by Aleksandr Mikhailovich Butlerov in 1858 [1], and originally called *formalin*, isolated formaldehyde is chemically unstable and will spontaneously polymerise into insoluble polyoxymethylene $((CH_2O)_n)$. The uses of formaldehyde itself are limited, due to its toxicity, volatility and acknowledgement as a human carcinogen [2]. Formaldehyde can be found, and used in many different applications, such as embalming fluids [3], resins for particle board and plywood [4], [5]. Applications for derivatives of formaldehyde are wide-reaching, including textiles, adhesives, paints, explosives, and the synthesis of some plastics. The ability for this functional *R* group to be substituted for other chemical groups allows the wide use of formaldehyde as a precursor to these more complex compounds. One particularly noteworthy application of formaldehyde is the synthesis of the early thermosetting plastic, Bakelite, in 1909 by L H Baekeland [6]. Bakelite is synthesised by a condensation reaction with formaldehyde and phenol (C_6H_5OH), and was used as an electrically insulative casing for many electronics, including radios and telephones, as well as in toys, and a variety of wartime equipment [7]. In 2017, the annual global demand of formaldehyde reached 30 megatons per year [8]. Formaldehyde is mostly synthesised through the oxidation of methanol (CH_3OH) in the presence of a suitable catalyst, as illustrated in Figure 6.1, which depicts both the silver process and the metal oxide process [9]. The silver process, using a silver catalyst, involves simultaneous dehydrogenation and selective oxidation processes, whereas the metal oxide process only involves selective oxidation [10]–[13].

$\Delta H = 85 \text{ kJ mol}^{-1}$

$$H_2 + \tfrac{1}{2} O_2 \xrightarrow{\text{Catalyst}} H_2O$$

$\Delta H = -242 \text{ kJ mol}^{-1}$

$\Delta H = -156 \text{ kJ mol}^{-1}$
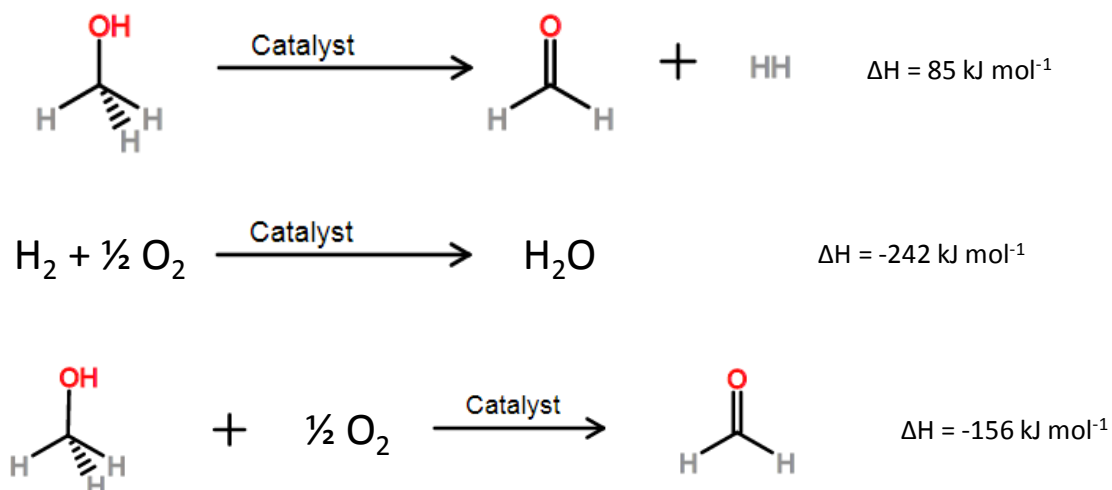
Figure 6.1. Simplified reaction pathways of the oxidation of methanol to formaldehyde [14]–[16]. Enthalpy changes for gas-phase reactions.

Molybdate oxides have been known to catalyse the oxidation of methanol to formaldehyde since at least 1931 when Adkins and Peterson presented iron, molybdenum and iron-molybdenum oxides as suitable catalysts [17]. The catalyst chamber used by Adkins and Peterson was designed and constructed by the Bakelite Corporation, suggesting their continued interest in formaldehyde. Modern reactors still use iron molybdates as their catalyst, from supplier such as Johnson Matthey [18], and there is still great interest in how these materials function, with a thorough review paper by Soares, Portela and Kiennemann in 2005 [19] and investigation into process improvements by Andersson, Holmberg and Häggblad in 2016 [9]. Multiple molybdate oxides have been found to be active catalysts for this reaction pathway, including K_2MoO_4, $CaMoO_4$, $Cr_2(MoO_4)_3$ and $Fe_2(MoO_4)_3$ [20], where the molybdenum is always Mo^{6+}. Allison and Goddard illustrated the surface of the molybdate catalyst in 1985, reproduced here in Figure 6.2. While the original authors do criticise this over-simplification, the illustration does serve a useful visualisation of the reaction.

$$\Delta H \approx +31.5 \text{ kcal/mol}$$
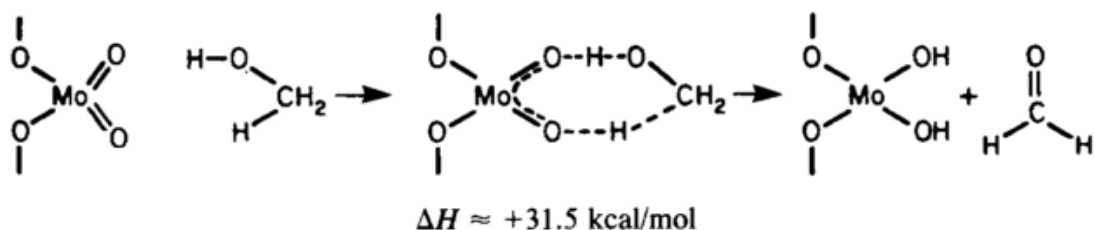
Figure 6.2. Simplified representation of molybdenum oxide catalyst surface [20].

Soares, Portela and Kiennemann present a more complete pathway, showing the adsorption of methanol and oxygen onto the surface of the catalyst, and the subsequent release of formaldehyde and water vapour, reproduced below, where square brackets represent an active site at the catalyst surface [19].

$$CH_3OH \text{ (g)} + [\ ] \leftrightarrow [CH_3OH]_{ads}$$

$$O_2 \text{ (g)} + [\ ] \leftrightarrow [O_2]_{ads}$$

$$[CH_3OH]_{ads} + [O_2]_{ads} \leftrightarrow CH_2O \text{ (g)} + [H_2O]_{ads} + [\ ]$$

$$[H_2O]_{ads} \leftrightarrow H_2O \text{ (g)} + [\ ]$$
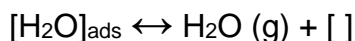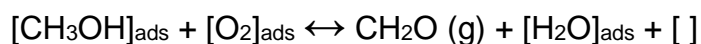
It can be seen in Figure 6.2 that with the molybdenum as Mo^{6+} there is an active site present to adsorb methanol, and upon release of formaldehyde the active site is reduced, where the two double bonded oxygen are left as two hydroxyl groups. The adsorption of oxygen re-oxidises the molybdenum to reactivate the site as the adsorbed water is released. This catalyst cycle was proposed by William Farneth and colleagues in 1985 [21], reproduced in Figure 6.3. This reaction cycle was later revised by McCarron, Harlow, Li, Suto and Yuen in 1998 to show the loss of α-MoO$_3$, a major deactivation mechanic [22]. In the 1931 study by Adkins and Peterson [17], differences between molybdenum oxide, iron oxide and iron-molybdenum oxide catalysts were characterised, with the summation of iron-molybdenum oxide proving the "best catalyst, so far described for the oxidation of methanol.", with > 90% conversion, with by-

products including CO_2, dimethylether (CH_3OCH_3) and methyl formate ($C_2H_4O_2$). The authors also provide evidence that the surface of these oxide catalysts are continually renewed during use, and "may be used continually for months", in reference to their stability.
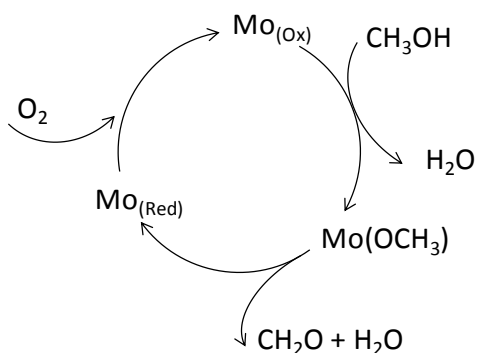
Figure 6.3. Catalyst cycle of CH_3OH oxidation over molybdate catalyst [21].

The model depicted in figures 6.1 through 6.3 are representative of the molybdate function of iron molybdate catalysts alone. The $Fe_2(MoO_4)_3$ phase of the catalyst is the more active phase, and this is understood to result from, not only the high Mo/Fe ratio at the surface, but the presence of Fe^{3+} ions enables a redox couple to exist between Fe and Mo, thus Mo^{4+} can be quickly re-oxidised to Mo^{6+} and in turn Fe^{3+} is reduced to Fe^{2+} [23]. In complex iron molybdate catalysts the surface is found to be molybdenum rich, present as MoO_X molybdate groups, with an iron rich core [13], [24]. The oxidation state of iron in the iron molybdate phases can vary between ferric and ferrous, as $Fe_2(MoO_4)_3$ and $FeMoO_4$ respectively, both of which host molybdenum (VI). As shown in Figure 6.3, oxidising methanol to formaldehyde involves the reduction of molybdenum to IV from VI; subsequent molybdenum oxidation can reactivate the catalyst site. The re-oxidation of molybdenum in this case can be facilitated by the reduction of the Fe(III) to Fe(II). The interactions between the iron and molybdenum, in the presence of oxygen, therefor maintains the $Fe_2(MoO_4)_3$ catalyst, with a molybdenum-rich surface and iron-rich core.

There are a number of theories regarding the deactivation mechanisms of such catalysts, although many involve molybdate loss. Iron rich sites, including iron oxide and $FeMoO_4$ produce more CO_2 from the over oxidation of formaldehyde, which becomes a concern as catalysts are aged. A simplified view of molybdate loss, following the redox catalytic process in which $Fe_2(MoO_4)_3$ is converted to $FeMoO_4$ and MoO_3 can be expressed as [25];

$$Fe_2(MoO_4)_3 + CH_3OH \rightarrow 2FeMoO_4 + MoO_3 + HCHO + H_2O$$

In this process, volatile MoO_3 groups are delaminated and iron is fixed in the ferrous $FeMoO_4$ structure, unable to facilitate re-oxidation of molybdenum. Further aging of the catalyst can lead to further molybdenum loss and Fe_2O_3 formation. The re-oxidation of $FeMoO_4$ can also result in the formation of Fe_2O_3 at the catalyst surface, such that;

$$3FeMoO_4 + \tfrac{3}{4}O_2 \rightarrow Fe_2(MoO_4)_3 + \tfrac{1}{2}Fe_2O_3$$

Conversely, the formation of volatile molybdate groups can be a result of the oxidation of $FeMoO_4$ and the formation of Fe_2O_3, as;

$$2FeMoO_4 + \tfrac{1}{2}O_2 \rightarrow Fe_2O_3 + 2MoO_3$$
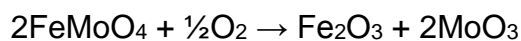
While this is a simplified overview of the deactivation mechanisms of these catalysts, the main phases formed through the process are included. To more completely discuss the processes involved would not be appropriate for this work and its diverse nature.

In this work four iron molybdate samples were studied in order to investigate the ageing mechanism and the effect of transition metal doping. Two industrial catalysts were studied, one being made in a Swedish plant and studied

as a *fresh catalyst*, the second taken from a U.S. plant after being used as a catalyst until such time that the catalyst required replacing, referred to as the *aged catalyst*. A lab-scale sample of the fresh catalyst material was prepared through a wet chemical synthesis route outlined in the following section, and was studied alongside a lab-made iron molybdate with 5 wt% Cu substitution (on the iron site) as a catalyst promoter, to study the effects of iron site doping. As the aging process of these catalysts can include the delamination of MoO_x groups and irreversible phase changes, the purpose of this investigation was to determine, where possible, which of these processes are being encountered in industry, under normal operation conditions.

6.2 Research Objectives

The studies conducted on iron molybdate catalysts were directed towards improving the understanding around catalyst ageing, and how to improve reactor productivity. The fresh catalyst used was an industrial material, and the spent catalyst was received from an industrial reactor operator. Various techniques were used by JMTC to analyse the spent material, including XRD, ICP and electron probe micro-analyser (EPMA). Mössbauer spectroscopy was considered to have great potential in providing further insightful information that would be directly relevant and useful for industries that involve formaldehyde production.

In comparing the fresh and spent catalysts from the production facility the aim was to determine whether Mössbauer spectroscopy could be used to characterise spent catalysts, for example whether there were additional non-crystalline phases not observed by more typical characterisation techniques, such as XRD. In specific customer cases, we aimed to learn whether Mössbauer spectroscopy could be used to identify reactor issues, such as if part of the overall catalyst load was aging more rapidly than in other parts. Considering the reactor being circular and containing thousands of reaction tubes, another question was whether can Mössbauer spectroscopy can be used to identify issues at specific locations within the reactor.

6.3 Material Characterisation

The industrial catalyst samples were prepared through co-precipitation, the specifics of which cannot be disclosed per commercial reasoning by JMTC, however, the following lab-scale approach is an approximation of the industrial process. The lab-scale material was synthesised through a nitrate precipitation route. 8g of ammonium dimolybdate was dissolved in 111.4 ml of deionised water. 3.31 ml of 25% aqueous ammonia solution was added which raised the temperature to 45 °C. The solution was heated to 60 °C and 2.99 mL of a 60% acetic acid solution was added to act as a pH buffer. The pH was adjusted to 4.95 through the addition of concentrated nitric acid. 7.563 g iron (III) nitrate nonahydrate was dissolved in 89.29 mL of deionised water. The iron nitrate solution was moderately stirred using a magnetic stirrer and was added to the ammonium solution using a peristaltic pump at a rate of 5 mL per minute; over 18 minutes. The reaction was left to take place over 2 hours before being decanted through filter paper using a Buchner funnel four times to attain the sample materials, which were subsequently washed to remove any nitrate residues. The copper-containing sample was prepared by wet milling ammonium paramolybdate with iron (III) nitrate and copper (II) nitrate (5 mol%), the nitrate salts were dissolved in a minimum amount of water.

X-ray diffraction of the fresh industrial material showed a majority $Fe_2(MoO_4)_3$ phase (PDF 01-083-1701, monoclinic unit cell, space group P21/a), and a minority contribution attributed to MoO_3 (PDF 00-035-0609, orthorhombic unit cell, space group Pbnm) as illustrated in the diffraction pattern in Figure 6.4. The aged catalyst sample diffraction pattern agreed with that of the fresh sample, with the addition of peaks attributed to α-$FeMoO_4$ (PDF No 00-022-1115, monoclinic unit cell, C2/m space group) and β-$FeMoO_4$ (PDF No 00-022-0628, monoclinic unit cell), see Figure 6.5. The X-ray diffraction pattern of the lab-made, copper-free sample diffraction data, shown in Figure 6.6, agrees with the pattern of the industrial sample, with a slight negative shift of all peaks suggesting lattice expansion or differences in sample height. The diffraction peak centred at ≈ 26.5 2θ, attributed to the (221) plane of $Fe_2(MoO_4)_3$ [26], is much less intense in the lab-made material, as highlighted in the inset of Figure 6.6, the reason for this is

unclear. Inductively coupled plasma mass spectrometry (ICP-MS) analysis indicated 53.7 and 13.3 wt% for molybdenum and iron respectively for the lab-made material. The X-ray diffraction pattern of the copper doped sample shows similar diffraction peaks to that of the fresh sample, assigned to $Fe_2(MoO_4)_3$ and MoO_3. All peaks in the copper doped sample are shifted by approximately -0.1 2θ, as presented in Figure 6.7, suggesting a small lattice expansion – no unique peaks were observed for the copper-containing material, indicating the copper is being successfully substituted into the lattice. Elemental mapping by electron microprobe micro-analyser, shown in Figure 6.8, shows well-dispersed iron and molybdenum throughout the catalyst, whereas aged catalyst, shown in Figure 6.9 show iron enrichment at the edges, as α-$FeMoO_4$, consistent with the deactivation mechanisms described.
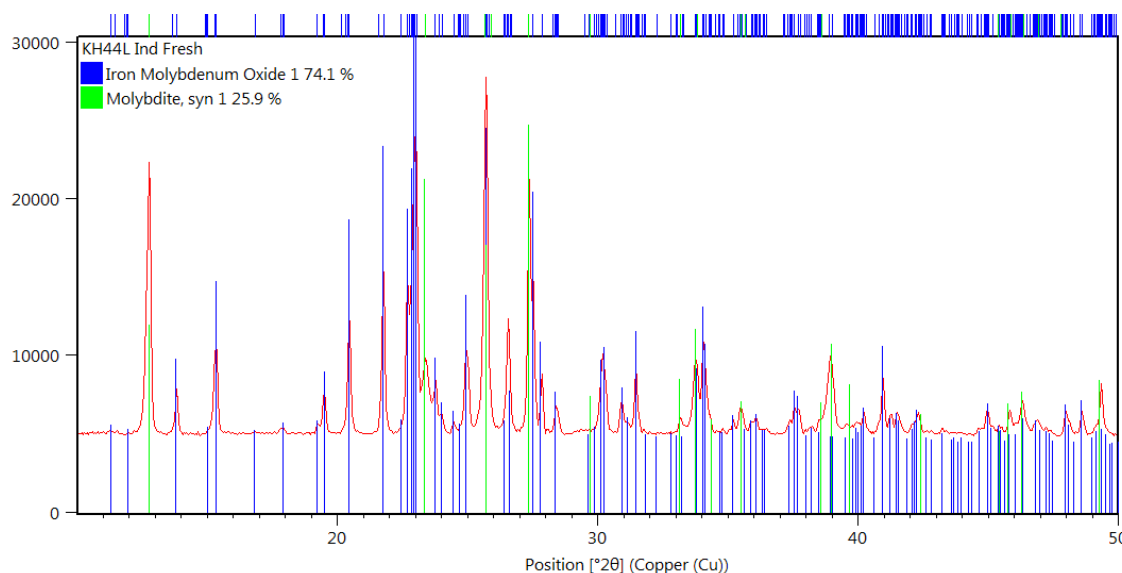
Figure 6.4. X-ray diffraction pattern of fresh industrial iron molybdate catalysts. Circles denote peaks assigned to MoO_3 (PDF #00-035-0609) and squares denote peaks assigned to $Fe_2(MoO_4)_3$ (PDF #01-083-1701).
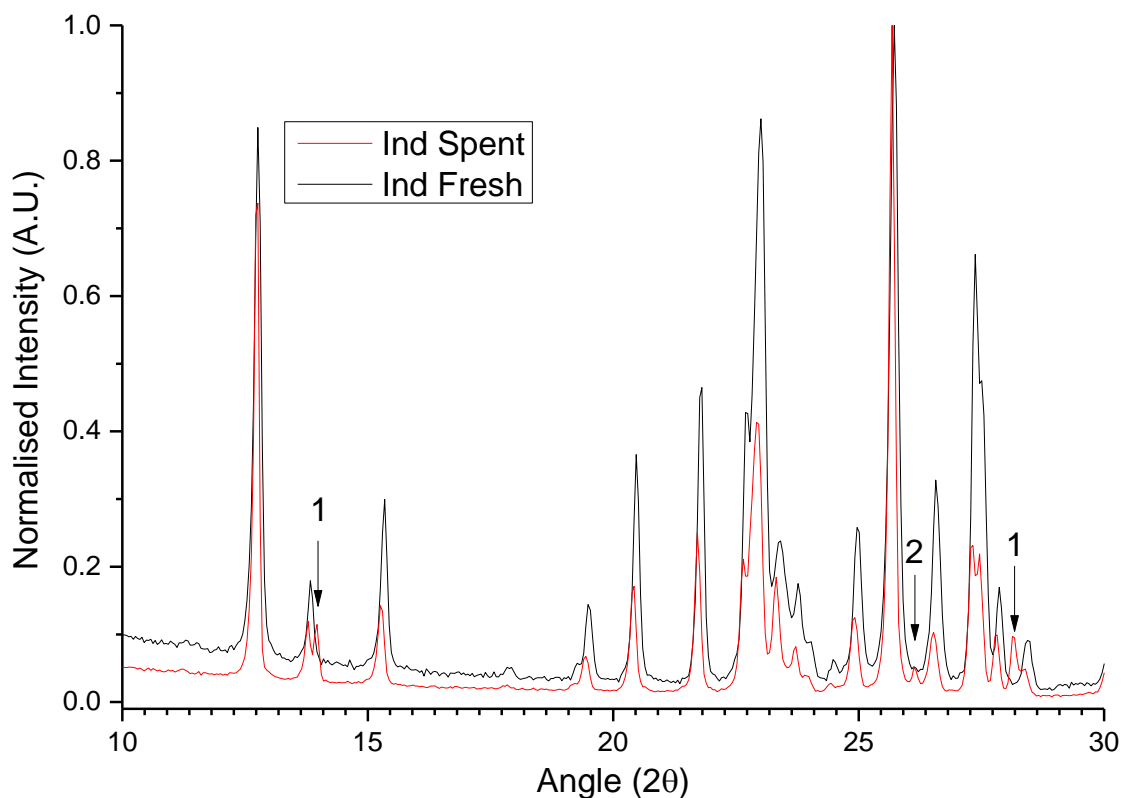
Figure 6.5. X-ray diffraction pattern of iron molybdate catalysts. Peaks highlighted with (1) assigned to α-FeMoO$_4$ (PDF 00-022-1115), and peak highlighted with (2) assigned to β-FeMoO$_4$ (PDF 00-022-0628).
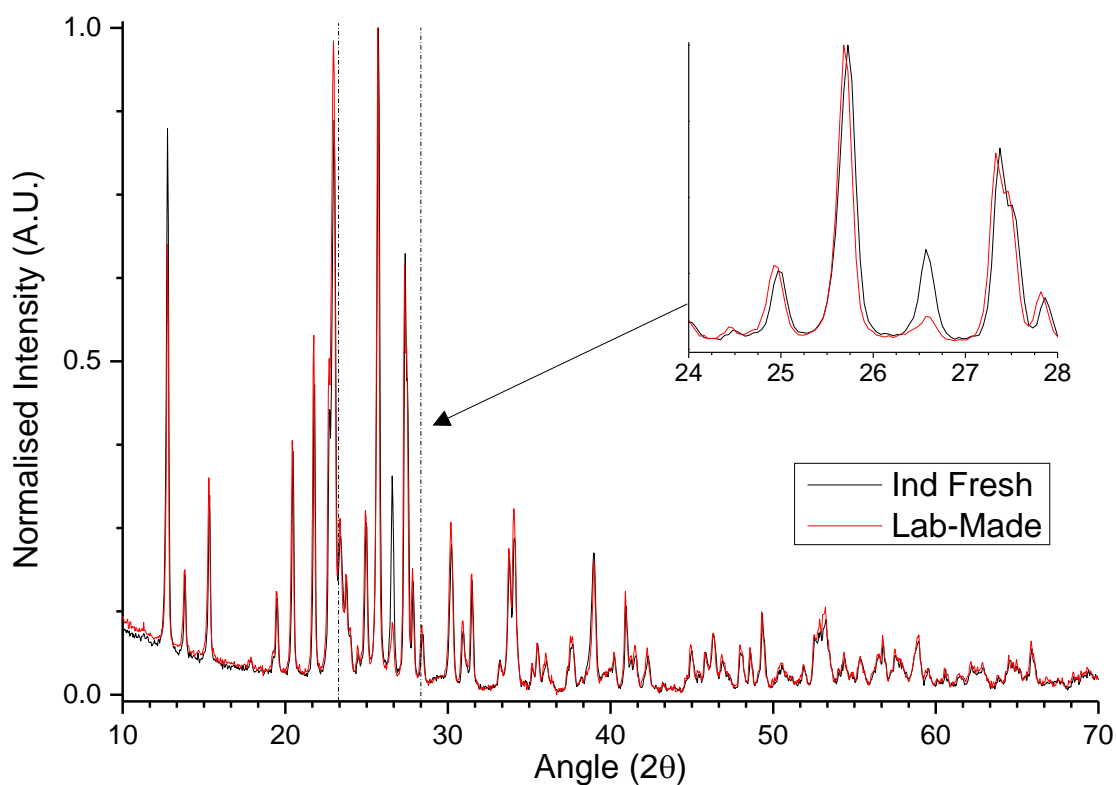

Figure 6.6. X-ray diffraction patterns of industrial and lab-made iron molybdate catalysts. Phases identified as in Figure 6.4.
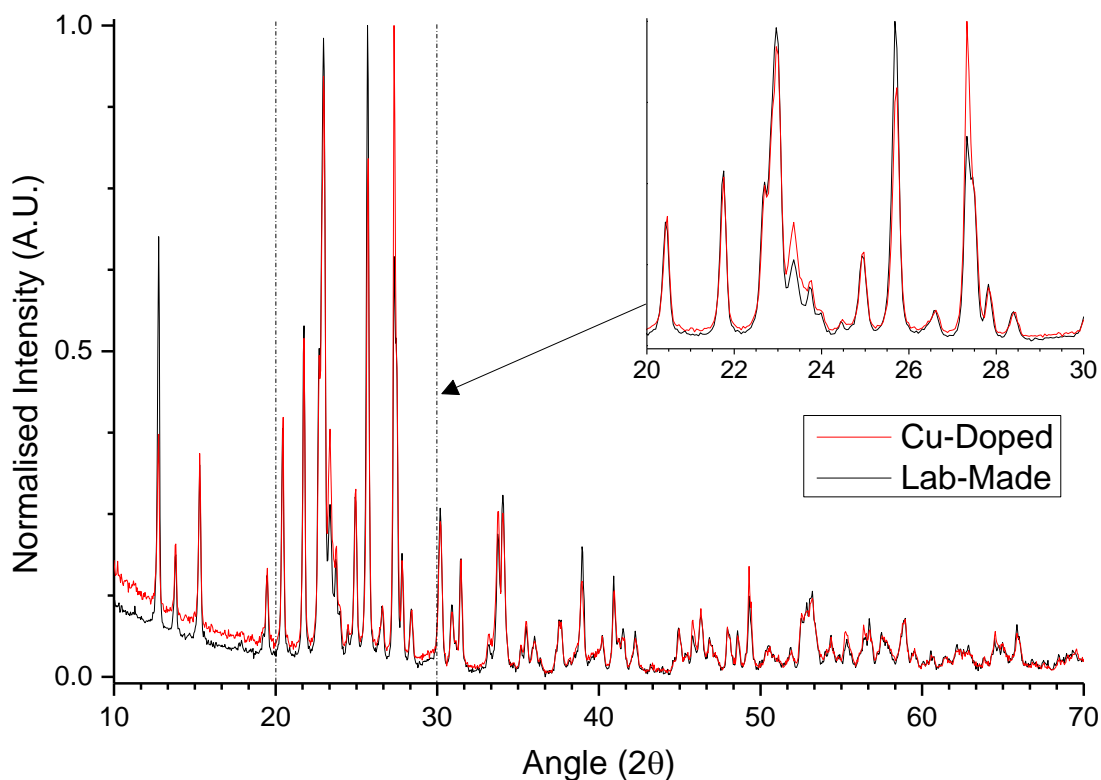
Figure 6.7.X-ray diffraction patterns of the lab-made iron molybdate catalyst, with and without copper substitution. Phase identified as in Figure 6.4.
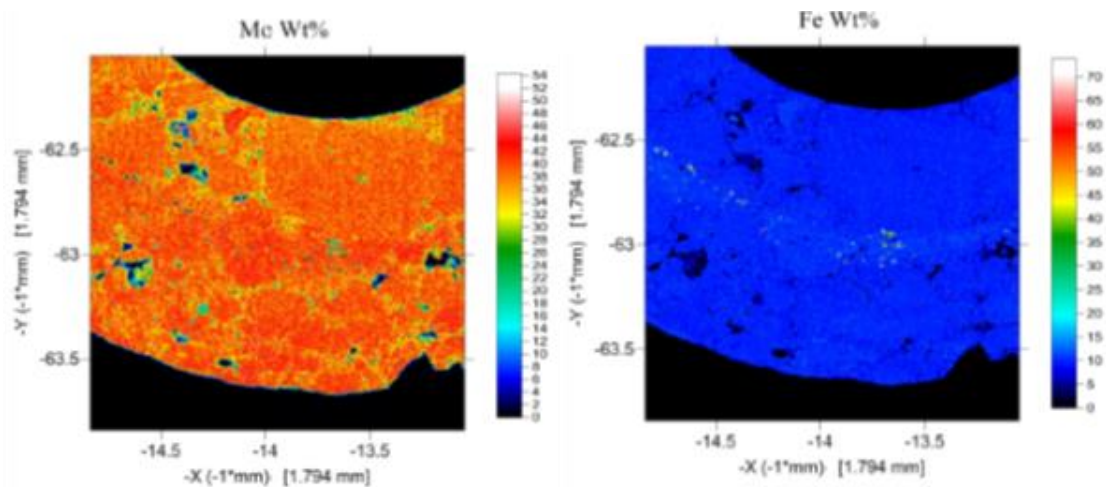
Figure 6.8. Electron Probe Microanalysis of fresh iron molybdate catalyst rings.
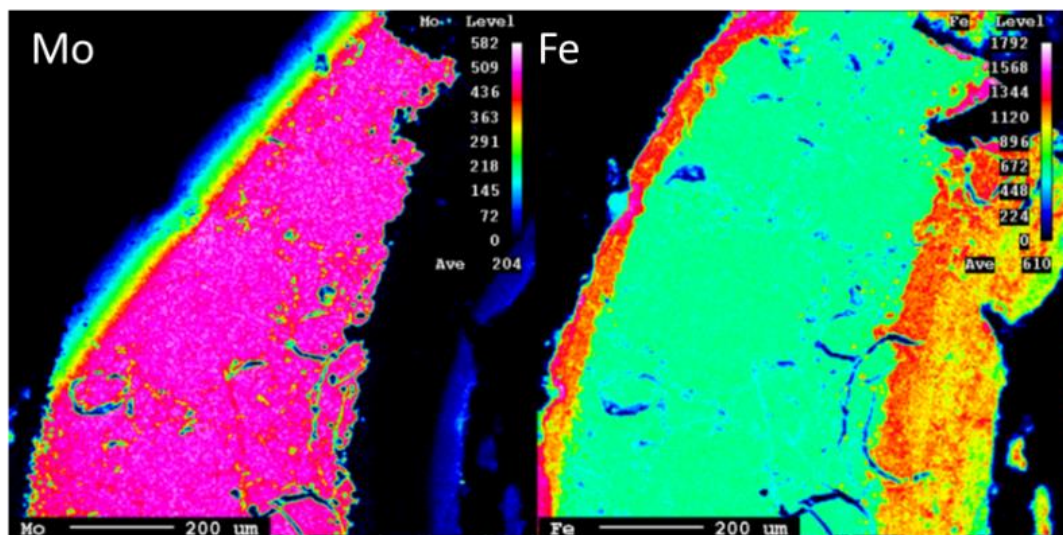
Figure 6.9. Electron Probe Microanalysis of iron molybdate catalyst rings post-catalysis.

6.4 Mössbauer Spectroscopy
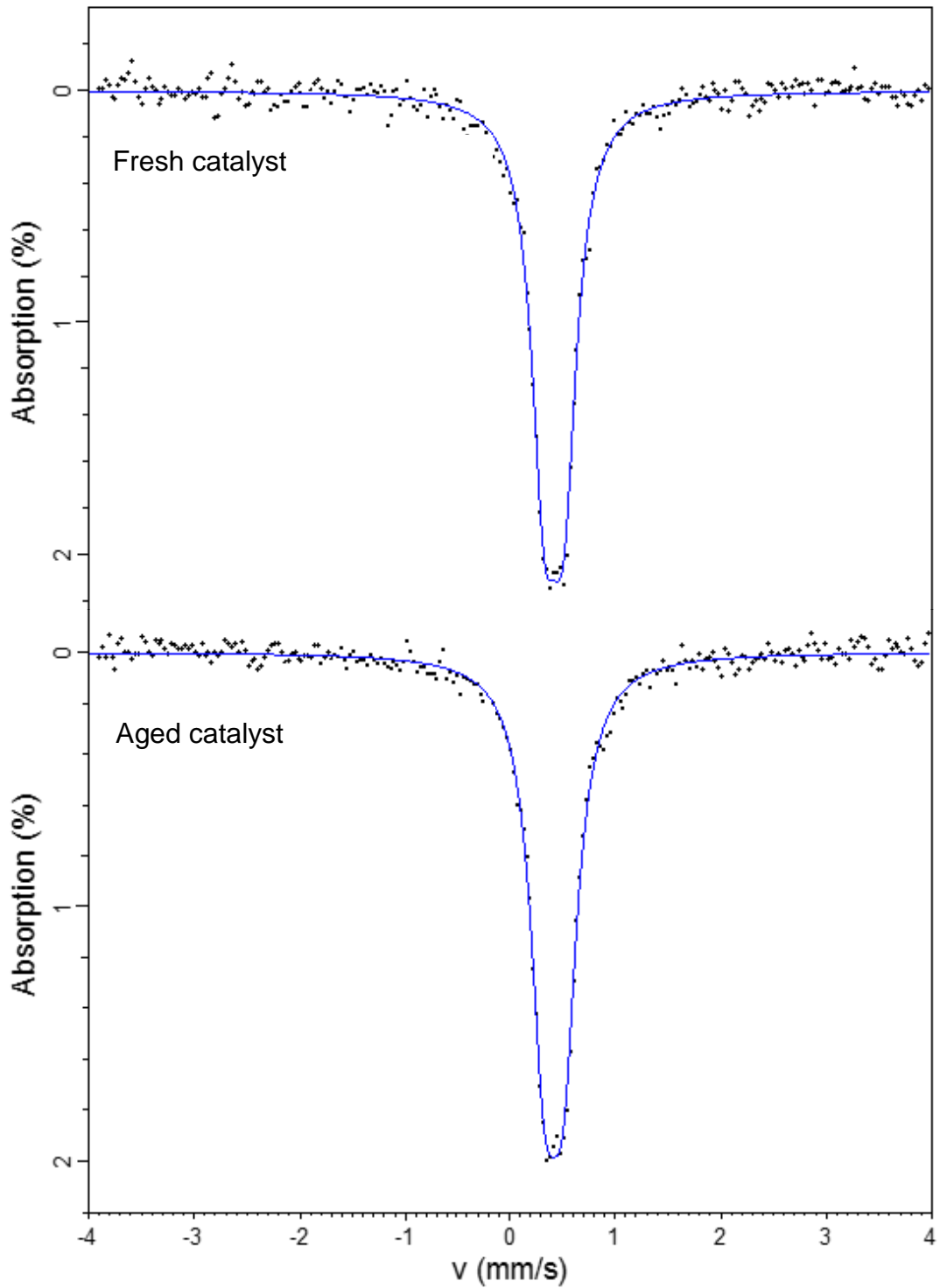
Figure 6.10. Room temperature Mössbauer spectra of industrial $Fe_2(MoO_4)_3$-MoO_3 catalysts.
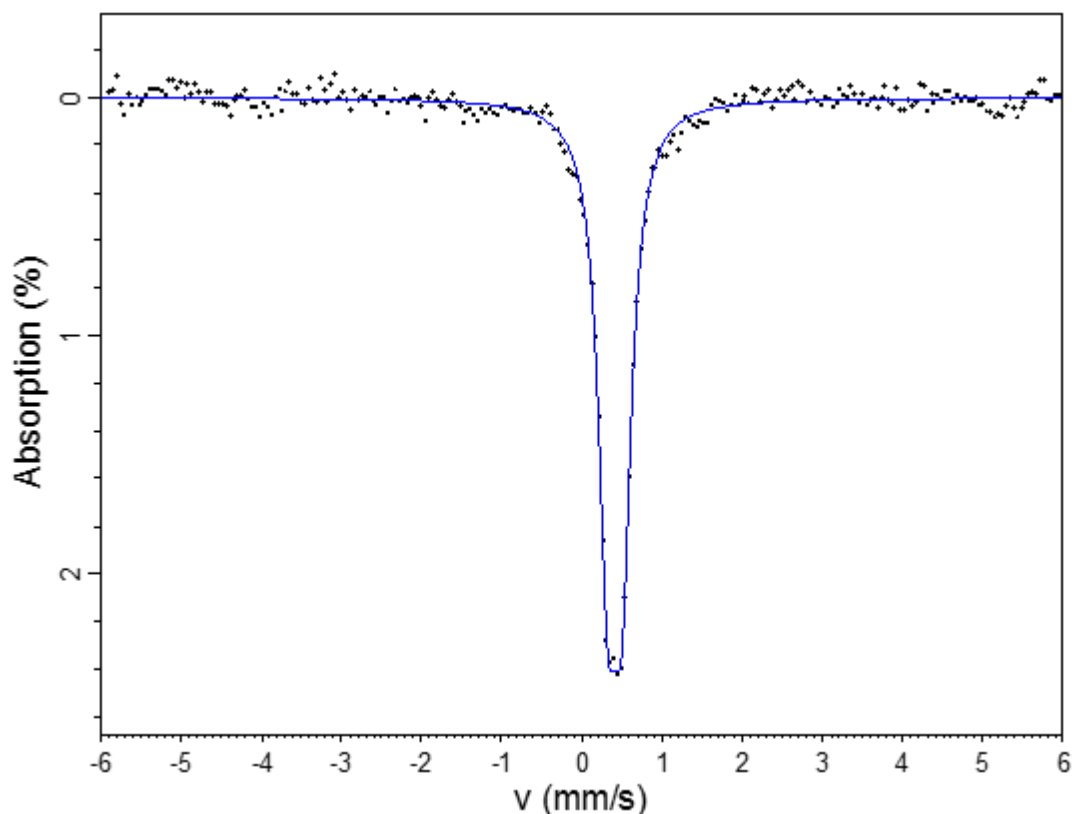
Figure 6.11. Room temperature Mössbauer spectrum of lab-made $Fe_2(MoO_4)_3$-MoO_3

Sample	CS (mm s^{-1})	QS (mm s^{-1})	Γ/2 (mm s^{-1})
Fresh	0.42	0.18	0.15
Aged	0.41	0.18	0.16
Lab-made	0.41	0.18	0.15

Table 6.1. Hyperfine parameters of fresh, aged and lab-scale $Fe_2(MoO_4)_3$-MoO_3 catalysts, at 293 K.

All of the three spectra(figures 6.10 and 6.11) were fit using a doublet, as expected for $Fe_2(MoO_4)_3$ from existing literature (CS 0.41 mm s^{-1}; QS 0.2 mm s^{-1}; FWHM 0.28 mm s^{-1} [15], [27]) consistent with paramagnetic high-spin ferric ions. The 0.01 mm s^{-1} decrease in CS in the aged sample compared to the fresh can either attributed to the previously defined experimental error of ± 0.02 mm s^{-1}) No second doublets, or sextets were observed, indicating that there has been no phase transformation from $Fe_2(MoO_4)_3$, or not sufficient concentration to be detected through Mössbauer spectroscopy. The α- and β-$FeMoO_4$ phases

both contain ferrous iron, with centre shifts of 0.86 (α) and 0.9 (β) mm s^{-1} and quadrupole splitting values of 1.52 (α) and 2.6 (β) mm s^{-1} [19], [28], which would be clearly visible in the spectra provided.

The phase transformations, from $Fe_2(MoO_4)_3$ to $FeMoO_4$, are understood to be depth-dependent, through the catalyst – the surface of these catalysts is expected to form ferrous phases before the centre. The aged sample studied here was a pulverised catalyst ring, containing the interior and exterior of the ring. To improve the information accessible through Mössbauer spectroscopy it may be necessary to analyse the interior and exterior separately and to compare how the iron species vary through the depth of aged catalysts. A study of this type would require a collaborative effort between the researcher and the user, to ensure the catalysts are handled with care as to minimise the loss of exterior surfaces.

It is also understood that the catalyst reactors do not experience uniform environments, and that there are so-called "hot spots". The area from which the aged catalyst was extracted is known only by the reactor tube that it was housed in, but its position within its tube is not known. This tube may have contained a hot spot, however the sample that was taken was not necessary within this region and may have been from an area of relatively mild conditions. The influence of these hot spots on the phases formed could be better investigated by studying catalysts from along the length of a tube, instead of one ring from the entire tube.
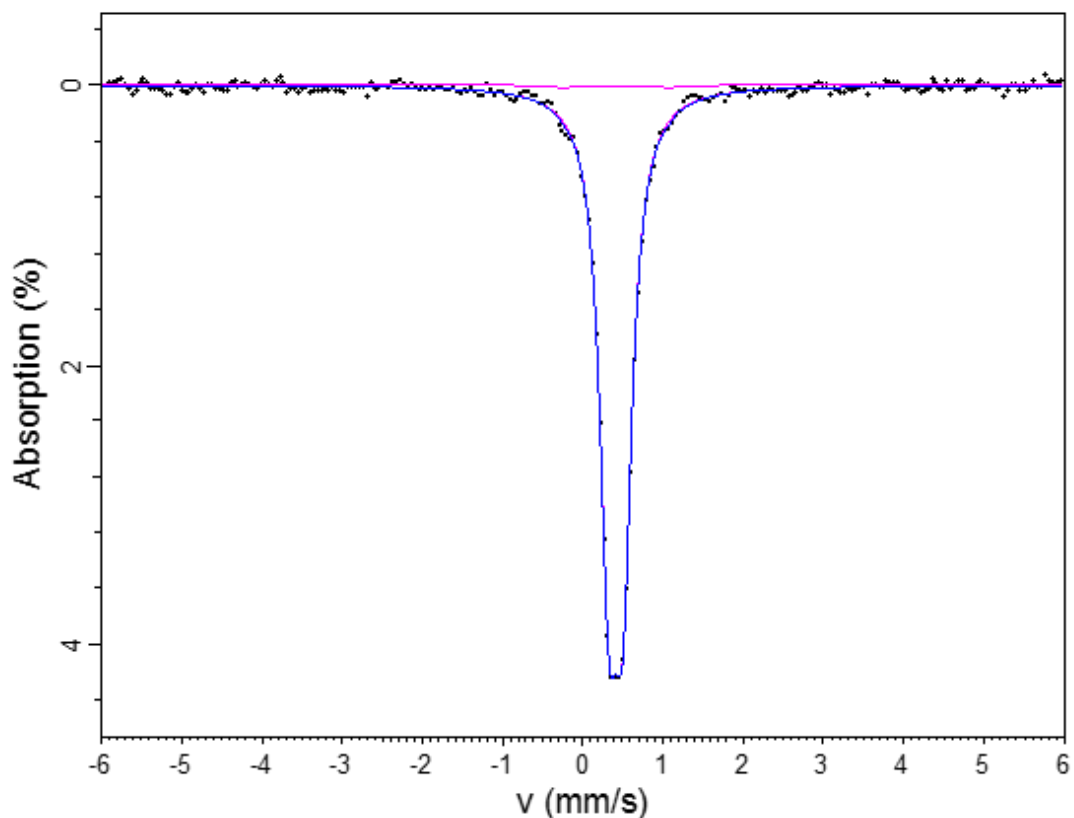
Figure 6.12. Room temperature Mössbauer spectrum of lab-made, copper substituted $Fe_{1.9}Cu_{0.1}(MoO_4)_3$-$MoO_3$.

Table 6.2. Hyperfine parameters of Cu-substituted $Fe_{1.9}Cu_{0.1}(MoO_4)_3$-$MoO_3$ catalyst.

Sample	CS (mm s^{-1})	QS (mm s^{-1})	Γ/2 (mm s^{-1})	Area (%)
Cu-substituted	0.41	0.18	0.14	98
	0.41	1.31	0.10	2

The hyperfine parameters, in Table 6.2, of the primary doublet are in good agreement with the single doublet used to fit the copper-free materials as seen in Table 6.1. In this copper-loaded sample there is a minor spectral contribution most observed around -0.2 mm s^{-1} and + 1 mm s^{-1}, on the negative and positive sides of the main absorption peak respectively. The parameters used to fit this feature indicates the presence of a secondary octahedral ferric iron site. The relatively low value for the QS in the primary doublet is due to the high-spin state of this site, while the greater QS of the minor site is due to this site being in a low-spin state [27], [29]. In a 2014 publication from Srirapu and colleagues [30], it was reported that increasing the copper content from x = 0 to x = 1 of $Cu_xFe_{2-x}(MoO_4)_3$

does not introduce additional X-ray diffraction peaks, only shifting diffraction peaks slightly towards higher angle, reflecting a slight lattice contraction. As the copper substitution was increased the diffraction peaks at 6.935 and 3.248 Å, attributed to the MoO_3 phase, increased in intensity. In the $Fe_2(MoO_4)_3$ structure the iron has an electronic charge of Fe^{3+}, and molybdenum Mo^{6+} and oxygen O^{2-}, such that the MoO_4 groups are overall negatively charged as MoO_4^{2-}; three such molybdate groups are charge balanced by the two ferric iron ions. With the substitution of iron for copper, the copper oxygen octahedra has an additional electron which cannot be balanced by molybdenum in neighbouring MoO_4 tetrahedra. This may result in either Jahn-Teller distortion of the copper oxygen octahedra causing stretching in the c axis [31], or localised oxygen vacancies. An oxygen anion removed from a specific site would affect both the $CuO_{6-\delta}$ and molybdenum tetrahedra. Where MoO_4 is now MoO_3 due to the lost oxygen, the MoO_x tetrahedra is no longer negatively charged which would affect the Fe-O-Mo bond to the nearest FeO_6 octahedra. The increase in copper content into $Cu_xFe_{2-x}(MoO_4)_3$ resulted in an increase in MoO_3 related diffraction peaks, according to Srirapu [30], which is consistent with theory of oxygen vacancies. The presence of the low spin Fe^{3+} site in this Mössbauer spectrum may therefore be a result change in Fe-O-Mo bonding when the molybdate group is oxygen deficient. The low relative area of this site reflects the low level of copper loading.

In an effort to discern if there were observable differences between the fresh and the aged catalyst samples both were measured with Mössbauer spectroscopy at 10 K. Jirak et al. published work on $Fe_2(MoO_4)_3$ in 1982, showing a Néel temperature of 13 K [27] for pure, powdered material. Once magnetically ordered, the Mössbauer spectra of $Fe_2(MoO_4)_3$ was reported to consist of two sextets with "practically zero quadrupole perturbations" where the more intense of the two corresponds to the small hyperfine field with high linewidth. The two sextets were found to have relative area ratios of around 3:1 between 6 and 10 K [27]. The purpose of the low temperature Mössbauer measurements was to attempt to observe any additional phases that may be superimposed into the room temperature doublet.
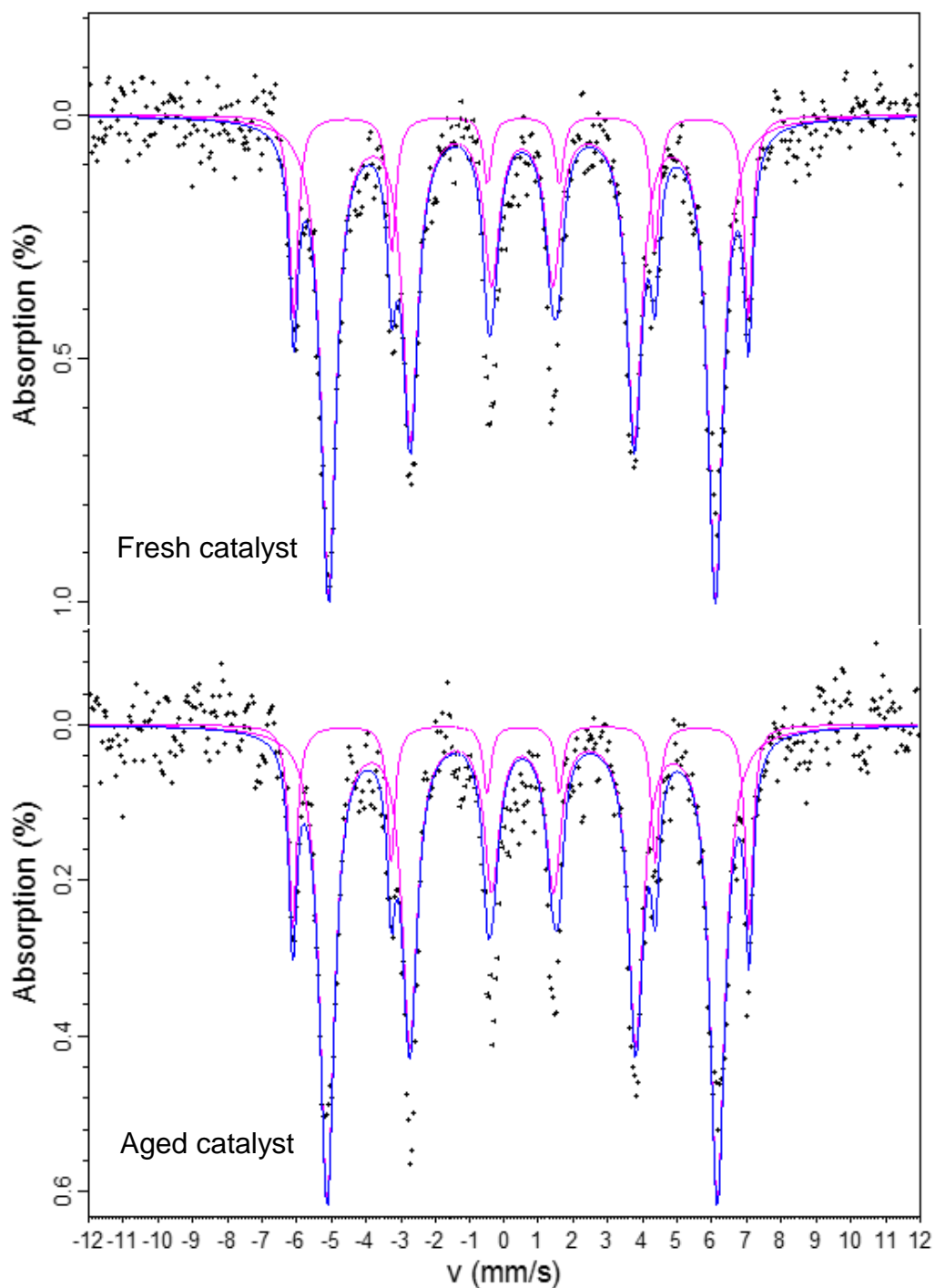
Figure 6.13. Mössbauer spectra of industrial $Fe_2(MoO_4)_3$ catalysts, at 10 K.

Table 6.3. Hyperfine parameters of fresh & aged $Fe_2(MoO_4)_3$ catalysts at 10 K.

Sample	CS (mm s^{-1})	ε (mm s^{-1})	B$_{eff}$ (T)	Γ/2 (mm s^{-1})	Area (%)
Fresh	0.53	0	34.6	0.27	81
	0.53	-0.03	40.7	0.15	19
Aged	0.52	0	34.9	0.26	82
	0.51	-0.03	40.8	0.14	18

The spectra of both the fresh and aged catalysts are as described by Jirak in 1982 [27]; two sextets with practically no quadrupole interaction, and the sextet with the smaller hyperfine field having a greater linewidth. Spectra of $Fe_2(MoO_4)_3$ at temperatures including 10 and 1.3 K were presented by G. Long in 1984 [32] where the 10 K spectrum agrees with those presented here, and at 1.3 K the two sublattices are "virtually equivalent" resulting in complete data fitting using one sextet. Comparison of the two spectra shows no significant variation, indicating that both materials only have $Fe_2(MoO_4)_3$ as iron-bearing phases. Due to the isotope specific nature of Mössbauer spectroscopy it is not possible to identify any volatile molybdate loss, at least not in the aged sample presented here. As previously stated, this aged material was removed from the reactor once the catalyst was no longer performing at high enough efficiency for the user to continue. Due to the nature of the sample recovery process, the mixing of 'fresh' and spent components of the catalyst, what can be concluded is that no additional phases can be observed in the samples that have been analysed.

The issue of localised reactor hot spots is so established that the winter 2017 edition of *Informally Speaking*, a Johnson Matthey publication focused on formaldehyde, contained an article specifically addressing the topic [33]. Due to the fact that the catalyst in the reactor does not experience a uniform environment, the extent of aging that this sample has experienced is unknown; only that the overall reactor had become unprofitable to operate. To more thoroughly investigate the aging of these catalysts it would be important to extract multiple samples from the length of a reactor tube, known to host a hot spot, and to compare how the catalyst has aged in different environments, and how the catalyst sample phases vary between the interior and exterior.

6.5 Conclusions

In the context of industrial catalysts for the oxidation of methanol to formaldehyde, four iron molybdate samples were studied in this chapter; two industrial catalyst samples, pre- and post-reaction, and two lab-scale materials, one of pure $Fe_2(MoO_4)_3$-MoO_3 and one with 5 wt% copper substitution for iron. It was concluded that the synthesis route used in the lab-scale operation and at industrial scale resulted in no observable differences to the iron environment, as seen by the experimentally identical hyperfine parameters of these two samples. The fresh and aged catalysts samples showed no significant spectral differences, at room temperature of at 10 K, indicating that the aged sample had no yet formed reduced iron molybdate, $FeMoO_4$, or that it was below the detection limit of Mössbauer spectroscopy. Localised degeneration of catalyst in reactor hot spots may result in the formation of $FeMoO_4$ and overall reduction in reactor efficiency – further investigation into this would be required before making definitive conclusions on the usefulness of Mössbauer spectroscopy in observing iron molybdate catalyst aging. The Mössbauer spectrum of the copper-containing material indicated the presence of a second, minor iron environment consistent with low spin Fe^{3+}. Oxygen vacancies within the lattice caused by the bivalent copper substitution is believed to be the cause of this new site, as molybdate tetrahedra are affected by the oxygen vacancy resulting in MoO_3 instead of MoO_4. The bond between Fe-O-Mo will differ when the molybdenum is bonded to three oxygen rather than four, and this difference is likely the cause of the low spin iron. It is not possible to determine whether one neighbouring MoO_3 group is sufficient to cause this change or whether this site is the result of multiple MoO_3 around one FeO_6 octahedra.

References

[1]   R. Seymour and G. Kauffman, "Formaldehyde: A simple compound with many uses," *J. Chem. Educ.*, vol. 69, no. 6, pp. 457–458, 1992.

[2]   NTP: National Toxicology Program, "Formaldehyde," *14th Rep. Carcinog.*, no. 2000, 2016.

[3]   E. Brenner, "Human body preservation - old and new techniques," *J. Anat.*, vol. 224, no. 3, pp. 316–344, 2014.

[4]   Healthy Building Network, "Alternative Resin Binders for Particleboard, Medium Density Fiberboard (MDF), and Wheatboard," *Glob. Heal. Saf. Initiat.*, no. May, pp. 1–6, 2008.

[5]   X. Tang, Y. Bai, A. Duong, M. T. Smith, L. Li, and L. Zhang, "Formaldehyde in China: Production, consumption, exposure levels, and health effects," *Environ. Int.*, vol. 35, no. 8, pp. 1210–1224, 2009.

[6]   L. H. Baekeland, "Original papers: The synthesis, constitution, and uses of bakelite," *Ind. Eng. Chem.*, vol. 1, no. 3, pp. 149–161, 1909.

[7]   J. Graf, *Warman's World War II Collectibles: Identification and Price Guide*. Krause Publications, 2007.

[8]   L. E. Heim, H. Konnerth, and M. H. G. Prechtl, "Future perspectives for formaldehyde: pathways for reductive synthesis and energy storage," *Green Chem.*, vol. 19, no. 10, pp. 2347–2355, 2017.

[9]   A. Andersson, J. Holmberg, and R. Häggblad, "Process Improvements in Methanol Oxidation to Formaldehyde: Application and Catalyst Development," *Top. Catal.*, vol. 59, no. 17–18, pp. 1589–1599, 2016.

[10]   I. Bibicu and L. Frunza, "Characterization of Oxide Catalysts by In Situ Mössbauer Spectroscopy," *Rom. Reports Phys.*, vol. 58, no. 4, pp. 427–453, 2006.

[11]   K. I. Ivanov, I. G. Mitov, S. V Krustev, and B. S. Boyanov, "Mössbauer study of modified iron-molybdenum catalysts for methanol oxidation," *J. Phys. Conf. Ser.*, vol. 217, p. 012046, 2010.

[12]   C. Brookes *et al.*, "The Nature of the Molybdenum Surface in Iron Molybdate. the Active Phase in Selective Methanol Oxidation," *J. Phys. Chem. C*, vol. 118, no. 45, pp. 26155–26161, 2014.

[13]   B. R. Yeo *et al.*, "The surface of iron molybdate catalysts used for the selective oxidation of methanol," *Surf. Sci.*, vol. 648, pp. 163–169, 2016.

[14]   F. D. Rossini, "Heat and Free Energy of Formation of Deuterium Oxide *," *Natl. Bur. Stand.*, vol. 24, no. April, 1940.

[15]   A. P. V. Soares, M. Farinha Portela, A. Kiennemann, L. Hilaire, and J. M. M. Millet, "Iron molybdate catalysts for methanol to formaldehyde oxidation: Effects of Mo excess on catalytic behaviour," *Appl. Catal. A Gen.*, vol. 206, no. 2, pp. 221–229, 2001.

[16]   J. Khorshidi, M. Kalbasi, and A. Kabir, "Study of Methanol to Formaldehyde Reaction in Fluidized Bed Reactor," *Eng. Conf. Int. Conf. Proc.*, 2007.

[17]   H. Adkins and W. R. Peterson, "The Oxidation of Methanol With Air Over Iron, Molybdenum, and Iron-Molybdenum Oxides," *J. Am. Chem. Soc.*, vol. 53, no. 4, pp. 1512–1520, 1931.

[18]   Johnson Matthey, "Formox Assessment data," 2017.

[19]   A. P. V. Soares, M. F. Portela, and A. Kiennemann, "Methanol Selective Oxidation to Formaldehyde over Iron-Molybdate Catalysts," *Catal. Rev.*, vol. 47, no. November, pp. 125–174, 2005.

[20]   J. N. Allison and W. A. Goddard, "Oxidative dehydrogenation of methanol to formaldehyde," *J. Catal.*, vol. 92, no. 1, pp. 127–135, 1985.

[21]   W. E. Farneth, F. Ohuchi, R. H. Staley, U. Chowdhry, and A. W. Sleight, "Mechanism of partial oxidation of methanol over molybdenum(VI) oxide as studied by temperature-programmed desorption," *J. Phys. Chem.*, vol. 89, no. 12, pp. 2493–2497, 1985.

[22]   E. M. McCarron, R. L. Harlow, Z. G. Li, C. Suto, and Y. Yuen, "$Mo_2O_5(OCH_3)_2$ and $Mo_2O_5(OCH_3)_2 \cdot 2CH_3OH$: New Structural Insights Derived from Reaction Chemistry and Diffraction Techniques," *J. Solid*

State Chem., vol. 136, no. 2, pp. 247–252, 1998.

[23]   G. I. Golodets, "Chapter XVI: The Oxidation of Paraffin Derivatives," in *Heterogeneous Catalytic Reactions Involving Molecular Oxygen*, vol. 15, no. Supplement C, G. I. Golodets, Ed. Elsevier, 1983, pp. 470–497.

[24]   K. Routray, W. Zhou, C. J. Kiely, W. Grünert, and I. E. Wachs, "Origin of the synergistic interaction between MoO_3 and iron molybdate for the selective oxidation of methanol to formaldehyde," *J. Catal.*, vol. 275, no. 1, pp. 84–98, 2010.

[25]   N. Burriesci, F. Garbassi, M. Petrera, G. Petrini, and N. Pernicone, "Solid state reactions in Fe-Mo oxide catalysts for methanol oxidation during aging in industrial plants," *Stud. Surf. Sci. Catal.*, vol. 6, no. C, pp. 115–126, Jan. 1980.

[26]   H. yih Chen, "The crystal structure and twinning behavior of ferric molybdate, $Fe_2(MoO_4)_3$," *Mater. Res. Bull.*, vol. 14, no. 12, pp. 1583–1590, 1979.

[27]   Z. Jirak, R. Salmon, L. Fournes, F. Menil, and P. Hagenmuller, "Magnetic and Mössbauer resonance investigations of the weak ferrimagnet iron molybdate $(Fe_2(MoO_4)_3)$," *Inorg. Chem.*, vol. 21, pp. 4218–4223, 1982.

[28]   A. W. Sleight, B. L. Chamberland, and J. F. Weiher, "Magnetic, Moessbauer, and structural studies on three modifications of $FeMoO_4$," *Inorg. Chem.*, vol. 7, no. 6, pp. 1093–1098, Jun. 1968.

[29]   A. Vértes, L. Korecz, and K. Burger, *Mössbauer spectroscopy*. Elsevier Scientific Pub. Co., 1979.

[30]   V. K. V. P. Srirapu, C. S. Sharma, R. Awasthi, R. N. Singh, and A. S. K. Sinha, "Copper-iron-molybdenum mixed oxides as efficient oxygen evolution electrocatalysts," *Phys. Chem. Chem. Phys.*, vol. 16, no. 16, pp. 7385–7393, 2014.

[31]   H. Kamimura, H. Ushio, T. Hamada, and S. Matsuno, *Theory of Copper Oxide Superconductors*. Springer, 2005.

[32]   G. J. Long, "A Mössbauer Effect and Magnetic Study of $Fe_2(SO_4)_3$ and

Fe$_2$(MoO$_4$)$_3$, Two L-Type Ferrimagnets," in *Chemical Mössbauer Spectroscopy*, 1st ed., R. H. Herber, Ed. New York: Plenum Press, 1984, pp. 95–111.

[33]   Simon Smrtnik, "Hot Spot Temperatures," *Informally Speaking*, pp. 16–17, 2017.

7. Energy Storage and Lithium Iron Phosphate

7.1 Introduction

At the turn of the 19th century, Alessandro Volta invented the first battery, following successfully proving his hypothesis that animal electricity – the cause of deceased frogs twitching during dissection – was due to the dissimilar metals of the brass hooks and iron scalpel, with the frog itself providing a "moist intermediary", or as would now be called, electrolyte [1], [2]. Volta's invention, which came to be known as the *voltaic pile* was made of anodic copper and cathodic zinc discs separated by brine-soaked cloth acting as an electrolyte. In the more-than-200 years since the voltaic pile, modern batteries have gone through many iterations to improve the performance – charge / discharge times, storage capacity, voltage, safety – of the great many devices batteries now power. The basic operating principle of batteries is the movement of ions between the two sides, the positive anode and negative cathode, which causes a flow of electrons. During charging electrons flow to the cathode from the power source causing the ions to move to the anode, the inverse being true for discharge, or operation [3]. In modern rechargeable batteries lithium is used as the mobile ion; lead-acid batteries operate through the movement of sulphate ions. Current materials for the anodes and cathodes rechargeable batteries are rich in cobalt and nickel, the reserves of which a recent Nature contributor warned would not meet the future demands of the increasing electric vehicle market [4]. Iron, being much more abundant and cheaper, is one alternative to cobalt and nickel in the form of lithium iron phosphate – $LiFePO_4$, or LFP. The first journal article on $LiFePO_4$ as a cathode material was published in 1997 by John Goodenough and his research group, in which they outlined what they considered the most desirable characteristics for rechargeable cathode materials – inexpensive, easy to fabricate, environmentally benign, and safe in handling and operation [5]. In the 21 years that have passed, this publication has been cited 5,380 times as of August 2018, according to *Scopus*. In this chapter changes on $LiFePO_4$ during lithiation and delithiation will be studied *in -situ* and *in-operando*.

Following Volta's invention in 1800, the first mass produced battery was designed in 1802 by William Cruickshank [6] by arranging sheets of copper and zinc held in place with grooves in rectangular wooden boxes, using an acid or a brine as the electrolyte. John F. Daniell improved on this technology in 1836 with the first rechargeable battery based on copper and zinc in sulphuric acid, called the Daniell Cell [6], [7]. Gaston Planté developed this further, making the Planté Cell, the first lead acid battery in 1859 [8], which are still commercially available as car batteries today. The nickel-cadmium battery was developed by Swedish Waldmar Jungner in 1899, using cathodic nickel alloy and anodic cadmium alloy with potassium hydroxide electrolyte [8]. The nickel cadmium batteries were expensive due to material costs, limiting their use. Further improvements on nickel-based batteries came from Thomas Edison in 1901 by replacing cadmium with iron, reducing the unit cost at the expense of lower specific energy and issues with self-discharge. In 1947 batteries were made portable by the ability to seal the cell, developed by Georg Neumann. The sale of nickel cadmium batteries is restricted within the European Union since the 2006 Battery Directive due to environmental concerns regarding their disposal [9], [10]. Lithium-ion (Li-ion) batteries were first commercialised by Sony Japan in 1991 for use in mobile phones [11]. In the years since Sony's first lithium battery the research into battery technology has focused largely on lithium systems, although there have been recent efforts towards replacing lithium for sodium [12], [13]. In 1997 the research group of John Goodenough published their findings on using lithium iron phosphate – LFP – as a battery cathode material [5]. Since Goodenough's first identification of LFP there has been much work on improving the system through compositional changes, synthesis routes, electrolyte optimisation, and studying the kinetics of the system in order to better understand the variables that produce preferential outcomes [14]–[20]. The increasing progress of portable and wearable electronics, and the increasing demand for renewable energy – with its issues of intermittency – drive further progress in battery technologies, including Li-air, Na-ion, and the recent work of John Goodenough looking towards all-solid-state batteries [21].

Lithium iron phosphate has an *olivine* crystal structure of corner-sharing FeO_6 octahedra and PO_4 tetrahedtra that form channels through which lithium

ions can move in and out [5], [16], [22], [23], as depicted in Figure 7.1. When used as a cathode material, a fully lithiated structure would represent a discharged cell, where there is no lithium on the anode [24]. A cathode without lithium, $FePO_4$, would be considered fully charged, with lithium found in the anode. Charging an LFP cell therefore involves redox reactions of iron, from ferric phosphate, $FePO_4$, to ferrous $LiFePO_4$ as lithium ions occupy the channels. This process is shown schematically in Figure 7.2. During use lithium ions move through the electrolyte from the cathode to the anode resulting in the flow of electrons through the connected circuit, also from the cathode to the anode, and generating a current. Charging the battery is the opposite process, whereby the energy provided by the current of the external power source causes the lithium ions to move from the anode to the cathode, storing the energy as electrical potential, ready for re-use.
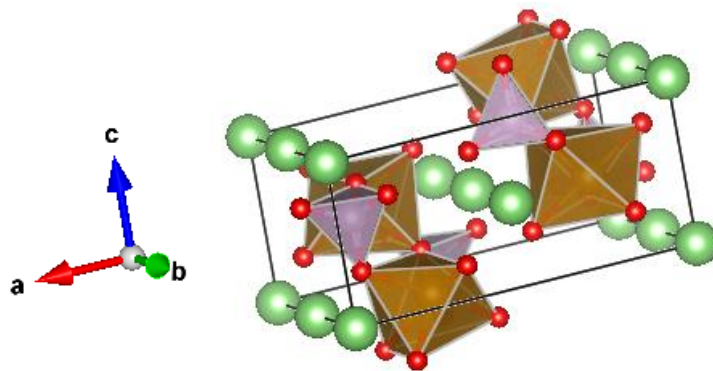

Figure 7.1. Unit cell of $LiFePO_4$ crystal structure, rendered in Vesta © [25], [26].
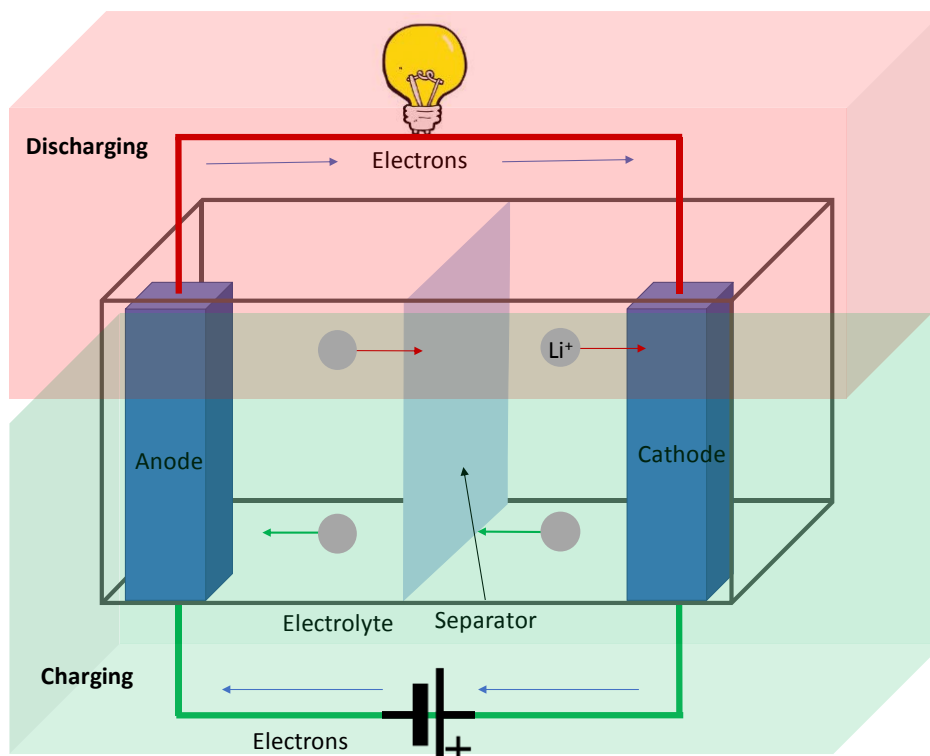
Figure 7.2. Schematic representation of LFP cell during discharging (top) and charging (bottom).

Two of the primary reasons for using lithium as the mobile ion in battery applications are its low mass (6.94 g mol^{-1}) and its high reduction potential (-3.04 V vs. normal hydrogen electrode [27], [28]). In terms of their operational competitiveness, Li-ion batteries out-perform lead-acid, nickel-cadmium and nick-metal hydride batteries in their working potential, specific energy (both gravimetric and volumetric) and in their lifetime in terms of charge/discharge cycle capabilities [28], [29]. The increased working potential of Li-ion batteries compared to nickel-metal hydride (3.6 V vs 1.2 V) was one of the factors allowing Li-ion technologies to enable the technological advancements seen since their advent [12]. Much of the research focus in the battery field since 1991 has been to optimise the Li-ion technology to simultaneously improve their performance and reduce the cost of production – a great volume of which has focused primarily on the electrode materials. To this author's best knowledge, at the time of writing, the cathode materials with the highest energy densities (that being the amount of Watt-hours stored per unit of mass) are Ni-Mn-Co-O based ($610 – 650$ Wh kg^{-1}) and Ni-Co-Al-O based systems ($680 – 760$ Wh kg^{-1}) [12], [30]. The energy density of LFP is lower than these systems, at $518 – 587$ Wh kg^{-1}, however the cost of LFP is much lower, and does not contain nickel or cobalt, of which there is the

fear of depleting [4]. Lithium-ion battery anodes are often made of metal oxides, although more recently metal oxide have been explored as potential candidates to replace graphite anodes; an electrochemical cell with lithium as the anode is called a *half cell* and are not commercially used [28], [31]. The medium through which ions move in an electrochemical cell is called the electrolyte, a focus of its own volume of research entirely, with more recent studies investigating solid-state electrolyte due to their increased safety [21], [32]–[34]. The optimisation of batteries is more complex than a facile material selection process, as each component can have many variables to be studied and considered, including; the synthesis route of the electrode materials, the fabrication of the electrodes and selection of polymer binder, the use of dopants and the effect that these factors have on the energy density, the cost of the end unit, and its lifetime. The ever-increasing demand for performance enhancement can have devastating effects if not properly safeguarded with rigorous and thorough investigation, as evidenced by the 2016 incident of the *Samsung Note 7*, the recall of which is reported to have cost the company upwards of £4 bn [35], [36].

Due to its high iron content (35.4 wt%), the absence of any heavy, gamma attenuating elements, and the facile nature of the redox reactions employed in service, Mössbauer spectroscopy is a powerful technique to study $Li/FePO_4$. The structural effects as a result of the synthesis route were studied by Hannoyer et al. in 2006 [37], the stability of $LiFePO_4$ in water was studied by Porcher in two 2008 publications [38], [39], the effects of air moisture studied by Cuisinier in 2010 [40], and by Martin for nano-particles in 2011 [41]. Recent studies into LFP have observed enhanced electrochemical properties as a result of oxygen-site doping with sulphur and fluorine [19], [20], [42]. The hyperfine parameters reported in existing literature of $LiFePO_4$ and $FePO_4$ are summarised in Table 7.1.

Table 7.1. Hyperfine parameters of LiFePO$_4$ and FePO$_4$.

Phase	CS (mm s^{-1})	QS (mm s^{-1})	Source
LiFePO$_4$	1.22	2.97	[23]
	1.22	2.96	[43]
	1.22	2.96	[44]
FePO$_4$	0.41	1.54	[23]
	0.45	1.53	[43]
	0.42	1.52	[44]

The next significant breakthrough in battery technology _could_ come in the form of improvements to the LFP system; to significantly increase the energy density to be competitive with the nickel and cobalt systems previously outlined, while maintaining the low cost, facile synthesis, long-term stability and availability of precursor materials that favour LFP-based systems. Although LFP may not be competitive with the nickel and cobalt systems, its greater long term stability and lower costs can prove more useful than the higher energy density of the most expensive systems, in some applications, where lower energy for longer periods of time is preferable – such as mobile devices. There are other candidate systems being explored recently, including layered metal oxides (Li$_2$MO$_3$) that show potential for high voltage applications [45], and exploration into new synthesis routes such as flame spray pyrolysis [46], [47], or sol-gel synthesis [15], [37], [48], [49]. In this chapter LFP is studied across a number of dimensions, principally through Mössbauer spectroscopy, studying the effect of synthesis route, charge state, and the origin of an impurity phase in Mössbauer spectra. Analysis of LiFePO$_4$ was carried out in powders, when processed onto electrodes and _in-operando_ during the charge and discharge process.

7.2 Research Objectives

The initial objective for this work was to investigate the usefulness of Mössbauer spectroscopy in the study of LFP cathode materials, targeting industrially-focused questions unanswered by conventional lab-based techniques. The main objective in the LFP studies was to determine whether the key electrochemical performance indicators of the cathode materials could be qualitatively observed using Mössbauer spectroscopy – does a "good" cathode material present a different Mössbauer spectrum to a "bad" one. Two benchmark materials, identical through X-ray diffraction pattern analysis, were analysed to determine whether the differences in capacitance, as determined by electrochemical techniques, could be observed using Mössbauer spectroscopy. From the industrial perspective, the need was for a technique that could determine all of the iron environments – XRD could show the crystalline phases, but could not identify amorphous iron-bearing phases, and was unable to explain the differences observed in electrochemical performance. The influence of processing LFP powders into functional electrodes was investigated to understand any potential effect or changes on the structure of the material. Investigations on changes on the Fe environment during the charge (delithiation) and discharge (lithiation) of $LiFePO_4$ were studied with Mössbauer spectroscopy, focusing on the influence of synthesis route. The progressive discoveries of Mössbauer spectroscopy's usefulness in the study of LFP cathodes culminated in the final objective of this body of work being operando measurements, using a portable potentiostat at the ESRF Synchrotron Mössbauer Spectroscopy beamline at Grenoble. In order to achieve this objective it was necessary to develop a specific cell holder to carry out in-operando synchrotron measurements, without losing any capacity due to poor conductivity, or a lack of compression.

7.3 Materials Characterisation

7.3.1 Synthesis and coin cell fabrication

Two process routes were used to synthesise $LiFePO_4$ materials; solid state ball milling, and flame spray pyrolysis. Due to the sensitive nature of this research the details of the synthesis – times, temperatures, precursors etc, cannot be disclosed by JMTC, however, these are kept constant for each process, unless specifically stated otherwise. X-ray diffraction of the LFP powders used in this body of work indicated olivine $LiFePO_4$ (PDF 04-015-6070). Figure 7.3 shows the X-ray diffraction pattern of the ball milled $LiFePO_4$ batch used in the state-of-charge studies, a pattern representative of all LFP materials used. ICP elemental analysis of the ball milled LFP indicated 4.36 wt% Li, 34.8 wt% Fe and 19.9 wt% P with the balance being carbon and oxygen. Particle sizes determined with SEM analysis of the ball milled LFP indicated a mean particle size of 144 nm (σ = 70 nm).
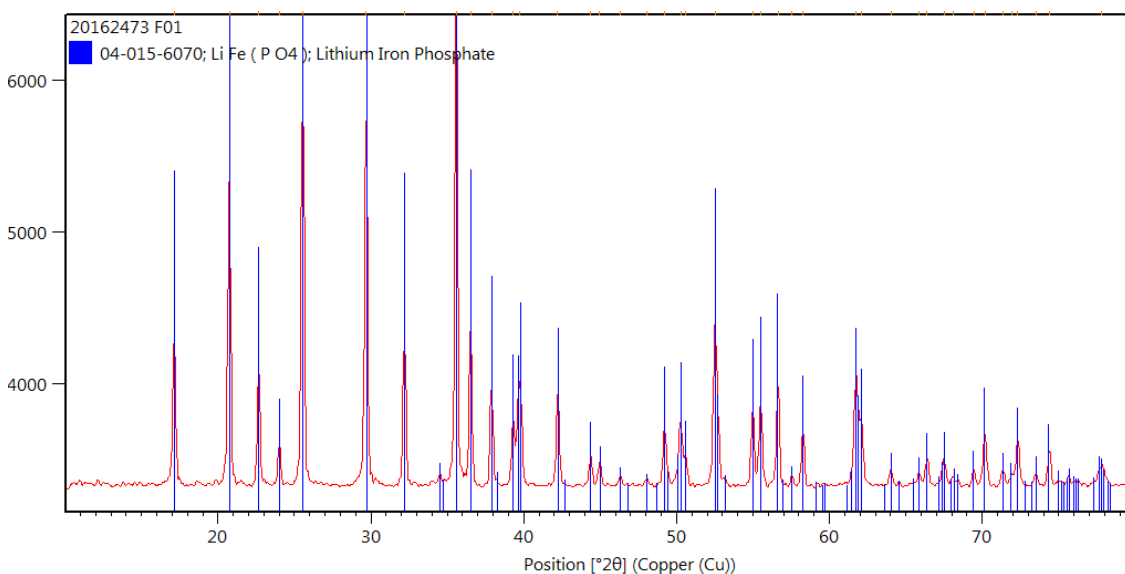

Figure 7.3. X-ray diffraction pattern of ball milled $LiFePO_4$.
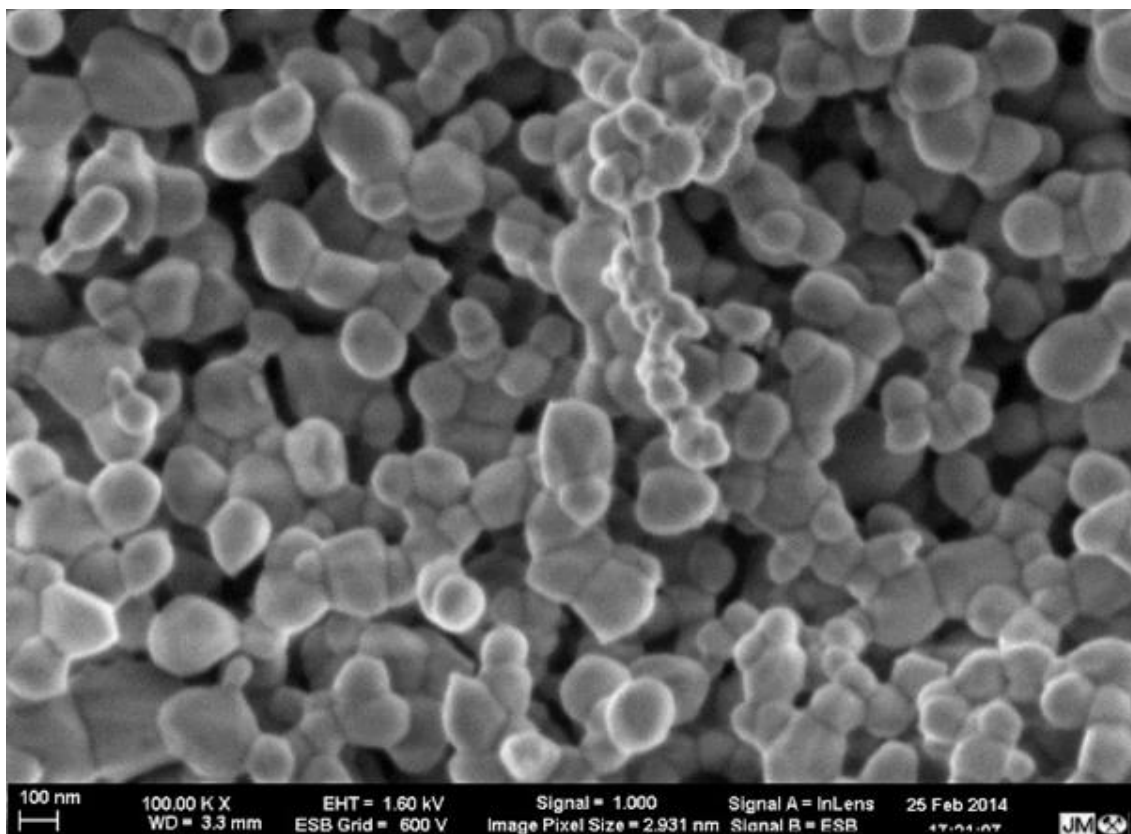
Figure 7.4. BSE SEM image of ball milled LFP at x100,000 magnification.

LiFePO$_4$, being a poor electronic conductor, was carbon coated either during the synthesis process or post-synthesis for the ball-milled materials and FSP materials respectively – details of this are also sensitive and therefore not disclosed, however can be considered constant for each synthesis route.

The fabrication of electrodes was achieved by dissolving the carbon coated LFP powder in N-Methyl-2-pyrrolidone (NMP; C$_5$H$_9$NO) with an inorganic binder, polyvinylidene fluoride (PVDF; (C$_2$H$_2$F$_2$)$_n$) at a constant ratio. Thin aluminium sheets were cleaned with ethanol onto which the LFP slurry was printed at a constant thickness using a motorised film applicator / doctor blade. These sheets were dried at 120 °C overnight before discs were cut using an electrode punch (hand-operated die press cutter). Each electrode was individually calendered to get a 2 mg/cm^3 density. Each electrode was weighed, and its overall thickness recorded to calculate their active mass loading for subsequent calculations. Electrodes were dried in a Bucky oven at 120 °C for 10 hours prior to cell construction.

Each metallic component of the coin cells was individually cleaned with ethanol, dried and stored in a vacuum oven. Each coin cell was constructed in an inert atmosphere, negative pressure glove box. Lithium metal (constant thickness and supplier) was used as the anode for each coin cell, resulting in half cells. Glass fibre discs were used as the separator material, and 85 µl of LP30 electrolyte (1.0 M LiPF$_6$ in ethylene carbonate and dimethyl carbonate solution) was applied to the separator. Each cell was sealed by crimping using a constant force for a constant time. Following electrochemical testing the coin cells were opened in the glove box and the electrodes thoroughly washed in acetonitrile to remove any electrolyte and were sealed in airtight containers after drying, prior to removal from the glove box.

7.3.2 Electrochemical Testing

The electrochemical testing was carried out using a Vötsch Industrietechnik VTL 4010 Maccor battery testing rig, and Maccor software. The open circuit potentials of each cell were taken and recorded, and a 10-hour rest period allowed for the electrolyte to fully wet the electrodes before any testing occurred. Electrochemical impedance spectroscopy (EIS) measurements were taken prior to and following galvanostatic charge-discharge (GCD) measurements. The values of different electrochemical properties cannot be disclosed; however, the different cells can be compared qualitatively where necessary. The cells produced using either ball milled or FSP LFP were made using material from the same batch to reduce sample variability, consequently the cells made using one synthesis route resulted in similar electrochemical properties – specific capacity (mAh g^{-1}), open circuit potential and charge transfer resistance.

7.3.3 Mössbauer Spectroscopy

Two benchmark, ball milled, materials were studied first, to determine whether Mössbauer spectroscopy was able to identify the cause of a substantial difference in their specific capacity (see Figure 7.5) that other characterisation techniques could not. Due to the sensitive nature of these materials, the details regarding their synthesis are unknown, however it was thought that the outcome of the investigation could provide useful information for subsequent studies.
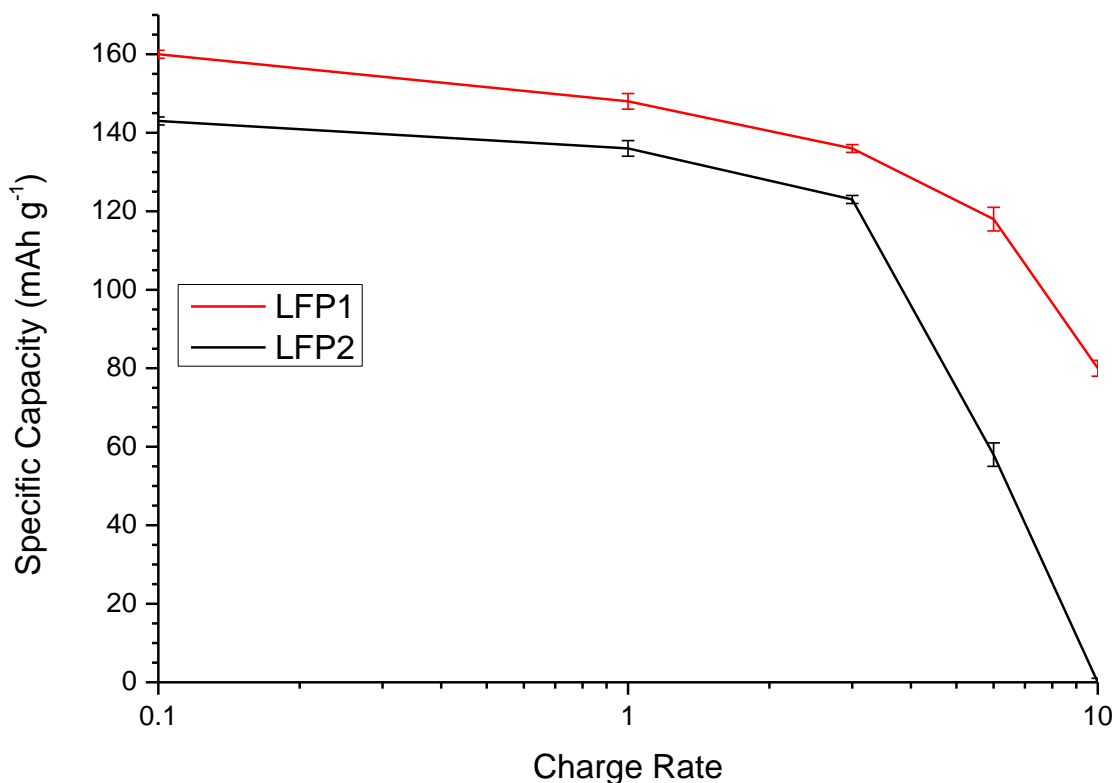

Figure 7.5. Rate capability plots of 2032 coin cells, half-cell testing (23°C) vs Li (Alfa Aesar) in LP30 electrolyte, using CCCV testing in the voltage range of 2.0V – 4.0V. a) benchmark LiFePO4 1 (LFP1); b) benchmark LiFePO4 2 (LFP2).

The Mössbauer spectra of these two materials and the hyperfine parameters of the fits are provided in Figure 7.6 and Table 7.2. The two materials are denoted as LFP1 and LFP2; the material with the greater specific capacity is LFP1 as seen in Figure 7.5.

Table 7.2. Hyperfine parameters of two benchmark LFP powder materials.

	CS (mm s^{-1})	QS (mm s^{-1})	Γ/2 (mm s^{-1})	Area (%)
LFP1	1.24	2.97	0.17	97.8
	0.25	0.74	0.17	2.2
LFP2	1.24	2.98	0.19	36.0
	1.19	3.01	1.63	62.8
	0.41	0.68	0.19	1.3

Both materials indicated a minor contribution of Fe^{3+} that is not consistent with the expected hyperfine parameters of $FePO_4$ and is considered an impurity phase, not identified through x-ray diffraction, that is investigated in more detail in subsequent spectra. The XRD data of these material both show well crystalline, single-phase olivine $LiFePO_4$, and no indication of second phases, or amorphous components. The majority of the area for each Mössbauer spectrum indicates Fe^{2+} with hyperfine parameters consistent with $LiFePO_4$. LFP1 can be fit using a single Fe^{2+} doublet, where LFP2 requires 62.8% of the spectral area to be fit using an additional doublet with very high linewidth.
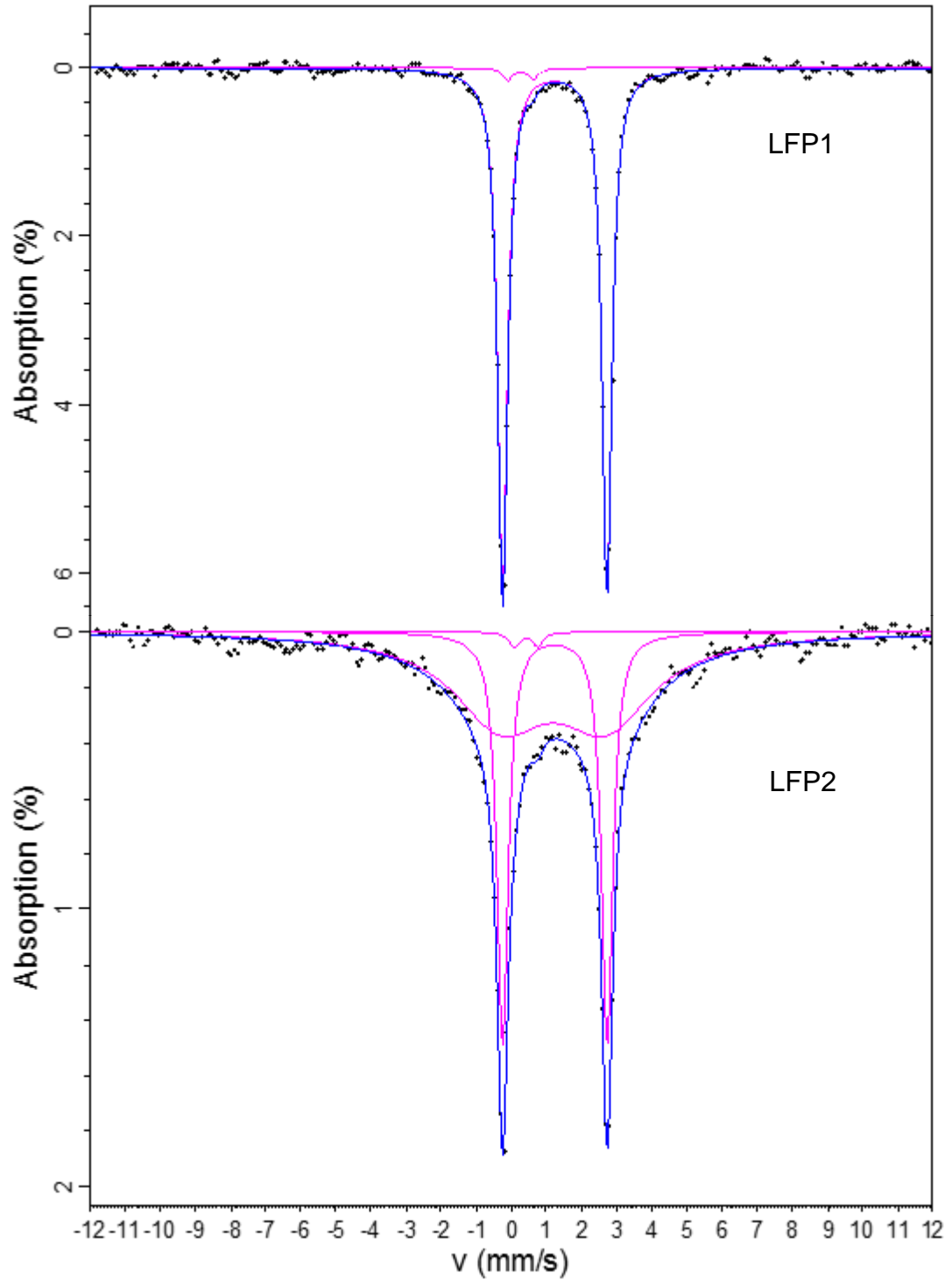
Figure 7.6. Room temperature Mössbauer spectra of two benchmark LFP powder materials. (LFP1 top and LFP2 bottom).

Both doublets in LFP1 have narrow linewidths, indicating a high degree of crystallinity, while the large, high linewidth doublet in LFP2 indicates that most of the LFP (which all of the Fe^{2+} is indicative of) is much less crystalline, or much more distorted. The cause of this site distortion is unclear, due to the limited access to information regarding these materials, however these two spectra suggest that the presence of this high linewidth doublet may be connected to poor electrochemical properties, qualitatively. As both materials were studied as powders their differences must be attributed to the synthesis of the LFP – synthesis route, calcination times / temperatures etc. – and not differences in the electrode fabrication process.

To identify the minor Fe^{3+} contribution, and as a gateway to determine whether Mössbauer measurements could be taken of LFP in-situ, on electrodes, a measurement of the aluminium foil used as the current collector was taken for one week (longer than the measurements for LFP1 and LFP2) which resulted in zero absorption. The Mössbauer spectra of LFP1 and LFP2 are presented in Figure 7.7 and Figure 7.8 respectively, and the hyperfine parameters of both fits in Table 7.3.
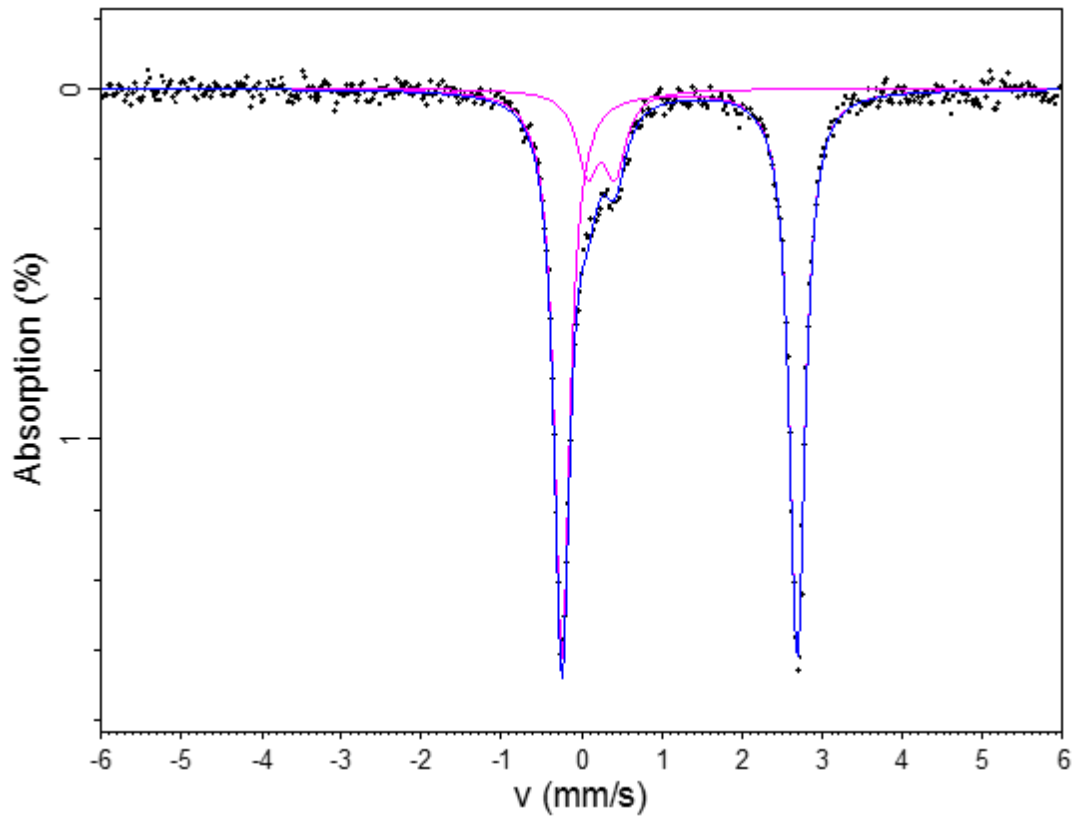
Figure 7.7. Room temperature Mössbauer spectrum of LFP1, high capacitance LFP electrode.
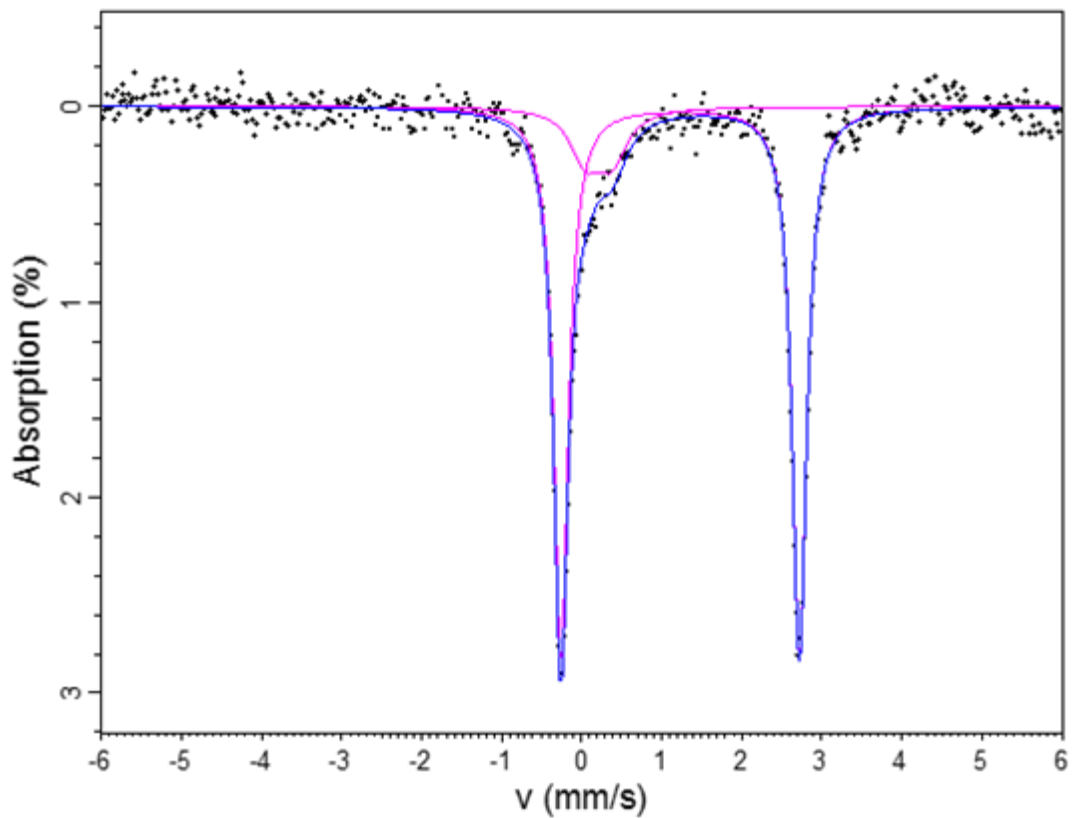

Figure 7.8. Room temperature Mössbauer spectrum of LFP2, low capacitance LFP electrode.

	CS (mm s^{-1})	QS (mm s^{-1})	Γ/2 (mm s^{-1})	Area (%)
LFP1	1.22	2.93	0.12	84.3
	0.24	0.34	0.17	15.7
LFP2	1.23	2.97	0.11	84.3
	0.21	0.33	0.23	15.7

Table 7.3. Hyperfine parameters of two benchmark LFP electrodes.

Comparing the spectra in Figure 7.7 and Figure 7.8 there is no significant difference in the fits applied. This observation indicates that the process of fabricating electrodes effects the hyperfine structure of LFP, suggesting that studying electrodes may not be suitable for understanding differences in performance, and that studying LFP powders may be more suitable for such objectives. The study encapsulated in upcoming Figure 7.9 indicates that this change is observable for LFP that has been dissolved in NMP to form a printable ink, and is not caused by calendering, heating or any other step of the electrode fabrication process.

A preliminary investigation was conducted on lab-scale LFP samples, extracted from the cell fabrication process at different points, to isolate the process step during which the hyperfine structure is most significantly altered, as observed in the Mössbauer spectral changes between powders and electrodes. This investigation involved samples of; LFP powder, LFP ink directly encapsulated in sample holder (no Al foil), LFP electrode pre-electrolyte, LFP electrode after complete cell fabrication.

Analysis of the spectra presented in Figure 7.9 indicates that the LFP powder used in this study contained the "less crystalline" Fe^{2+} phase observed in the benchmark material with the reduced specific capacity, as seen in the top-most spectrum. It would be inappropriate to suggest that the Fe^{3+} impurity phase is or is not present in this spectrum due to the high amount of absorption present from this "less crystalline" Fe^{2+} phase. In the second spectrum this "less crystalline" phase is no longer present, indicating that the process of fabricating the powder into an electrode is influencing the crystallinity of the LFP. As this has not been observed previously, more extensive studies would be required to determine the precise cause of this observation. The small changes in the

hyperfine parameters of the Fe^{3+} impurity phase are due to the small relative area of this site and this phase can be considered unchanged by the cell fabrication process. As this phase was observed in the spectra of both benchmark powder materials it must be a result of the synthesis process, and the results of this brief investigation show that its hyperfine structure and its relative abundance are not affected by the cell fabrication process.

	CS (mm s^{-1})	QS (mm s^{-1})	Γ/2 (mm s^{-1})	Area (%)
Ink	0.46	0.72	0.22	3.7
Electrode	0.43	0.43	0.18	3.7
Fabricated cell	0.47	0.52	0.17	4.5

Table 7.4. Hyperfine parameters for Fe^{3+} doublet from fits of spectra presented in Figure 7.9.
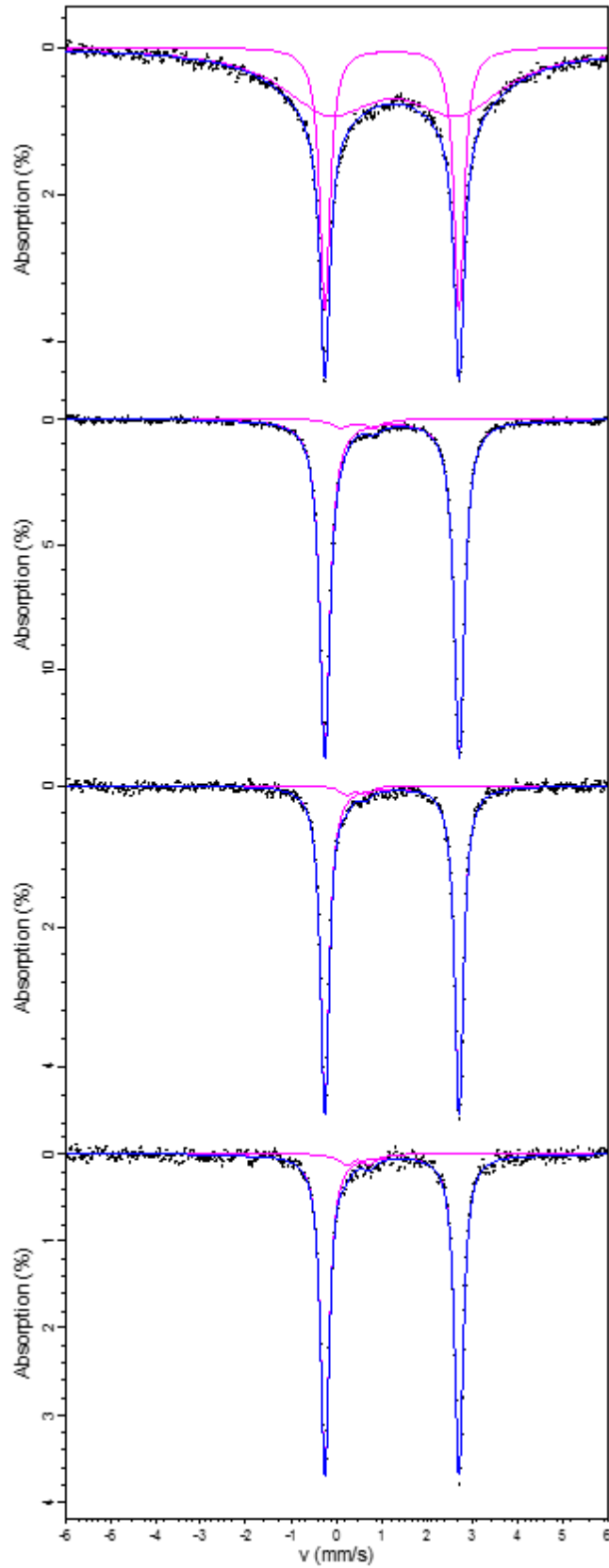
Figure 7.9. Room temperature Mössbauer spectra of LiFePO$_4$ at various process steps during fabrication process. Top to bottom - Powder, ink, electrode, electrode following cell fabrication.

The Fe^{3+} impurity phase is not observed using other characterisation techniques, including x-ray diffraction, HR-TEM and Raman spectroscopy. From the hyperfine parameters of this site it is known that the iron is ferric, paramagnetic, and likely IV co-ordinated. The presence of this phase in Mössbauer spectra has been documented previously, and its exact composition not identified. Yamada et al. shows that its abundance can be reduced by increasing the sintering temperature of $LiFePO_4$ although it is still present at their highest explored temperature of 800 °C, and they suggest it may be formed by small amounts of oxygen in the inert flow gas used during synthesis and may be amorphous or nanoparticulate due to it not being detected by x-ray diffraction [3]. Prince et al. made similar comments regarding this phase, suggesting it may be attributed to nanoparticulate material or defects in the crystal structure [14]. Hannoyer et al., also observing this spectral feature, concluded that it may be caused by Fe^{3+} occupancy of cationic positions in the olivine structure, agreeing with Prince's suggestion of crystal defects [37]. In the Hannoyer study, this phase was observed in $LiFePO_4$ material synthesised by solid state reaction, spray pyrolysis and through a wet chemical route, indicating that it is not process route specific.

To identify this phase low temperature Mössbauer spectroscopy measurements were taken of an LFP electrode that had been discharged to approximately 50%, at temperatures from 293 K to 10 K, in order to determine a range for its magnetic ordering temperature, as shown in Figure 7.10. The 75 K spectrum is presented in Figure 7.10, showing no significant change to this site, and the expected magnetic ordering of $FePO_4$ (first observed at between 100 and 125 K). Spectra collected below 75 K are not presented due to the complex magnetic ordering of both $FePO_4$ and $LiFePO_4$ causing the area of interest to be obscured. The Mössbauer spectra of FeP, Fe_2P and Fe_3P all show ferric paramagnetic doublets at room temperature; FeP broadens largely by 90 K, Fe_2P and Fe_3P express complex magnetic ordering [50]. The paramagnetic nature of the site observed in the measured 75 K spectrum indicates that this phase is not an iron phosphide. Further study would be required to identify the structural origin of this site, which is not within the scope of this work to do.
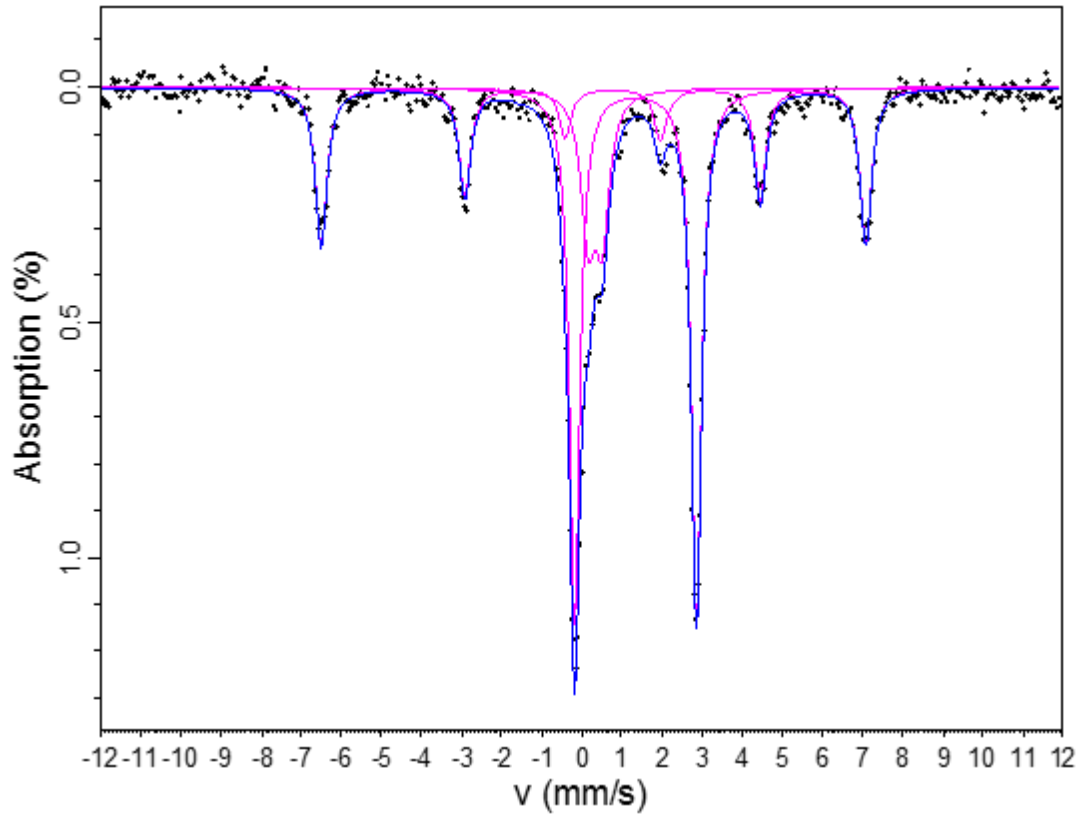
Figure 7.10. Mössbauer spectrum of 50 % discharged $LiFePO_4$ electrode, collected at 75 K.

To better understand how LFP functions as an energy storage material, and how Mössbauer spectroscopy may aid in this, the final objective was to collect Mössbauer spectra while cells were in operation. During operation lithium is transported between the anode and cathode, and the iron in $Li/FePO_4$ will be present as ferric or ferrous, this is known and well understood. One purpose for studying LFP operando was to determine whether any intermediate phases are present only during operation, as the lithium ions leave or enter the structure. The ability to observe the redox ratio of iron and relate it to a position along a charge / discharge curve could provide useful information for battery scientists as a cell that is 50% through a charge cycle may not necessarily have a 1:1 ratio of Fe^{2+} to Fe^{3+}. This information may be useful in observing the aging process of a cell, or in investigating differences in other key performance indicators. Mössbauer data collection typically occur over several days, as such operando measurements would cover a range of charge states, tailorable with charge rate.

A series of LFP electrodes were prepared using a 90:5:5 recipe (active material: Super P: PVDF (Solvay (5300)) with an electrode loading of ~ 5 g/cm^2 and an electrode density of ~ 2.0 g/cm^3. The electrodes were coated onto 20μm bare aluminium foil. Coin cells 2032 were tested in half-cell configuration vs lithium metal in LP30 electrolyte and cycled at C/10 rate several times to allow maximum electrode wetting and for the system to reach electrochemical equilibrium before each cell was stopped at a predetermined point along a discharge cycle. The electrodes from each cell were extracted as described previously, stored in airtight containers and transported from JMTC to SHU for analysis. Each electrode was taken from its container immediately prior to being placed in the spectrometer, to ensure each cell had been exposed to the atmosphere for the same duration. The cells collected were stopped at 20%, 50%, 70%, 80% and 100% through a discharge cycle – increasing the discharge % increases the lithium concentration in the electrode. The Mössbauer spectra of these five electrodes are presented in Figure 7.11 and the hyperfine parameters of the fits in Table 7.5.

Table 7.5. Hyperfine parameters of LFP electrodes at different discharge states.

| Discharge %	CS (mm s^{-1})	QS (mm s^{-1})	Γ/2 (mm s^{-1})	Area (%)
20%	1.24	2.92	0.11	21
	0.43	1.53	0.11	58
	0.21	0.36	0.24	21
50%	1.22	2.95	0.12	48
	0.44	1.53	0.12	34
	0.21	0.30	0.20	18
70%	1.23	2.95	0.12	72
	0.42	1.53	0.13	11.5
	0.19	0.31	0.17	16.5
80%	1.23	2.95	0.12	74
	0.44	1.52	0.12	9.4
	0.23	0.32	0.17	16.6
100%	1.23	2.96	0.12	84
	0.24	0.36	0.19	16
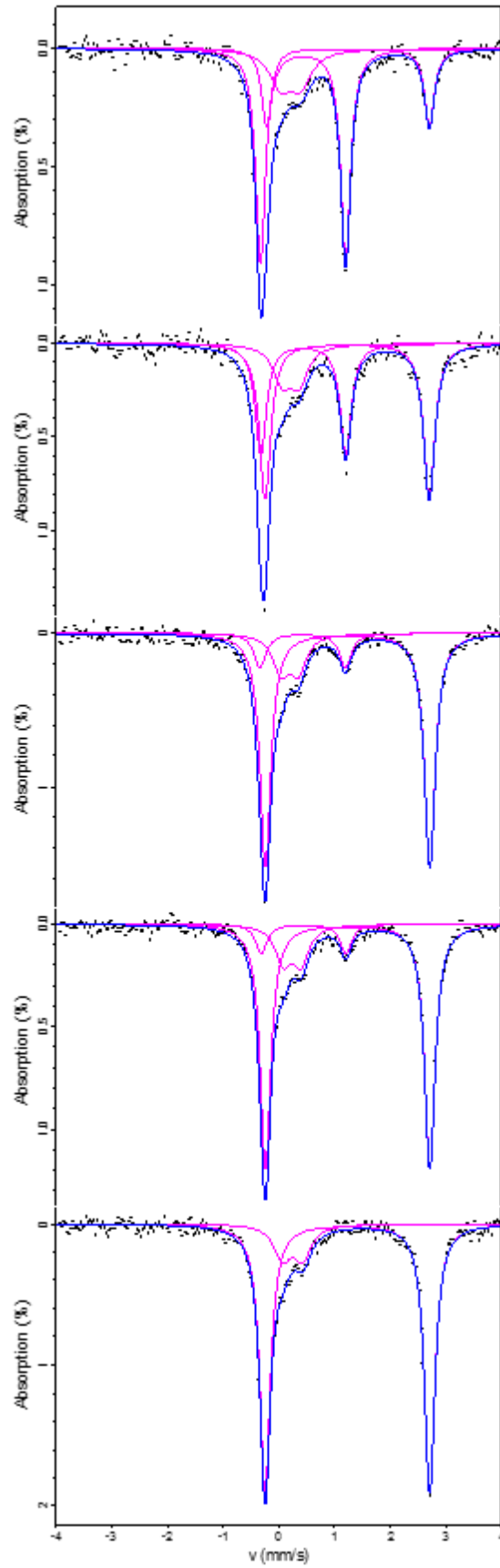
Figure 7.11. Room temperature Mössbauer spectra of LFP electrodes at, 20%, 50%, 70%, 80% and 100% discharged (top to bottom).

Each spectrum is fit using one ferrous doublet (CS ≈ 1.23 mm s⁻¹), and a ferric doublet (CS ≈ 0.24 mm s⁻¹), attributed to the LiFePO₄ phase and unidentified impurity phase respectively. In the four spectra presented for electrodes that are not 100% discharged there is a third doublet (CS ≈ 0.44 mm s⁻¹) associated with FePO₄. The relative areas of each spectral component vary as a function of the discharge percentage, as summarised in Figure 7.12.
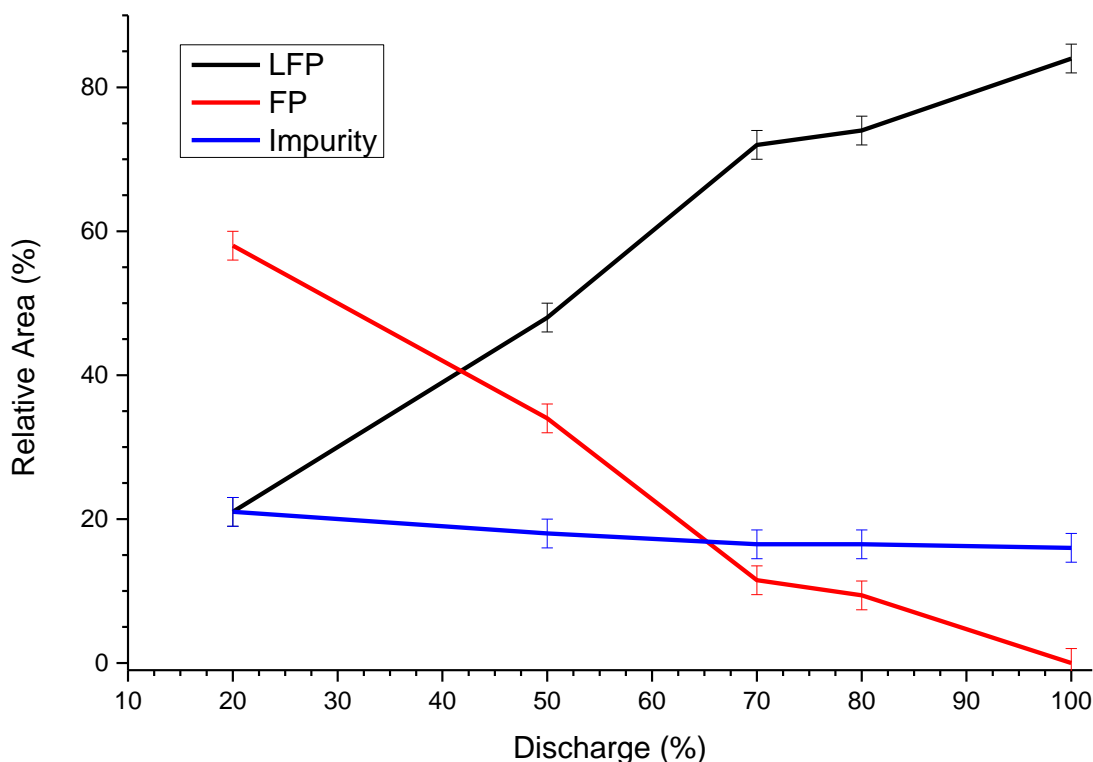

Figure 7.12. Relative spectral areas of doublets from Figure 7.11.

The capability of Mössbauer spectroscopy to study LFP electrodes, without extracting the active material from the electrode, may prove industrially useful in investigations where bulk, isotope specific characterisation is required. As the electrodes contain carbon and the PVDF polymer binder other techniques will be observing these phases as well as the LFP phase. X-ray diffraction may be useful for analysing the surface of the electrodes but not the bulk depth; Raman spectroscopy may cause sample burning and is site specific; sample preparation for electron microscopy and the high bias voltage during operation may affect the electrode and is also site specific. Lab-scale investigations into such electrodes, using Mössbauer Spectroscopy, may aim to probe the failure

mechanisms of electrode aging through excessive cycling, or further investigations into the influence of the otherwise unseen impurity phase.

All the LFP presented thus far were synthesised through a conventional solid-state sintering, ball milling process which produces well crystalline particles. A series of electrodes were prepared using flame spray pyrolysis (FSP), also at the five levels of discharge as those presented in Figure 7.11. The average crystallite size of materials prepared by FSP are typically nanoparticulate and are not subject to a sintering process [37], [47]. The FSP electrodes were prepared using the same mass of LFP, carbon black and PVDF binder, and following the sample fabrication process as previously outlined. The spectrum presented in Figure 7.13 of the 70% discharged electrode was collected for the same duration as the ball milled LFP electrodes. Due to the poor signal-to-noise ratio, the $LiFePO_4$ doublet in this fit exhibits the theoretical minimum linewidth of 0.097 mm s^{-1} and the second doublet has CS and QS values of 0 and 0.06 mm s^{-1} respectively. The maximum absorption value in this spectrum is approximately 0.23%, which is almost 90% lower than the 70% discharged ball milled electrode. Due to these factors, no further FSP electrodes were studied – meaningful data may take more than thrice the collection time for FSP compared to ball milled. Spectra could be collected at lower temperatures to increase the recoil-free fraction, thus improving data quality, however this would not allow for operando measurements to be conducted with the current spectrometer arrangement at SHU. Low temperature data collection would also only allow for comparison with other low temperature data, and was determined to not be within the scope of this project.
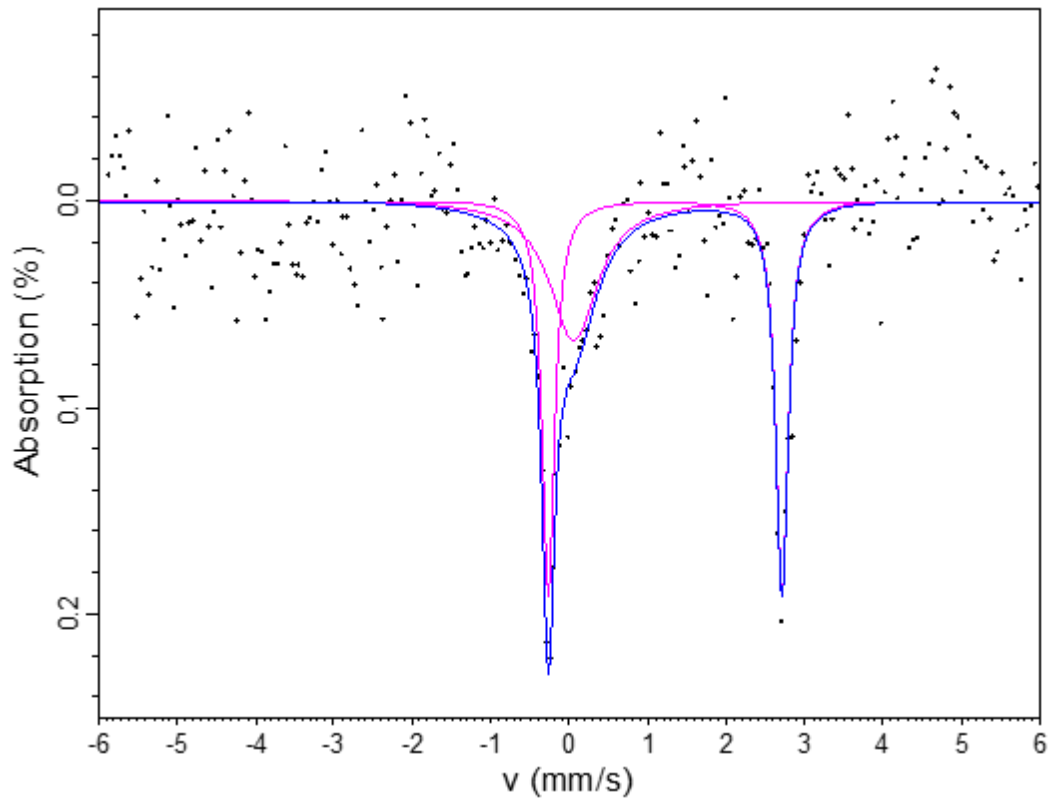
Figure 7.13. Room temperature Mössbauer spectrum of 70% discharged LFP, prepared by FSP.

7.3.4 Synchrotron Mössbauer Spectroscopy

The previous studies detailed in this chapter were found to be insightful for JMTC battery scientists, providing new and useful information in relation to LFP performance and a potential new method through which to characterise electrodes across various axes of interest (aging, etc.). The aim for the JMTC battery department was to achieve operando measurements as this would enable electrode to be analysed without having to open cells, and to collect data during their operation. There have been operando studies conducted using pouch cells [23], [43], however the objective of the work herein was to enable these studies using coin cells. In order to achieve operando measurements of coin cells there must be an opening in the cell casings which are too thick to allow γ-ray photons to pass through, while maintaining sufficient compression between the internal components and an airtight seal. The coin cell holders used during testing (as in Figure 7.14) have their contact points in the centre of the cell, which would also be problematic for operando Mössbauer measurements. The possible avenues

to achieve operando Mössbauer measurements of LFP were to either implement a pouch cell fabrication process, or to engineer a solution around the barriers to entry for using the existing coin cells. To use pouch cells would require new axillary accessories for the testing equipment, new electrode fabrication process, and a lengthy study into the comparability between coin cells and pouch cells, all of which would garner high time, capital and experimental costs that would be disruptive to the other members of the battery department.
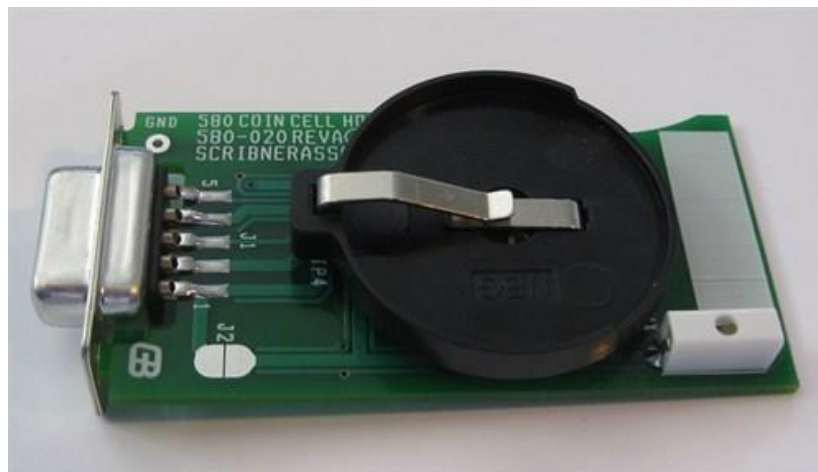

Figure 7.14. Commercial coin cell holder for electrochemical testing [51].

The most direct solution to the issue of γ-ray transmission was to produce coin cells with holes through which measurements could be obtained. The shape and size of the holes would need to be optimised such that suitable compression could still be achieved, and an airtight seal would still be maintained. Four candidate holes were produced;

Coin Cell A – 11 x 4 mm slit with rounded corners, approximately 44 mm^2 area

Coin Cell B – 10 mm diameter circle, 157 mm^2 area

Coin Cell C – 13 x 5 mm slit with rounded corners, approximately 65 mm^2 area

Coin Cell D – 11 x 6 mm slit with rounded corners, approximately 66 mm^2 area

One coin cell was constructed using each different hole geometry, with no electronic internal components, and placed into the Mössbauer spectrometer. Data collected through coin cell B provided the greatest number of counts per

second, as expected by its increased area. The obstacle in using coin cell B was that the compression between internal components was thought to be a concern even with an adapted commercial coin cell holder. To overcome this a new coin cell holder was designed with the help of Dr Noelia Cabello of JMTC, and was fabricated by the JMTC engineering department. Figure 7.15 depicts the final assembly concept drawing, and Figure 7.16 shows a selection of the engineering drawings.
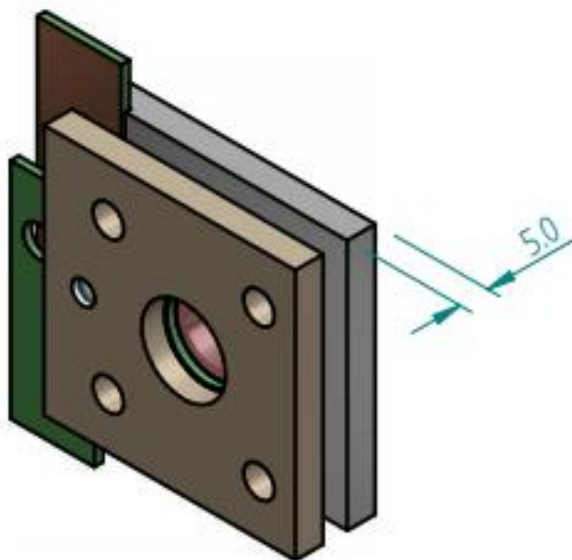

Figure 7.15. Final assembly concept drawing of custom coin cell holder.
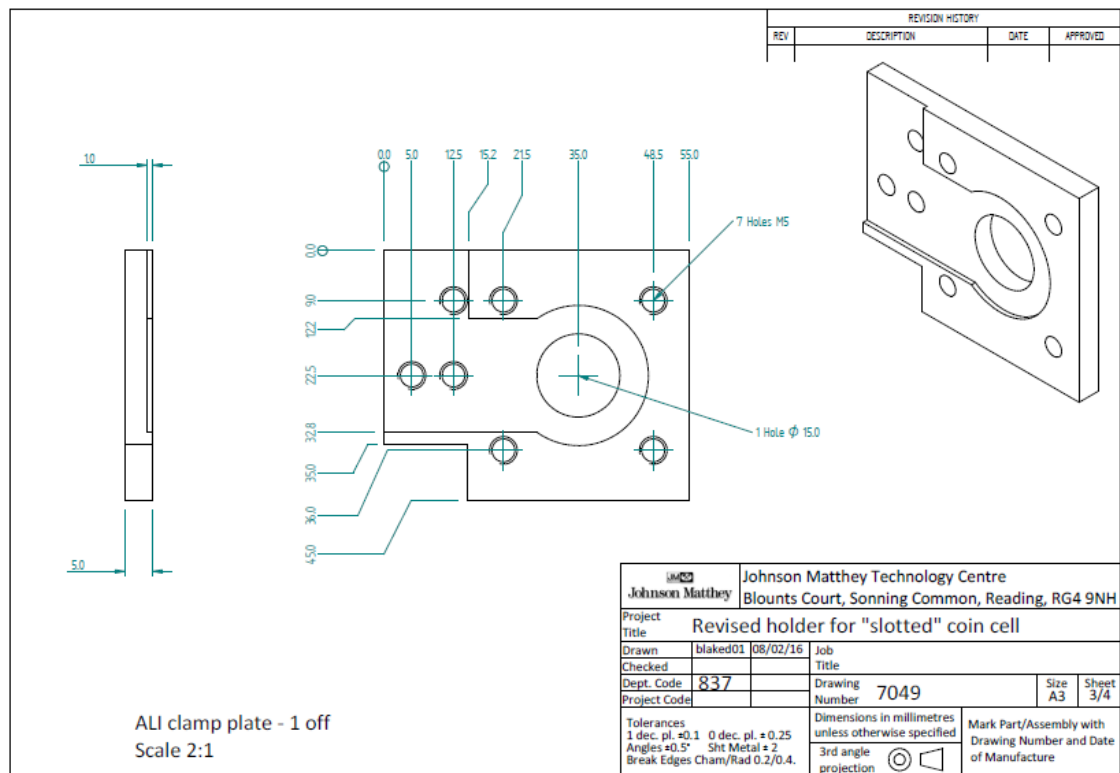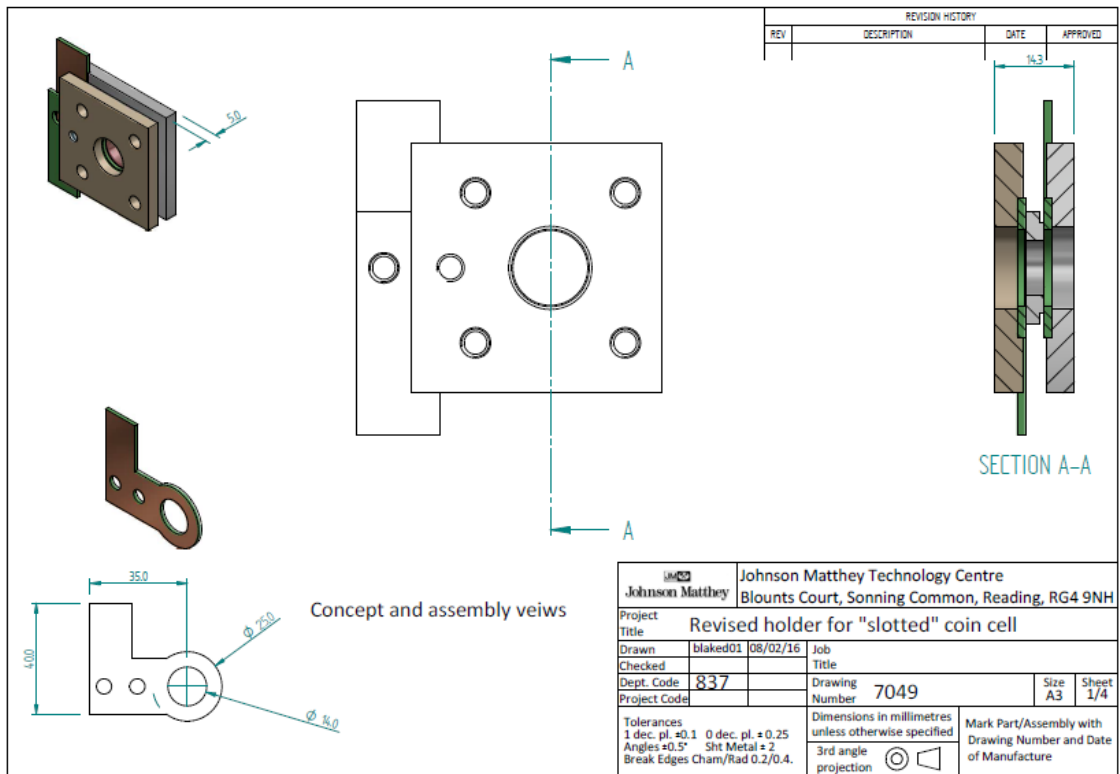
Figure 7.16. Engineering drawings of bespoke coin cell holder for operando transmission measurements.

The coin cell holder was fabricated out of plastic with copper plates facing one another for coin cell contact and electronic conduction. Four holes equidistant from the central hole were included in the design through which screws were used to apply adequate compression to the coin cell, while a smaller hole was included for a fixed spacer to be used, to avoid over compression. With this design it was possible to use the 10 mm diameter, coin cell B design as this coin cell would provide electronic contact around its circumference while allowing γ-ray transmission. Photographs of the finished, manufactured product can be seen in Figure 7.17.
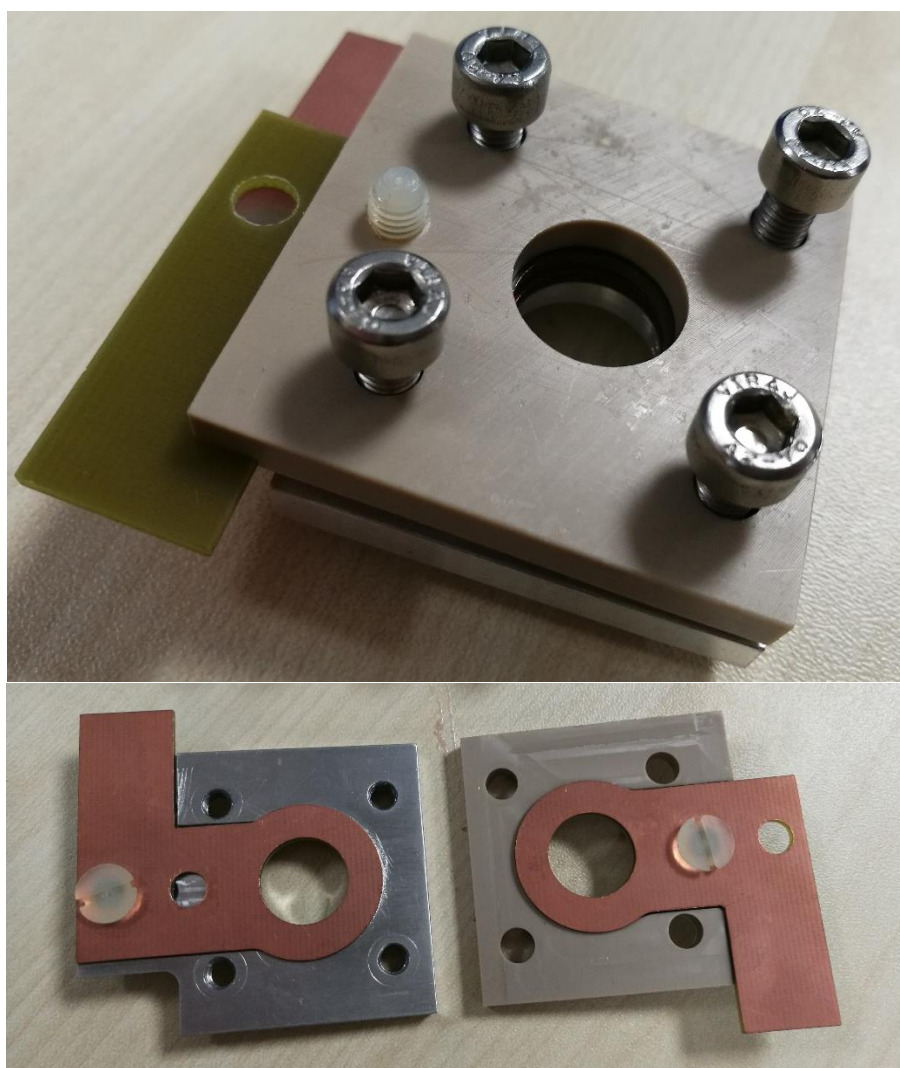
Figure 7.17. Custom made coin cell holder for operando Mössbauer measurements.

The custom cell holder was validated through using it to take electrochemical measurements and compare the results to those collected using a conventional cell holder. A standard coin cell was used for the first validation test, the EIS results, which are presented in Figure 7.18, showed no appreciable difference in the resistances between the two coin cell holders. Following this finding, coin cells were fabricated with the 10 mm diameter hole for γ-ray transmission. The hole in each cell was sealed using a different material – Kapton tape, aluminium foil or copper foil, the latter two of which may provide electrical conductivity at the possible expense of some γ-ray attenuation. It was found that using self-adhesive copper foil on the interior and exterior of the cell hole resulted in a reduction in the internal resistance of the cell when compared with the standard coin cell, as shown in Figure 7.19. Due to concerns of leakage it was decided that Kapton tape should be used, which resulted in no appreciable difference in internal resistance. The diameter of the semi-circle region of an EIS plot can be considered to be representative of the internal resistances [52]–[54].
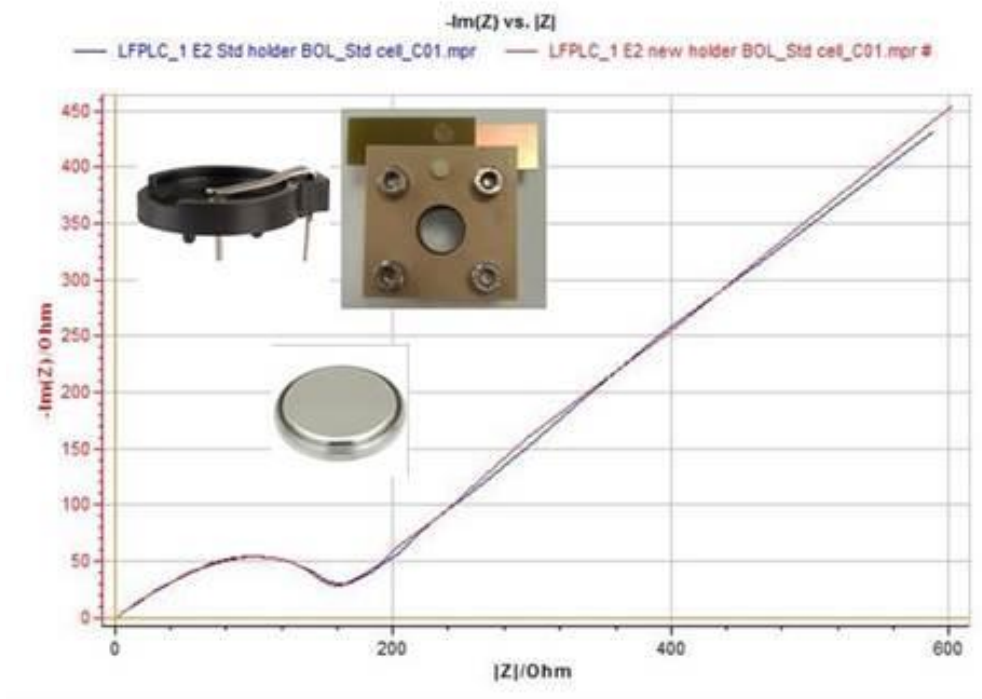

Figure 7.18. Beginning of life EIS measurements of standard coin cell with different holders.
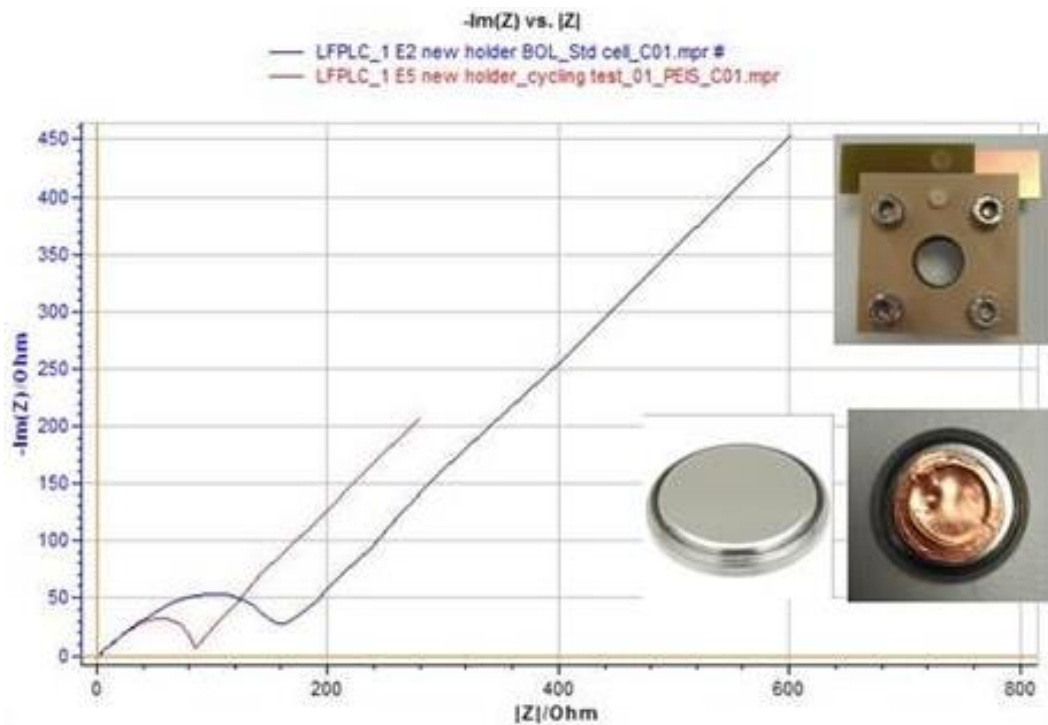
Figure 7.19. Beginning of life EIS measurements of standard coin cell and cell with 10 mm diameter hole covered with copper foil.
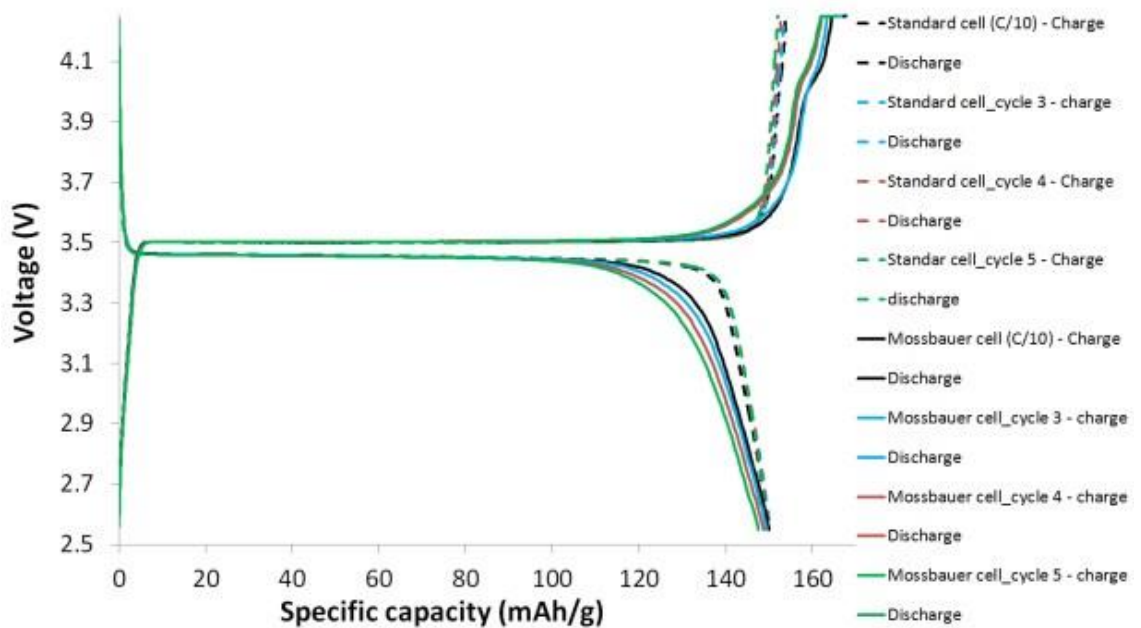

Figure 7.20. Charge-discharge curves at C/10 of LFP coin cell in standard coin cell holder (dashed lines) and novel, bespoke coin cell holder (solid lines).

With these validating EIS measurements, and charge / discharge curve comparison between the standard and novel cell and cell holder showing no appreciable differences (Figure 7.20), operando Mössbauer Spectroscopy using coin cells was feasible with these novel constructs.

A portable *Ivium CompactStat* was procured to enable operando Mössbauer measurements following a successful application for synchrotron beamtime at the European Synchrotron Radiation Facility, Grenoble, to utilise their ID18 Nuclear Resonance Beamline. For the synchrotron measurements the diameter of the hole in the coin cells was reduced to 5 mm as the beamline spot size is < 1 mm diameter and reducing the hole size improved the device safety, reducing the likelihood of electrolyte leakage or air ingress. Following on-site optimisation the charge / discharge regime was arranged to allow for a series of 20 minute data collection windows; open circuit potential, charge over 100 minutes, hold at 4.2 V for 20 minutes, discharge over 100 minutes and a final 20 minute hold at 2.5 V, as shown in Figure 7.21. The optimisation process involved collecting spectra for various durations to ensure suitable signal-to-noise was achieved in the shortest time possible. Figure 7.22 shows the custom coin cell holder, loaded with a coin cell with 5 mm diameter hole, in the ID18 synchrotron beamline.
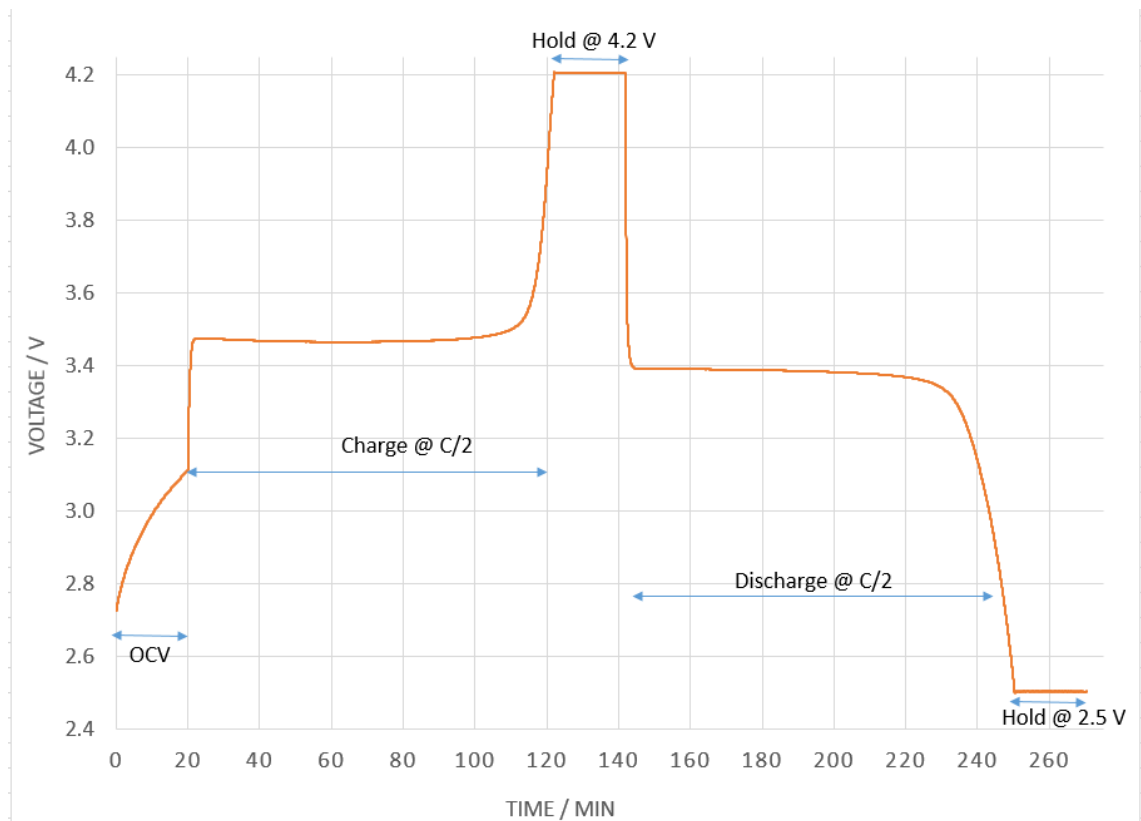

Figure 7.21. Charge / discharge regime for operando synchrotron Mössbauer measurements.
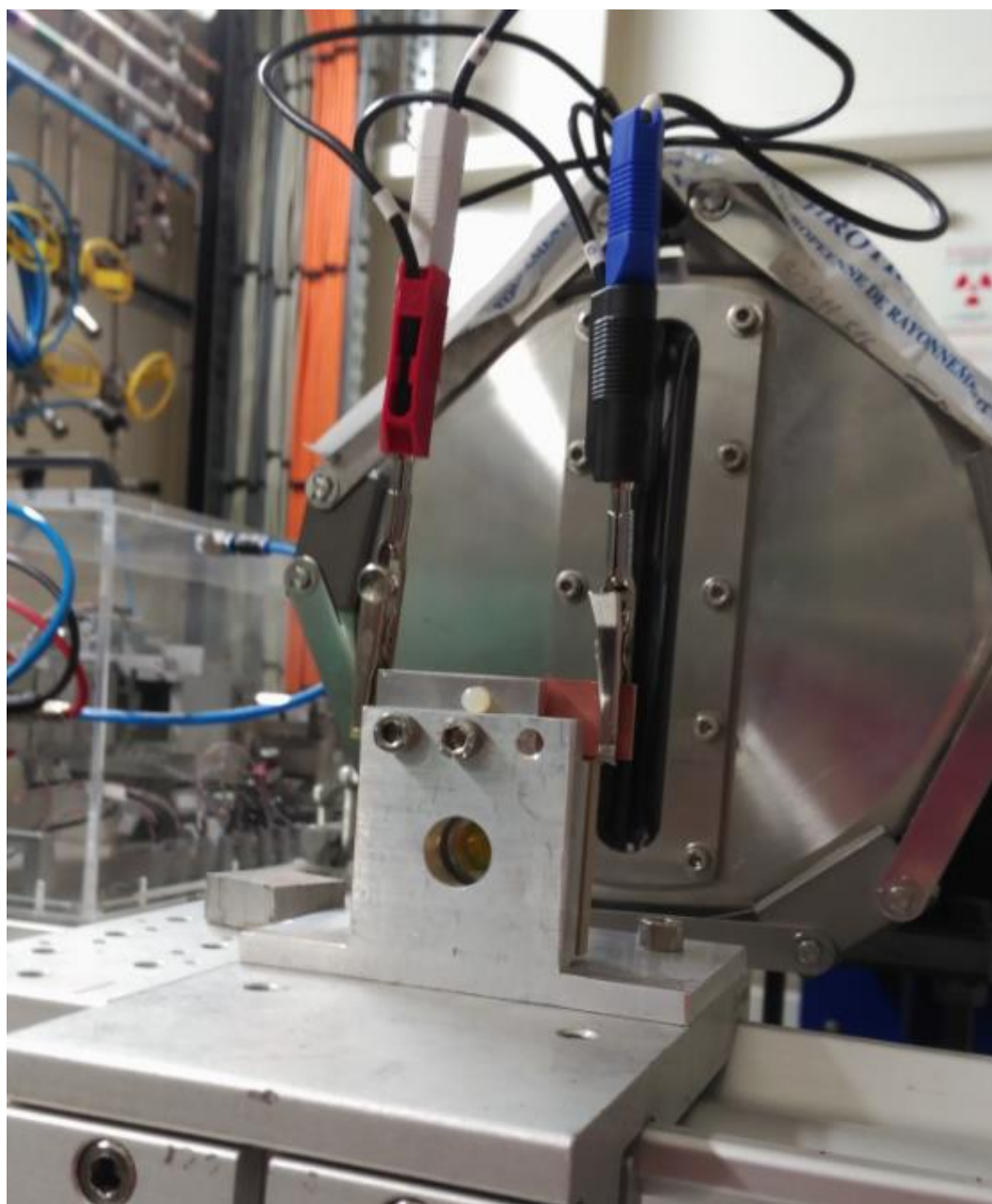
Figure 7.22. LFP coin cell in ID18 beamline at ESRF, Grenoble.

A summary of the data collected is presented in Figure 7.23, due to compatibility issues between ESRF and SHU data analysis software, this data could only be processed using Microsoft Excel. Analysis of the bottom-most spectrum and the middle "fully charged" spectrum show $LiFePO_4$ and $FePO_4$ respectively. The spectra collected during the charge and discharge periods show a reduced signal-to-noise ratio but do indicate the presence of both phases.
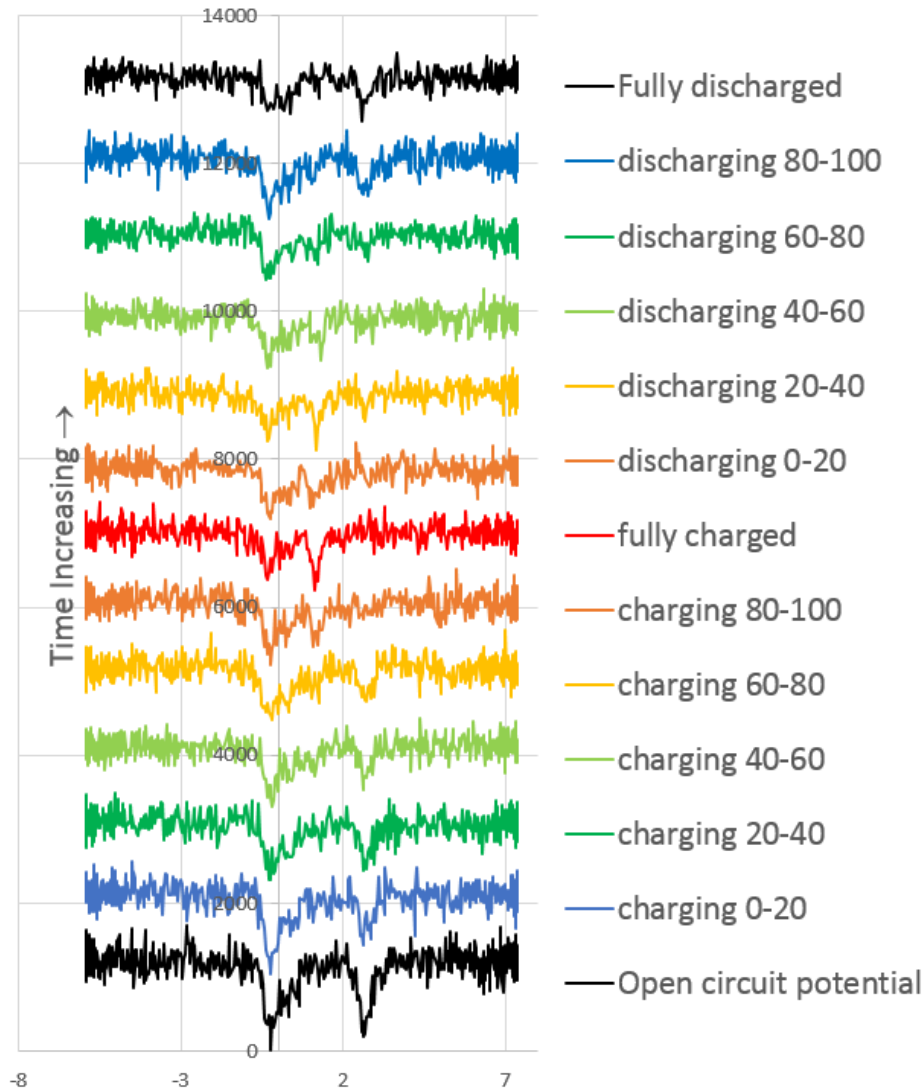
Figure 7.23. Summary of synchrotron LFP Mössbauer data.

The most significant issue in these data sets came from the relatively low iron loading of the electrodes. While lab-based Mössbauer is able to collect good quality data, this occurs over a period of days, where the duration is often not a deciding factor. There may have been some attenuation of the beam caused by the Kapton tape covering the windows, or from the metallic lithium anode, however both of these factors should have had minimal impact as both are made

of light elements. It may have been possible to have collected data with an increased signal-to-noise ratio if the charge / discharge cycles had been longer, and the data collection windows proportionally longer also, however this is not a practical solution due to the great instrument demand at ESRF and the limited time provided, whilst thoroughly appreciated. To overcome this issue, the two most direct solutions both bear some significant investment – one solution being to invest in pouch cell fabrication, as these have multiple layers and would have a greater amount of LFP through the γ-ray path; the second is to synthesise LFP using enriched ^{57}Fe which would allow for up to 50 times the amount of Mössbauer active isotope to be presented to the beam. Along with the previous factors concerning the use of pouch cells, when using them for operando measurements, with their multi-layered structure, there may be an increased tendency for beam attenuation. The use of enriched ^{57}Fe would be the most direct approach for a second round of synchrotron measurements, as this could be relatively easily implemented provided the phase that the isotope is presented in is compatible with LFP synthesis – that the precursor material is unchanged, other than the enrichment. The potential to increase the amount of Mössbauer active iron in the LFP would provide a great enhancement to the signal-to-noise ratio of the data, if it was not overly enriched to cause saturation effects, and this may enable for measurements of greater quality to be collected over shorter durations. Although the data collected from ESRF has a low signal-to-noise ratio, and the software compatibility issues have hindered the processing ability of the data collected, both of these issues can be overcome, and the data presented shows a clear proof-of-concept for operando Mössbauer measurements of energy storage – not only of LFP, as this concept could be used for other iron bearing battery materials too, and potentially to supercapacitors [55], [56].

7.4 Conclusions

This body of work, working to provide solutions to industrially relevant problems concerning LiFePO$_4$ as an energy storage material, garnered insightful information in the field that aided in the development and understanding of the system. The analysis of benchmark materials provided information inaccessible through other characterisation techniques into the cause of differences in specific capacity. It was also found that the process of fabricating electrodes may impede some kinds of investigations, as the Mössbauer spectra will be affected and some information may be lost in the process. A ferrous impurity phase was observed through Mössbauer spectroscopy that was undetected through other techniques, and some information was provided regarding its composition (not an iron phosphide). A proof of concept was developed for the operando collection of Mössbauer spectroscopic data using modified coin cells, using ID18 at ESRF, which could prove useful for many areas of energy storage material research. The works conducted for this body of work have provided gateway information to the strengths of Mössbauer spectroscopy and its usefulness in understanding current issues faced by the energy storage sector.

In the words of Johnson Matthey battery research scientist, Noelia Cabello, regarding the design and execution of the custom coin cell holder that was produced as a part of this study "In my opinion it was one of the main achievements and something that we would like to use at the synchrotron. In the past, previous designs lead to leaks or lack of compression, but we manged to make this design work without problem and get in-operando Mossbauer data!" The coin cell holder that was produced will not only be useful in future operando Mössbauer studies, but also has application for other transmission techniques that may be desired.

References

[1]   A. Volta, "On the electricity excited by the mere contact of conducting substances of different kinds," *Philos. Trans. R. Soc. London*, vol. 90, no. January, pp. 403–431, 1800.

[2]   C. Daniel, D. Mohanty, J. Li, and D. L. Wood, "Cathode materials review," *AIP Conf. Proc.*, vol. 1597, pp. 26–43, 2014.

[3]   A. Yamada, S. C. Chung, and K. Hinokuma, "Optimized $LiFePO_4$ for Lithium Battery Cathodes," *J. Electrochem. Soc.*, vol. 148, p. A224, 2001.

[4]   K. Turcheniuk, D. Bondarev, V. Signhal, and G. Yushin, "Ten years left to redesign lithium-ion batteries," *Nature*, vol. 559, pp. 467–470, 2018.

[5]   A. K. Padhi, K. S. Nanjundaswamy, and J. B. Goodenough, "Phospho-olivines as Positive-Electrode Materials for Rechargeable Lithium Batteries," *J. Electrochem. Soc.*, vol. 144, no. 4, pp. 2–8, 1997.

[6]   R. M. Ferguson, *Electricity*. William and Robert Chambers, 1873.

[7]   Encyclopedia Britannica, "John Frederic Daniell," 2018. [Online]. Available: https://www.britannica.com/biography/John-Frederic-Daniell#ref234214. [Accessed: 13-Nov-2018].

[8]   R. M. Dell and D. A. J. Rand, *Understanding Batteries*. The Royal Society of Chemistry, 2001.

[9]   The European Parliament and The Council of The European Union, *EU Battery Directive (2006/66/EC)*. 2006.

[10]   Eveready Battery Company, *EU Battery Directive (2006 / 66 / EC)*, vol. 44145, no. 440. 2012.

[11]   Sony, "Keywords to understanding Sony Energy Devices," 2016. [Online]. Available: http://www.sonyenergy-devices.co.jp/en/keyword/. [Accessed: 13-Nov-2018].

[12]   N. Nitta, F. Wu, J. T. Lee, and G. Yushin, "Li-ion battery materials: Present and future," *Mater. Today*, vol. 18, no. 5, pp. 252–264, 2015.

[13]   C. Heubner, S. Heiden, B. Matthey, M. Schneider, and A. Michaelis,

"Sodiation vs. Lithiation of FePO$_4$: A comparative kinetic study," *Electrochim. Acta*, vol. 216, pp. 412–419, 2016.

[14] A. A. M. Prince *et al.*, "Investigation of Fe valence in LiFePO$_4$ by Mössbauer and XANES spectroscopic techniques," *Solid State Commun.*, vol. 132, no. 7, pp. 455–458, 2004.

[15] M. A. E. Sanchez, G. E. S. Brito, M. C. A. Fantini, G. F. Goya, and J. R. Matos, "Synthesis and characterization of LiFePO$_4$ prepared by sol-gel technique," *Solid State Ionics*, vol. 177, no. 5–6, pp. 497–500, 2006.

[16] T. Shiratsuchi, S. Okada, J. I. Yamaki, S. Yamashita, and T. Nishida, "Cathode performance of olivine-type LiFePO$_4$ synthesized by chemical lithiation," *J. Power Sources*, vol. 173, pp. 979–984, 2007.

[17] D. Jugović *et al.*, "Preparation of LiFePO$_4$/C composites by co-precipitation in molten stearic acid," *J. Power Sources*, vol. 196, no. 10, pp. 4613–4618, 2011.

[18] J. Wu *et al.*, "*In situ* Raman spectroscopy of LiFePO$_4$: size and morphology dependence during charge and self-discharge," *Nanotechnology*, vol. 24, p. 424009, 2013.

[19] K. Okada, I. Kimura, and K. Machida, "High rate capability by sulfur-doping into LiFePO$_4$ matrix," *RSC Adv.*, vol. 8, no. 11, pp. 5848–5853, 2018.

[20] A. V Radhamani, "Magnetic phase investigations on fluorine (F) doped LiFePO$_4$," *Mater. Res. Express*, vol. 5, 2018.

[21] M. H. Braga, C. M Subramaniyam, A. J. Murchison, and J. B. Goodenough, "Nontraditional, Safe, High Voltage Rechargeable Cells of Long Cycle Life," *J. Am. Chem. Soc.*, vol. 140, no. 20, pp. 6343–6352, 2018.

[22] C. W. Kim, M. H. Lee, W. T. Jeong, and K. S. Lee, "Synthesis of olivine LiFePO$_4$ cathode materials by mechanical alloying using iron(III) raw material," *J. Power Sources*, vol. 146, no. 1–2, pp. 534–538, 2005.

[23] L. Aldon, A. Perea, M. Womes, C. M. Ionica-Bousquet, and J. C. Jumas,

"Determination of the Lamb-Mössbauer factors of LiFePO$_4$ and FePO$_4$ for electrochemical in situ and operando measurements in Li-ion batteries," *J. Solid State Chem.*, vol. 183, no. 1, pp. 218–222, 2010.

[24] M. Z. Bazant, "Theory of Chemical Kinetics and Charge Transfer based on Nonequilibrium Thermodynamics," 2012.

[25] K. Momma and F. Izumi, "VESTA: A three-dimensional visualization system for electronic and structural analysis," *J. Appl. Crystallogr.*, vol. 41, no. 3, pp. 653–658, 2008.

[26] M. Roberts *et al.*, "Design of a new lithium ion battery test cell for in-situ neutron diffraction measurements," *J. Power Sources*, vol. 226, pp. 249–255, 2013.

[27] P. Vanýsek, "Electrochemical series," in *Handbook of Chemistry and Physics*, 2010, p. 8.20-8.29.

[28] N. Spinner, L. Zhang, and W. E. Mustain, "Investigation of metal oxide anode degradation in lithium-ion batteries via identical-location TEM," *J. Mater. Chem. A*, vol. 2, no. 6, pp. 1627–1630, 2014.

[29] B. Wu, Y. Ren, and N. Li, "LiFePO$_4$ Cathode Material," in *Electric Vehicles – The Benefits and Barriers*, 2011, pp. 199–216.

[30] G. Berckmans, M. Messagie, J. Smekens, N. Omar, L. Vanhaverbeke, and J. Van Mierlo, "Cost projection of state of the art lithium-ion batteries for electric vehicles up to 2030," *Energies*, vol. 10, no. 9, 2017.

[31] Y. P. Wu, E. Rahm, and R. Holze, "Carbon anode materials for lithium ion batteries," *J. Power Sources*, vol. 114, no. 2, pp. 228–236, 2003.

[32] N.-S. Choi, J.-G. Han, S.-Y. Ha, I. Park, and C.-K. Back, "Recent advances in the electrolytes for interfacial stability of high-voltage cathodes in lithium-ion batteries," *RSC Adv.*, vol. 5, no. 4, pp. 2732–2748, 2015.

[33] Y. Sheng, "Investigation of Electrolyte Wetting in Lithium Ion Batteries : Effects of Electrode Pore Structures and Solution," *Thesis*, no. December, 2015.

[34] Z. Zhang *et al.,* "Advanced Construction Strategy of All-solid-state Lithium Batteries with Excellent Interfacial Compatibility and Ultralong Cycle Life," *J. Mater. Chem. A*, 2017.

[35] BBC, "Samsung confirms battery faults as cause of Note 7 fires," 2017. [Online]. Available: https://www.bbc.co.uk/news/business-38714461. [Accessed: 16-Nov-2018].

[36] Samsung Newsroom, "[Infographic] Galaxy Note7: What We Discovered," 2017. [Online]. Available: https://news.samsung.com/global/infographic-galaxy-note7-what-we-discovered. [Accessed: 16-Nov-2018].

[37] B. Hannoyer, A. A. M. Prince, M. Jean, R. S. Liu, and G. X. Wang, "Mössbauer study on LiFePO$_4$ cathode material for lithium ion batteries," *Hyperfine Interact.*, vol. 167, no. 1–3, pp. 767–772, 2006.

[38] W. Porcher, P. Moreau, B. Lestriez, S. Jouanneau, F. Le Cras, and D. Guyomard, "Stability of LiFePO$_4$ in water and consequence on the Li battery behaviour," *Ionics (Kiel).*, vol. 14, no. 6, pp. 583–587, 2008.

[39] W. Porcher, P. Moreau, B. Lestriez, S. Jouanneau, and D. Guyomard, "Is LiFePO$_4$ Stable in Water?," *Electrochem. Solid-State Lett.*, vol. 11, p. A4, 2008.

[40] M. Cuisinier, J. F. Martin, N. Dupré, A. Yamada, R. Kanno, and D. Guyomard, "Moisture driven aging mechanism of LiFePO$_4$ subjected to air exposure," *Electrochem. commun.*, vol. 12, no. 2, pp. 238–241, 2010.

[41] J. F. Martin, M. Cuisinier, N. Dupré, A. Yamada, R. Kanno, and D. Guyomard, "More on the reactivity of olivine LiFePO$_4$ nano-particles with atmosphere at moderate temperature," *J. Power Sources*, vol. 196, no. 4, pp. 2155–2163, 2011.

[42] X. Li, Z. Shao, K. Liu, Q. Zhao, G. Liu, and B. Xu, "Effect of F-doping on the properties of LiFePO$_{4-x/3}$F$_x$/C cathode materials via wet mechanical agitation-assisted high-temperature ball milling method," *J. Solid State Electrochem.*, pp. 1–7, 2018.

[43] P. E. Lippens *et al.,* "How Mössbauer spectroscopy can improve Li-ion

batteries," *Hyperfine Interact.*, vol. 206, pp. 35–46, 2012.

[44] A. S. Andersson, B. Kalska, L. Haggstrom, and J. O. Thomas, "Lithium extraction/insertion in LiFePO$_4$: An X-ray diffraction and Mössbauer spectroscopy study," *Solid State Ionics*, vol. 130, no. 1–2, pp. 41–52, 2000.

[45] M. M. Thackeray, C. S. Johnson, J. T. Vaughey, N. Li, and S. A. Hackney, "Advances in manganese-oxide 'composite' electrodes for lithium-ion batteries," *J. Mater. Chem.*, vol. 15, no. 23, pp. 2257–2267, 2005.

[46] R. Strobel and S. E. Pratsinis, "Flame aerosol synthesis of smart nanostructured materials," *J. Mater. Chem.*, vol. 17, no. 45, pp. 4743–4756, 2007.

[47] W. Y. Teoh, R. Amal, and L. Mädler, "Flame spray pyrolysis: An enabling technology for nanoparticles design and fabrication," *Nanoscale*, vol. 2, no. 8, p. 1324, 2010.

[48] K. Vasundhara, S. N. Achary, S. K. Deshpande, P. D. Babu, S. S. Meena, and A. K. Tyagi, "Size dependent magnetic and dielectric properties of nano CoFe$_2$O$_4$ prepared by a salt assisted gel-combustion method," *J. Appl. Phys.*, vol. 113, no. 19, 2013.

[49] J. Reklaitis, R. Davidonis, A. Dindune, and D. Valdniece, "Characterization of LiFePO$_4$/C composite and its thermal stability by Mössbauer and XPS spectroscopy," *Phys. Status Solidi Basic Res.*, vol. 253, no. 11, pp. 2283–2288, 2016.

[50] R. E. Bailey and J. F. Duncan, "Mossbauer and Nuclear Magnetic Resonance Studies of Several Iron Phosphides," *Inorg. Chem.*, vol. 481, no. 17, pp. 1444–1447, 1966.

[51] Alvatek, "580 Battery Test System," 2016. [Online]. Available: https://www.alvatek.co.uk/580-battery-test-system/.

[52] N. Dupré, J. F. Martin, J. Degryse, V. Fernandez, P. Soudan, and D. Guyomard, "Aging of the LiFePO$_4$ positive electrode interface in electrolyte," *J. Power Sources*, vol. 195, no. 21, pp. 7415–7425, 2010.

[53] H. D. Yoo, J. H. Jang, J. H. Ryu, Y. Park, and S. M. Oh, "Impedance analysis of porous carbon electrodes to predict rate capability of electric double-layer capacitors," *J. Power Sources*, vol. 267, pp. 411–420, 2014.

[54] B. A. Mei, O. Munteshari, J. Lau, B. Dunn, and L. Pilon, "Physical Interpretations of Nyquist Plots for EDLC Electrodes and Devices," *J. Phys. Chem. C*, vol. 122, no. 1, pp. 194–206, 2018.

[55] C. V. V. M. Gopi, A. Somasekha, A. E. Reddy, S. K. Kim, and H. J. Kim, "One-step facile hydrothermal synthesis of Fe_2O_3@$LiCoO_2$composite as excellent supercapacitor electrode materials," *Appl. Surf. Sci.*, vol. 435, pp. 462–467, 2018.

[56] C. Lee, S. K. Kim, J. H. Choi, H. Chang, and H. D. Jang, "Electrochemical performances of iron-cobalt oxides nanoparticles loaded crumpled graphene for supercapacitor," *J. Alloys Compd.*, vol. 735, pp. 2030–2037, 2018.

8. Conclusions

The development of communication between industrial scientists and Mössbauer spectroscopists, and the realisation of the technique's capability, were the overarching themes of the studies discussed in this thesis. In each of the catalytic materials studied, the pertinent questions revolved around understanding the materials, how they function, how they age, and how to characterise differences in these materials where other techniques were unable to do so. Determining the active phases for different catalysts was a common objective, as well as the desire to characterise the phases present before and after the catalyst had been used. Once the phases caused by ageing can be identified, their formation can be observed and assessed by altering the materials used – for example, does doping this material result in a greater abundance of the active phase after a given amount of service time? One common rationale for using Mössbauer spectroscopy in these studies was that the techniques readily available to the industrial scientists were unable to observe differences, whether crystallographic or vibrational; or through electron microscopy, where there were significant differences in materials performance. In the studies presented in these works, Mössbauer spectroscopy of materials that, when observed through these other techniques gave similar results, have shown significant differences.

A series of rare earth orthoferrites ($LaFeO_3$, $NdFeO_3$, $SmFeO_3$, $EuFeO_3$ and $GdFeO_3$) was studied using a comprehensive suite of characterisation techniques; X-ray fluorescence, X-ray diffraction, Raman spectroscopy and Mössbauer spectroscopy. Debye temperatures were approximated, with good agreement with existing literature, through the interpretation of the temperature dependence of the centre shift observed through low temperature Mössbauer spectroscopy. The approximated Debye temperatures were related to the vibrational modes of the materials, and their structural properties were derived from Rietveld refinement of XRD patterns. This study culminated in a journal publication in the Journal of Physics: Condensed Matter.

Lanthanum ferrite perovskites were also studied for their application as heterogenous catalysts in petrol car emission control. The influence of particle size, as a result of different synthesis methods, was investigated through

Mössbauer spectroscopy. The magnetic structure of $LaFeO_3$ was observed becoming superparamagnetic as the particle size decreased, exhibiting full superparamagnetism where the particle size was < 15 nm when synthesised by flame spray pyrolysis. The effect of catalytic ageing was investigated on a sample of $LaFeO_3$ synthesised by flame spray pyrolysis and aged in a catalytic testing rig. The ageing process was found to cause heat-induced sintered of the particles, causing the previously-superparamagnetic material to form magnetically ordered phases of $LaFeO_3$ and $\alpha\text{-}Fe_2O_3$. The effects of calcination temperatures were investigated in $LaFeO_3$ synthesised through a citrate-nitrate auto-combustion method, wherein increasing the temperature caused an increase in particle size, and the onset of superparamagnetism was observed in the material calcined at the lowest temperature (500 °C), which had the smallest crystallite size (18 nm). These studied aided in understanding the influence of material synthesis parameters and how these influence the catalytic performance of $LaFeO_3$ perovskites that showed no appreciable differences through X-ray diffraction patterns.

Nanoparticles of the iron carbides Fe_3C and Fe_5C_2, which play important roles in catalysts for Fischer-Tropsch synthesis, were studied using low temperature Mössbauer spectroscopy, and their Debye temperature were established. The Debye temperatures reported in this work differ from those found in existing literature, due to the nanoparticulate nature of the materials studied here, whereas much of the literature is concerned with bulk / sintered materials – however, good agreement is found with first principles Debye temperature calculations. Recoil-free fractions can be calculated by using the Debye temperature of a material, enabling relative quantification of different phases in a mixed-phase material. The room temperature recoil-free fractions of these iron carbides phases were calculated as 0.77 for Fe_3C, and as 0.799, 0.746 and 0.706 for the three iron sites of Fe_5C_2. The recoil-free fractions reported will allow for these important iron carbide phases to be relatively quantified in catalysts materials that have been aged to varying degrees, and to monitor how the phase abundances vary with age – this could be conducted on a number of candidate materials to observe how to ensure the most active phases are present

for the longest service lives, by varying the compositions, support matrices or post-synthesis treatments.

Iron molybdates ($Fe_2(MoO_4)_3$-MoO_3 were investigated as catalysts for the oxidation of methanol to formaldehyde, a widely used chemical precursor. The Mössbauer spectroscopy studies revealed that the synthesis methods conducted at lab-scale are representative of those conducted on industrial scale, indicating the direct relevance of lab-scale testing and materials modification. The ageing process of these catalysts was investigated by comparing two industrial catalyst samples – one fresh sample and one that had been used until the reactor was replenished with fresh catalyst. The Mössbauer spectrum of the aged material showed no significant difference to that of the fresh material at room temperature or at 10 K, indicating that the degree to which the material had been aged had not affected the Fe environments or oxidation states in these materials. This finding is consistent with the view that the primary mode of catalyst deactivation is the loss of molybdate groups from $Fe_2(MoO_4)_3$-MoO_3, through which the iron in the observed $Fe_2(MoO_4)_3$ phase is unaffected.

Investigations into $LiFePO_4$ were conducted on two commercial battery materials to investigate the origin of observed differences in their electrochemical properties. Mössbauer spectroscopic studies of the commercial powders indicated a second, less crystalline $LiFePO_4$ phase present in the material with the lower specific capacity. This spectral feature was not observed in electrodes fabricated using the two commercial materials, indicating that the fabrication process influences the hyperfine structure of $LiFePO_4$. The differences observed in the Mössbauer spectra of powders and electrodes made from the same $LiFePO_4$ indicate the necessity to observe these materials in both forms, so as to avoid the loss of information. A series of $LiFePO_4$ electrodes was discharged to different levels and studied through Mössbauer spectroscopy, revealing a change in relative abundances of $LiFePO_4$ and $FePO_4$ – a greater concentration of $LiFePO_4$ was observed with increased levels of discharge. In-operando synchrotron Mössbauer experiments were conducted at the ESRF synchrotron in Grenoble, France. A bespoke coin cell holder was successfully designed, fabricated and used in-operando, and its' use circumvented issues regarding electronic connectivity whilst maintaining internal pressure between components.

The synchrotron Mössbauer spectra were collected in 20 minutes intervals during charging and discharging. The in-operando measurements indicated that this experiment is viable, but future experiments will require ^{57}Fe sample enrichment in order to improve data quality.

Future work

Further work is suggested on the heterogenous catalyst perovskite materials, to better identify the active phase in catalysis, and to better explore the relationships between the particle size, hyperfine structure and the catalytic performance. The versatility of the perovskite structure to host a variety of elements in their ABX_3 structure means that studies pertaining to doping or co-doping, led by catalytic performance, can be explored and may yield new catalyst materials with enhanced performance or longevity. The influence of ageing on these catalysts, and how this affects relative phase abundance, should be investigated through Mössbauer spectroscopy by studying a series of samples, of the same material, aged for varying amounts of time, or in environments simulating varying degrees of extreme (temperature, oxidising, reducing, moisture, contaminants etc). This research area should be further investigated through more comprehensive single-synthesis route studies, such as increasing the range of temperatures of interest for the CNAC materials to better observe the perceived superparamagnetism or studying more than a single "aged" material, but a number of materials aged to varying degrees in order to study the process more closely.

The information obtained from the iron carbide studies should be developed by producing mixed phase systems, even mechanically mixed, with known ratios of the phases, to determine how accurately the Fe_3C and Fe_5C_2 phases could be distinguished. Additionally, studies with materials on various support matrices or with catalyst promoters would also yield more information. For all of the catalyst materials studied, where "aged" samples were studied, the ageing process was either complete or partial – further work should be pursued here by varying the extent of ageing in order to monitor the process across time from fresh to wholly inactive.

Further investigations into iron molybdate catalysts for the oxidation of methanol to formaldehyde may look to expand on the work presented herein. The work presented in this thesis suggest that the "aged" material observed was not aged to a degree capable of producing a phase change in $Fe_2(MoO_4)_3$, and only the delamination of molybdate groups was observed – a more comprehensive suite of samples could be studied, representing varying degrees of the ageing process, from mild to extreme, similar to the suggestion for the lanthanum ferrite catalysts. In addition to a more thorough ageing study, the influence of doping the material with different metals (other than copper), and in varying concentrations (other than 5 wt%) should be investigated, and the influence these dopants have on the catalytic properties be analysed and related to the Mössbauer spectra.

For the energy storage materials, doping and co-doping is one suggested area for further work, where certain elements prove to enhance performance and further understanding of how or why is desired. Recent literature suggests that anionic doping, such as with fluorine or sulphur, can enhance the electrochemical properties of $LiFePO_4$, however, there are currently issues regarding the formation of second phases from the fluorination / synthesis processes used. The author hopes to investigate processes to fluorinate iron phosphate and study the influence this has on the electrochemical properties and relate these observations to changes in the hyperfine structure as observed through Mössbauer spectroscopy – as well as through any crystallographic changes observed through XRD and Raman spectroscopy. Variations to the electrode components should be explored, such as changing the PVDF polymer binder potentially to bio-derived or electronically conductive polymers, or in exploring different forms of carbon. The ability to conduct lab-scale operando Mössbauer spectroscopic studies of cells would open a variety of potential for further work, where this is currently limited to synchrotron facilities or through drastic changes to the cells themselves, e.g. the use of pouch cells, which is not preferred. Some effort has been made since the conclusion of this thesis to enable lab-scale in-operando measurements to be made, however due to limitations of the current γ-ray sources such measurements are yet to be undertaken.